COLLEGE OF AGRICULTURE, ENGINEERING AND SCIENCE – UNIVERSITY OF KWAZULU NATAL

Optimisation of welding parameters to mitigate the effect of residual stress on the fatigue life of nozzle–shell welded joints in cylindrical pressure vessels

In fulfilment of the PhD-Eng. degree in mechanical engineering

Mthobisi Clyde ZONDI - 210556841

8/03/2018

Supervisor: Prof. Sarp Adali

Co-Supervisor: Dr Clinton Bemont

DECLARATION 1 – PLAGIARISM

I, **Mthobisi Clyde Zondi** declare that:

(i) The research reported in this thesis, except where otherwise indicated, is my original work.
(ii) This thesis has not been submitted for any degree or examination at any other university.
(iii) This thesis does not contain other persons' data, pictures, graphs or other information, unless specifically acknowledged as being sourced from other persons.
(iv) This thesis does not contain other persons' writing, unless specifically acknowledged as being sourced from other researchers. Where other written sources have been quoted, then:
   a. their words have been rewritten but the general information attributed to them has been referenced;
   b. where their exact words have been used, their writing has been placed inside quotation marks, and referenced.
(v) This thesis does not contain text, graphics or tables copied and pasted from the Internet, unless specifically acknowledged, and the source being detailed in the thesis and in the References section.

Signed:……..

Date:……..

Place:…….

SUPERVISORS' CONSENT

As the candidate's Supervisors, we agree to the submission of this thesis:

Prof. Sarp Adali	**Dr Clinton Bemont**
Signed:……	…….
Date:……	…….
Place:……..	…….

DECLARATION 2 – PUBLICATIONS

DETAILS OF CONTRIBUTION TO PUBLICATIONS that form part of this thesis, or include research presented in it, are as follows:

Publication 1:

M. Clyde Zondi. (2014). "Factors that affect welding-induced residual stress and distortions in pressure vessel steels and their mitigation techniques: a review." *Journal of Pressure Vessel Technology*, vol. 136 (4), 9 p. [Published]

Publication 2:

M. Clyde Zondi; Y. Tekane; E. Magidimisha; E. Wium; A. Gopal; C. Bemont. "Characterisation of submerged arc welding using infrared imaging technique." *R&D Journal of the South African Institute of Mechanical Engineering*, vol. 33, pp. 66-74. [Published]

Author contributions: M.C. Zondi compiled the protocol of experiments, assisted with conducting experiments, and wrote the paper. The other authors assisted with conducting experiments and reviewed the paper.

Publication 3:

M. Clyde Zondi; A. Venter; D. Marais; C. Bemont. "Characterisation of welding-induced residual stress using neutron diffraction technique." *Journal of Pressure Vessel Technology*, vol. 139, DOI: 10.1115/1.4037445. [Published]

Author contributions: M.C. Zondi compiled the protocol of experiments, assisted with conducting experiments, and wrote the paper. The other authors assisted with conducting experiments and reviewed the paper.

Publication 4:

M. Clyde Zondi; E. Wium; L. Shoke; A. Gopal; Y. Tekane; C. Bemont. "A 3D numerical model for a submerged arc welding nozzle-shell circumferential joint of high strength carbon steel." *Journal of Mechanical Engineering*. [Submitted]

Author contributions: M.C. Zondi compiled the protocol of experiments and the procedure for numerical modelling, assisted with conducting experiments, and wrote the paper. E. Wium developed the numerical model. The other authors assisted with conducting experiments and reviewed the paper.

Publication 5:

M. Clyde Zondi; L. Shoke; E. Wium; A. Gopal; Y. Tekane; C. Bemont. "The impact of welding-induced residual stress on fatigue strength of nozzle-shell weld joint of high strength carbon steel." *R&D Journal of the South African Institute of Mechanical Engineering*. [Submitted]

Author contributions: M.C. Zondi compiled the protocol of experiments, assisted with conducting experiments, and wrote the paper. L. Shoke oversaw the experimentation process. The other authors assisted with conducting experiments and reviewed the paper.

SIGNATURES:

STUDENT:……**Date**……

SUPERVISOR……..**Date**…….

ACKNOWLEDGEMENTS

The past five years have been long and exhausting in some regards, and challenging and exciting in others. I would not have made it thus far without the people who stood by me and rendered much-needed support.

I extend my sincere gratitude to my supervisors, Professor Sarp Adali and Doctor Clinton Bemont. Their guidance and assistance helped me eventually to finish this thesis within the targeted timelines. I also thank the team at the Council for Scientific and Industrial Research (CSIR), namely Dr Ajith Gopal, Mr Jonathan Stipinovich, Ms Lerato Shoke and Ms Elsmari Wium. Deon Malherbe and Leon Broodryk at the mechanical workshop provided assistance with the experimental setup and recordings. Dr Andrew Venter and Deon Marais from the South African Nuclear Energy Corporation (NECSA) were very helpful with coordinating access to the Neutron Diffraction facility, and assisting with the experiments. Thank you all.

I am indebted to my fellow engineers and colleagues who walked the path with me and were always available as a sounding board. Mr Yanga Tekane and Mr Sujo Mulamattathil have been reliable friends throughout. To my office manager, Ms Nitasha Boodhoo, my thanks go to you for organising my life.

To my close friend Chi – I'm grateful for all the support you continue to give me emotionally and spiritually. A big "thank you" to my little brother Njabulo for his unwavering support, even when he did not understand what I was doing. I thank my lovely wife for her understanding and patience when I took time away that should have been spent on family events – thank you kindly, my dear. Thanks to my children for their unwavering love, and to my mother for her support and prayers. Thank you, Mother.

The LORD is my Shepherd, I shall not want. I thank God for the strength, the gift of mental capacity to get through this project, and for His everlasting graciousness over me. Amen.

ABSTRACT

The process of welding steel structures inadvertently causes residual stress as a result of thermal cycles that the material is subjected to. These welding-induced residual stresses have been shown to be responsible for a number of catastrophic failures in critical infrastructure installations such as pressure vessels, ship's hulls, steel roof structures, and others. The present study examines the relationship between welding input parameters and the resultant residual stress, fatigue properties, weld bead geometry and mechanical properties of welded carbon steel pressure vessels. The study focuses on circumferential nozzle-to-shell welds, which have not been studied to this extent until now.

A hybrid methodology including experimentation, numerical analysis, and mathematical modelling is employed to map out the relationship between welding input parameters and the output weld characteristics in order to further optimise the input parameters to produce an optimal welded joint whose stress and fatigue characteristics enhance service life of the welded structure. The results of a series of experiments performed show that the mechanical properties such as hardness are significantly affected by the welding process parameters and thereby affect the service life of a welded pressure vessel. The weld geometry is also affected by the input parameters of the welding process such that bead width and bead depth will vary depending on the parametric combination of input variables. The fatigue properties of a welded pressure vessel structure are affected by the residual stress conditions of the structure. The fractional factorial design technique shows that the welding current (I) and voltage (V) are statistically significant controlling parameters in the welding process.

The results of the neutron diffraction (ND) tests reveal that there is a high concentration of residual stresses close to the weld centre-line. These stresses subside with increasing distance from the centre-line. The resultant hoop residual stress distribution shows that the hoop stresses are highly tensile close to the weld centre-line, decrease in magnitude as the distance from the weld centre-line increases, then decrease back to zero before changing direction to compressive further away from the weld centre-line. The hoop stress distribution profile on the flange side is similar to that of the pipe side around the circumferential weld, and the residual stress peak values are equal to or higher than the yield strength of the filler material. The weld specimens failed at the weld toe where the hoop stress was generally highly tensile in most of the welded specimens.

The multiobjective genetic algorithm is successfully used to produce a set of optimal solutions that are in agreement with values obtained during experiments. The 3D finite element model produced using MSC Marc software is generally comparable to physical experimentation. The

results obtained in the present study are in agreement with similar studies reported in the literature.

TABLE OF CONTENTS

LIST OF FIGURES

LIST OF TABLES

LIST OF APPENDICES

LIST OF ACRONYMS

LIST OF ACRONYMS

ABC	-	artificial bee colony
AC	-	Alternating current
ACO	-	ant colony optimisation
ANOVA	-	analysis of variance
ANN	-	artificial neural network
ASME BPVC	-	American Society for Mechanical Engineers, Boiler and Pressure Vessel Code
AIS	-	artificial immune system
ASTM	-	American Society for Testing and Materials
AWS	-	American Welding Society
bcc	-	body-centred cubic
BH	-	bead height
BP	-	bead penetration
BPNN	-	back-propagation neural network
BW	-	bead width
CA	-	constant amperage
C	-	Celsius
CP	-	compromised programming
CRS	-	controlled random search
CW	-	constant wire
DC	-	direct current
DF	-	desirability function
CCD	-	central composite design

CCT	-	continuous cooling temperature
CG HAZ	-	coarse grain heat affected zone
DC	-	direct current
DoE	-	design of experiment
DHD	-	deep-hole drilling
DM	-	decision maker
EA's	-	evolutionary algorithms
ES	-	evolutionary strategies
ESAB	-	Elektriska Svetsnings-Aktiebolaget
EDS	-	Energy Dispersive X-Ray Spectroscopy
ENS	-	effective notch stress
EPFM	-	elastic-plastic fracture mechanism
fcc	-	face-centred cubic
FCAW	-	flux cored arc welding
FCG	-	fatigue crack growth
FEA	-	finite element analysis
FE	-	finite element
FEM	-	finite element method
FG HAZ	-	fine grain heat affected zone
FD	-	fibre diameter
FM	-	filler metal
FNN	-	fuzzy neutral network
FR	-	feed rate
FSIR	-	FLIR short-wave infrared
FSW `	-	friction stir welding
FZ	-	fusion zone
GA	-	genetic algorithm

GA-NN	-	genetic neural network
GP	-	global programming
GMAW	-	gas metal arc welding
GTAW	-	gas tungsten arc welding
HAZ	-	heat-affected zone
HIC	-	hydrogen-induced cracking
HSLA	-	high strength low alloy
Hz	-	hertz
kN	-	kilonewton
MIG	-	metal inert gas
HSLA	-	high-strength low-alloy
I	-	current
IR	-	Infra red
JMAK	-	John-Mehl-Avrami-Kolmogorov
LBW	-	laser beam welding
LENS	-	laser-engineered net shaping
LEFM	-	Linear elastic fracture mechanics
LOM	-	light optical microscopy
LOP	-	lack of penetration
LP	-	laser power
MAUA	-	multiple attribute utility analysis
MEES	-	multi-objective elitist evolution strategy
MOEA	-	multiple objective evolutionary algorithm
MOGA	-	multi-objective genetic algorithm
MOP	-	multiple objective problem
MMC	-	metal matrix composition
MPA	-	Megapascal Pressure Unit

MPISI	-	materials probe for internal strain investigations
MRA	-	multiple regression analysis
MSR	-	mechanical stress relief
ND	-	neutron diffraction
NPP	-	nuclear power plant
NPGA	-	niche pareto genetic algorithm
NSGA	-	non-dominated sorting genetic algorithm
N-SIF	-	notch stress intensity factor
OA	-	optimisation algorithm
PCA	-	principal component analysis
PM	-	parent metal
PF	-	parent front
POS	-	pareto optimal set
PSO	-	particle swarm optimisation
PTAW	-	plasma transferred arc welding
PV	-	Pressure Vessel
PWHT	-	post-weld heat treatment
RA	-	regression analysis
RS	-	residual stress
RSM	-	response surface method
S	-	speed
SAW	-	submerged arc welding
SDSS	-	super duplex stainless steel
SEM	-	scanning electron microscopy
SIF	-	stress intensity factors
SFE	-	single factor effects
SMAW	-	shielded metal arc welding

SPEA	-	strength pareto evolutionary algorithm
SVR	-	support vector regression
SWIR	-	short-wave infrared
SSE	-	sums of squares due to error
TIG	-	tungsten inert gas
TS	-	tensile strength
TSR	-	thermal stress relief
TMM	-	thermal-mechanical-metallurgical
TTT	-	temperature time transformation
V	-	voltage
VEGA	-	vector-evaluated genetic algorithm
WBGA-MO	-	weight-based genetic algorithm for multi-objective optimisation
WFD	-	welding flux design
WPPOP	-	welding process parametric optimisation problem
WRS	-	welding-induced residual stress
WSS	-	weighted sum scalarisation
WM	-	weld metal
WCL	-	weld centreline
3D	-	three dimensional
4D	-	four dimensional

CHAPTER 1: INTRODUCTION

1.1 Background

Within certain industries and industrial operations, pressure vessels are a critical component of the plant equipment and operations. The fact that the vessel operates under pressure and may carry toxic, dangerous or hazardous contents means that great care is needed to ensure the safety of people who operate the equipment, and the environment within which it operates. Therefore, diligence must be applied when designing, fabricating or repairing pressure vessels. Any deviation from the specified principles and guidelines may lead to catastrophic consequences. Pressure vessels may be fixed through permanent attachment to infrastructure, or they might be mobile and transportable from one site to another. Figure 1.1 illustrates typical layouts for a pressure vessel. As illustrated in the figure, cylindrical pressure vessels typically consist of the following main parts:

- The *shell* comprises the largest portion; it is made of steel plate that has been subjected to forming processes (using heat and cold) and welding processes.
- The *spherical dome (head)* is placed at one end of the vessel and is joined to the shell by welding. It is built through metal pressing, spinning and roller-forming processes.
- *Nozzles* are pipe attachments used to fill or evacuate fluid into or from the vessel respectively. They can also be used for the mounting of instrumental equipment.
- *Man-holes* are inlets that are large enough to accommodate a person. They provide access into the pressure vessels, mainly for inspection purposes.
- *Compensation plates* are normally welded onto the shell in the circumferential direction to provide further stiffness, to compensate for strength lost due to nozzles and man-holes.

Commonly used pressure vessels in industry include boilers, reactors, condensers, columns, heat exchangers, pressurised tanks, drums, towers and air coolers. Typical shapes for these items are the sphere, cone and cylinder (Nabhani et al., 2012).

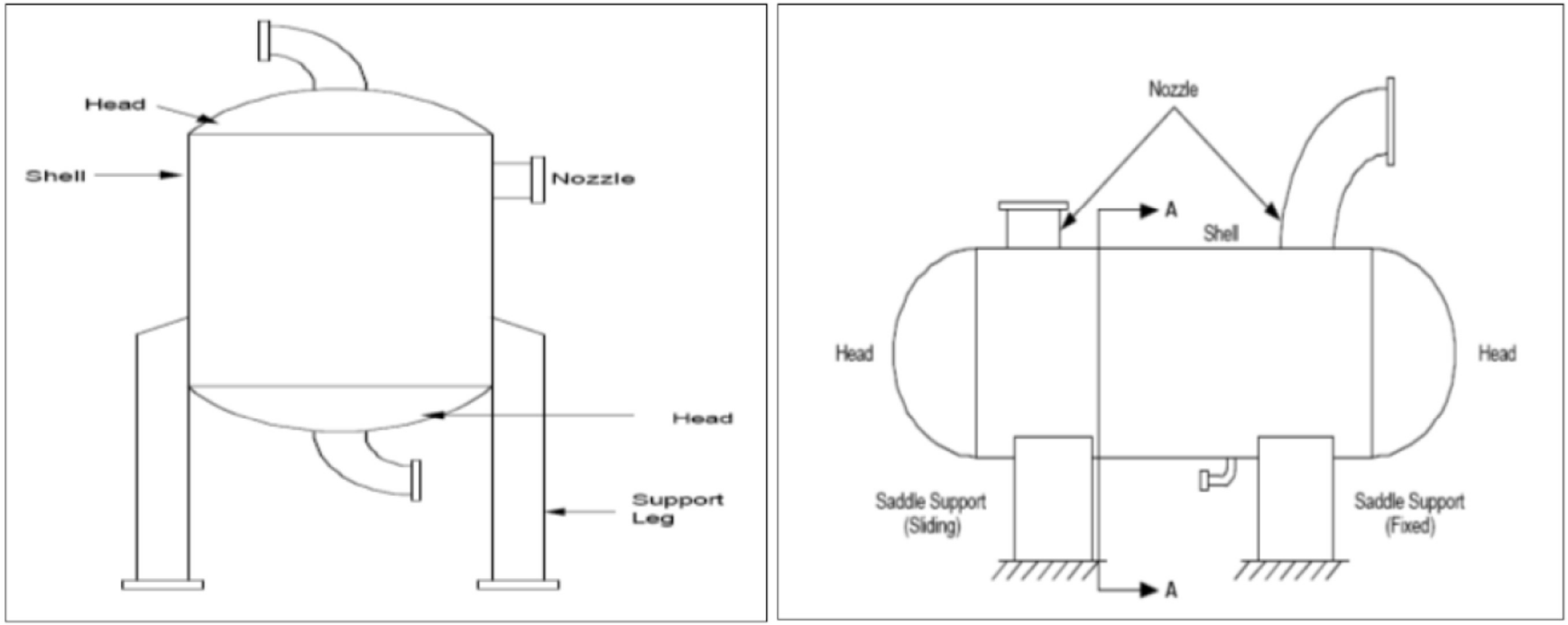

Figure 1-1: Typical pressure vessel layout
Source: Nabhani et al. (2012)

1.2 Nozzle-shell welded joints

In most industrial applications, pressure vessels require in-built nozzles for operational purposes. Nozzles or openings in pressure vessels are necessary for safe and optimal functionality but they result in structural vulnerability or even weakness of the pressure vessel. The nozzles range from small inert gas purge nozzles (e.g. for reactors) to large man-hole covered access nozzles (e.g. for large pressurised tanks).

Nozzles are usually attached onto pressure vessel shells using welding as a joining process. This renders such nozzle–shell joints vulnerable to failure, due to notch-related increases to local stress, welding-induced residual stress and other imperfections associated with welded joints. The reason is that nozzles are "discontinuities" which attract local intensification of stresses, thereby increasing the peak stress in the welded structure and reducing its fatigue strength (among other things). Furthermore, welded joints of pressure vessels are usually exposed to multi-axial loads and hence stresses. Multi-axiality may be further exacerbated by exposure to corrosive mediums and high temperatures, which some pressure vessels are likely to experience in certain industries (e.g. petroleum and chemical industries).

To ensure the integrity of welded pressure vessel structures, the design process for the nozzle–shell weld joint is comprehensively specified in most international design codes. This includes the code of the American Society for Mechanical Engineers, Boiler and Pressure Vessel Code (ASME BPVC), Section VIII, Divisions 1&2, 2007/2010. Welding joint types that are widely used in nozzle–shell applications include the following (Al-Mukhtar, 2010):

- Single fillet T-joint with partial penetration
- Angle joint with full penetration
- Cruciform joint with V-butt weld and partial penetration
- Cruciform joint with K-butt weld and partial penetration
- T-joint with fillet welds

1.3 The rate of failure in pressure vessels

According to Nabhani et al. (2012), stress-induced operating factors and stress-related defects account for approximately 24.4% of recurring catastrophic pressure vessel failures in process industries. Such factors and defects include fatigue, creep, stress corrosion cracking and embrittlement. Statistics from the US-based National Board of Boiler and Pressure Vessel Inspectors show that between 1992 and 2001, as many as 23 338 failure incidents in pressure vessels were reported in the US. The main causes of failure included stress, faulty design,

improper installation, fatigue, creep, corrosion and welding problems (Nabhani et al., 2012). Examples of major pressure vessel failures that have been reported over the years are shown in Table 1.1.

Table 1-1: Examples of pressure vessel failures

Vessel Description	Year	Place	Extent of Damage
22 680-kg pressure vessel (PV) in chemical plant exploded	2004	Houston, Texas, US	Damaged the church and nearby vehicles
20 petrol tanks, each carrying 3 million gallons, exploded in Buncefield Depot	2005	UK	43 people injured. 2 000 people evacuated from nearby neighbourhood
Heat exchanger exploded in a resin production facility	2008	Houston, Texas	Killed veteran plant supervisor
Storage tank exploded into flames in an oil refinery	2010	New Mexico, US	Two people died; two more were critically injured
90-m^3 PV exploded into flames at a petroleum refinery	1984	Chicago, US	17 people killed and extensive property damage

Source: Ramesh et al., 2015

It can be argued that the biggest danger concerning pressure vessels is the potential serious injuries or loss of lives that could occur if the vessel fails. This concern is especially relevant to vessels that contain hazardous or harmful media at elevated temperatures.

1.4 The arc welding process

The American Welding Society (AWS) defines welding as a

> localised coalescence of materials or non-metals produced by either heating of the materials to a suitable temperature with or without the application of pressure, or by application of pressure alone, with or without the use of filler metal.
>
> (cited in Anca et al., 2010).

The term *arc welding* refers to a sizeable group of welding processes that join metals through using an electric arc. Such welding processes include gas metal arc (GMAW), flux cored arc (FCAW), submerged arc (SAW), gas tungsten arc (GTAW) and shielded metal arc (SMAW). The joining process is achieved through maintaining the heat from the arc between the tip of the electrode and the work-piece. The heat ensures that the metals are melted and joined together through the use of a filler metal.

This study is focused on the SAW process, which is illustrated in Figure 1.2. The SAW process generates an arc between the weld-piece and the continuously fed electrode that precipitates into the cavity filled with ionised gases and vapours (Kou, 2003). The important feature of the SAW

process is that the arc is submerged and hence is invisible to the operator. The flux is supplied through the hopper (Figure 1.2 a) that travels with the torch. The molten slag and the granular flux protect the metal from the surroundings, hence there is no need for the shielding gas (Figure 1.2 b). For arc currents below 900 A, the direct-current (DC) electrode positive is normally used. Alternating current (AC) is used for settings above 900 A. The main advantages of the SAW process are that it has a slag-action that produces cleaner welds than other processes, and its high deposition rate makes it suitable for welding thick materials. However, the fact that its heat input is relatively high can result in poor quality welds (Kou, 2003).

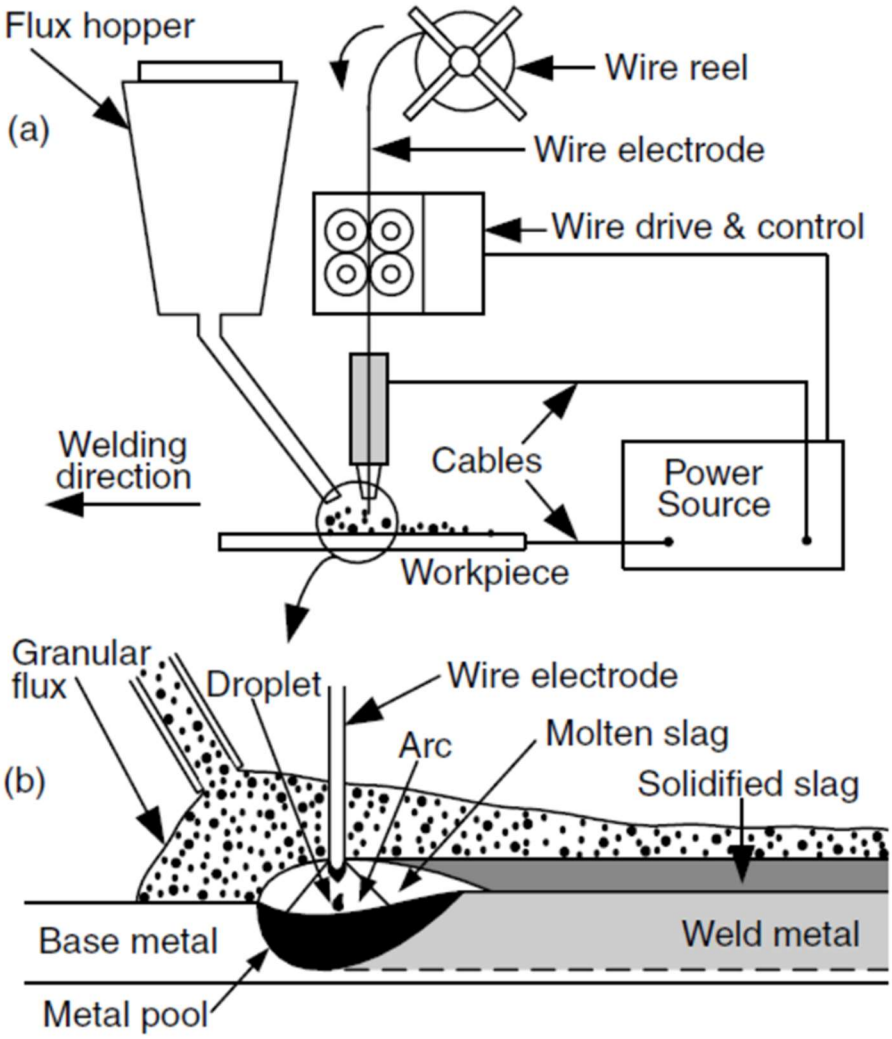

Figure 1-2: The submerged arc welding process: (a) overall process; (b) welding area enlarged
Source: Kou (2003)

1.5 Welding-induced residual stress

Residual stress can be defined as "those stresses that exist within a body in the absence of external loading or thermal gradients" (www.residualstress.org). According to Sterjovski (2003), residual stresses are the stresses that remain in a structure after the removal of any externally induced

loading. There are several reasons why residual stresses develop in metal structures; these include manufacturing processes such as rolling, forging, milling, casting and welding.

Residual stresses may be beneficial or harmful to the structure, depending on their direction and magnitude. Compressive residual stresses have been shown to have favourable effects in that they increase fatigue strength through retarding fatigue cracks, among other things. For this reason, compressive stresses may be deliberately introduced after the manufacturing process through techniques such as shot-peening and autofrettaging (Siddique, 2005). The tensile residual stresses, by contrast, have the opposite effect on a welded structure and are therefore not required. They reduce the fatigue strength of the welded structure through accelerating the fatigue cracks (Siddique, 2005).

In arc welding, the parent and filler metals are melted and joined together through the formation of the weld liquid pool. In steels, depending on the material properties, the surface temperature of the piece varies from 1700 K (1430 C) to 2500 K (2230 C) (Anca et al., 2010). In the weld liquid pool, convective effects occur that improve the transportation of heat; once the heat source is removed the metal solidifies. Such post-melting solidification causes the weld fusion zone to contract and "pull" the surrounding parent metal towards it. The parent material naturally resists the pulling, thereby causing the welded structure to be subjected to post-cooling internal stresses (Anca et al., 2010). Such welding-induced residual stresses (WRS) remain internally trapped within the metal until some form of stress-relieving activity is performed thereon. The process of stress development during welding is shown in Figure 1.3. As the weld pool moves in the y direction, the cooling process causes contraction, which "stretches" the weld. The weld is therefore under tensile stress in the longitudinal direction (i.e. parallel to the weld line). Further from the weld, the longitudinal stress changes to compression to maintain the equilibrium. Transversal stress (i.e. perpendicular to the weld line) is highly tensile in the weld centreline, and decreases to zero as the distance from the weld centreline increases. Thereafter it changes direction to compression at the weld edges (Scharenberg, 2008).

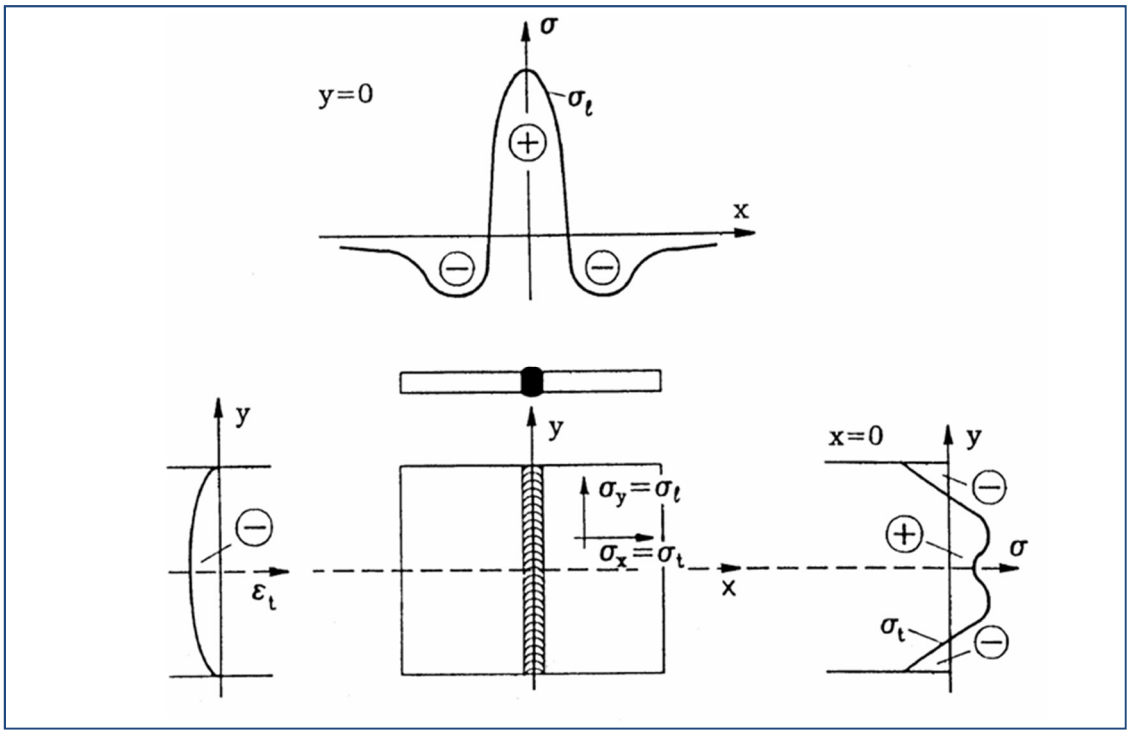

Figure 1-3: Stress distribution in a single-pass weld
Source: Scharenberg (2008)

Studies have shown that welding-induced residual stress has a significant effect on fatigue crack initiation and the early stages of crack propagation. The effect of residual stresses is two-fold: firstly, they distort the welded structure; secondly, they may cause premature fatigue-related failure even under relatively low external cyclic loads (Al-Mukhtar, 2010).

1.6 Objectives of the thesis

This study aims to fulfil the following objectives:

a. Experimental characterisation of temperature distributions for the welding cycle during the SAW process of a multipass nozzle–shell joint of a welded pressure vessel structure.

b. Experimental evaluation of welding-induced residual stresses in a multipass nozzle–shell weld joint.

c. Experimental assessment of fatigue life of multipass nozzle–shell weld joints in a pressure vessel structure.

d. Numerical analysis of thermal residual stresses, considering metallurgical transformation effects.

e. Optimisation of SAW process parameters to determine an optimal parametric combination that will produce weld joints with optimal properties.

1.7 Scope of the thesis

The study focuses on the single-sided full-penetration pipe-to-plate multipass weld, indicative of the nozzle–shell joint in welded pressure vessel structures. The chosen material was pressure vessel steel plate ASTM A516 and high-strength seamless carbon steel pipe (nozzle) ASTM A106 Grade B, joined together by the semi-automatic SAW process.

The experimental work comprised the following aspects: i) manufacturing of welding specimens, ii) the characterisation of welding cycles using infrared thermography, iii) measuring the welding-induced residual stresses using the neutron diffraction method, vi) conducting metallurgical analysis of welded specimens, and v) determining the fatigue lives of welded specimens.

The numerical analysis model was generated using MSC MARC finite element code, and a 3D elastic-plastic model was developed to simulate the SAW process. Optimisation of welding parameters using the evolutionary algorithm was conducted using data collected from all the welded specimens.

1.8 Structure of the thesis

This thesis consists of eight chapters, which are constructed as follows:

a. Chapter 1 gives the introduction of the subject of interest, and the overview of the thesis report.

b. *Chapter 2* describes the "state of the art" according to relevant literature. The work performed in each of the focus areas is comprehensively discussed, and a summary of lessons and gaps identified in literature is provided.

c. *Chapter 3* details the motivation for the study. The chapter focuses on how this thesis adds to the body of knowledge in the field of study, and how the study builds on the work of other researchers (discussed in Chapter 2). Methods, approaches and techniques chosen for the present study are briefly mentioned in this chapter, and the research questions are articulated.

d. *Chapter 4* outlines the following procedures: preparing welding specimens; measuring temperature histories using infrared thermography; measuring welding-induced residual

stress using neutron diffraction; and measuring the fatigue lives of welded specimens, using a servo-hydraulic machine.

e. *Chapter 5* presents the 3D numerical model generated using the finite element code and the validation thereof using experiments.

f. *Chapter 6* describes the process of parametric optimisation, including the design of experiments (DoE) approach, and the evolutionary strategy used to generate optimal welding parameters.

g. *Chapter 7* presents the results of the work discussed in Chapters 4, 5 and 6. These results are then discussed in the context of the study objectives and research questions.

h. *Chapter 8* is the final chapter and it comprises the conclusions derived from the extensive discussion in the preceding chapters. Recommendations for practical implementation of the research findings, and for future research, are provided.

Several appendices appear at the end of this thesis. They provide detailed information on specific portions of work performed for this research.

CHAPTER 2: STATE OF THE ART

2.1 Introduction

The purpose of this chapter is, first, to briefly introduce each of the sub-topics of interest to this study, and secondly to present a review of literature on each sub-topic. The sub-topics are linked to the main subject of interest through applicable methodologies, techniques or strategies, each of which addresses an aspect of the main topic of interest. Collectively such sub-topics provide a holistic perspective of the "state of the art" regarding the subject of this study.

This chapter is divided into three parts. Section 2.2. evaluates the *experimental methods* applied in addressing the relevant sub-topics under the subject of this thesis. Section 2.3 provides insight into *numerical analysis* that can be applied to such work, through reviewing relevant studies within the field. Section 2.4 examines recent research in the design of experiment *strategies and optimisation* techniques applicable to this study. The chapter concludes with a summary of lessons drawn from the review.

2.2 Experimental methods

2.2.1 Pressure vessel design codes

The design, manufacture, repair and inspection of pressure vessels are controlled through a set of codified guidelines or standards, called "design codes". The purpose of a design code is to ensure that minimum standards regarding the safety and integrity of the design are complied with, when working on pressure vessels and ancillary equipment. Few design codes are internationally recognised and most of them originate from the western world. Some widely used design codes for pressure vessel design include the following:

a. British Standard PD 5500
b. European Standard for Water Tube Boilers, EN 12952-3
c. European Standard for Unfired Pressure Vessels, EN 13345
d. ASME BPVC, Section VIII, Div.2 2007/2010

Tjelta (2012) compared two common pressure vessel design codes, namely American Standard ASME VIII Division 2 and European standard EN 13445. That study used a combination of experimental and numerical analysis. Recent versions of design codes recognise the use of finite element analysis (FEA) as a design tool for pressure vessel structures – for example, the design by analysis approach given in EN 13445, and ASME VIII elastic-plastic analysis. Design codes, like any other set of technical standards, continue to evolve as new techniques emerge and design principles are refined.

The present study focuses on nozzle-shell joints, which can be sources of fatigue-related failure in pressure vessels. The various pressure vessel codes specify the type of geometry that must be applied in a nozzle-shell joint. The geometry chosen in the present study is in line with ASME VIII code described above.

2.2.2 Application of infrared thermography in arc welding

Infrared (IR) thermography is becoming more popular in arc welding applications. This measurement method continuously records welding temperatures in the weld pool and the surrounding surface, without any physical interference in the actual welding process. That is, IR thermography is a non-contact process, which renders it preferable to the use of point sensors such as thermocouples (Usamentiaga et al., 2014). IR thermography produces continuous temperature distribution profiles for the weld area of interest through recordings from a thermal camera. Application of IR thermography in metal welding includes real-time monitoring of the weld pool, weld defect identification, weld geometry determination, auto-correction of welding parameters (when used with soft computing), and many more (Venkatraman et al., 2006).

IR thermography is also used for on-line monitoring and control of welding parameters in automation processes that use intelligent methodologies. Online defect identification saves on costs related to post-weld defect identification, which inevitably leads to rejection or rework. The basis for using thermal sensors to identify defects or monitor weld geometry is that the surface temperature distribution during welding should ideally show a regular and repeatable pattern. Any deviation can be identified through perturbations or variations in temperature profiles (Vasudevan et al., 2011).

Wikle et al. (2001) developed a rugged, low-cost point-infrared sensor that is used to monitor and control the welding process. Heat transfer analysis is performed to study the effects of the plate surface temperatures on the weld geometry – a process that occurs during welding. The results are correlated with actual measurements from the IR sensor, which monitors changes in the plate surface temperature during the welding process. The weld bead penetration depth is measured

and compared with the predictions of the heat transfer analysis. IR thermography is used to monitor and control weld geometry during the tungsten inert gas (TIG) welding process for stainless steel 316LN plates (Menaka et al., 2005). The produced thermal images are analysed to determine the temperature distribution patterns that give effect to particular weld geometries and which indicate the nature of weld defects in the weld pool. The developed technique can be used as a basis for adaptive or intelligent weld methodology.

Venkatraman et al. (2006) highlighted the application of thermal imaging sensors in detecting defects such as lack of penetration, and estimation of depth of penetration, during TIG welding. Results show that IR imaging techniques can adequately detect a lack of penetration and the depth of penetration online. Thermal imaging and visual band cameras are the main vision sensors used during online monitoring. A system based on the application of one thermal vision camera and two charge-coupled device cameras for assessing a welding process and welded joints was presented by Bzymek et al. (2008). Machin et al. (2008) proposed a method for calibrating, tracing and accrediting thermal imagers through the implementation of best international measurement practices. Vasudevan et al. (2011) used thermography to determine weld bead geometry and weld defects in real-time during the gas tungsten arc welding (GTAW) process for stainless steel. The weld bead geometry results, obtained using line-scan analysis of the IR thermal profiles, were strongly correlated with the values obtained through experimentation, with a correlation coefficient of 0.8. The defects identified through thermal images were verified using X-ray radiography.

In their study on identifying weld defects of the TIG welding process through thermal imaging, Sreedhar et al. (2012) showed that weld defects identified through thermography were similar to those discovered through the X-ray method. One of the main challenges in that study was the task of tracking the correct thermal history of the weld region, because the IR camera targeted a moving region of interest. To mitigate the effect of this limitation, the area of interest can be increased to include more than just the weld pool. IR thermography is used to perform seam tracking, penetration control, bead width control, and cooling rate control in order to ensure acceptable weld quality (Chokkalingham et al., 2012).

Bai et al. (2013) introduced a new approach to calibrating welding parameters in the weld-based additive manufacturing process, using IR imaging and inverse analysis. In-depth analysis of thermal images *vis-à-vis* the simulation results produces comparable parameters, such as mean layer temperature and cooling rate, which are used in cost functions. Bai et al. concluded that temperature measurements using IR imaging were far better than those from thermocouples, for weld-based additive manufacturing applications.

IR thermography has been used experimentally to validate the FEA model for a submerged arc welding (SAW) joint on a steel plate (Negi and Chattopadhyaya, 2013). The authors observed that the insulating granular flux present in the SAW process renders thermal imaging difficult. Some researchers have suggested the use of flux removal methods, such as vacuuming immediately behind the weld-pool. To address the flux insulation problem, Negi and Chattopadhyaya (2013) manufactured a special U-shaped piece to keep the flux away from the region of interest, so that temperature measurements – which were performed away from the fusion zone – could be taken efficiently. The temperature values predicted using numerical methods were found to be in reasonable agreement with the experimental results.

IR thermography was used to validate the numerical model in Sloma et al. (2014). A thermal camera was used to determine temperature distribution through recording the temperature at various points of a surface. The images from numerical analysis were compared with those produced through thermal imaging, and they appeared highly similar.

Chen and Gao (2014) applied an IR imaging technique to a high-power fibre laser welding process for stainless steel 304L, to monitor the weld pool width and automatically control the welding process. Comparison of the predicted and measured values showed good correlation, with a maximum error of 0.0994. A proposed remote welding process, based on a methodology that combines image processing with soft computing to estimate bead geometry, was presented by Chandrasekhar et al. (2015). The real-time bead geometry monitoring allows for online parametric adjustments during the TIG welding process for stainless steel.

2.2.3 Residual stress measurement by neutron diffraction

Welding-induced residual (WRS) stress is multi-axial in nature with its main components being hoop, axial and radial. Chapter 4 below discusses the components of WRS in detail. Several residual stress measurement techniques have been developed and have been used successfully in recent decades. With regard to their application for welding-induced residual stress, such techniques fall into three main categories: non-destructive, semi-destructive and destructive (Rossini et al., 2012). Non-destructive techniques usually rely on measurement of a parameter related to the stress, and subsequent calculation of the stress using standard formulae. Examples of non-destructive techniques are X-ray diffraction and ultrasonic methods. The semi-destructive and destructive techniques usually involve the complete (destructive) or partial (semi-destructive) removal of material portions from the piece under investigation. The stress relieved by removing such material is then used to infer the original stress condition of the specimen (Rossini et al., 2012). Examples of semi-destructive and destructive techniques are deep-hole drilling (DHD) and the contour method, respectively.

The method discussed in this study, namely neutron diffraction (ND), falls in the non-destructive category. The ND method is based on the Bragg principle, which states as follows:

> The scattering of the incident radiation with wavelength, λ, from a crystalline lattice with lattice distance, d, in the direction of the vector, Q, can only produce a diffraction peak in the direction, θ, in cases where the Bragg equation is fulfilled.
>
> (Ohms et al., 2009)

In Bragg's law, the neutron wavelength and the angular diffraction peak position are used to determine the average inter-planar lattice spacing of a defined volume of a specimen. The result enables the strain to be calculated, provided the reference stress-free lattice spacing is also known (Pratihar et al., 2006). Hooke's law can then be applied to calculate the stresses from the determined strain values.

The Bragg principle is represented in Figure 2.1, and the Bragg equation is written as follows:

$$n\lambda = 2dSin\theta \qquad \textbf{(2.1)}$$

Strain ε can then be determined by measuring the scattering angle of a material under stress θ, and the scattering angle of the same material in a stress-free state θ_0. The following equation is then applied:

$$\varepsilon = \frac{sin\theta_0}{sin\theta} - 1 \qquad \textbf{(2.2)}$$

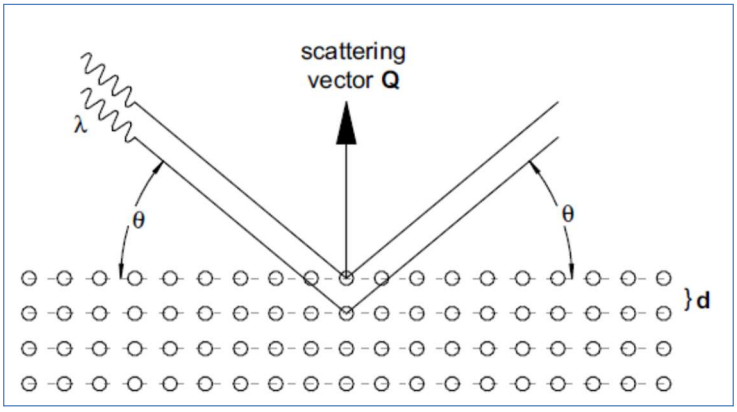

Figure 2-1: Schematic of the Bragg principle
Source: Ohms et al., 2009

Other stress measurement methods, such as hole-drilling and X-ray diffraction, are limited to measuring near-surface stresses only. By contrast, the penetrative capabilities of the ND technique make it possible to measure through-thickness residual stresses in metals. Neutrons can penetrate up to 50 mm of wall thickness in steels (Pratihar et al., 2006). The ND method is also

usually preferred for its high spatial resolution, its flexibility regarding sample geometry, its non-destructive nature, and its tri-axial through-thickness measurement capability. Thermal neutrons have high penetrability characteristics, and hence can be used to measure stress distribution through-thickness in steel materials such as plates and pipes (Ohms et al., 2009). The challenge with ND is that it is only available in specialised atomic research facilities.

A European-wide study on the behaviour of residual stresses in a stainless-steel repair weld, known as the NeT TG1 study, was one of the biggest stress measurement and modelling studies to date. NeT GT1 was the first phase of various studies conducted by different task groups in various EU countries, with the intention of establishing standards for residual stress measurement and modelling. This first phase considered the bead-on-plate weld analysis of a single bead produced using the TIG welding process. The ND results showed that residual stresses are highly tensile at the weld centre line (WCL), and they decrease in magnitude as the distance from the WCL increases (Smith et al., 2014). The NeT round robin programme adopted the approach of using various stress measurements techniques, including hole-drilling, X-ray diffraction, the contour method and the ND technique. Results obtained by Wohlfahrt (2007) and Wohlfahrt and Dilger (2008) showed that longitudinal tensile stress maxima lay in the vicinity of the WCL. The balancing compressive stresses were visible several millimetres away from the WCL. Residual stresses above 300 MPa, which is higher than material yield strength, were observed. The ND technique showed its distinct capabilities for measuring through-thickness stresses to a depth of 15 mm (Wohlfahrt et al., 2012).

Paradowska et al. (2006) applied the ND method to measure welding-induced residual stresses (WRS) in a multi-pass weld. The authors emphasised the changes in residual stress distribution as a result of depositing additional passes. The study showed that adding a layer of weld pass reduced the peak stresses in the passes below the added layer, especially in the weld toe area. This finding means that a multi-pass weld of certain geometrical dimensions will have lower residual stresses than a single-pass weld of the same dimensions.

Sumin et al. (2010) considered the residual stress distribution in the WWER-1000 reactor vessel, which has a stainless-steel facing in the internal surface. The researchers investigated whether the tangential stress on the facing was compressive or tensile. Results from the ND technique showed that the tangential stresses inside the reactor wall were compressive and hence favoured resistance to stress-corrosion cracking. Woo et al. (2015) examined through-thickness stress distribution in an 80-mm thick steel plate, using a combination of ND techniques and contour methods. Hoop stresses were found to be as high as 660 MPa (representing 116% of yield strength) in the WCL. The authors commented that low-carbon steel welds have been shown to exhibit such high

residual stresses due to the strain-hardening effect caused by multi-pass welds and the multi-axial nature of welding-induced residual stress.

Yuen et al. (2008) studied the fatigue behaviour of welded stiffened 350WT steel plates with centre cracks. The ND technique was used to characterise residual stress fields near the crack tips. The calculated stress intensity factors (SIFs) were then used to estimate fatigue growth rates. Longitudinal stresses were found to be compressive near the notch tip, and tensile near the stiffener. Pierret et al. (2012) applied the ND technique together with neutron tomography to measure residual stresses in a turbine blade. Neutron tomography assists in optimally positioning the diffraction volume inside the turbine blade's internal hollow structure.

Neeraj et al. (2011) measured residual stresses on girth welds of thick-walled pipes using the ND technique. Through-thickness residual stress measurements showed that hoop stresses were high (>400 MPa) and tensile close to the outside diameter, and mildly tensile (<200 MPa) close to the inner diameter. The researchers examined two weld metals, namely carbon steel and IN625 dissimilar material. Tensile hoop stresses in the carbon steel weld were as high as 600 MPa, which was 20% higher than yield strength. For both metals, the magnitude of the axial stress was about half that of the hoop stress. In both weld specimens the stresses were asymmetrical about the WCL. Multi-pass bead-on-groove welds were performed on a stainless steel (SUS304) plate using A316L filler material from the TIG welding process. Stress measurements from samples that were annealed at 650 C before welding were compared with samples that had been welded without pre-heating. The results showed that pre-heating reduced the residual stress magnitude. The study also showed that residual stress varied proportionally with welding current; this finding was congruent with the known proportional relationship between heat input and residual stress (Muslih et al., 2008).

Suzuki et al. (2011) investigated residual stress distribution in spot-welded sheet metal using the ND technique. The authors demonstrated that tensile stresses were the dominant stress component around the region in which fatigue fracture occurred. Olson et al. (2015) compared the residual stress maps yielded by various measurement techniques – namely slitting, DHD and ND – for large cylindrical nozzles on pressurised water reactors. First the contour method was used to measure hoop stress and then the axial stress was measured in thin slices, which were removed adjacent to contour planes using ND, DHD and slitting. The resultant axial stress profiles showed tensile stress fields close to the inside diameter, and compressive stresses close to the outside diameter. The results from ND and slitting were generally similar, whereas the DHD results differed.

Haigh et al. (2013) applied the ND technique to measure residual stress of the girth weld in a pipe-to-pipe joint. Two types of stainless-steel weld specimens were measured, one with filler material deposited up to half the pipe wall thickness and the other with a full wall thickness deposit. The objective was to evaluate the change in residual stress profiles as the weld was filled. Through-thickness ND results were compared with near-surface measurements obtained by X-ray diffraction. The residual stress at the weld toe was found to be tensile in the half-filled weld, and compressive in the fully filled weld. The stress profiles produced by X-ray and ND had similar shapes.

Serasli et al. (2016) compared four residual stress measurement techniques, namely standard DHD, incremental DHD (iDHD), the contour method and ND. The experimental setup included several T-plate samples of low carbon steel S355 with multi-pass manual metal arc weld joints. The results from the DHD, iDHD and ND methods were consistent and in line with similar results in literature and assessment procedures for BS7910 standard. The contour method results, however, showed discrepancies associated with intrinsic technical challenges in the technique. The authors identified such challenges and suggested corrective measures.

In their investigative work, Skouras et al. (2013) determined residual stress distributions of a thick-walled welded pipe using DHD and ND methods. All three sections of the weld-piece, namely parent metal, weld metal and heat-affected zone (HAZ) were measured. The residual stress measurement results provided by the two techniques were generally consistent with similar studies. To evaluate whether post-weld rolling might significantly reduce welding residual stress, Coules et al. (2013) used ND to investigate the state of residual stress in two bead-on-plate welds, one with post-weld rolling and one without. The ND method was found to adequately represent the stress fields in both cases. Pratt et al. (2008) similarly applied ND to measure residual stress in stainless steel plates welded through a laser-engineered net shaping (LENS) process. Longitudinal stress was the component that had the highest magnitude in triaxial residual stress, and displayed the same direction as the laser beam.

2.2.4 Residual stress and fatigue strength of welded structures

Failure in mechanical structures is caused by a complex interaction of load, material, time, manufacturing process, geometry and environment. Environment in this context includes temperature, corrosion and fluids within which the mechanical structure operates. Loads may be variable, monotonic, uniaxial, steady or multi-axial. Furthermore, loading can occur for a very short time (e.g. firing a gun) or for a sustained period (e.g. on a busy railway line) (Khurshid, 2017). Ductile failure and fatigue failure make up the top 13 identified common failure modes in

metals. Fatigue is responsible for between 50% and 90% of all mechanical failures (Khurshid, 2017).

The word "fatigue" is based on the concept that the material becomes tired and fails at a stress level below the nominal strength of the material. Fatigue cracking is one of the primary damage mechanisms of structural components, and it results from cyclic stresses that are below the ultimate stress – or even yield strength – of the material (Al-Mukthar, 2010). The fatigue life of a structural component indicates how many load cycles are required to initiate and propagate a fatigue crack to a critical size. There are three stages of fatigue life, namely crack initiation, crack growth and rapid fracture. Once a crack has propagated far enough, the fracture toughness is exceeded and the remaining cross-section of the material experiences rapid fracture, that is, the third stage of fatigue failure (Schijve, 2009).

2.2.4.1 Fatigue categorisation

Fatigue properties of components can be categorised according to whether or not the component has a pre-existing crack. Most welded components are considered to have pre-existing cracks because of the imperfect joining process. Fatigue failure can be divided into two groups: high cycle fatigue (HCF) and low cycle fatigue (LCF). The HCF group refers to fatigue failure that occurs at low stress amplitudes and high frequencies, where the number of cycles before failure generally exceeds 10^6. By contrast, LCF failure occurs at high stress amplitude and low frequencies, in under 10^4 cycles (Zabeen, 2012). An example of HCF is an aircraft engine, which incurs vibrational stresses from the rotary motion of engine components. An example of LCF is a bridge structure used for vehicle or human traffic crossings. Figure 2.2 illustrates the classification in detail.

Research has shown that most fatigue-related failures in nuclear power plants occur in welded joints under high and low cycle fatigue loading conditions. Lu (2002) studied many such fatigue failures which occurred in the 1990s, and discovered that they took place within the first 10 years of service life. This was much earlier than the expected 40 years for a nuclear plant lifespan.

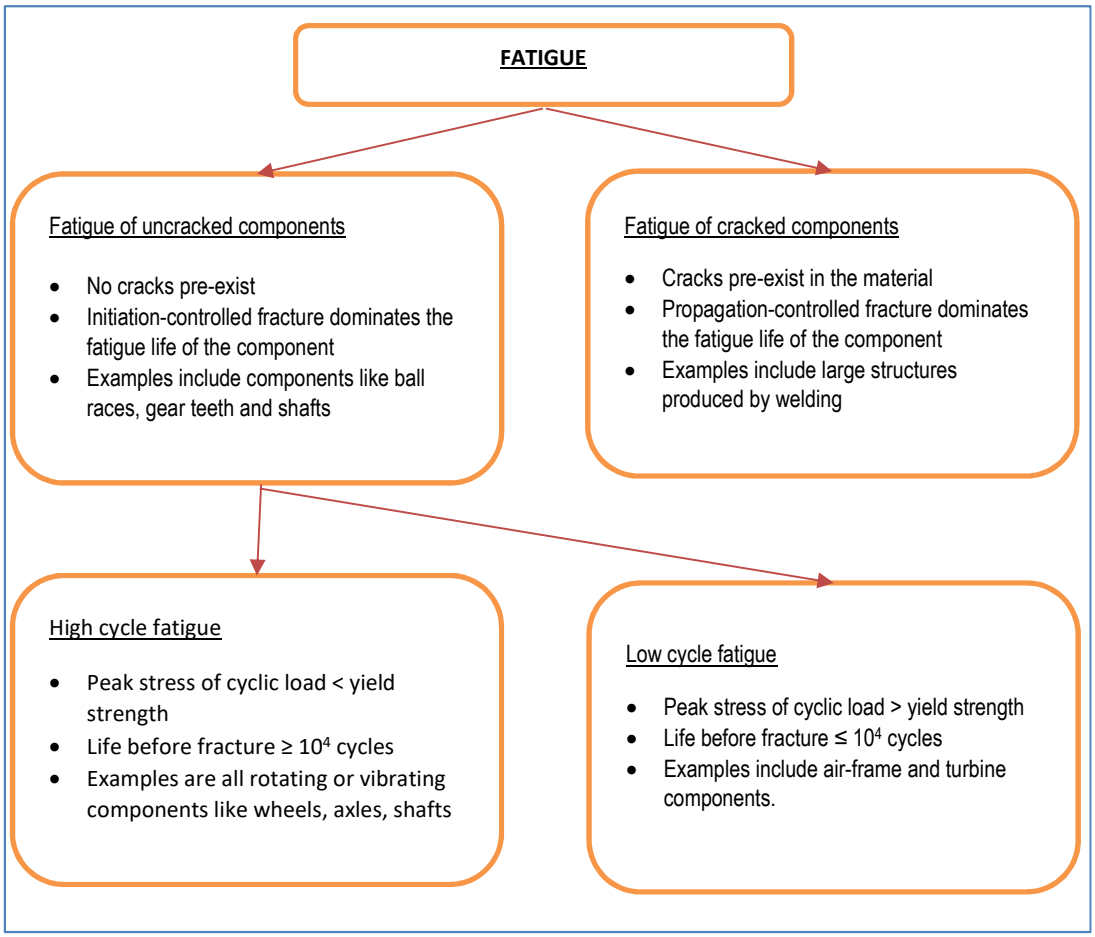

Figure 2-2: Categories of metal fatigue

2.2.4.2 Fatigue assessment techniques

The fatigue strength assessment procedures that are widely used to estimate fatigue properties of welded structures include the following steps (Khurshid, 2017):

a. Identification of critical locations (i.e. vulnerable spots) regarding potential failure.

b. Determining stresses in critical locations using methods for nominal stress, structural hotspot stress, effective notch stress or linear elastic failure mechanics.

c. Estimation of fatigue life using S-N curves (described in the point below).

Fatigue assessment is based on the following two main relationship curves (Fricke, 2012):

a. S-N curves, describing the relationship between fatigue life in cycles (N) and applied stress parameter (S). Examples of stress parameters include nominal stress, maximum stress, or stress amplitude.

b. Crack growth curve, developed using crack propagation laws (e.g. Paris law) based on fracture mechanics, and assuming an initial crack length.

2.2.4.3 S-N curve approach

S-N curves are generated for specific weld joint geometries based on experimental data and are usually included in design codes (Al-Mukhtar, 2010). The stress component used in plotting the S-N curve for a welded structural component can be determined using a number of methodologies, depending on the applicable loading, geometry of the structural component, and other factors. The following are the main methods used to determine the stress component in welded structures. They differ mainly in the stress parameter used in the assessment (Fricke, 2010).

a. *Nominal stress method* includes calculation of nominal stress (i.e. stress due to applied load) and uses S-N curves to estimate the fatigue life. This method is only applicable to simple configurations; it does not yield optimal results for complex structures and/or loading scenarios.

b. *The structural hotspot method* was primarily developed for the offshore industry. It considers the stress-raising effects due to joint member design, but excludes stress concentration due to weld geometry. The determined hotspot stress is a function of weld toe frontline stresses, and its location is influenced by the type of loading and material thickness. The method is only suited for weld toe failures, not root failures. Radaj et al. (2009) observed that structural stress designates the basic stress in a structure in areas of geometrical inhomogeneity that are hotspots for crack initiation; however, the method ignores the notch effect.

c. *Effective notch stress* (ENS) involves the stress-raising effects of the weld geometry. Based on Neuber's notch plasticity theory, the ENS method accounts for weld toe and weld root failures. Neuber's equation is used to calculate the fictitious radius that is used to determine effective notch stress.

Once the stress component has been determined using the above methods, fatigue life can be calculated using the von Mises or principal stress hypotheses, depending on the type of loading and the extent of multiaxiality. Radaj et al. (2009) argued that the benefit of using the local concept for fatigue assessment is that the fatigue process has a local character and cannot be adequately described by global (nominal) stresses alone.

In a fatigue test, a specified mean load – which may be zero – and an alternating load are applied to the test specimen and the number of cycles required to cause failure is recorded. Loads can be applied axially (perpendicular), torsionally or in flexure. Data recorded from the fatigue test are

plotted as an S-N diagram, representing the number of cycles (N) until failure against the amplitude of cyclical stress developed (S). The S term can refer to stress amplitude, maximum stress or minimum stress (Chaudhari & Belkar, 2014)

The S-N or stress life approach is based on fatigue test data, and offers the advantage of a simple yet effective method for fatigue assessment. The method's simplicity derives from the fact that it is based on a single parameter called the stress range, ΔK. The S-N curve represents ΔK versus the cycles to failure, N. The curve represents components' resistance to fatigue. S-N curves are usually specific to component geometry and loading conditions, and hence they lack generality. The S-N method is not without drawbacks; one of its disadvantages is that it assumes elastic strain behaviour and ignores true stress-strain behaviour (Ngiam, 2007). This challenge can be substantial, since crack initiation is usually caused by plastic deformation.

2.2.4.4 Fracture mechanics approach

The fracture mechanics approach is generally used in applications where there is an existing crack, and the method is based on crack growth data. In fracture mechanics, the crack initiation phase is assumed to be negligible and the determined fatigue life is based on the SIF, which accounts for crack size, weld joint geometries and stresses at the tip of the crack. The American Society of Testing and Materials Standard (ASTM) E647 is an international standard used to evaluate fatigue properties of a notched specimen with a fatigue pre-crack under cyclic loading. Crack size is measured as a function of elapsed fatigue cycles, and resultant data are subjected to numerical analysis to determine the crack growth rate (da/dN) as a function of the stress range (ΔK). The calculation is shown as da/dN(ΔK), which characterises the material's resistance to stable crack extension under cyclic load. The da/dN versus ΔK relationship is independent on planar geometry, which effectively means that cracks of different magnitudes that are subjected to the same nominal ΔK will advance by equal increments of crack extension per cycle (ASTM E647, 2015).

The fracture mechanics approach is anchored in the modelling of crack behaviour in cracked structures. The method examines design stress, flaw size and material property of fracture toughness as variables in assessing the structural integrity of cracked components. The utility of the fracture mechanics approach lies in understanding the safety thresholds of cracked structures in operation, such that incidents related to production disruption, injuries to humans, and damage to property and plant equipment can be averted. The nature of analysis therefore allows the determination of residual fatigue strength of the structure as a function of crack size, crack growth rate and critical crack size tolerance (Ngiam, 2007).

Fracture mechanics concepts are grouped into two categories: *stress intensity* concepts and *crack propagation* concepts. The *notch stress intensity factor* (N-SIF) approach uses the notch SIF at the weld toe with zero radius, and crack-tip SIF for the weld root. In the *crack propagation approach,* the Paris law is used to determine the fatigue life of a propagating crack. Linear elastic fracture mechanics (LEFM) and elastic-plastic fracture mechanics (EPFM) are two main methods in the crack propagation approach. LEFM is often used to estimate the fatigue life of a weld joint where a linear relationship exists between fracture toughness of the material and applied stress. By contrast, EPFM is used if the relationship is non-linear. The non-fused part of the root is considered to be the initial crack, whereas initial crack depth has to be assumed at the weld toe (Fricke, 2012). The SIF concepts can also be assigned to ENS concepts (Radaj et al., 2009).

The fatigue crack growth (FCG) behaviour can be divided into three main regions, as described below (Caine & Frain, 2016). The three regions are illustrated in Figure 2.3 through the FCG curve.

a. *Region I:* The growth rate in this region is very slow and is not measurable. Threshold SIF range (ΔK_{th}) is found within this region, and this is the SIF range below which fatigue life is infinite or where crack growth rate (da/dN) is 10^{-10} m/cycle.

b. *Region II*: In this region, the curve of FCG rate versus SIF range (da/dN vs. ΔK) is almost linear, and is defined by the Paris equation. Note that C and *m* are constants of the Paris equation, as shown in Figure 2.3.

c. *Region III*: Rapid unstable crack growth, which leads to fracture, occurs in this region.

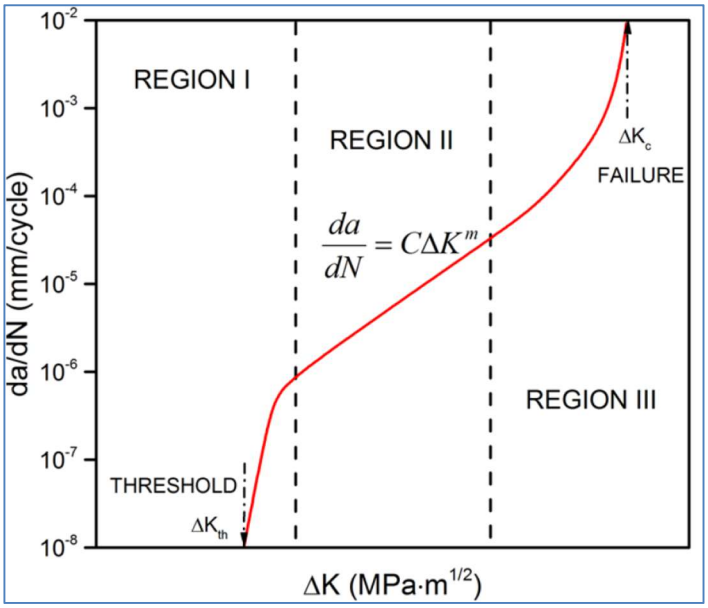

Figure 2-3: Characteristic curve for fatigue crack growth
Source: Cain and Frain, 2016

FCG is difficult to predict in welded structures, which are subjected to multi-axial loads. One of the main reasons for such difficulty is the statistical variations related to the weld parameters. Parameters such as toe radius and weld bead geometry tend to vary from joint to joint, even if the welding conditions for different joints are deemed identical (Lazzarin et al., 2004). For this reason, the approaches used in the evaluation of fatigue strength for welded joints tend to pick and choose parameters considered to be key for fatigue behaviour within the context of a chosen approach (Lazzarin et al., 2004). Studies have shown that in welded structures, most of the fatigue life is consumed during the crack nucleation stage and subsequent V-notch singularity-controlled growth. Furthermore, in welded joints subject to multi-axial loading, it is not nominal or hotspot stresses that cause the damage but local stresses at the notch of the weld – that is, the root or the toe (Nazzarin et al., 2004). In a fillet weld, fatigue crack usually begins at the weld toe and propagates either into the weld metal or the parent metal, depending on the type of loading. Such cracks are likely to originate from the HAZ or fusion zone of the weld (Al-Mukhtar, 2010). Using high-strength materials can achieve the generic objective of attaining higher stresses using reduced parent material dimensions, but this would not change the fatigue strength. Fatigue strength does not depend on parent metal strength but rather on the geometry of the weld joint (Al-Mukhtar, 2010). The notch SIF approach implies that "the fatigue strength assessment of welded joints failing at the weld root or weld toe is essentially a notch effect problem" (Meneghetti, 2013). The weld geometry, including weld root and weld toe, is discussed in detail in Chapter 4 below.

Weld root cracks are considered more dangerous than weld toe cracks, because the former are difficult to detect before it is too late. Weld root cracks originate from the root and usually

propagate through the weld throat into the surface. Only after such propagation do they become visible. Furthermore, stress-relieving processes such as post-weld heat treatment[1] are more effective at the weld toe region than at the weld root (Fricke, 2012). Weld roots of fillet and butt welds have been shown to be under compressive residual stresses of magnitudes approaching the material yield strength, for multi-pass welds of mild steel. The residual stress distribution at the weld toe of the multi-pass weld depends on the number of passes, weld penetration and inter-pass time (Fricke, 2012).

Khurshid and Muntaz (2011) compared various standards for joint design in a welded high-strength telescopic beam of a heavy-weight lifting spreader. They also evaluated the effect of weld defects, such as lack of penetration, on fatigue strength of the joint. A combination of 3D numerical analysis and the analytical effective notch stress method (ENS) was used to evaluate the fatigue life of the weld joints. The ENS method is recommended for plate thicknesses above 5 mm, and a fatigue life value (characteristic fatigue strength) of 225 MPa is recommended for steel in fatigue calculations. The notch can be keyhole-shaped or U-shaped, depending on how the weld is prepared. The effect of the shape on the value of the stress has been shown to be negligible. The authors concluded that the ultimate strength of the weld increases with penetration (Khurshid & Mumtaz, 2011).

Khurshid et al. (2017) investigated tube-to-plate welded joints in terms of fatigue resistance to multi-axial stress state and weld root failure analysis. The researchers used local stress evaluation methods. The stress concentration factor due to pure torsion load was $K_{tt} = 2.31$, and the fictitious notch radius was 1 mm. Only stress concentration factors at weld roots were considered. All cracks initiated at the weld root and hence weld start/stop had no influence. Two modes of failure were observed; in the first mode the crack propagated through the leg size, then through the throat of the weld. The second mode saw the crack propagate through the weld throat.

Meneghetti (2012) applied FEA to determine the fatigue strength of welded lap joints and cover plate joints. The peak stress method was used for assessment of Mode I and Mode II loading of weld toe and weld root geometries. The peak stress method is a simplified numerical method to estimate the notch SIF parameters. The notches at weld root and weld toe are referred to as V-notches, with angles of 0˚ and 135˚ respectively. Pre-cracked joints (e.g. root gap) are regarded

[1] Sterjovski et al. (2004), in an analysis of cross-weld properties of quenched and tempered steels, define post-weld heat treatment as "a stress-relieving process whereby residual stresses are reduced by heating between 540 and 590 ºC for a set time depending upon plate thickness."

as Mode II stress problems. Load-carrying cruciform fillet joints are considered to be Mode I (Meneghetti, 2012)[2].

Meneghetti (2013) provided a simplified method to measure Mode III stresses at the weld toe, by correlating the FEA technique with the notch SIF values. Tube-to-flange fillet welded joints subjected to torsional loading were evaluated using LEFM. Similarly, Lu (2002) examined the extent of the influence of WRS on the fatigue life of welded components. Low-cycle fatigue tests in a cantilever setup were conducted. Fatigue cracks occurred at the weld toe in all the experiments, and ratcheting strain was highest at the weld toe. The fatigue life of materials is therefore reduced in the presence of ratcheting[3] (Lu, 2002).

2.2.4.5 Factors affecting fatigue strength

Fatigue properties of welded components are affected by several factors, including material thickness, environmental effects, discontinuities and residual stress (Ngiam, 2007).

Material thickness: The thickness of a component has been shown to affect the stress gradient to which the component is exposed. This is because a specific fatigue crack (of a given size) will be subjected to a higher stress level across a larger region in a specimen having greater thickness than one with less thickness (Ngiam, 2007). Hence, the effect of the dimensions of a component must be considered when the fatigue behaviour of two or more structures is compared. After comprehensive review of relevant studies, Ngiam (2007) concluded that fatigue performance of welded joints is influenced by member thickness, such that it decreases with increasing thickness for a given nominal stress range.

Environmental effects: Welded pressure vessel structures that operate in industries such as nuclear, offshore, petrochemical, power generation and process engineering can be exposed to environments that are structurally harsh. The environment may be detrimental to the integrity of the structure. Environmental factors such as corrosive media and high temperatures can adversely affect the fatigue life of a welded structure. Oxygen, sulphur and temperature are some of the environmental media that influence fatigue-related failure. These environments have been shown to result in a reduction of fatigue life of 30% to 50% in carbon steels, compared with air environments (Lu, 2002).

[2] There are three basic mode of fractures called Mode I, II, and III. They are fracture by pulling, pushing, and tearing respectively (Fricke, 2012).
[3] Ratcheting occurs when both axial and hoop strains increase gradually with cycles, and it is caused by the presence of mean stress in the stress cycles.

Discontinuities: In a case where continuity of structure cannot be satisfied by membrane forces alone, a discontinuity is said to exist. Discontinuities are potential nests of localised stress concentration. The three main categories of discontinuities in welded pressure vessel structures are as follows (Chaudhari and Belkar, 2014):

a. *Geometric discontinuities*, which comprise abrupt changes in the curvature radius, connections (e.g. nozzles) and material thickness.

b. *Load discontinuity*, which refers to an abrupt change in load type or intensity.

c. *Material discontinuity*, which constitutes an abrupt change in the mechanical properties of a material.

d. *Metallurgical discontinuities*, which involve a change in microstructure from the PM to HAZ to the fusion zone.

The stress magnification at the discontinuity is called the *stress concentration.* The factor by which it is magnified, relative to the nominal stress, is referred to as the stress concentration factor (SCF) or SIF. The calculation can be represented as follows:

SIF x nominal stress = max stress = hotspot stress

In welded structures, the weld notches at the toe and root, which are often characterised by imperfections due to the sub-optimal joining process, are locations of high stress concentration that can act as crack initiators. The question of whether the weld toe or root crack type would dominate the fatigue criterion of the welded structure is a function of several variables. These include the ratio of throat-to-plate thickness, type of loading, weld geometry and residual stress (Fricke, 2012).

Nozzle–shell joints: Pressure vessels are generally exposed to fatigue loading resulting from pressure fluctuations, mechanical loading or thermal loads (Pasha et al., 2008). Furthermore, in pressure vessel structures, circular holes made in the shell for the purpose of plugging nozzles increase the maximum stress experienced by the vessel. This is a result of stress concentration and high magnitude of localised stresses around such a geometrical discontinuity (Paraschiva et al., 2016). The sudden change in geometry and direction at the nozzle–shell joint of the pressure vessel causes high stress concentrations, thereby increasing the chance of failure during operations. A study of the effect of nozzle openings on stress concentrations showed that the two variables were proportionally related. Vessels with larger nozzles experience higher maximum stresses than vessels with smaller nozzles. Stress concentration also increases with an increase in the nozzle angle (Paraschiva et al., 2016).

Lewinski (2016) considered the effect of the configuration and geometry of the manhole to the stress state of the pressure vessel. As manhole thickness increases, the stress decreases, up to a certain level of thickness – in that study, 25.8 mm. Thereafter, the stress starts to increase with increasing thickness. Where the shape of the manhole is elliptical, the equivalent stresses are larger than those for a manhole having consistent radius.

Pasha et al. (2008) evaluated the fatigue life of an operational pressure vessel using a combination of numerical modelling and experiments. Reasonable agreement was noted between the numerical and experimental results. The pressure vessel tested by Pasha et al. (2008) was designed for a fatigue life of 4500 cycles; the fatigue life analysed through numerical modelling was 5234 cycles, and the actual fatigue life was 5051 cycles. Furthermore, the stresses on the pressure vessel shell, flat head and nozzle as analysed by the numerical methods were acceptably close to the experimental results. The numerical results showed that the nozzle's inner corner was the weakest spot for fatigue. The actual fatigue failure during experiments occurred at the same nozzle corner (Pasha et al., 2008).

Peng (2011) applied a combination of experimental and finite element methods to determine methods for controlling welding distortion in nozzle-shell weld joints of stainless steel pressure vessels. Two welding processes of GTAW and SMAW were selected for the study given their popularity in stainless steel pressure vessel welding applications. The results showed that GTAW showed higher levels of distortion than SMAW. The alternating (i.e. welding internal diameter and external diameter in an alternating fashion) welding sequence was found to generate the least welding distortion. Petrovic et al (2011) proposed a procedure to determine the stress state of the pressure vessel shell that is provoked by a torque loading at the free end of the nozzle. The developed method showed that maximum stresses appear on the envelope near the nozzle.

Baloc et al. (2015) examined the influence of two nozzles welded onto the shell, regarding the stress profile of the pressure vessel. The authors combined experimental and numerical methods. The comparison of experimental and simulation results showed a difference of up to 17.4%, which is considered acceptable. Xuedong et al. (2002) studied shaped compact specimens simulating high-strain characteristics of pressure vessel nozzles to understand their fracture fatigue behaviour. The effect of welding-induced residual stress and performance deterioration of the material adjacent to the weld joint rendered the area of the nozzle susceptible to fracture and fatigue damage in the pressure vessel (Xuedong et al., 2002).

Residual stress in welded structures occurs because of heterogeneous plastic deformations, thermal contractions and phase transformation. The contribution of residual stress in fatigue failure properties of the component occurs through the so-called *mean stress effect*. Mean stress

results in material experiencing repeated excursions into the plastic range, even for small loading amplitudes. Residual stress in welded joints acts as mean stress, and facilitates the stress-controlled repeated excursions into the plastic range; in turn, this process causes degradation and failure resulting from accumulated deformation or ratcheting (Lu, 2002). The material behaves in a linear elastic manner for low-amplitude fatigue cycles in the absence of mean stress.

Al-Mukthar (2010) considered the effect of residual stress on crack propagation in welded components. The author observed that fatigue cracks can develop and propagate around the weld joint of a structure during service life, even if the dynamic stresses are well below the yield limit.

2.2.4.6 The Effect of WRS

It has already been stated that residual stress can have a substantial influence on the fatigue strength of welded joints. The influence can either be favourable (compressive residual stress) or detrimental (tensile residual stress), depending on the magnitude and direction of the stress component. A further complication regarding residual stress comes from the fact that many factors influence residual stress – from welding sequence to weld geometry; from material thickness to welding parameters; from filler material type to post-weld heat treatment, and many more. Hence a combination of residual stress and applied stresses in a specific loading condition have a good chance of differing from the combination stress of the next loading condition. The generalisation of results from laboratory-based fatigue-life experiments has little meaning in real-life applications. The interactions among different applied stresses and different residual stress distributions are likely to result in different strain responses and fatigue lives, compared with those from laboratory-based experiments (Lu, 2002).

According to the ASTM E647, the impact of residual stress on FCG behaviour includes the following points:

a. It changes the crack-tip maximum and minimum stress intensities.

b. It may cause irregular crack growth during fatigue pre-cracking.

c. It may cause dramatic relaxation in crack closing forces.

Two approaches are widely used to account for residual stresses when predicting their influence on the FCG rate. These are *superposition* and *effective SIF* (ΔK_{eff}). Superpositioning involves adding the residual stress range to the applied stress range ($\Delta K_{res} + \Delta K_{app} = \Delta K_{tot}$). In the effective

SIF approach, the SIF range at which the crack occurs (ΔK_{eff}) is calculated from K_{app}, K_{max} and K^{4}_{op} (Liljedahl et al., 2007).

According to ASTM E647, residual stress and/or crack closure may significantly affect FCG rate data, particularly at low SIFs and low stress ratios. However, such variables are not incorporated into the computation of ΔK. Residual stresses are thought to undergo a relaxation process under thermal or mechanical loading, due to cyclic plastic strain. Given the favourable effect of compressive residual stresses on fatigue properties, their relaxation through cyclic loading should be avoided (Ngiam, 2007). Lu (2002) argued that although certain design codes (e.g. ASME) allow the influence of residual stress in low-cycle fatigue range to be ignored – because it would likely relax to zero only after a few cycles, experimental analysis showed that this assumption did not hold for all low-cycle fatigue cases.

Rading (1993) observed that most of the fatigue cracks that developed in structural steel used in the fabrication of buses in Kenya originated from the HAZ region of the weld joints. Rading used a combination of experiments (i.e. ASTM E647 fatigue tests) and analytical methods (i.e. fracture mechanics) to evaluate the impact of welding on FCG behaviour of low-carbon structural steel. The study established that the FCG rate in the weld metal, HAZ and parent metal differed depending on which stage (I, II, or II) the FCG occurred on – that is, the beginning, mid-range or threshold. Where the residual stresses had been released almost completely, the FCG rate (da/dN) was essentially the same throughout the parent metal and weld metal (Rading, 1993). The grain size of the microstructure affected the FCG rate. Given that the three main regions of the weld (i.e. weld metal, HAZ and parent metal) had different-sized grain microstructures, it was expected that the FCG rate would differ in each region accordingly (Rading, 1993). Rading's study showed that the FCG rate was faster in the HAZ region than in the parent metal region. The HAZ grain size is finer than that of the parent metal, and hence the parent metal microstructure displays relatively high resistance to FCG.

Lu (2002) examined the extent of the influence of WRS on the fatigue life of welded components. Tensile residual stresses that were greater than the yield stress were observed close to the weld toe area. Fatigue crack was first noticed after 800 cycles of a 5000-lb load, and through-thickness crack growth was realised at 980 cycles in a stainless-steel 304 material. The results showed that the dominant components of residual stress in a circumferential weld are hoop and axial stresses. The socket welds were shown to have shorter fatigue life than butt welds (680 vs 980 cycles). The four-pass weld bead was shown to have shorter fatigue life than the three-pass weld bead. Lu

[4] SIF at crack tip opening.

(2002) concluded that residual stress at the weld toe acts as mean stress, causes ratcheting and reduces fatigue life.

Pasta and Reynolds (2007) applied the adjusted compliance ratio (ACR) method together with the online crack-compliance technique to determine the influence of WRS on FCG behaviour during fatigue testing of the titanium alloy structure. The ACR method allows crack closure effects due to WRS to be separated from effects due to other factors in the FCG data. FCG was measured using online crack compliance, and the influence of WRS on FCG behaviour was measured using the ACR method. This method uses residual stress SIF; and a constant stress-range test was performed in a servo-hydraulic machine. The results showed that longitudinal residual stress was highly tensile in the weld fusion zone, then it reduced in magnitude as the distance from the WCL increased, and eventually changed direction to becoming compressive. Similarly, the FCG rate was higher in the weld fusion zone (tensile WRS) and lower outside the weld border line or weld toe (compressive WRS).

Rosenfeld and Kiefner (2006) investigated residual stress fields around the weld toe and weld root for multi-pass pipe-to-plate circumferential weld joints, their influence on fatigue resistance, and the effect of weld penetration. Two types of joints were examined, namely U-groove 3-pass and fillet 2-pass weld joints. The measured residual stress fields were further used in a fatigue life assessment for welded structures. The authors noted that previous studies showed that the weld root of the pipe-to-plate circumferential weld is under compressive stress, whereas the weld toe is under tensile stress. The fatigue life of the fusion zone is enhanced as a result of the presence of compressive stresses at the root. The authors concluded that the resistance to fatigue crack initiation is generally proportional to the ultimate strength properties of the material (Rosenfeld & Kiefner, 2006).

Liljedahl et al. (2007) studied the residual stress re-distribution resulting from FCG in aluminium alloy 2024-T3 specimens. Three ΔK values were tested. For the medium-tension specimen, M(T), the FCG rate was significantly higher in the weld metal than the parent metal for $\Delta K = 6$ and $\Delta K = 11$. The gap between the two metals closed at $\Delta K = 15$. For the compact tension specimen, CT, crack arrest at all three SIF ranges (ΔK) occurred at the weld metal. The micro-hardness profile suggested significant change in the microstructures of the weld metal, HAZ and parent metal. The residual stress fields were found to redistribute during FCG, and such distribution differed between M(T) and CT specimens. Results from the experiments were compared with results predicted using empirical methods; the CT results showed good agreement (Liljedahl et al., 2007).

Ngiam (2007) presented the results of analytical and experimental work to investigate the favourable and the detrimental effects of surface residual stress on FCG in structural components. Ngiam applied LEFM to assess the fatigue life in offshore structures, considering fillet and butt welds. The author concluded that incorporating residual stress fields into the processes to determine the fatigue properties of welded structures can significantly alter the FCG data.

Garcia et al. (2016) developed the FCG model using the LEFM and EPFM approaches to predict FCG behaviour in residual stress fields of aluminium sections. A combination of experiments and numerical modelling was used to evaluate crack propagation in residual stress fields of aluminium specimens. The fatigue tests were performed on a single-edge notched tension specimen using a servo-hydraulic machine. Four-point bending tests were performed on these specimens to introduce residual stress fields onto the material, and strain gauges were used for strain measurement. Strong correlation was noted between the residual stress results obtained through experiments and those obtained through finite element modelling. The EPFM method was found to have better accuracy than LEFM in matching the WRS field results from experiments. It was also established that compressive WRS fields have a deceleration effect on the FCG rate.

Bozic (2016) investigated the influence of residual stress on FCG behaviour in welded stiffened panel structures. The researcher determined Mode I total SIF (ΔK_{tot}) based on the superposition rule of LEFM. To account for residual stress, the nominal stress ratio R was replaced by the effective SIF ratio R_{eff} during empirical analysis. Residual stresses were found to be tensile along welded stiffeners and compressive between stiffeners.

Given that residual stress can be either beneficial or detrimental to fatigue properties of a welded structure, it is important to monitor the process of residual stress relaxation, especially in situations where benefits are derived from its presence. The two main forms of residual stress relaxation are mechanical relaxation and thermal relaxation. Mechanical relaxation depends on factors such as magnitude and gradient of initial residual stress and the extent of cold working. Thermal relaxation is also influenced by the degree of cold working (Zabeen, 2012). Zabeen (2012) evaluated the stability of intentionally-induced compressive residual stresses on the surface of aircraft engine components under cyclic loading. The residual stress fields associated with mechanically-induced surface residual stress are likely to redistribute and relax as the fatigue crack propagates through the material. Relaxing surface-based compressive residual stresses would accelerate FCG rate. The author concluded that laser peening introduced compressive residual stress of up to 0.6 times the yield stress of the material in the longitudinal direction of the aerofoil specimen (Zabeen, 2012).

2.3 Numerical methods

2.3.1 Numerical analysis approaches

Since the early 1970s, several studies have been performed on welding process simulations, ranging from heat-source modelling to material micro-structure investigations and related aspects. One of the initial works on the finite element method application to stress/strain analysis produced a finite element (FE) algorithmic procedure to numerically generate residual stress through a moving heat source, simulating the welding process. This work was performed by Rybicki et al. (1977). The authors employed a hybrid analysis that combined experimental and computational methods, whereby simple FE techniques were used to incorporate the measured (through ultrasonic shear waves) residual stress during crack analysis. The study identified the significance of the residual stress distribution ahead and behind the advancing crack tip in relation to plastic zone size within the area.

Other early work on heat source modelling included models on multiple-point heat sources, by Rybicki et al. (1978). Ueda and Yamakawa (1971) and Hibbitt and Marcal (1973) also performed early simulation studies of welding processes, using the finite element method. Friedman (1978), Rybicki et al. (1978) and Andersson (1978) presented further works on simulation methodology using the sequentially coupled analysis technique.

Subsequent to the early research described above, many studies on the welding process used the finite element method, and a corresponding number of experiments were conducted to validate the results from modelling techniques. Welding-induced residual stress (WRS) has received growing attention from welding researchers in the last few decades. Dong et al. (2005) observed that the driving force behind such interest is that effective assessment of structural integrity in welded structures, especially defective ones, requires good understanding of residual stress behaviour within a material. Furthermore, the need to better understand and characterise residual stresses associated with pressure vessel repairs has become more evident. Weld repairs have become a structural integrity concern for ageing pressure vessel and piping components (Dong et al., 2005).

In their study on developing a residual stress prediction model for multi-pass butt-welded 2.25 Cr-1Mo steel pipes, Deng and Mukarawa (2008) proposed a thermal-metallurgical-mechanical computational procedure based on an ABAQUS code. The authors established that on the inside surface of the pipe, tensile residual stresses are produced near the weld fusion zone and the HAZ. Compressive residual stresses are generated away from the fusion zone and HAZ. The outside

surface shows the opposite pattern, with compressive stresses generated at the fusion zone and relatively large tensile stresses produced away from the fusion zone.

2.3.2 Definitions used in numerical analysis

In the context of this thesis and in the literature review to follow, the terms used are defined as follows (Lingren, 2006):

a. A *model* refers to a finite element model that is used to present certain aspects of the behaviour of the system.

b. *Simulation* refers to an imitation of the internal process, rather than just the outcome, of the system under investigation.

c. *Validation* is the process in which the accuracy of a model is evaluated by comparing its results with observed experimental results.

d. *Calibration* is the determination of parameters to create a match with certain predetermined measurements.

e. *Verification* is the process of ensuring that the model is correct with reference to the conceptual model.

f. The *conceptual model* comprises the governing mathematical equations chosen to define the various aspects and parameters of the FE input file.

g. *Qualification* is the process of ensuring the integrity of the conceptual model with reference to reality.

The above are but some of the terms used in finite element analysis; a more comprehensive list of terms can be found in Goldak and Akhlaghi (2005). The discussion below considers applicable studies in the analysis of residual stress in typical thermo-mechanical problem applications.

2.3.3 The thermo-mechanical problem

Smith and Smith (2009b) investigated cyclic thermo-mechanical (combination of thermal and structural) loading history in stainless-steel type 316L bead-on-plate specimens using 3D finite element modelling and experiments. The experiments included welding several single-pass bead-on-plate specimens whose residual stress profile resembled that of a repair weld. It was established that high tensile transversal stresses were prevalent beneath the weld bead, with the highest residual stress at the stop-end. Tensile longitudinal stresses were also predicted beneath the weld bead, with balancing compressive stresses beyond the weld stop-end. In the plate depth

direction, beneath the melted zone, the parent material experienced biaxial stresses. A tension-compression-tension transversal stress cycle occurred as well as the compression-tension longitudinal stress cycle, with yield taking place only in the longitudinal cycle. Plastic flow occurred both during heating in the compression direction and during cooling in the tensile direction. In the weld metal, stresses depended on the material's yield strength and plastic strain. Isotropic hardening models tended to produce higher longitudinal stresses (above 400 MPa), whereas kinematic hardening models showed relatively lower longitudinal stresses (200 MPa – 300 MPa). This finding can be attributed to the Bauschinger effect[5]. Transversal stresses were generally not sensitive to material properties, whereas longitudinal stresses were. Plastic strain seemed to be informed by the assumed "annealing temperature" and the chosen heat source model. The 2D "block-dumped" heat source approach[6] resulted in higher plastic strain than the 3D moving heat source model. The best results, compared with measurements, were obtained when applying the non-linear kinematic hardening model with plastic strain set to zero at 850 ^{0}C. Using isotropic hardening models resulted in overly conservative predictions of stress in the parent material, especially longitudinal stresses. The effect of material "annealing" during modelling[7] was to increase predicted stresses when using non-linear kinematic hardening, and to decrease them when using isotropic hardening.

Smith and Smith (2009a) compared experimental and numerical studies of bead-on-plate analyses that were performed to investigate residual stress fields of the stainless-steel 316L plate. The authors stated that the far-field mid-length thermo-couples were best suited for calibrating the transient heat source model. Start and stop conditions are normally difficult to model due to complex multidimensional transient arc commencement and decaying processes. The uncertainties in the heat input and arc behaviour, which are present at the stop and start ends of the bead, can adversely influence thermo-couple readings at these locations. The authors argued that a dedicated heat source modelling tool provides more accurate heat input estimation than ad hoc heat source models, body/surface flux distributions or fixed weld temperatures. They identified three advantages of using dedicated heat source modelling tools: i) they apply a Gaussian ellipsoidal moving heat source; ii) they reduce uncertainty in heat source modelling; and iii) they apply fusion boundary as a fitted output in the analysis, not as input. Smith and Smith

[5] The characteristic of materials whereby yield strength is increased by plastic deformation in the direction of plastic flow and concurrently decreased in the opposite direction. This phenomenon is usually associated with conditions in metals where yield strength decreases as a result of changes in the direction of strain.

[6] A simultaneous bead deposition technique is the process whereby the FE model considers the weld metal to be deposited all at once, for the purposes of thermal analysis. This is also known as "block dumping".

[7] ABAQUS has an annealing functionality. The "annealing temperature" is set, above which equivalent plastic strain is zero. Plastic history of prior passes is "annealed" by the successive passes. Accumulated plastic strain is discarded if annealing temperature is reached but is retained if annealing temperature is not attained.

(2009a) concluded that heat-source steady-state calibration should occur close to the bead's mid-length.

To evaluate formation of WRS on a three-pass bead-in-slot weld joint of austenitic stainless steel, Muransky et al. (2012) developed an uncoupled 3D thermal-mechanical model on ABAQUS code. A dedicated heat source modelling tool was utilised to model the ellipsoidal Gaussian volumetric heat source. The Lemaitre-Chaboche mixed isotropic-kinematic hardening was adopted for mechanical analysis. The simulation process was split into consecutive, uncoupled thermal and mechanical analyses. Firstly, thermal analysis was performed; then the resultant temperature field data were fed into the mechanical analysis through the "predefined field" interface in ABAQUS. Muransky et al. observed that transversal stress was compressive at the ends of the weld bead and became tensile towards the middle of the bead. Transversal stress peaked at the weld–parent-metal interface. In the fusion zone (weld metal), temperature rose above 1500 ˚C during heating, bringing the temperature-dependent yield strength close to zero. As the molten weld metal cooled, the bead contracted into tension. Tensile stresses were therefore prevalent in the weld bead. The parent metal just below the weld metal was exposed to temperatures around 1300 ˚C during heating. This material was first subjected to compression, and then the direction of the load changed as the material cooled down. During the second pass the material behaved the same as in pass-1. The metal just beneath the weld metal in pass-2 (i.e. pass 1 weld metal) behaved the same as the parent metal just below the weld pool in pass 1. In a multi-pass weld, each successive pass generated sufficient plastic flow to neutralise the stress field developed from the preceding pass. Most of that stress would have developed through the compression that arose during heating. Hence, the final residual stress distribution was mostly influenced by the last pass (Muransky et al., 2012).

Heinze et al. (2012) calculated the WRS in a six-pass bead-on-groove GMAW weld of structural steel. A thermo-mechanical numerical model was developed from the SYSWELD(R) code. The problem was sequentially-coupled, and the thermal model was developed using temperature-dependent, homogenous and isotropic material properties. Results of the thermal analysis were then used as input into the mechanical problem. Both 2D and 3D models were developed, and sufficient agreement was evident between the 2D and 3D models. Longitudinal and transversal residual stresses were measured. Longitudinal stresses were generally tensile in nature in both the fusion zone and HAZ regions, with maximum stress values found in the plate centre at mid-plate thickness. The WRS was affected by preheat and inter-pass temperatures. The inter-pass temperature exerted more influence than preheat temperature; a change of 100 C upwards decreased the residual stress by between 60 MPa and 70 MPa (Henze et al., 2012).

Chand et al. (2013) presented a 2D FEM solution for prediction of the GMAW process using a multi-pass weld of thick SS400 steel plate. The "element birth and death" technique was applied in ANSYS software to simulate multiple weld beads. The numerical model was validated using experiments and the results showed that residual stress was significantly affected by the heat input of the welding process. Culha (2014) derived a numerical solution for predicting the design parameters, such as temperature-stress distribution, for the submerged arc welding process of the AH 36 T-beam profile. The developed 2D FE model was used to investigate the WRS and strain distributions around weld and HAZ using a coupled temperature-displacement transient modelling approach. Simulation results revealed the existence of residual stresses in excess of material yield strength in the welding zone. The magnitude of the stresses decreased as the distance away from the welding zone increased.

Islam et al. (2014) attempted to optimally reduce welding-induced distortions using finite element analysis alongside a genetic algorithm procedure. The numerical model was a classical coupled thermo-mechanical model with elastic-plastic behavioural assumptions. Experiments were used to validate the 3D finite element model of a 70 mm long longitudinal lap joint weld in a 3.2 mm thick steel plate. The developed tool is recommended for early-stage design investigations such as parametric study or sensitivity analysis in industrial applications.

Nezamdost et al. (2016) attempted to understand and improve computer modelling of the submerged arc welding process in an API X65 steel pipe application. The welding thermal cycle and the residual stress distributions were modelled using 2D axi-symmetric and 3D finite element models. The results from the numerical models and bead-on-plate welding experiments were compared and found to be in good agreement. Rusu et al. (2013) presented 3D finite element models for the analysis of heat transfer induced by a double SAW process, using two or three wires in longitudinal welds of natural gas pipelines. Gaussian's moving double ellipsoidal heat source distribution was used for the formulation of heat source models, and temperature-dependent properties were incorporated into the prediction models. Thermal history plots revealed maximum temperatures as high as 1990 ^{0}C, which was consistent with similar studies.

Lorza et al. (2017) applied isotropic hardening and non-linear kinematic hardening rules to reproduce cyclic plasticity behaviour of material welded using the GMAW process. The developed numerical model was used to predict welding-induced residual stress in a single V-groove butt joint of low carbon steel. Experimental results obtained by the hole-drilling method were found to be in reasonable agreement with the FE model predictions. The ANL (2016) performed a detailed study on the thermal-mechanical stress behaviour of a reactor pressure vessel and its nozzle under typical reactor heat-up, cool-down and load-following modes. In general, for elastic-plastic analysis, a commercial FEA code such as MARC requires elastic

modulus (E), Poisson's ratio, yield stress and kinematic hardening properties as input (ANL, 2016).

2.3.4 Effect of phase transformation on WRS

Yaghi and Becker (2004) explained that local material dilatations introduce strains during the decomposition of austenite when the weld cools down. Such dilatations are assumed to be proportional to the fractional quantities of the transformed material phases, which in turn are iteratively determined for each time-step in the thermal analysis. Leggatt (2008) observed that phase change is yet another material property factor that affects residual stresses. In particular, the temperatures at which the phase transformation commences and terminates are sensitive to the cooling rate. Where the cooling rate is fast (e.g. HAZ), phase transformation occurs at relatively low temperatures.

Deng and Murakawa (2008) studied incorporated solid-phase transformation effects in 2.25Cr-1Mo steel pipes. They established that the weldment and HAZ consisted mainly of the bainite/martensite mixture, with the fractional portion of bainite being higher. Their simulation results demonstrated that to obtain precise prediction results, phase-dependent material properties such as yield strength were needed. Deng (2009) observed that previous experimental studies showed that measured stresses in the fusion zone and HAZ are lower than those in the base metal adjacent to the HAZ. This is because of the volumetric change of the material due to martensitic transformation at a relatively low temperature. The author concluded that martensitic transformation has a significant influence on the welding residual stress for mid-carbon content steels. Previous studies showed that when analyzing welding-induced residual stresses on high-strength carbon steels, solid-state phase transformation should be taken into account in the welding simulation because it induces important physical and mechanical effects, such as volumetric changes, in the material (Lee & Chang, 2009).

Figure 2.4 illustrates the phase transformation behaviour of steel during the welding cycle. The A_1 temperature represents the temperature at which austenitic transformation begins during heating. When steel is heated above A_1, its structure starts to transform from a body-centred cubic (ferritic) structure to face-centred cubic (austenitic) structure (Deng & Murakawa, 2006). At temperature A_3, the pearlite-ferrite phase has completely changed to austenite. During rapid cooling, a portion of austenite converts to martensite. In Figure 2.4, the volume change due to this martensitic transformation occurs between the start temperature (M_s) and completion temperature (M_f). The rest of the austenite converts to other phases such as bainite or pearlite, depending on the cooling rate. The quantity of martensite formed depends on the temperature reached during cooling (Lee & Chang, 2009).

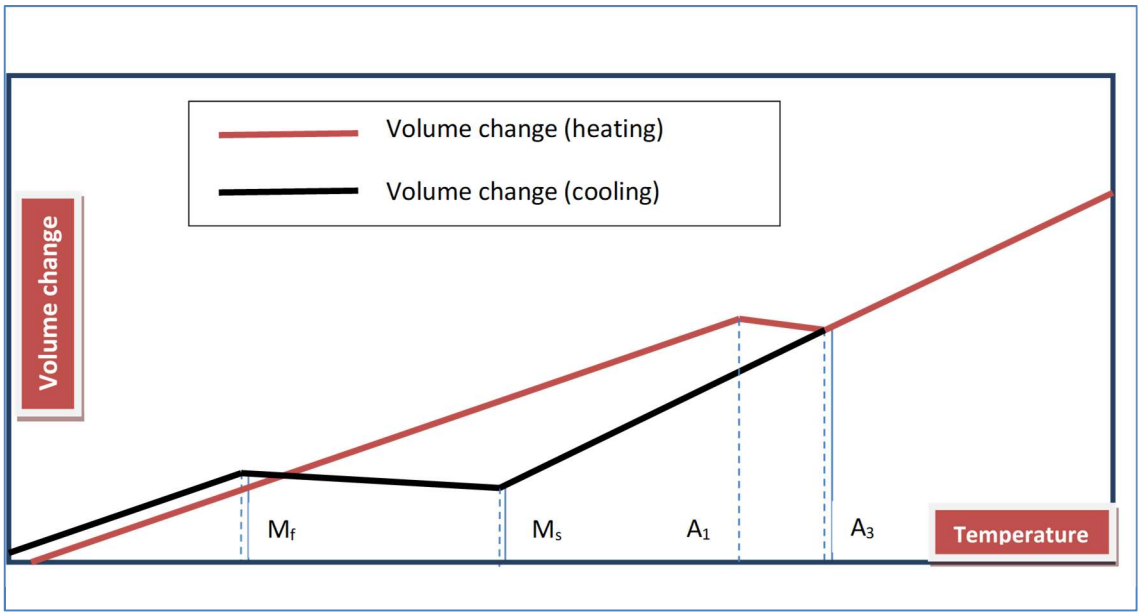

Figure 2-4: Volume Change due to Phase Transformation
Source: Lee and Chang (2009)

Pilipenko (2001) observed that microstructural transformation at low temperatures (i.e. martensitic) in the fusion zone and the HAZ can change the residual stress distribution significantly. By contrast, transformations achieved at high temperatures (i.e. austenitic) might have no significant effect on residual stress distribution. Lee and Chang (2009) determined the residual stresses in a multi-pass butt-welded high-strength steel plate through employing a sequentially-coupled 3D thermo-metallo-mechanical FE analysis. The developed FE model incorporated volumetric change and variation in yield stress of the base metal and weld metal due to martensitic and austenitic transformations. The authors established that volumetric increase during the austenitic-martensitic transformation (i.e. during cooling) had an effect of reducing longitudinal tensile residual stresses in the weld region and the HAZ.

Deng and Murakawa (2006) analysed thermal effects, phase transformation effects and mechanical effects in multi-pass butt-welded steel pipes. Using a thermal elastic-plastic finite element model, they concluded that the volumetric change that resulted from martensitic transformation had a significant influence on welding residual stress. The effect leads to a change in both the magnitude and the direction of residual stress in the weldment. They further stated that the yield strength change induced by solid-state phase transformation also influenced the resultant welding-induced residual stress.

2.4 Optimisation techniques

2.4.1 Design of experiment and statistical methods

Design of experiments (DoE) is a powerful strategy used to address problems associated with quality in various manufacturing industry sectors. This approach is cost-effective as it allows for a minimum number of experiments to be conducted to obtain sufficient data to model the behaviour of critical parameters. DoE is an effective process for maximising analytical output while minimising resource input, because it can impose multiple changes on several parameters simultaneously, rather than the one-change-at-a-time approach (Dhas & Dhas, 2012). This ability makes the DoE a resourceful technique for obtaining information from experiments. The alternative method, namely implementing one change at a time, carries the inherent risk of missing out on multi-factor interactions (MFIs) while concentrating on single-factor effects (SFEs).

The principle of operation of the DoE approach is that the experimental plan directs the experimenter as to where each test parameter must be set for each run of the test. The analysis is based on identifying the resultant differences in the response variable, for each variation of input parameters. The identified variations are then attributed to either the SFEs or MFIs. The main DoE techniques used in the welding process application include fractional factorial design, full factorial design, central composite design (CCD) and the Taguchi method. Both Taguchi and CCD are derivatives of the factorial design technique. The origins of experimental design can be traced back to the 1920s, when an English statistician named Sir Ronald A. Fischer developed a factorial design and a technique for analysing the experimental data statistically. The method was called analysis of variance (ANOVA). Fischer studied the improvement of agricultural crop yields (Kondapalli et al., 2015).

Gupta and Parmar (1989) successfully applied the fractional factorial technique to determine the interactive behaviour of welding input parameters in a SAW process. Murugan and Parmar (1994) also used the fractional factorial technique to predict weld bead geometry of an MIG stainless-steel-to-structural-steel weld. Balasubramanian and Guha (1998) provided a mathematical model to predict the fatigue life of FCAW-welded cruciform joints that contained lack-of-penetration imperfections. A two-level, four-factor ($2^4 = 16$) full factorial design of experiments was used. Analysis of variance (ANOVA) was used to determine the significance of parameters and model terms. The developed model predicted the fatigue life of cruciform joints at the 95% significance level.

Ni et al. (2011) considered the optimisation of laser welding process parameters for the titanium neuro-stimulator shell using Taguchi L_{18} orthogonal array (OA) design. The input parameters of the Nd:YAG pulse laser welding process included pulse shape, laser power, weld speed, defocusing amount and shielding gas. The response variable comprised the bead depth-to-width ratio. The results showed that the average response value was affected by laser power, welding speed and defocusing amount, whereas the S/N ratio was affected by laser power and weld speed. Optimised values were verified using experiments and good agreement was found between the two.

Datta and Mahapatra (2010b) suggested an application of principal component analysis (PCA) together with the Taguchi technique, to address the issue of correlation among response variables during parametric optimisation of a straight turning process for mild steel machined products. PCA converts correlated responses into non-correlated principal components or quality indices. The technique applies utility theory to convert multiple responses to a single equivalent objective function, that is, overall utility degree. The process input variables for the turning process include spindle speed, feed and depth of cut. The output parameter of surface roughness was chosen. The study successfully determined the optimal parametric combination that can be used for continuous quality improvement in machining of mild steel products.

Khan et al. (2011) attempted to optimise weld control parameters that explain weld geometry and weld strength, using statistical and experimental methods. The input parameters of laser power (LP), welding speed (S) and fibre diameter (FD) were chosen. Full factorial design was used to relate the input parameters to the response variables of weld zone width, penetration depth, resistance length and weld shearing force, through developed mathematical models. An F-test was used to determine the terms and significance of the regression model. Step-wise regression eliminated insignificant model terms automatically, and ANOVA tables summarised the analysis of variance and provided the significant model terms. It was established that welding input parameters (LP, S and FD) varied linearly with fusion zone width. Penetration depth was affected by LP, S, FD and two-factor interactions or 2FIs of LP*S and S*FD. Significant model terms for weld resistance length were LP, S, FD and 2FIs of LP*S, S*FD and LP*FD. For weld shearing force, the significant model terms included LP, S, FD and 2FIs of LP*S and S*FD. Laser power and welding speed exerted significant effects on weld bead geometry and bead shearing force. Fibre diameter alone had little effect on weld bead geometry and shearing force, but its effect became more significant combined with other parameters (i.e. 2FI level).

Yang et al. (2012) applied the Taguchi method to measure and optimise laser welding process parameters with filler metal. The process parameters included laser power, welding speed and wire-feed rate, and the response variables were bead width and fusion area. Welding speed was

the most influential factor for the response of bead geometry, followed by wire-feed rate. Speed varied inversely with bead width and bead height. The wire-feed rate varied proportionally with bead geometry parameters.

Ilo et al. (2012) evaluated the impact of plasma transferred arc welding (PTAW) process parameters on quality characteristics of hard-facing parameters in hard-particle metal matrix composite (MMC) applications. Parameters that influence MMC microstructure formation during PTAW process included welding current, welding speed and oscillating speed. A two-level L_8 Taguchi OA design was used to implement the experiments. Accordingly, eight experimental runs were conducted, allowing for experimental error at 1 degree of freedom. Micro-hardness measurements were conducted on unetched specimens. Multiple quality characteristics were optimised using grey relational Taguchi analysis.

Sapakal and Telsang (2012) considered the optimisation of MIG process parameters of welding current, voltage, and welding speed using the Taguchi method. The effect of input parameters on weld penetration was investigated using L_9 orthogonal array at three levels. ANOVA revealed that voltage had a significant effect on weld penetration, whereas current and speed had negligible effects.

The Taguchi method was also applied by Juang and Tarng (2002) in a modified form, to determine the parametric combination of the TIG process that would result in optimal weld bead geometry for stainless steel plate. An L_{16} orthogonal array was applied to investigate the effect of process parameters of arc gap, flow rate, current and welding speed to weld bead geometry. ANOVA showed that all chosen input parameters significantly affected the response variables of bead geometry. The optimal parameters were successfully calculated using the suggested Taguchi technique. Balasubramanian and Guha (2004) examined the fatigue life of load-carrying cruciform joints in pressure vessels. They used the DoE technique to develop mathematical models to predict the fatigue life of SMAW and FCAW cruciform joints. The factorial experimentation technique of DoE was effective at predicting multi-factor effects on fatigue life.

Yousefieh et al. (2011) investigated the influence of pulsed current gas tungsten arc welding (PCGTAW) process parameters on the corrosion and metallurgical properties of super duplex stainless steel (SDSS), using the Taguchi L_9 OA design. PCGTAW is a variation of the GTAW process that involves alternating between high-level and low-level arc currents at a selected frequency. Four process parameters were identified: pulse current, background current, pulse frequency and % duration. Parameter levels were set at three (i.e. 4^3 design). Experiments were conducted using a 500 mm diameter, 5 mm thick SDSS pipe. Pulse current and background current were significant control factors, whereas % duration and pulse frequency were

insignificant. The predicted and observed response parameter values for optimal control factors were in reasonable agreement.

Friction stir welding (FSW) process parameters and their effect on tensile strength of welded joints were investigated by Lakshminarayanan and Balasubramanian (2008). The analysed input parameters included rotational speed, traverse speed and axial force. The experiments were designed using the Taguchi L_9 OA with three levels (i.e. 3^3). The ranges of parameters were determined through pilot experiments. Experiments were conducted on 300 mm x 150 mm x 6 mm rolled RDE-40 aluminium alloy plates using square butt joint configuration. The S/N ratio analysis was performed using statistical software and ANOVA was used to test the parametric significance. All parameters were found to significantly affect tensile strength in the FSW joints.

Song et al. (2005) studied the effects of main welding parameters in a 3D welding process[8] on the bead geometry and mechanical properties of mild steel. The chosen input parameters included voltage, wire-feed rate, gap between welding gun and weld-piece, and shielding gas composition (i.e. ratio of argon/CO_2). The response variables were bead width and weld spatter. A three-level L_9 Taguchi OA matrix was developed. ANOVA revealed that voltage, wire-feed rate and welding gap were significant determinants of weld spatter, whereas shielding gas had negligible effects. Similarly, voltage and wire-feed rate affected the bead width, but welding gap and shielding gas did not.

Gunuraj and Murugan (1999) presented a study on the effects of heat input on the HAZ area generation of SAW-welded carbon steel bead-on-plate and bead-on-joint pipe specimens. The identified welding process parameters included voltage, welding speed, wire-feed rate and nozzle-to-plate distance. The working range of parameters was determined through experimental trial runs, by varying one parameter at a time while inspecting the bead integrity. A CCD was chosen to develop the matrix with 2^4 (=16) factorial design, 7 centre points and 8 star points. Multiple regression analysis was used to develop model terms for the polynomial function, and ANOVA was applied to evaluate the model's significance. Both SFEs and MFIs were included in the objective function. The predicted values and experimental results were in good agreement. The MFI of wire-feed rate and speed showed that heat input was lowest when wire-feed rate was at a minimum and speed at a maximum level. The HAZ area was at its lowest when the wire-feed rate was minimal and nozzle-to-plate distance was at its highest.

Yang (2008) studied the impact of SAW parameters on the quality and strength of the weld in high-strength low-alloy (HSLA) steels, using DoE and statistical methods. The author selected a

[8] A hybrid freeform fabrication process that uses GMAW as an additive technique and conventional milling as a subtractive technique.

parametric combination that produced optimal results in the SAW process. The results showed that reinforcement, penetration depth and HAZ size of both SA516 and A709 steels varied proportionally with the welding current. Welding current was found to have little effect on weld bead width. Travel speed co-varied inversely with both reinforcement and bead width. This finding occurred because travel speed is inversely proportional to heat input, which varies directly with reinforcement. The undercut increased with increasing travel speed and decreased with increasing heat input. Lack-of-penetration defects were caused by low heat input, and lack of penetration increases with increasing travel speeds and decreases with increasing current.

Shen et al. (2012) investigated the effect of SAW-process heat input on the weld bead geometry for the ASTM A709 grade 50 steel weldment. Experimental measurements and empirical calculations were used to determine the effect of heat input on weld geometry. The results showed that bead width (BW), bead penetration (BP), bead reinforcement (BR) and HAZ size all increased with increasing heat input. The width-to-depth (WB/BP) ratio and percentage dilution remained roughly the same as heat input increased. Electrode melting efficiency increased with increasing heat input, whereas parent-metal melting efficiency did not change with increasing heat input.

Sensitivity analysis of SAW process parameters was performed by Karaoglu and Secgin (2008). The authors related the welding parameters of arc current, voltage and welding speed to the response variables of bead height and penetration, using empirical models developed from multiple regression analysis. The main utility of sensitivity analysis is that it informs the analyst of the process parameters that must be adjusted to enhance performance. Experiments were designed using the $3^3 = 27$ factorial design, and bead-on-plate welds were conducted on mild steel plate having the dimensions 180 mm x 80 mm x 10 mm using 3.2 mm filler material. Bead width was found to be sensitive to arc current, voltage and welding speed. Bead width was also more sensitive to parameter variation than bead height and penetration. Bead height was shown to be sensitive to all three parameters. Increasing the voltage and speed resulted in a decrease in bead height. Arc current strongly influenced penetration, whereas variations in voltage and speed had negligible effects on penetration.

A quantitative investigation of the effects of the two-wire tandem submerged arc welding (T-SAW) process parameters on weld bead quality and mechanical properties was conducted by Kiran et al. (2012). The authors performed an experimental study using the CCD technique to investigate the following welding parameters: leading arc current, trailing arc positive and negative current pulses, welding speed and trailing arc negative current duration. The experiments included bead-on-groove single-pass welds on 12 mm thick HSLA steel plates. The trailing wire current significantly affected the weld bead geometry. Increasing the trailing wire current

increased the weld bead dimensions and degenerated the mechanical properties. Higher welding speeds reduced the bead geometrical dimensions and improved the mechanical properties.

Tarng et al. (2002) employed the Taguchi method together with the grey relational analysis to evaluate multiple parametric effects on multiple performance responses in the hard-facing process applied using SAW. Hard-facing is a process whereby an alloy is homogeneously deposited onto a surface of a soft material using the welding process, in order to increase the hardness and wear resistance of the latter, while concurrently maintaining the ductile properties of the material (Buchely et al, 2005). The welding input parameters in Tarng et al (2002) were identified as arc current (C), arc voltage (V), welding speed (S), electrode stick-out (E) and pre-heat temperature (T). The output variables were taken as dilution (%), deposition rate (kg/s), and hardness (Rockwell C). Arc current, welding speed and electrode stick-out had significant effects on the response variables, with electrode stick-out being the most influential parameter.

Ghosh et al. (2011) analysed SAW parameters (i.e. arc current, wire-feed rate, stick-out and travel speed) using the Taguchi L_{16} OA design. Experiments were performed on two plates, each measuring 400 mm x 75 mm x 6 mm, to study the parametric effect on the response variable of bead geometry. No significant interaction was observed among input parameters for bead geometry. S/N ratio analysis provided the optimal parametric combination corresponding to the highest S/N value.

Datta et al. (2009) solved a multiple response optimisation problem in the SAW process using the grey-based Taguchi technique together with the PCA method. The input parameters included voltage, wire-feed rate, traverse speed and electrode stick-out. The responses (which were assumed to be correlated) comprised penetration depth, reinforcement (bead height), bead width and dilution. The orthogonal array of L_{25} experimental design was implemented through bead-on-plate welds using an automated SAW process on a mild steel plate of 10 mm thickness. Optimal results comprised low voltage, low feed rate, high speed and high stick-out. The grey-based Taguchi (i.e. grey relational analysis) is a useful method for solving multi-objective optimisation problems without compromising the correlation amongst responses (Datta et al., 2009).

Purohit and Digamber (2012) investigated the influence of voltage, wire-feed rate, traverse speed and nozzle-to-plate distance of the SAW process on the response variable of weld bead geometry using the Taguchi method. The ANOVA findings showed that traverse speed and wire-feed rate were the only significant model terms. Saluja and Moeed (2012) utilised the fractional factorial design method to investigate the cause-and-effect relationships between, on the one hand, SAW input parameters of welding current, voltage, travel speed and electrode stick-out and, on the

other hand, the responses of bead width and bead height. Welding current and voltage significantly affected the bead width. Current, voltage and speed all influenced the bead height, whereas electrode stick-out had no significant influence on bead geometry.

Kumanan et al. (2007) applied the Taguchi technique in their investigation of SAW parametric effects on weld geometry and hardness. The parameters considered in the study included welding current, voltage, travel speed and electrode stick-out, and the response variables were bead width, reinforcement, penetration and hardness. The ANOVA results showed that welding current affected hardness; current and voltage significantly affected bead width and reinforcement; current and speed influenced penetration; and stick-out had no significant influence on any parameters.

Reddy (2013) employed an L_8 orthogonal array design matrix to study the relationships between the SAW input parameters of current, voltage, speed and stick-out, and the responses of bead width, reinforcement, penetration and hardness. The data sets obtained from the OA were used to train an artificial neural network (ANN) model to predict optimal SAW input parameters that would yield the desired response variables. Reddy concluded through sensitivity analysis that bead width is affected by current; reinforcement and hardness are sensitive to electrode stick-out; and penetration reacts to changes in welding speed.

2.4.2 Global search and optimisation techniques

Search and optimisation methods can be divided into two main categories according to their application. The first category is *deterministic*, which refers to the optimisation of problems that have the same outcome for the same input conditions (i.e. no randomness). The second category is *stochastic* methods, which relates to indeterminate problems – with the problem evolving in several possible ways. Deterministic methods are unsuited for solving NP-complete problems[9] because they are limited by the requirement for domain knowledge (heuristics) to guide the search within large search spaces.

[9] According to Erickson (2009), a P-decision problem means there is a known polynomial-time algorithm to obtain the answer. An NP-problem means there is a known polynomial-time algorithm for non-deterministic machine (i.e. unlimited parallelism) to obtain the answer. NP-complete means one can i) prove that the problem is NP, ii) show it is polynomial-time reducible (i.e. transforming a solution for Q into a solution for P in polynomial time) to a problem already known to be NP-complete (i.e. reducible to Boolean satisfiability). A problem is NP-hard "if and only if" it is at least as hard as an NP-complete problem.

2.4.3 The nature of the problem

The welding process parameter optimisation problem (WPPOP) is a multiple-input, multiple-output, and multiple-constraint problem, which employs parametric interaction. The problem is at least NP-complete. Like most problems related to engineering systems, this is a complex multi-objective problem that seeks to satisfy several objectives which are usually in conflict. Coello Coello et al. (2007, p. 5) defined the multi-objective optimisation problem (MOP) as

> a problem of finding a vector of decision variables which satisfies constraints and optimises a vector function whose elements represent the objective functions. These functions form a mathematical description of performance criteria which are usually in conflict with each other. Hence, the term "optimise" means finding a solution which would give the values of all the objective functions acceptable to the decision maker.

These problems therefore require the best possible trade-offs, such that the best possible solution provides the best possible collective outcome for the objectives. Such an outcome is normally presented as a set of compromise solutions, called the pareto optimal set (POS). The elements of the POS are used to generate objective function values, known as the pareto front (PF) (Coello Coello, 2009). In mathematical terms, MOP is given by the following equation:

$$MOP = f_1(x), f_2(x),\ldots,f_k(x) \quad \textbf{(2.3)}$$

where k is the number of objective functions making up the MOP.

MOPs are therefore problems whose goal is to optimise k objective functions simultaneously. This may involve minimisation of all k functions, maximisation of all k functions, or a combination of the two for k functions (Coello Coello et al., 2007). The key criterion in the above definition is that "all elements" of the vector function must be simultaneously optimised to achieve equally acceptable values of all objective functions. Objective functions may be commensurable (i.e. measured in the same units) or non-commensurable (i.e. measured in different units). These objective functions are almost always in conflict; that is, improving one function tends to degrade the other.

In a minimisation MOP having K objectives (e.g. K = {minimise bead width, minimise residual stress, minimise hardness}), a given decision variable vector x has n dimensions. That is, $x = \{x_1, x_2,\ldots,x_n\}$ in the solution space X. The task is to find a vector x^* that minimises K objective

functions; that is, $z(x^*) = \{z_1(x^*), z_2(x^*),...,z_k(x^*)\}$. The relevant restricting constraints are applied to the solution space. This produces a set of non-dominated solutions, the POS. Each solution in the POS satisfies the objective (K) at an acceptable level without being dominated by any other solution. If all objectives relate to minimisation, as in the above example, a feasible solution x is said to dominate another feasible solution y, if and only if $z_i(x) \leq z_i(y)$ for $i = 1,...k,$ and $z_j(x) < z_j(y)$ for at least one objective function j.

Moradpour et al (2015) solves an MOP for the SAW process using an approach comprising fuzzy logic and evolutionary algorithm. The welding process parameters of welding current, voltage and speed were successfully optimised to achieve the desired values of convexity.

2.4.4 Non-conventional optimisation methods

As mentioned above, the WPPOP is at least NP-complete. Therefore, the relationship between input welding parameters and output responses is complex and non-linear, and hence is difficult to determine using conventional mathematical models. Conventional optimisation techniques – such as geometric programming, multiple integer programming, dynamic programming and branch and bound techniques – all have difficulty solving problems of complexity such as that which occurs in welding process problems. This is mainly because the search space is too wide and these methods are inclined to converge towards local optimal solutions, which is unsuitable for these types of problems. The suitable techniques to solve such a problem therefore fall within the stochastic category. Commonly used stochastic optimisation techniques include simulated annealing (SA), tabu search, ant colony optimisation (ACO), particle swarm optimisation (PSO), and artificial immune system (AIS) (Coello Coello et al. 2007). Optimisation techniques can also be combined to maximise their respective strengths and improve the combined algorithmic efficiency. As is evident, most of these optimisation techniques are named after groups of biological species. This is because the concept the methods apply when converging to a solution can be related to the natural behaviour of a species.

2.4.5 Evolutionary algorithms

Evolutionary algorithms (EAs) are generally considered to be meta-heuristic problem solvers. That is, they are high-level general strategies which guide other heuristics (lower-level search procedures) to find feasible solutions from a complex search landscape (Coello Coello et al., 2007). EAs operate according to Darwin's evolutionary theory of survival of the fittest. Evolutionary operators (i.e. mutation, recombination/crossover, and selection) operate on a given set of individuals, termed the population, in an attempt to generate solutions in an ascending scale

of fitness. Parents are recombined to form children, who in turn create the next generation – which is selected based on fitness levels. Figure 2.5 illustrates the basic components of EAs.

Fitter individuals are selected from the population to become members of the next generation. The selection operator assigns higher probability of contributing one or more children in the next generation to strings of higher fitness. Common selection techniques include roulette-wheel, tournament and ranking. Other selection techniques are the (μ+λ) and (μ,λ), where μ is the number of parent solutions and λ is the number of children. The former selects the best individuals from both parent and children subsets, whereas the latter selects only from the child population.

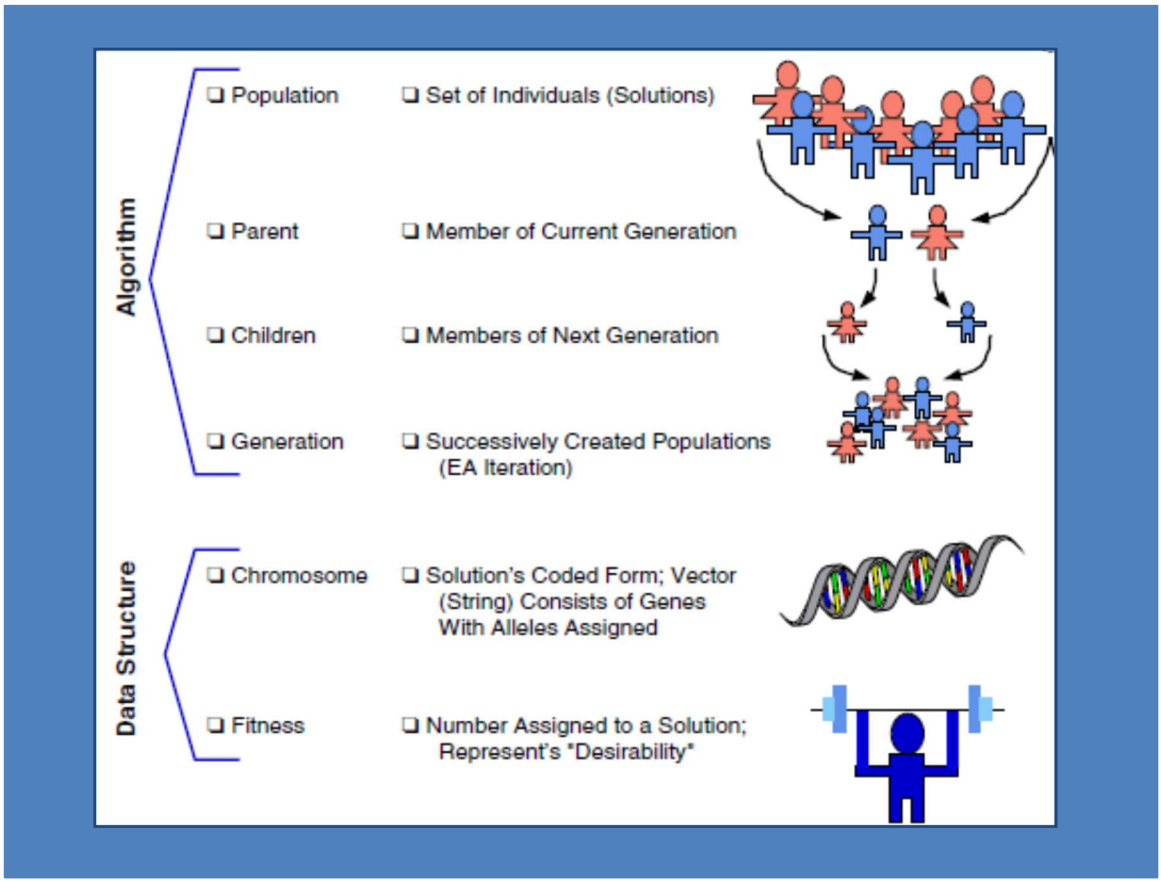

Figure 2-5: The Basics of the Evolutionary Algorithm
Source: Coello Coello et al., 2007

EAs are effective for solving complex search, classification and optimisation problems. Two main characteristics of EAs make them suitable for solving MOPs, namely i) the ability to assign a rank to each solution based on its Pareto dominance (i.e. Pareto ranking), and ii) the mechanism to maintain population diversity (i.e. density estimator). The suitability of EAs for solving MOPs is also evidenced by their ability to simultaneously consider a set of possible solutions (i.e. population), thereby achieving a goal of finding several members of the POS in a single run of the algorithm. This characteristic makes EAs far superior to the conventional mathematical programming techniques, which must perform a series of separate runs to achieve similar results.

In addition, EAs are less prone to be affected by the shape or continuity of the Pareto front; that is, they can handle concave or discontinuous Pareto fronts. By contrast, conventional methods do not easily accommodate these two issues (Coello Coello et al., 2007). EAs that are used to solve MOPs are called multi-objective optimisation evolutionary algorithms (MOEAs).

Fonseca and Fleming (1993) suggested that a multi-objective evolutionary optimisation process could be generalised through considering it as a structured interaction between the decision maker (DM) or artificial selector and an EA. In this interactive process, the DM assigns certain utility to the current set of candidate solutions, and the EA produces a new set of solutions by applying the same utility. This conceptualisation is illustrated in Figure 2.6.

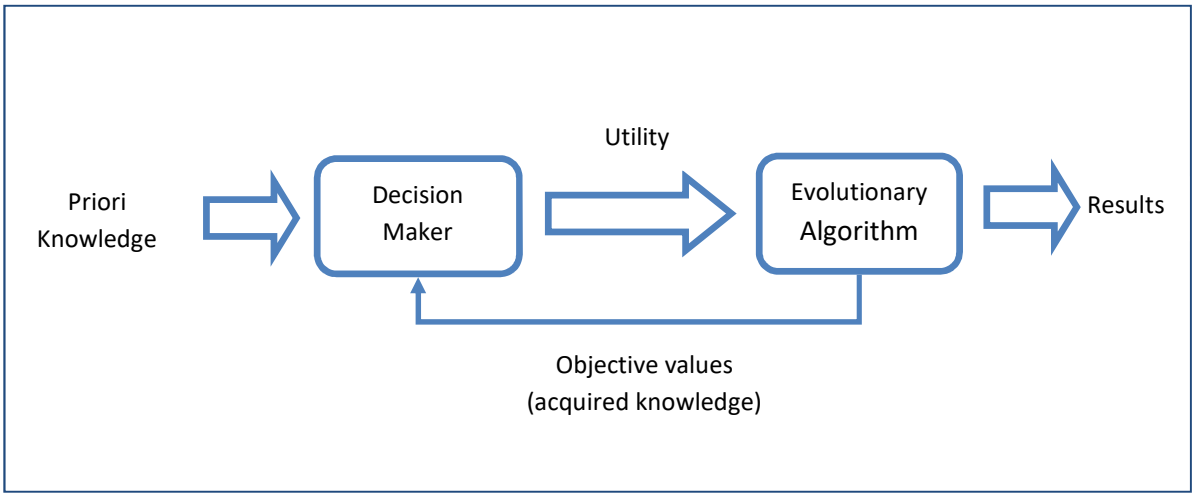

Figure 2-6: The DM/EA Interactive Relationship
Source: Franseca and Fleming (1993)

Coello Coello et al. (2007) mention four generic goals of the MOEA, namely i) preserving non-dominated points; ii) progressing towards points on the true pareto front or PF_{true}; iii) maintaining population diversity; and iv) providing the DM with limited number of known pareto front or PF_{known} points to choose from.

Performance attributes of real-life engineering problems usually exhibit non-commensurable and often competing objectives. The choice of a suitable compromise solution depends not only on determining the non-dominated vector solutions, but also through the subjective preferences of the decision maker (DM). The MOP can generally be classified into four main categories, depending on when the DM articulates its preference on the various objectives – that is, never, before, during or after (Andersson, n.d.).

a. **Never** – when the DM does not state a preference, the min-max formulation is developed, and the output comprises only one solution and not a set; the solution is accepted as the final optimal one.

b. **Priori** – when the DM aggregates various objectives into one according to a formula which represents its preference. This could be achieved through the weighted-sum approach, non-linear weighting, fuzzy logic, utility theory, acceptability functions, goal programming or lexicographic. Priori techniques involve determining the level of relative priority for each objective before the search, for example through aggregate weighting. One of the biggest criticisms of the priori technique is that its arbitrary limitation of search space, through the ranking or weighting of objectives, might not lead to P_{true}.

c. **Progressive** methods avail the DM preferences at the same time that the algorithm searches through the solution space, hence they are referred to as the interactive method. The principle is that "more interaction means better results". In this approach, the DM's preferences are incorporated during the search. The main challenge with the progressive technique is that when nothing much is known about the problem, the DM's process of defining preferences may be difficult and inefficient. The quality of a solution in this case depends on how well the DM can articulate its preferences and on the DM's subjective choices.

d. **Posteriori** techniques allow first for determining the POS of solutions and then presenting them to the DM. The posteriori approach therefore involves a situation in which the decision-making process occurs after the optimisation process.

Fitness allocation involves the assignment of importance level to the candidate solution based on certain criteria. Examples of fitness assignment approaches are listed below.

a. *Weighted-sum approach*. This entails assigning weights to each normalised vector objective function and converting the MOP to a single-objective problem with an aggregated scalar objective function. The approach is called *priori* since DM articulates its preferences before optimisation. There is only one resultant optimal solution in this case. An automation of the weighted-sum approach was provided by Hajela and Lin (1992), with the authors proposing a weight-based genetic algorithm for multi-objective optimisation (WBGA-MO). The algorithm allocates a different weight vector w_i for each solution x_i in the population during the calculation of an aggregated solution. Because w_i is embedded on the x_i chromosome, multiple solutions can be simultaneously worked out in one run. In this approach, weight vectors can also promote diversity of the population.

The advantage of the weighted-sum approach is its simplicity and computational efficiency. The disadvantage is that it has difficulty finding solutions that are uniformly distributed over a non-convex trade-off surface.

b. *Altering objective functions*. A single-objective approach may be implemented in a similar way to the vector-evaluated genetic algorithm (VEGA), which entails breaking the main population into sub-populations. In this case, the model repeatedly establishes an objective function randomly during the selection process. This approach is simple and computationally efficient. However, the shortcoming of objective switching is that the population tends to converge to suboptimal solutions.

c. *Pareto ranking*. Pareto ranking is based on the principle of assigning equal probability of reproduction to all non-dominated individuals in a population. The technique assigns a rank to each set of non-dominated candidate solutions. Fitness assignment is then implemented in accordance with allocated individual ranks. Pareto ranking was introduced by Goldberg (1989). Dominance-based ranking is a method of allocating a rank to the individual based on its level of dominance within a population. Relaxed dominance entails the recognition of an "inferior" solution (i.e. dominated) in a particular objective space, with the intention of compensating for such recognition by improving other objectives.

2.4.6 Popular MOEAs

The origins of the concept of MOP and the solving thereof using MOEAs can be traced back to Rosenberg's PhD research in the 1960s (Rosenberg, 1967). However, since Rosenberg's GA contained only a single property – and not multiple properties as suggested – at the implementation level, it was only when Schaffer (Schaffer, 1985) introduced his VEGA that the actual implementation of MOEAs was realised. Since then, interest in applying MOEAs to solve MOPs has flourished. This growing interest has led to the discovery and development of new MOEAs. Below is a brief introduction to some MOEAs that are currently widely used.

a. Vector-evaluated genetic algorithm (VEGA)

VEGA uses sub-populations that separately optimise each objective. This method does not directly incorporate the Pareto optimum. It has no intrinsic capability to maintain diversity, and it does not necessarily produce non-dominated vectors (Coello Coello et al. 2007).

b. Multi-objective genetic algorithm (MOGA)

MOGA was proposed by Fonseca and Fleming (1993). Individuals are ranked in line with their dominance within the population. Fitness assignment is executed according to the following steps:

- Population is first sorted according to rank.
- Goldberg's fitness assignment method, which interpolates individuals from the best to the worst according to some function, is used.
- Individual fitness values are then averaged according to rank categories to ensure a constant sampling rate.

Comparative studies in the 1990s showed that MOGA outperformed most MOEAs in terms of efficiency and effectiveness (Coello Coello, 2009). The difference between traditional GAs and GAs for MOP applications is that the latter utilise special fitness functions and techniques to promote population diversity. MOGA uses Pareto-based ranking and niching techniques collectively to encourage a diversified search towards the Pareto optimum. Niche formation is used to prevent premature convergence.

c. Niched pareto genetic algorithm (NPGA)

NPGA uses a technique of tournament selection, whereby two randomly chosen individuals are compared to a subset from the population. The individual found to be non-dominated when pitched against a sub-set of the population wins the tournament. Where a tie occurs between the two (i.e. both non-dominated or both dominated), the tournament result is decided by fitness sharing (Coello Coello, 2009). Whereas the NPGA version initially did not use Pareto ranking, the later version, NPGA 2, uses both Pareto ranking and continuously updated fitness sharing.

d. Strength pareto evolutionary algorithm (SPEA)

SPEA uses an external archive containing non-dominated solutions that were previously determined (Coello Coello, 2009). Diversity is maintained using a clustering technique called the "average linkage method." SPEA2 incorporates a fine-grained fitness assignment strategy, nearest neighbour density estimation technique, and an enhanced archive truncation method.

e. Non-dominated sorting genetic algorithm (NSGA)

NSGA is based on Goldberg's proposed multi-layer classification of individuals. Population is first ranked on the basis of dominance such that all non-dominated individuals are classified in one category. Then the classified category is put aside and another layer of non-dominated individuals is classified the same way to form a second category. Once all the individuals have

been classified, fitness sharing is used to ensure diversity. NGSA II employs elitism and a crowded comparison operator to maintain diversity (Coello Coello, 2009).

f. Other MOEAs

Other MOEAs include the Pareto archived evolution strategy (PAES), Pareto envelope-based selection algorithm (PESA), multi-objective messy genetic algorithm (MOMGA – II), and micro genetic algorithm or μGA (applied in populations of less than five individuals) (Coello Coello et al. 2007). It should be noted that non-Pareto MOEAs have become less prevalent over the years as Pareto-based techniques take preference.

2.4.7 Solving MOPs

MOPs are solved using global search strategies, or a combination of global and local search strategies. These problems can be solved in two ways. The first is by aggregating several objective functions into one compromise function, and then solving the problem using an appropriate algorithmic procedure. Alternatively, MOPs can be solved using Pareto-based methods, where multiple objectives are simultaneously optimised to find a set of non-dominated solutions.

Aggregating functions. In aggregating function applications, objective vector functions are normally scalarised to suit the EA's fitness information requirements. Several arithmetical combinational methods can be used to aggregate various objectives into a single scalar function. Examples are the weighted-sum approach, goal attainment technique, desirability functions, multiple attribute utility analysis (MAUA), and constraint-penalty functions. All these approaches yield one optimal solution that represents a compromised optimal level of combined objectives. The challenge with this method is that its effectiveness depends on the shape or continuity of the Pareto front. For instance, the methods do not work if the Pareto front is concave. Furthermore, weight allocation can be challenging even for an experienced researcher. Weights characterise the DM's preferences, and small perturbations in scaling of objectives can yield disproportionately large deviations in the solutions.

Adeyeye and Oyawale (2010) discussed several aggregating techniques used to solve the multi-objective welding flux design (WFD) problem. WFD is a process that purports to provide flux parameters that ensure optimal weld properties, minimal environmental pollution and optimal welding costs during the welding process. The WFD problem therefore seeks to provide flux ingredients that yield the best compromise among certain variables. Experiments were prepared using DoE techniques, and objective functions were developed by regression analysis. The researchers examined several multi-objective decision-making techniques, including weighted-sum scalarisation (WSS), goal programming (GP) and compromise programming (CP). Goal

programming works on a conceptualisation of the fact that in an MOP with conflicting objectives, it is impossible to achieve all the optimisation goals; some goal values would deviate from the ideal state. These deviations are therefore unfavourable and should be avoided or minimised. The deviations are assigned weights according to their relative importance, and their overall sum is minimised (non-preemptive). Alternatively, priorities could be allocated in a hierarchical format to response variables, and then the aggregated function is sequentially (or lexicographically) solved according to primary and secondary priority levels (pre-emptive). Compromise programming works on the principle of identifying the ideal optimal point where all objectives would reach their optimum simultaneously. The best compromise solution is then the one with shortest distance to the ideal point. Adeyeye and Oyawale (2010) concluded that the various techniques were suitable for their respective applications.

The *desirability function* (DF) approach allocates a value between 0 and 1 to indicate the acceptability of property levels of a variable (i.e. priori). The most popular DF method currently used in engineering MOPs was developed by Derringer and Suich (1980). DF formulas for larger-the-better, smaller-the-better and nominal-the-best are formulated to solve maximising, minimising and target value-based objective functions respectively. The composite desirability function is determined by taking the weighted geometric mean of all the individual DFs for each objective. The composite DF is then solved by finding property levels that maximise overall desirability. The paper by He et al. (2012) provided a robust desirability function for multi-objective optimisation. The developed method was tested using a known example, and the outputs were compared with those of previous studies. The authors combined the GA with the pattern search procedure in a pipeline fashion.

The *artificial neural network* (ANN) technique involves the modelling approach based on the artificial intelligence concept, which is used to determine input/output relationships through learning mechanisms. Juang et al. (1998) applied the ANN approach to study the relationship between TIG welding input parameters and output responses while welding aluminium plate, through comparing back-propagation and counter-propagation networks. Counter-propagation displayed better learning ability, whereas back-propagation showed better generalisation ability. A back-propagation model was proposed by Chan et al. (1999) to predict the bead-on-plate GMAW weld geometry of low-alloy steel. The model was successfully applied to define a new weld bead parameter $l_{22.5}$ (i.e. length from origin to periphery at 22.5° from work-piece surface).

Olabi et al. (2006) combined the ANN and Taguchi methods to optimise CO_2 laser welding parameters. Input parameters considered included laser power (LP), welding speed (S) and focal position (F). Response variables included penetration-to-FZ (fusion-zone) width ratio (P/W_{FZ}) and penetration-to-HAZ width ratio (P/W_{HAZ}). Ranges of welding parameters were chosen

through experimentation while regulating weld quality. The L_9 Taguchi orthogonal array was used together with triple-hidden-layered ANN with 21 neurones per hidden layer. Good agreement was noted between the Taguchi results and the ANN results.

The *controlled random search* (CRS) algorithm is a global optimisation procedure that is similar to GA. The CRS algorithm uses the stochastic transition rule rather than the deterministic transition rule, as is the case with conventional algorithmic procedures. Kim et al. (2005) described the application of the CRS procedure to optimise welding parameters that affect bead geometry during the GTAW process, namely wire feed rate, welding voltage and welding speed. A minimisation objective function was formulated with front bead-height, back bead-width, and penetration as output variables. The authors concluded that welding conditions that produce desired outputs can be determined through systematic experiments for systems that are difficult to model with the CRS method, such as the welding process.

The *response surface method* (RSM) is a method wherein the experimenter attempts to approximate the defining function of the relationship between input parameters and output characteristics, using an empirical model called the response surface model. The RSM system function (*f*) is effectively a polynomial function that approximates the relationship between natural variable and output response variables, in the following form:

$$y = f(x_1, x_2, \dots x_n) \qquad \textbf{(2.4)}$$

where *f* is a polynomial function developed through linear regression techniques.

The RSM technique comprises four main steps, namely: i) conducting screening experiments; ii) attaining the near-optimal condition by moving the region of interest closer to optimum point; iii) development of the model within the region of interest around the optimum point; and iv) determining optimal settings for the process parameters, according to the orientation of objective function (Kim et al., 2005). The RSM was applied by Murugan and Parmar (1997) to study the direct and interactive effects of the SAW parameters on stainless-steel cladding geometry.

Gunuraj and Murugan (1999) considered the effect of SAW heat input on the size of HAZ in two weld joint types (i.e. bead-on-plate and bead-on-joint), and reported that the area of HAZ was larger for bead-on-plate than for bead-on-joint for the same heat input. The mathematical models used in that study were generated using the RSM technique. Gunuraj and Murugan (2002) further conducted a study to predict HAZ characteristics of SAW-welded pipes. Their successful application of the RSM model showed that heat input enhanced the HAZ characteristics, whereas welding speed had an adverse effect thereon.

Using the RSM technique, Benyounis et al. (2004) investigated the effect of SAW input parameters – namely travel speed, arc voltage and welding current – on the impact strength at two testing temperatures (50 ^{0}C and 27 ^{0}C). The authors observed that welding current exerted the most significant effect, followed by travel speed. The arc voltage lacked any significant effect on the behaviour of impact strength under the conditions of the investigation. The optimal welding input parameters were successfully worked out using the RSM model. Murugan and Gunuraj (2005) investigated the relationship between GMAW input parameters (inter-pass time, number of passes and wire feed rate) and angular distortion. They developed an RSM model to quantify the direct and interactive effects of the identified process parameters. Angular distortion was significantly affected by the number of passes. Furthermore, all identified parameters negatively affected the angular distortion.

Benyounis et al. (2005), in their study on AISI 304 stainless steel, demonstrated through the RSM model that the residual stress on CO_2 laser butt welds was mainly affected by travel speed and laser power. Benyounis et al. utilised the RSM to determine the effect of laser welding parameters on weld geometry and heat input. The welding input parameters considered were laser power (LP), welding speed (S) and focal position (F). Step-wise regression, which automatically eliminates insignificant model terms, was used to fit polynomial equations to the experimental data. The heat input model showed that the most significant parameters were LP, S, 2FI of LP*S, and second-order effect of welding speed (S^2). The researchers concluded that the size of HAZ was mainly influenced by S and focal position.

Sudakaran et al. (2010) developed a mathematical model based on RSM to predict angular distortion. The coefficients of the polynomial function were calculated through regression analysis. Conformity tests were experimentally performed to validate the model. The authors successfully applied an RSM second-order quadratic model to predict angular distortion in GTAW of 202 stainless steel plates. The CCD method together with RSM was used successfully to determine direct and interactive effects of different combinations of process parameters within a specific range of the investigation. Welding current was found to have a strong effect on angular distortion. Welding speed varied inversely with angular distortion.

The *genetic algorithm* (GA) modus operandi is that of sweeping the region of interest, and then selecting the near-optimal process settings. GA is a search and optimisation technique based on the principles of genetic evolution and natural selection. GA operates on a principle of searching for an optimal solution from a population of many individuals, utilising a predetermined objective function. The objective function determines the fitness of each candidate as a solution. Figure 2.7 explains the basic make-up of the GA.

- A solution vector $x \in X$ is an individual or *chromosome*
- Discrete units that make up the chromosome are called *genes*
- Each gene controls one or more features of the chromosome
- Because each chromosome corresponds to a solution within the solution space, there should be a mapping mechanism between the two, called *encoding*
- The GA therefore operates on an encoding of the problem and not on the problem itself
- Collection of chromosomes is called a *population*
- The population is normally initialised randomly
- *Converging* means that the solution space is dominated by one solution or one set of solutions
- *Crossover* is the most important GA operator. It comprises the exchange of genetic information between two chromosomes
- *Mutation*, which is normally applied at gene level, is the random variation of characteristics of the chromosomes
- *Mutation rate* is the probability of changing gene properties, and is usually very small; it is a function of chromosome length
- Mutation reinforces genetic diversity back into the population, thereby reducing chances of premature convergence (local optimum)
- *Selection* is the process of identifying individuals that are fit to mate and transfer their genes to the next generation

Figure 2-7: GA Basic Terminology
Source: Konak, et al. (2006)

To study the effect of TIG welding parameters on the weld strength of brass weld joints, Canyurt (2005) developed a procedure called the GA welding strength estimation model (GAWSEM), which searches and selects the best set of models by minimising error. The author concluded that root gap in brass welding reduces the weld strength. Increasing the torch angle from 60° to 90° doubles the weld joint strength. The GAWSEM results were found to be comparable with the experimental data.

Patnaik et al. (2007) optimised process parameters for the SAW hard-facing process using the GA method. The authors identified the main process parameters as arc current, arc voltage, welding speed, electrode stick-out, and pre-heat temperature. The most important performance outputs were identified as deposition rate (kg/hr), dilution (%) and hardness. The relationship of welding parameter → performance output → welding quality was established, and it underpinned the analysis. The Taguchi method was used as the experimental design, and regression analysis was performed to determine the significance of the effect for each parameter, and then multi-parameters, on all the performance outputs. The multiple objective GA procedure was then used to solve the optimisation problem. The author concluded that GA was adequately effective for an optimum search of SAW process parameters to maximise the deposition rate, minimise the

dilution and maximise surface hardness by solving a multi-objective, multi-variate and non-linear optimisation problem.

Correia et al. (2003a) determined near-optimal input welding parameters of the GMAW process using GAs. A GA objective function was designed to minimise the economic aspects (i.e. redeposition efficiency) and the weld bead geometry (i.e. penetration, width and reinforcement). Input variables were welding voltage, wire feed rate and welding speed. The authors concluded that GA can be an effective tool in experimental welding optimisation. The optimisation by GA technique requires a good setting of its own parameters, such as population size and number of generations.

Sudakaran et al. (2010) optimised GTAW process parameters in stainless steel 202 plates to minimise angular distortion. The input parameters were identified as welding gun angle, welding speed, plate length, welding current and gas flow rate. The working ranges of parameters were identified through a range of trial runs conducted while monitoring the integrity of the weld in terms of porosity, undercut, cracks and so on. The design matrix chosen for the experiments was a five-level, five-factor central composite design (CCD) with 32 experimental runs, which allowed the estimation of linear, quadratic and two-way interactive effects of the process parameters. The study established that bead width and HAZ size decreased with increasing welding speed (i.e. decreasing heat input). Angular distortion also decreased with increasing welding speed. The GA-optimised process parameters successfully reduced angular distortion to a minimal value.

Dey et al. (2008) considered the bead geometry optimisation problem. The authors determined the optimal bead geometry of a single-pass weld of stainless steel plate produced through electron beam welding. They reasoned that the weld bead geometry affects the residual stress, distortions, and mechanical properties of the welded structure. The authors developed a constrained optimisation problem through combining RSM and GA methods to minimise weldment area and maximise weld penetration. To obtain data for regression analysis, several bead-on-plate experimental runs were performed according to the central composite design method. A significance test was performed to determine the magnitude of effect that each parameter exerted on output responses. The developed GA attained the near-optimal global solution.

Sudhakaran et al. (2011) evaluated the effect of the GTAW input parameters of welding current, welding speed, shielding gas flow rate, and welding gun angle on bead geometry. Output parameters included depth of penetration, bead width and depth-to-width ratio. Experiments designed around CCD were used to develop mathematical models, and GA was used to optimise the process parameters. It was established that the increase in welding current caused a corresponding increase in weld penetration and bead width. This was because an increase in

current caused an increase in heat input, which in turn increased the molten volume of metal, thereby increasing penetration and width. Depth-to-width ratio also increased with increasing current. Increasing the welding current caused a decrease in HAZ size. Higher levels of shielding gas flow rate resulted in marginal decrease of penetration and significant decrease in bead width. Lower gun angles produced decreased penetration, whereas higher angles increased the bid width and decreased the depth-to-width ratio. A specific interaction was required between two or more parameters to affect responses. In other words, two-factor interactions (2FIs) influenced the responses more strongly than did SFEs.

Costa and Oliveira (n.d.) presented a new approach to solve MOPs using *evolutionary strategies* (ESs). These strategies are search procedures that are based on natural selection processes like GAs. However, they work directly with decision variables, unlike the coded variables of GA; and they are deterministic in nature, unlike the stochastic nature of GAs. ESs are normally used to solve single-objective problems, but Costa and Oliveira modified them to suit an MOP application. The modified ES was referred to as a multi-objective elitist evolution strategy (MEES). The elitist scheme is based on the secondary population, which is independent of the main population. The MEES was tested in several MOPs together with other multi-objective evolutionary techniques.

Hybrid Strategies. Global optimisation algorithms naturally must balance two competing objectives, namely exploiting the best solution found so far, while also exploring the search space for further potential solutions. Successful optimisation algorithms must manage this exploitation/exploration task well. Employing a local search strategy in combination with a global search algorithm can improve the exploitation capabilities of the optimisation procedure without degrading the exploration abilities. One of the main challenges of GA is that although it can quickly locate the global optimum region, it might be slow to converge to the exact optimal solution within such a region (Coello Coello et al. 2007). *Hybridisation* of GAs with local search strategies is one way of solving this problem. The resultant hybrid GA can reduce premature convergence by maintaining the diversity while increasing the convergence speed. Hybridisation is based on a realisation that the two search methods can be complementary if combined. The intention is to capture the best of both schemes. Local search methods are considered to be learning processes in that they use the knowledge of the local environment to increase the individual solution's chances to transmit its traits to the next generation within the GA process. This is similar to the natural evolution process, in which learning increases the individual's chances of survival. GA local search hybrids use the GA's global search capability to explore a space with the intention of isolating the region of interest, after which the local search algorithm rapidly focuses on the optimal solution.

El-Mihoub et al. (2006) discussed various ways of combining the GA search framework with a different search method. In a GA application, search techniques may be incorporated into the GA framework to enhance the search capability, improve the solution quality, improve the efficiency (i.e. convergence speed, and/or population size), and to ensure that feasible solutions are generated. A different technique can be used in place of one of the GA operators to enhance performance (e.g. substituting crossover operator with a guided local search criterion). Figure 2.8 illustrates how hybridisation methods can be implemented, and for which targeted outputs.

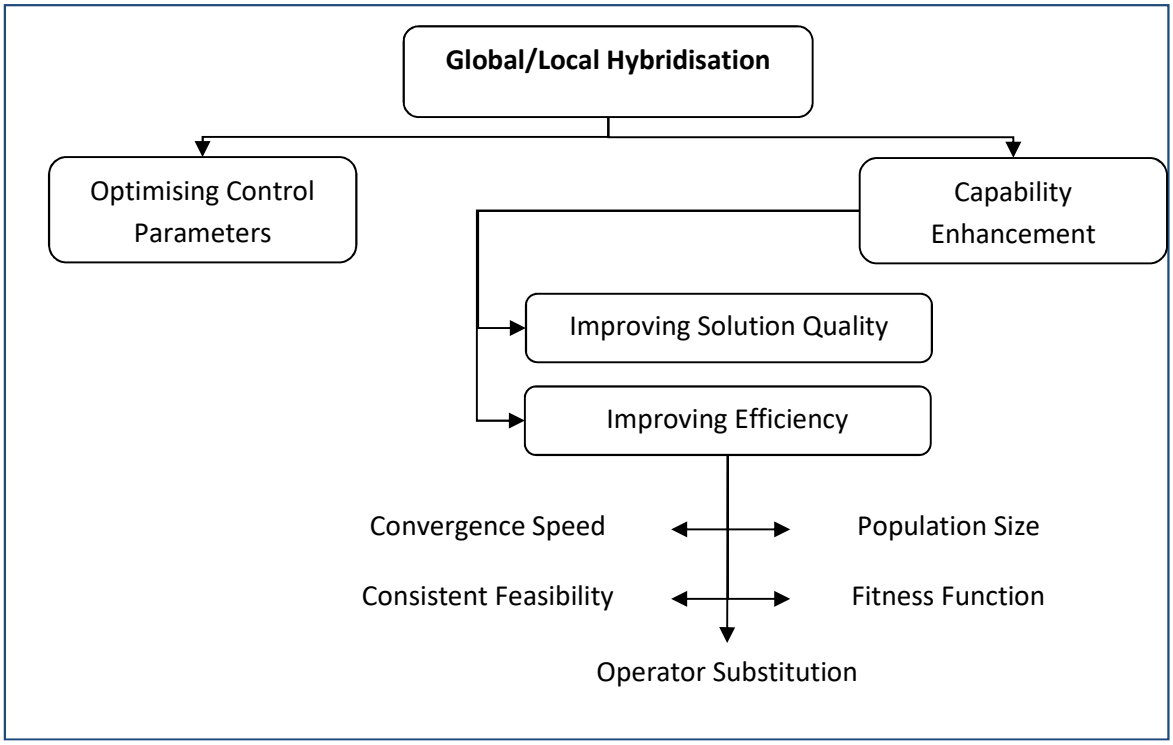

Figure 2-8: Implementation of Hybridisation Methods

Correia et al. (2003b) compared the RSM and GA techniques for determining optimal GMAW process parameters – that is, voltage, wire feed rate and welding speed. The specified output responses were deposition efficiency, penetration, bead width and reinforcement. The authors established that all experiments performed by RSM and GA yielded good-quality welds in terms of bead defects, including melt-through, porosity and cracks. They further observed that the challenge with RSM is it can provide good results only for regular experimental regions that have no irregular points. Moreover, although GA and RSM both show good optimisation results, the advantage of GA over RSM is the latter does not need to generate models.

Dutta and Prathar (2007) determined the relationship between TIG input parameters and the weld bead geometric variables, and calculated the optimal values for these parameters and variables. The cause/effect relationship premise was presumed to be welding-input-conditions → geometric-parameters → bead-mechanical-properties. Input parameters included welding speed,

wire feed rate, cleaning percentage, gap and welding current. The output geometric parameters comprised front height, front width, back height and back width. A full factorial design of experiments was used, in which two levels of five variables produced $2^5 = 32$ combinations. Data used in the analysis were obtained from literature. Three modelling approaches were used, namely conventional regression analysis (RA), back-propagation neural network (BPNN) and genetic neural system (GA-NN). Both BPNN and GA-NN performed better than RA, and GA-NN performed better than BPNN. BPNN used the steepest descent algorithm, which tends quickly to converge to a local minimum, whereas GA uses exhaustive search capabilities that yield an optimal global solution.

In a study that evaluated welding-induced residual stress for pipe weld joints in dissimilar metals for nuclear power plant (NPP) applications, Lim et al. (2010) analysed the impact of uncertainty in a residual stress prediction model. The researchers utilised data-based models formulated through support vector regression (SVR), fuzzy neural network (FNN) and a combination of the two artificial intelligence methods. They applied statistical and analytical uncertainty analysis to work out the 95% significance prediction interval. Models predicted the welding-induced residual stress within RMS error levels of 7% for FNN, 4% for SVR and 4% for combined models. A confidence level of 95% was obtained through statistical and analytical-uncertainty analyses. The combined SVR/FNN model showed the best performance.

In their study on optimisation of bead geometry parameters in a mild steel SAW weld joint, Datta and Mahapatra (2010) integrated an RSM-based desirability function with a PSO algorithm for multi-response optimisation. The input parameters were welding voltage, wire feed rate, travel speed and electrode stick-out. The method of least squares was used to estimate the regression coefficients. Full factorial DoE was used on a three-level, four-variable combination (i.e. $3^4 = 81$). Parametric interactive effects were assumed to be negligible. Three output responses were chosen, namely bead width, reinforcement and depth. Significance tests were performed using ANOVA. The developed models were successfully used for SAW parametric optimisation.

Nagesh and Datta (2010) studied the effects of welding parameters on bead geometry. The parameters included welding speed (S), wire speed (WS), cleaning percentage (CP), welding current (C) and arc gap (G) for the TIG welding process. The authors used published conventional data based on a two-level, five-factor fractional factorial DoE matrix (i.e. 2^{n-1}, n = number of variables) to develop regression equations to estimate the bead geometry parameters. The response variables were front height (FH), front width (FW), back height (BH) and back width (BW). Linear regression equations were developed considering main-factor effects and two-factor interaction effects (2FI) for bead geometry parameters. Back-propagation neural networks were postulated using experimental data to train the ANN model. The ANN model was used to

predict weld geometry parameters from a given set of TIG welding conditions. The GA objective function was defined from regression models and the mathematical equation was developed from experimental data.

Rao and Pawar (2010) discussed the application of optimisation algorithms in a manufacturing process, namely milling. Like most manufacturing processes, the quality of milled products is a function of parameter selection. Proper optimisation of process parameters reduces machining costs, increases productivity and improves product quality. A recent evolutionary optimisation technique is the artificial bee colony (ABC). The ABC algorithmic procedure, together with PSO and SA, were used to consider the minimisation of total production time as the objective function. Controlling parameters included feed per tooth, cutting speed and depth cut. ABC is a metaheuristic algorithm that imitates the intelligent behaviour of honeybee swarms. The concept behind the ABC algorithm is the "hunting bee" (known as a forager) finding and exploiting the food source. Foragers then share crucial information among themselves, related to the location and quality of the food source. Rao and Pawar found that ABC and PSO algorithms required fewer iterations before converging to optimal solutions, whereas the SA procedure required relatively more iterations to converge. The quality of solutions from the ABC and PSO procedures was better than that of SA.

Dhas and Kumanan (2011) determined the optimal weld bead width of a mild steel SAW weld, using Taguchi design methods together with GA and PSO metaheuristics. The independent variables of welding current (C), arc voltage (V), welding speed (S) and electrode stick-out were used to describe the response variable of weld bead width. Experiments were designed using a Taguchi L_8 orthogonal array layout. Statistical analysis of the experimental data was performed through multiple regression. The GA was developed using the regression equations as an objective function to minimise the weld bead width. Comparison of the computed and experimental results showed a good correlation between the two sets, demonstrating the effectiveness of GA.

Sathiya et al. (2012) studied predictions of the depth of penetration (DP), bead width (BW) and tensile strength (TS) of a laser welding process using a combination of ANN and GA techniques. The input parameters, and their significance in influencing output responses, were determined using the full factorial DoE. The relationship between input and output parameters was modelled using the back-propagation ANN technique. Back-propagation neural network is a "feed-forward, multi-layered network with a number of hidden layers, trained with a gradient descent technique" (Sathiya et al., 2012). The developed objective function models were then optimised through a GA. Good agreement was noted between the computed and experimental results for output responses, hence confirming the suitability of the developed models for welding application. Kim

et al. (2002) used a combination of GA and RSM techniques to determine optimal welding parameters for the GMAW process on mild steel plate. When comparing the same two optimisation methods, Correia et al. (2005) established that they were both effective optimisation tools for the GMAW process.

2.5 Concluding remarks

The above review provided a comprehensive evaluation of research performed to date within the field of interest. The following conclusions are drawn from the literature review:

a. The advantages of IR thermography in providing continuous temperature measurements and monitoring over a large area of interest was noted from the literature review. The suitability of the methodology and its maturity in arc welding applications was discussed. The identified challenges in applying IR thermography to monitor the SAW process are not insurmountable and should be overcome as more research is done in this area.

b. Neutron diffraction has been widely used in residual stress measurement experiments. The technique's through-thickness measurement capabilities and its non-destructive nature makes it attractive for stress measurement applications in which many measurement points are considered in a short time. The accuracy levels of ND add to its attractiveness. The technique is however still not widely accessible to many researchers given its high cost and its confinement to specialised atomic research laboratory facilities.

c. Fatigue strength assessment in welded structures is a complex phenomenon. In no small part this is because of factors such as multi-axiality of loading, uniqueness of weld geometry, different material thicknesses and residual stress distribution. In such welded components, various experimental studies have shown that local stresses are more influential on fatigue properties than global stresses. The interaction between applied stresses and residual stresses results in unique combination stresses, which makes inferences and generalisation from fatigue test results a challenging task. The inclusion of WRS fields into the fatigue properties assessment process in welded structures therefore significantly alters FCG data.

d. Finite element modelling is a useful tool to evaluate behavioural characteristics of the arc welding process. Increases in computational power and the refinement of commercially available FEA codes have made it possible to perform simulation modelling of complex systems and processes in the comfort of a computer laboratory – or even the researcher's office. These features save on costs and resources associated with physical experiments.

e. The DoE approach has been shown to be a useful and effective strategy to optimise the welding process parameters, through stretching the scope of conducted experiments and thereby maximising the analytical output of limited input resources. The ability of EAs to solve MOPs by producing a set of non-dominated solutions within the global solution space makes EAs attractive for complex problems, such as the welding parameter optimisation problem.

However, it is clear from the presented review that most of the welding experimental studies performed on steel materials have examined bead-on-plate and bead-on-groove longitudinal weld joints. Few studies have examined full penetration circumferential welds, whether pipe-pipe or pipe-plate joints. Furthermore, while the mentioned strategies and techniques have been used widely in addressing one or more welding process challenges, to the author's knowledge no compressive study has been conducted to date that has utilised all the methodologies together, to address challenges associated with nozzle-shell weld joints in pressure vessel structures. The present study is expected to fill this gap. The next chapter explains in detail how the research was conducted.

CHAPTER 3: RESEARCH FRAMEWORK AND QUESTIONS

3.1 Introduction

The first chapter of the thesis introduced the broad field of interest and the specific subject of this study. Context was provided regarding the research problem. The second chapter provided a comprehensive review of the literature on research performed to date within the field of interest. The second chapter also presented a discussion of various applicable methods, techniques and strategies, and how they have been applied in addressing similar research problems within the field of interest. That discussion gave insight into, firstly, the substance of work that has already been done in the field and, secondly, the nature and extent of the research gaps that need to be addressed. The current chapter builds on that foundation to discuss the utility of the present study in addressing the identified gaps in literature. The motivation for the study is discussed below, including the creation of linkages between the present work and the research gaps identified in section 2.5 above.

3.2 Motivation for the study

3.2.1 Weld joint type and geometry

The literature review demonstrated that there are countless studies in arc welding based on bead-on-plate, bead-on-joint or bead-on-groove weld configurations. This is mainly because welding experiments involving this type of configuration are relatively easy to conduct, and therefore become attractive to researchers who face funding and time constraints. However, in real-life applications, weld joint configurations are usually more complicated than the bead-on-plate scenario. This study considers the pipe-to-plate joint configuration, which is a typical configuration for the nozzle-shell joint of large pressure vessels.

This type of joint is relatively difficult to prepare and can pose challenges when post-weld experiments (e.g. residual stress measurements) are conducted on welded specimens. If comprehensively and correctly performed, however, studies involving this joint type can add

value to the research body of knowledge. A second aspect of importance about the pipe-to-plate joint is that it is a circumferential weld between two pieces having different material properties and geometries. The pipe and plate are usually made of different materials. This diversity can be contrasted with the homogeneous material usually used in the bead-on-plate joint. A third point to note is that the pipe-to-plate joint that was analysed in this study was a multi-pass weld bead conducted under natural cooling conditions. The residual stress fields and fatigue properties of such a weld joint present a scenario that has not been researched widely to date.

3.2.2 Experimental procedures

The arc welding process used in this study was submerged arc welding (SAW), and the temperature monitoring was performed using IR thermography. The challenges associated with continuous non-contact temperature measurement in a multi-pass SAW process were discussed in Chapter 2 and are applicable to this study. The present work therefore provides an opportunity to address such challenges during experimentation. The advantages of IR thermography as a continuous measurement technique, and those of neutron diffraction in performing through-thickness residual stress measurements, were discussed in Chapter 2. This study employed the two techniques together during experimentation in pursuit of optimal results. Conducting neutron diffraction in a geometry like the one investigated in this study poses a challenge, which is partly why it has not been widely researched. In this study, ND measurements were obtained at several points and from various positions of the specimen, for all the specimens under investigation.

3.3 Research Questions

This study aims to answer the following questions:

a. **What does the residual stress distribution look like in a multi-pass full-penetration weld of a nozzle onto a pressure vessel?**

The magnitude and direction of the residual stresses at various positions of the weld-piece were determined and plotted against the proximity to the weld zone. This step enabled the researcher to determine the distribution of the WRS field along various positions within the weld specimen.

b. **What types of distortions or deformations arise from the welding of nozzles onto cylindrical pressure vessels?**

The magnitude and characterisation of welding-induced distortions, and their influence on the life expectancy of the welded pressure vessel structure, were examined using numerical methods.

c. **What are the main factors affecting welding-induced residual stresses in pressure vessel nozzle welding? How can these be optimised to mitigate their impact?**

The study investigated which factors contributed substantially to the formation and behaviour of welding-induced residual stresses and distortions. After principal factors were identified, an optimisation process of each was performed to establish the optimal parametric composition of the welding process that will produce optimal nozzle–shell welded joints.

d. **What type of changes in mechanical properties of the weld region, HAZ and the parent metal does the SAW process induce? How can these properties be optimised to develop a welded structure with optimal fatigue performance?**

The mechanical properties (hardness and ultimate strength) of the welded specimens for all key weld regions were worked out through experimental methods. This step calculated the change in mechanical properties introduced by the welding process, and the effect thereof. Analysis of the mentioned properties for each weld specimen allowed a mapping of the relationship between mechanical properties and the parametric combination of the SAW process.

e. **How is the weld bead geometry affected by the input welding parameters? Which parametric combination produces the optimal weld bead geometry for the specific case under investigation?**

Analysis of weld bead geometry was performed for each weld specimen. The correlation between bead geometry and welding parameters was done using statistical methods. Relationships between welding parameters and resultant bead geometries were mapped and optimised through mathematical programming.

f. **How does the distribution of WRS fields in the case under investigation affect the fatigue properties of the welded specimens?**

The distribution of WRS fields and the fatigue strength of each welded specimen were determined through experimentation. The relationship between WRS distribution and FAT was mapped using the results from the experiments, to derive plausible deductions and conclusions about the research questions.

3.4 Methodology

3.4.1 Applicable analytical methods

Numerical analyses have proven useful in saving costs and time associated with "trial and error" experimentation over the years. This study employs the 3D elastic-plastic thermo-mechanical FE model with phase transformation effects to analyse the transient heat transfer process of SAW. The significant role played by volumetric expansion in influencing the WRS fields through phase transformation during the arc welding thermal cycle was discussed in Chapter 2. This study incorporates phase transformation effects during modelling of a multi-pass circumferential weld bead, which is expected to improve the agreement between experimental and numerical results of WRS distribution in the welded structure. DoE strategies are helpful in situations where a limited number of experiments can be conducted, mainly due to cost and time constraints, such as in this study. Multi-objective evolutionary algorithms (such as the one used in this study) are capable of solving multiple objective problems by simultaneously providing a set of non-dominated feasible solutions in a single run of an algorithm. The literature review showed that most studies in the field have applied aggregating methods in parametric optimisation of the arc welding process. The challenge of that approach, however, is it leads to only one "optimal" solution. The solution is based on pre-determined prioritisation of the effects of individual variables on the ultimate outcome. A solution obtained in this way cannot be optimal for all conditions of affected variables.

This study combines DoE strategies with a multi-objective optimisation algorithm to produce a set of solutions that hold true for all conditions of affected variables. The generated solutions are derived through the analysis of data from a limited number of experiments. This approach, as well as the results obtained through this study, are expected to add value to the relevant body of knowledge.

3.4.2 Relationships of interest to the study

It is clear from the review in the preceding chapter that several studies have successfully defined the cause-and-effect relationship between WRS and fatigue strength of a welded structure. However, WRS itself is influenced by several factors. Anca et al. (2010) observed that several factors influence the magnitude of the residual stresses and their distributions; these factors include the type of welding, number of passes, material properties and degree of constraint or restraint. Leggatt (2008) stated that residual stress is affected by many factors, including the geometry of the parts to be joined; the use of fabrication aids such as tasks, cleats and jigs; the pass sequence for multi-pass welds and the welding sequence for structures with more than one

weld. Furthermore, material properties – such as the coefficient of thermal expansion, yield strength, and metallurgical phase change – may also influence residual stresses.

This study takes the approach that the first step towards improving the fatigue properties of a welded structure in relation to WRS is to understand the welding factors that influence the generation of WRS. Secondly, such factors must be improved or optimised, thereby ensuring improved or optimal WRS conditions within the welded structure. The mean stress effect from the WRS fields will then be reduced, resulting in favourable fatigue properties of the welded structure. Figure 3.1 illustrates the cause-and-effect relationships that underpin the reasoning in this approach.

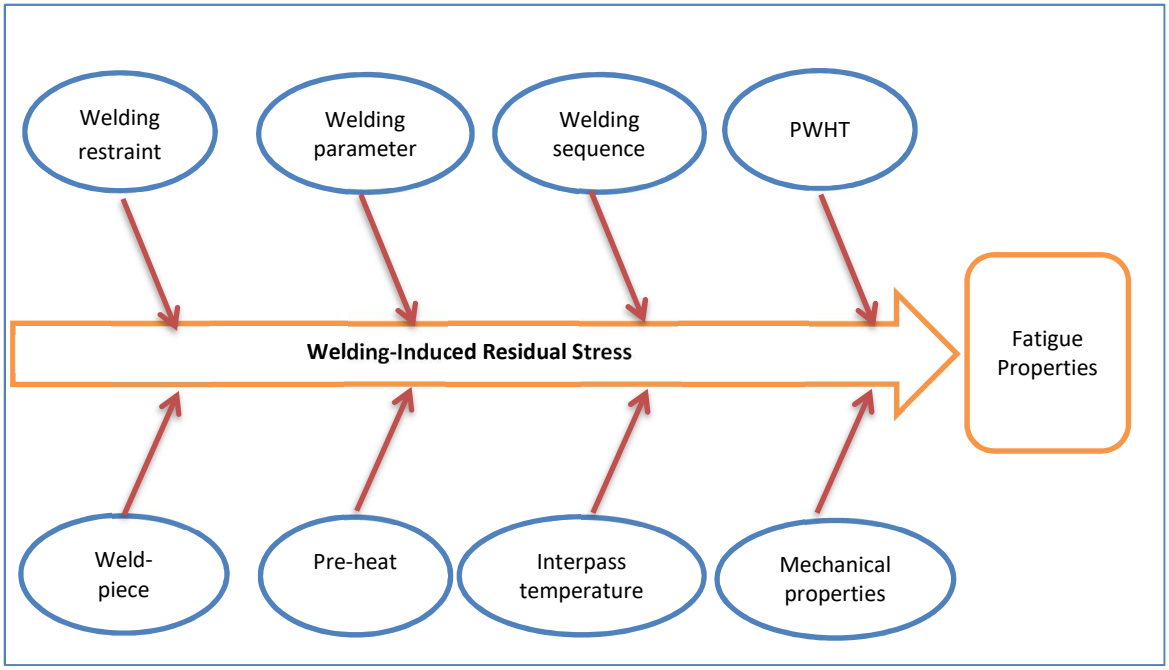

Figure 3-1: The Cause-and-Effect Relationship Between WRS and FAT

3.4.3 Hybrid model used in this study

A hybrid methodology that includes computational methods, empirical calculations, non-linear mathematical modelling and experimental measurements is used in this study. The methodological approach, and the discussion thereof in this chapter, can be divided into three parts. These parts are shown in Figure 3.2, which illustrates the framework, and are summarised below.

Part 1: Materials and experiments

i. The specification for all materials used in the study is discussed first. The preparation of the specimens and the welding conditions and procedures are also presented in this section.

ii. The procedures followed in conducting the experiments, including temperature measurements, WRS measurements, fatigue analysis, microstructure analysis and hardness testing, are presented in this section.

iii. Experimental validation of the numerical model is explained and discussed.

Part 2: Numerical analysis

iv. A finite element analysis (FEA) model is developed using the MSC software code.

v. A non-linear transient thermo-mechanical analysis, incorporating metallurgical effects, is performed in 3D formulation to establish residual stress and distortion distributions for various parametric compositions.

vi. Model is validated against the experiments performed in Part 1.

Part 3: Optimisation of parameters

vii. A multi-objective genetic algorithmic (MOGA) procedure is developed to solve the optimisation problem. The equations obtained from regression analysis are used as a multi-objective function for the MOGA.

viii. An optimal set of output responses and the required input characteristics are produced.

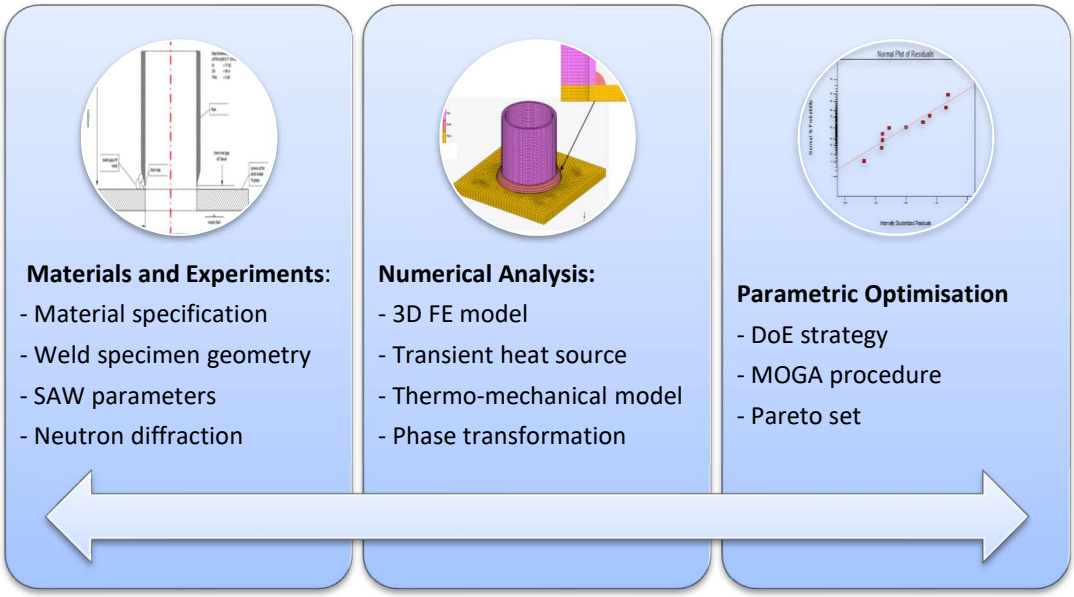

Figure 3-2: Research Methodology

3.5 Concluding remarks

The discussion in this section demonstrates the link between the research objectives of this study and the research gaps identified in the literature review. It is clear that the research content and the approach of this study can contribute to the body of knowledge within the research field of interest. The weld joint configuration, material types, and the collective techniques used in the analyses jointly present a unique research focus that has not featured in past studies. This study develops processes and procedures to control for the factors in the cause-and-effect relationship illustrated in Figure 3.1. By demonstrating the effectiveness of this model through applied examples, the study proves its utility.

CHAPTER 4: MATERIALS AND EXPERIMENTAL PROCEDURES

4.1 Introduction

As mentioned in Chapter 3, the methodology adopted in this study involved a hybrid of experimental procedures, numerical analysis and optimisation methods. This chapter discusses the materials and experimental procedures that were used to generate data to develop and validate the numerical and mathematical models. The experimental work included the research that was performed at laboratories and testing facilities in various locations. The experiments were conducted according to the guidelines outlined in the respective protocols (Appendices A and B).

4.2 Weld specimen preparation

The weld specimen was prepared as shown in Figure 4.1. A steel pipe of 80-mm bore (i.e. 3″) was welded onto a 10-mm thick steel plate by a full penetration multi-pass weld joint. The plate represented the cylindrical part of the pressure vessel shell and the pipe represented the nozzle. The material for the steel plate was high-strength carbon steel, used in pressure vessel applications, with a specification of ASTM 516 Gr. 70. The pipe material specification was ASTM A106 Gr B, seamless schedule 40. The low-hydrogen electrode EM12K was used as the filler metal throughout the experiments. The welding conditions are shown in Table 4.1. Figure 4.1 shows the process of preparing welding specimens.

Table 4-1: Welding Conditions

Welding Conditions
Room temperature: 29^{o}C
No preheat
Cooling at room temperature
Welding procedure: Semi-automatic SAW @ 85% efficiency
High strength pressure vessel plate 178 x 178 x 10 mm
80-mm (3″) seamless carbon steel pipe bevelled @ 45^{o}
Root gap of 2 mm
OK Autrod 12.22 (EM12K) low hydrogen electrode, 2.5 mm
OK Flux 10.72

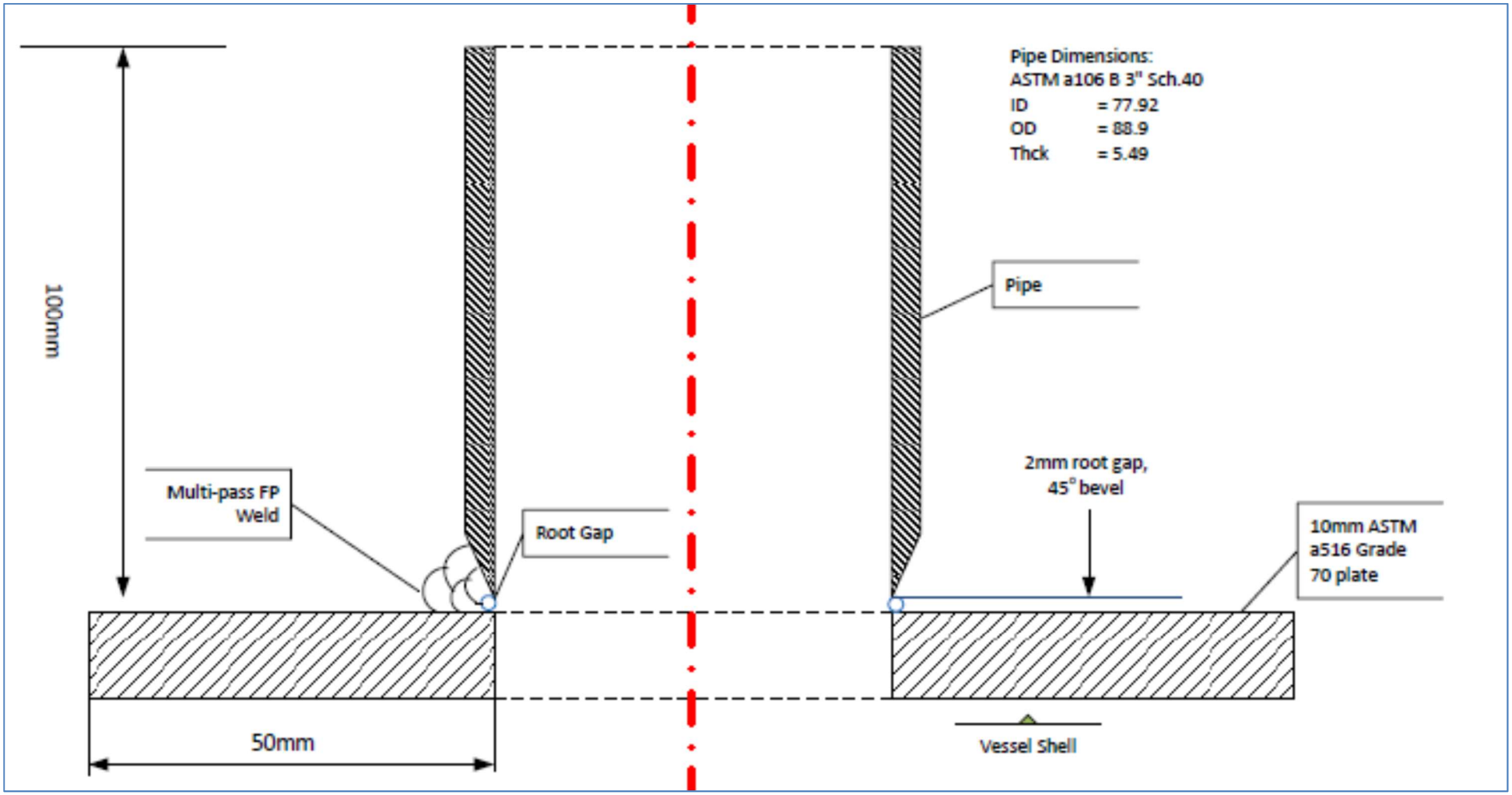

Figure 4-1: Weld Specimen Preparation

The joint geometry was that of a pipe-to-plate configuration with a single-bevel T-joint. The chosen geometry was in line with the ASME PVDC 2010 (discussed in Chapter 2, section 2.2.1). The welding was performed using the SAW semi-automatic machine. A three-pass weld was achieved using the ESAB welder and the turn-table assembly. Temperatures were recorded using an IR thermal imaging device. There was no pre-heating of the weld specimen prior to welding and there was no post-heat treatment after welding. The welded samples were cooled at room temperature after welding.

The chemical composition of the parent metals of both the plate and the pipe is shown in Table 4.2. The filler material's chemical composition is also illustrated.

Table 4-2: Material Chemical Composition

	C	Si	Mn	P	S	Ni	Cr	Mo	Cu	V	Nb	Ti	Al
Plate	0.197	0.307	1.03	0.011	0.0001	0.017	0.137	-	0.151	0.0012	-		0.027
Min/Max	0.201	0.327	1.04	0.013	0.002	0.021	0.15	0.001	0.184	0.0014	0.001		0.037
Pipe	0.198	0.24	0.79	0.009	0.004	0.05	0.09	0.011	0.08	0.001			
Min/Max	0.30	0.26	1.06	0.035	0.035	0.40	0.40	0.15	0.40	0.08	0.01	-	0.041
Filler	-	-	-	-	-	-	-	-	-	-	-	-	-
Metal	0.10	0.45	1.3	0.018	0.018	-	0.06	0.03	0.25	0.02	-	-	-

The mechanical properties of the applicable materials are summarised in Table 4.3. It can be seen from the table that the strength of the filler material properties was equal to or better than that of the parent material. The parent material is supplied in a normalised state with pearlite/ferrite microstructure. The chosen materials are generally used in industry for pressure vessel applications.

Table 4-3: Mechanical Properties of the Materials

	UTS (MPa)	YS (MPa)	%EL	Poisson ratio	Young modulus (GPa)
Plate	535	344	19	0.3	210
Pipe	510	260	31	0.3	210
Filler Metal	520	420	27	0.3	210

4.3 Welding experiment setup

The experimental setup that generated the joint configuration discussed in section 4.2 above consisted of the ESAB SAW machine and the short-wave infrared (SWIR) camera, as shown in Figure 4.2. The SAW machine has two major components, the wire feeder and the turntable.

The turntable is a requirement for conducting circumferential welds, in which the turntable speed and the welding speed are synchronised. The consumable welding electrode was fed into the weld-pool through the wire feeder during the welding process. The wire feed rate (FR) was controlled by the ESAB controller, as shown in Figure 4.2 to Figure 4.4.

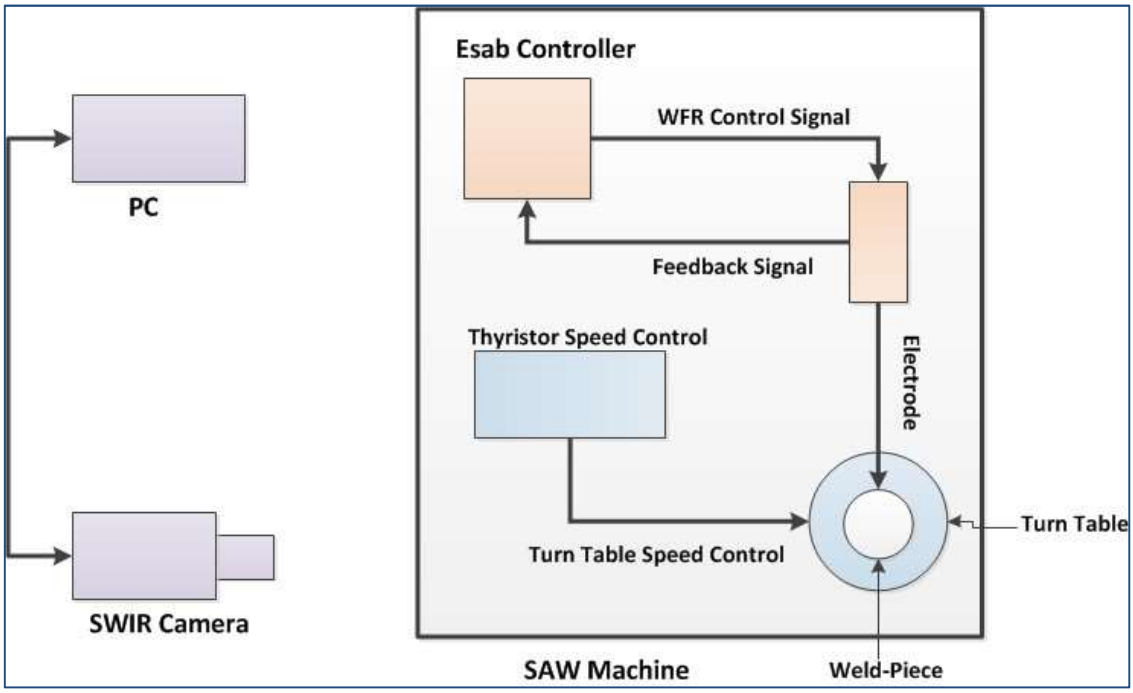

Figure 4-2: SAW Machine and SWIR Camera Layout

The controller used was commissioned with the SAW machine and operated in one of two modes; the user can either select a constant amperage (CA) mode or a constant wire (CW) feed rate mode. In CA mode, the operator selects the required current and the FR is automatically chosen by the controller, such that the operator has no direct control over the latter. In CW mode, a similar setup occurs but the operator selects the FR, and the current is automatically set by the controller. Figure 4.3 illustrates the setup for experiments as prepared in the mechanical workshop. Figure 4.4 shows a magnification of the turntable in Figure 4.3, indicating the location of the torch and flux delivery pipe relative to the weld specimen.

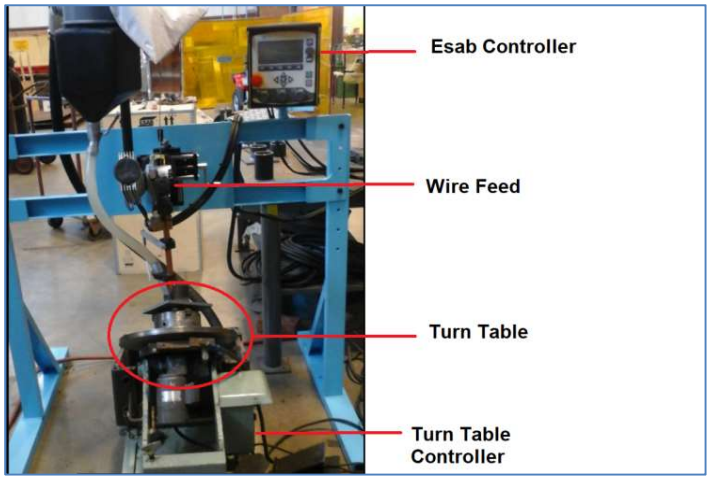

Figure 4-3: SAW Machine Setup in the Workshop

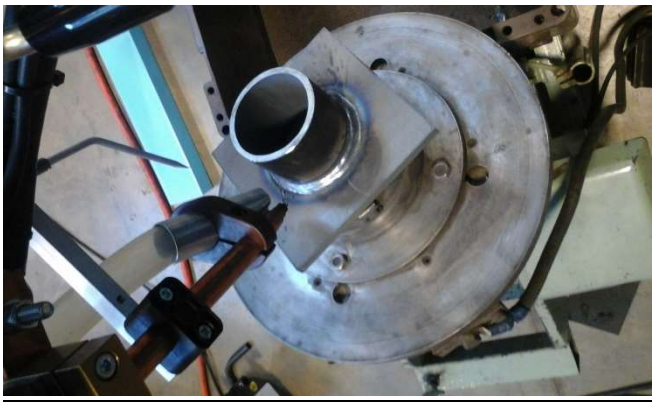

Figure 4-4: The Turntable with Weld Specimen

The SAW parameters chosen for the present study have been shown to demonstrate consistent and significant effects on the weld geometry, heat affected zone (HAZ) size, mechanical properties and residual stress, as discussed in the literature review. Chosen parameters included welding current (I), arc voltage (V), travel speed (S) and wire-feed rate (FR). Each parameter had an upper (+) and lower (-) limit, selected according to safe operational ranges (Table 4.4). The range of values was selected using guidelines from the SAW machine operator's manual and practical welding experience. The DoE strategy adopted is the fractional factorial design

When choosing the operational range for SAW parameters, care should be taken to include only parametric combinations that will not result in burn-through or lack of penetration. Table 4.4 shows the parametric settings used in each experimental iteration. Each specimen was welded using the same settings for all the three weld passes. All measurements were obtained only at the end of the third pass. The sample numbers were not always sequential because some samples were spoiled during the experiments and were discarded. For this reason, the unique sample numbers do not necessarily coincide with the experiment numbers.

Table 4-4: Welding Parameters for Each Specimen

Experiment #	Unique Sample #	I (Amp)	V (Volts	S (mm/s)	FR (mm/s)	Mode
1	4	380 (+)	30 (+)	10 (+)	18.3 (+)	CA
2	6	380 (+)	25 (-)	8 (-)	18.3 (+)	CA
3	7	360 (-)	25 (-)	8 (-)	18.3 (+)	CA
4	8	360 (-)	25 (-)	10 (+)	18.3 (+)	CA
5	9	380 (+)	25 (-)	10 (+)	18.3 (+)	CA
6	12	360 (-)	30 (+)	8 (-)	16.7 (-)	CW
7	13	360 (-)	30 (+)	8 (-)	18.3 (+)	CW
8	15	360 (-)	25 (-)	8 (-)	18.3 (+)	CW
9	16	360 (-)	25 (-)	8 (-)	16.7 (-)	CW

4.4 Temperature measurements

The experimental design was focused on capturing the temperature history and distribution across the overall structure of the weld sample. The advantage of the IR thermal imaging process over pointed sensor-based methods such as thermo-couples is that the former can record the entire area of interest at a single instance, given its broad coverage. This effectively means that data are recorded for a very large number of points of interest. During data analysis, such data can be retrieved from the image file for each point chosen. By contrast, pointed sensors record the data for only one point at a time, and data analysis is limited to such points.

As already discussed, the granular flux in SAW can present a challenge during IR thermography temperature measurements, given its tendency to insulate the surface. In this study, the metal inert gas (MIG) welding process was used, with the same heat input and welding parameters for the reference test specimen. This allowed the researcher to establish the temperature of the weld pool without the effect of insulation. It should be noted, however, that if the measurements are removed from the weld-pool and are obtained from an area with no granular flux insulation, this step is unnecessary. The latter approach was adopted for the purposes of validating the numerical model, as discussed in Chapter 5.

Temperature measurements were obtained using the Flir ultra-high resolution thermal camera (FLIR X6550SC) with a frame rate of 125 Hz (at 640 x 512 IR resolution pixels) and +/-1˚C accuracy. During measurement, the Flir short wave infrared (FSIR) radiometer was placed at a focus range of 3 m, as shown in Figure 4.2. Power to the FSIR was supplied by the standard 220 V 50 Hz single-phase municipal supply, and the FSIR was connected to the controller – a personal computer (PC) – using the original equipment manufacturer (OEM) supplied camera link cable. The FSIR was left for 5 min to acclimatise to ambient conditions before operation.

The Flir ResearchIR version 3.3 software was accessed on the controller, and the configuration setup which matched the temperature of the scene was selected. This included the sensitivity parameters (i.e. integration time and the neutral density filter). Before measurement began, a non-uniformity correction was performed to compensate for the variations in camera operating conditions and to improve the image quality. Measurements were then obtained rapidly within a closed environment to minimize the effect of path radiance and atmospheric effects, which were considered to be negligible. In addition, the SAW welding process was insulated by a layer of granular fusible flux to protect it from atmospheric attenuation.

Table 4-5: Location of Temperature Recording Points

Temperature	Location
*P*1	0 deg. on pipe side
*P*2	60 deg. on pipe side
*P*3	180 deg. on plate side
*P*4	240 deg. on plate side

Table 4.5 shows the locations of the respective recording points for the temperatures of interest on the sample. The data were later used to plot the temperature profiles for the welded samples. The recording points shown in Table 4.5 are illustrated graphically in Figure 4.5. The points P1 and P2 were measured from the inside of the pipe (weld root), whereas P3 and P4 were measured from the outside at weld-toe of the plate side.

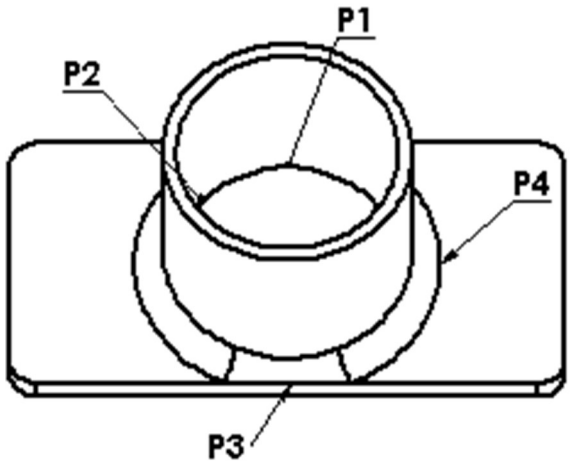

Figure 4-5: Temperature Measurement Points

4.5 Residual stress measurements

The residual stress measurements were obtained using the neutron diffraction (ND) technique, which is a non-destructive measurement approach. Whereas other stress measurement methods – such as hole-drilling and X-ray diffraction – are limited to measuring near-surface stresses only,

the penetrative capabilities of the ND technique make it possible to measure through-thickness residual stresses in metals. Neutrons can penetrate up to 50 mm of wall thickness in steels (Yuen et al., 2008). The ND method is usually preferred because of its high spatial resolution, its flexibility regarding sample geometry, its non-destructive nature and its tri-axial through-thickness measurement ability. Thermal neutrons have high penetrability characteristics and can be used to measure stress distribution in the through-thickness of steel materials, such as plates and pipes.

The ND technique requires a stress-free reference point to be determined before readings are obtained from the component under stress. A section was therefore cut out of each weld specimen using a waterjet cutter, as shown in Figure 4.6. The cut-out piece was then used as "stress-free" reference point, as the residual stress was released during the cutting-out process. The point on the inside of the weld specimen, indicated as the "heel" of the cut-out reference piece, was designated as point (0,0,0) in terms of (x,y,z,) coordinates. The spacing between measurement points was chosen as 3 mm. The flange was measured from 1.6 mm to 43.6 mm (15 points), and the pipe was measured from 10.6 mm to 73.6 mm (22 points). At each measurement point, strain was measured in three orthogonal directions: hoop or ε_h (y-axis), axial or ε_a (z-axis) and radial or ε_r (x-axis). To do so, the weld-piece was mounted in three orientations.

The flange line of measurement is shown in yellow in Figure 4.6, whereas the pipe-side measurements are shown as a green line. For the purposes of measurement, the weld centreline (WCL) was considered to be in the proximity of the coordinates (6,0,11). The measurement time varied due to path length changes, with the aim of providing strain errors of not more than 50 με.

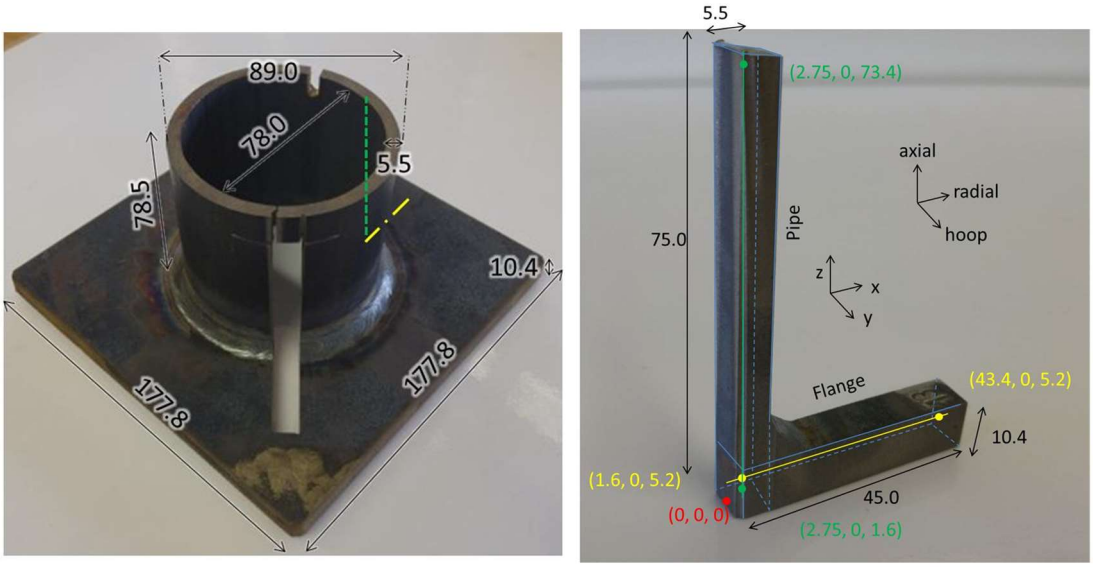

Figure 4-6: Stress Measurement Points

The materials probe for internal strain investigations (MPISI) was set up using a 2 mm radial collimator on the detector side, and the primary slit was adjusted to have a 2 mm x 2 mm window. A nominal gauge volume of 8 mm^3 was therefore defined. It was decided not to use neutron entry curves to determine the surface position of the material but rather to use only pre-calibrated theodolites aligned at the instrument's centre of rotation, due to the roughness of the welds, distorted flanges and the large gauge volume. Positioning using the theodolites can be assumed accurate to within 0.1 mm, which is less than the 10% margin normally applied for the setup accuracy. The measurement positions were chosen as far away as possible from the reference cut-out and start/stop position of the weld. To reduce sample setup complexity, the measurement positions were chosen to be tangential to a flat edge of the flange. To ensure that the gauge volume was always fully submerged in the sample material, the centre of the gauge volume was always at least 1.6 mm away from the sample surface. All measurements were taken along the mid thicknesses of the sections. The three components of stress were measured, namely hoop, axial and radial. The mounting setup for each measurement is shown in Figure 4.7.

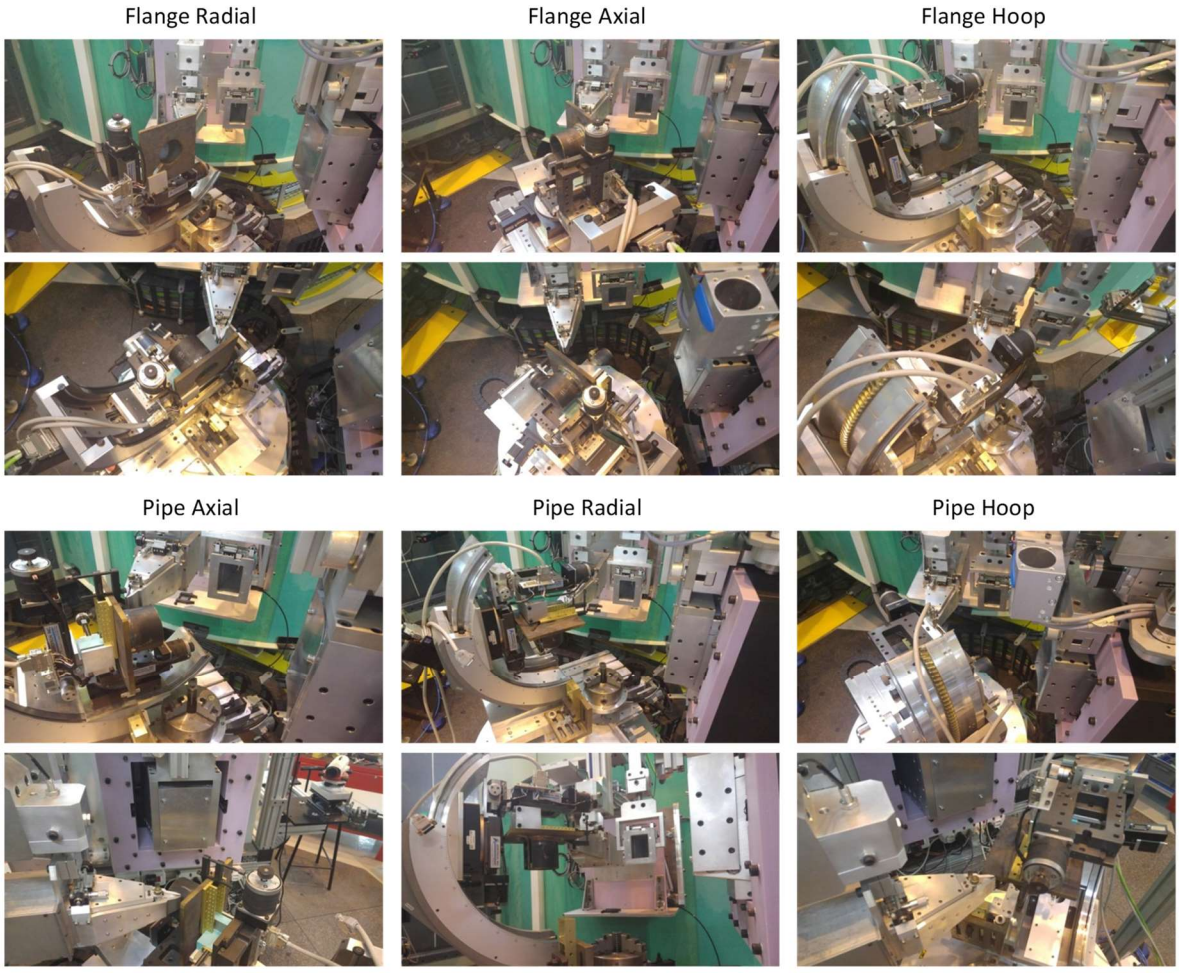

Figure 4-7: Welding Specimen Mounting for 3D Stress Measurements

4.6 Bead geometry measurements

Bead geometry is a response variable that has been monitored in many studies discussed in the literature. It is selected because the dimensions of the weld give an indication of the quality of the weld and hence its mechanical properties. The dimensions measured for the weld bead include bead width (BW), bead height (BH), bead penetration (BP) and width of the HAZ. Bead geometry was measured using stereo-microscopy to enlarge the weld bead, and the mapping of the dimensions was performed using appropriate software, as shown in Figure 4.8.

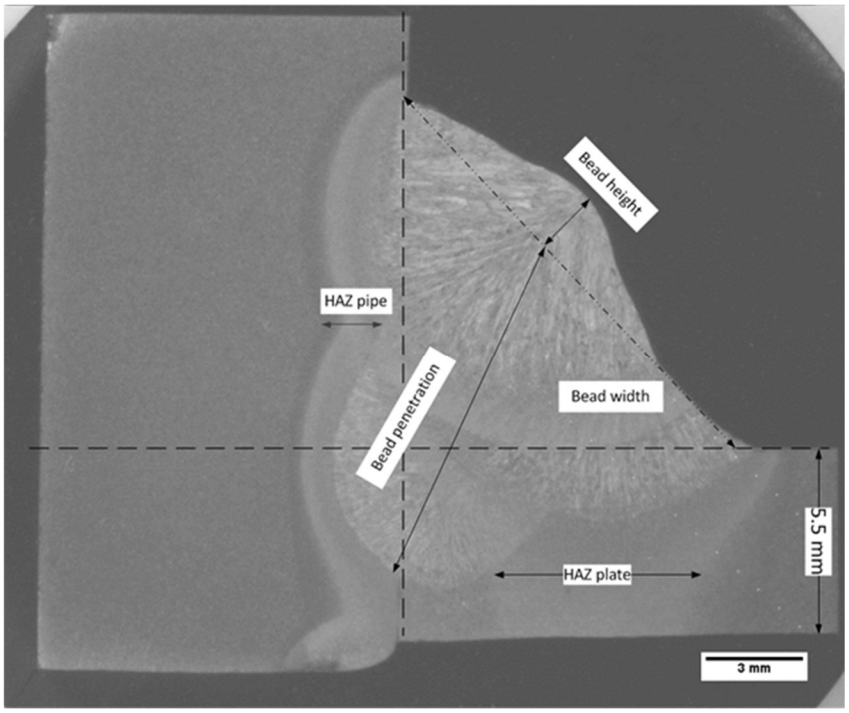

Figure 4-8: Sample Stereo Macrograph

All the measurements were done at the CSIR facility in Pretoria, South Africa. The instrument used comprised the scanning electron microscope (SEM) (Joel, Inc). The model was JSM 6010LA/Plus with a pulse processor and Optiflex accessories. The installation setup was shown in Figure 4.9.

Figure 4-9: SEM Instrumentation Setup

4.7 Microstructural analysis and hardness testing

The microstructural characterisation of the parent material (as-received), the weld metal and the HAZ are performed using the instrumentation mentioned in section 4.6 above. Received samples were subjected to grinding using an 80grit sand paper to remove the dirt and rust. The test specimen were etched in 2% Nital to reveal the size of the heat affected zone before sectioning the L-shaped test specimen to fit into the mounting machine. The sample was then hot mounted into a conductive resin, and subjected to further grinding, polishing and etching in 2% Nital for 5 seconds as specified in Appendix C.

Hardness tests were done to evaluate the mechanical properties of each test specimen. The Zwick/Roell micro Vickers indenter was used to measure hardness of parent metal, weld metal and HAZ. Five indents were made is each area and the average hardness is presented in chapter seven below. A load of 100gf was applied for 15 seconds in each indent. The indentations and measurements were automated and measured diagonally through the specimens. The instrumentation used to measure hardness is shown in Figure 4.9. The subsequent YS and UTS were calculated using mathematical models derived by Pavlina and van Tyne (2008) shown as Equations 4.1 and 4.2. These equations are easily applicable to hardness values obtained from a wide range of steels and do not require prior knowledge of the strain hardening coefficient or the Meyers index (Pavlina and van Tyne, 2008).

$$YS = -90.7 + 2.876Hv \quad \textbf{(4.1)}$$

$$TS = -99.8 + 3.73Hv \quad \textbf{(4.2)}$$

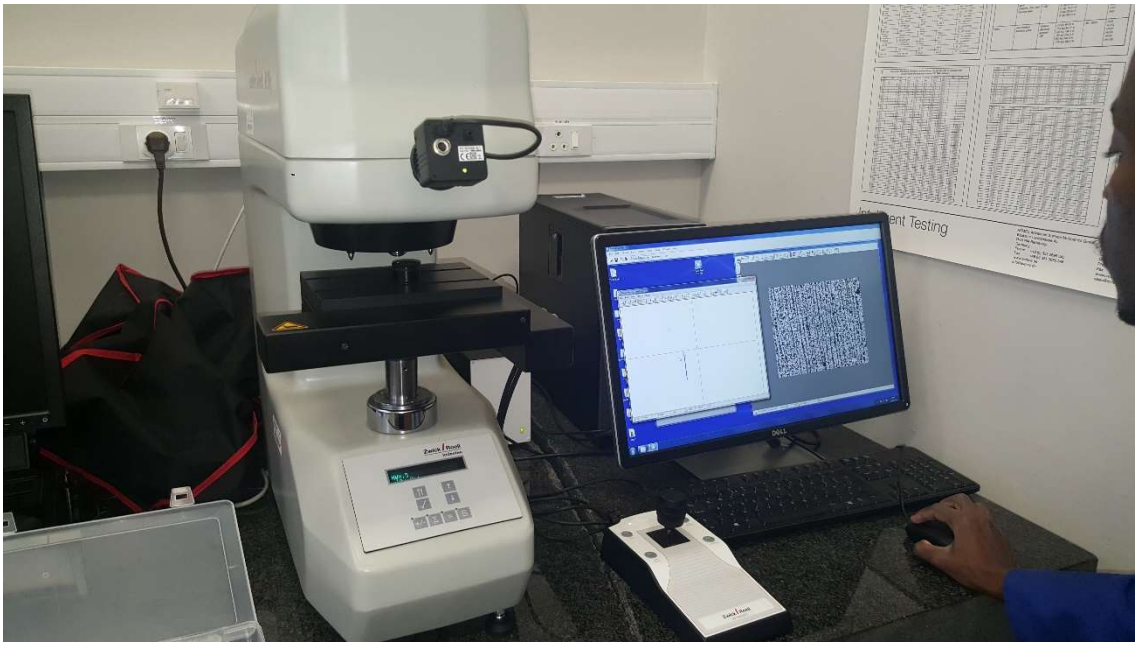

Figure 4-10: The Zwick/Roell Vickers Indenter

4.8 Fatigue testing procedures

Fatigue testing involves determining the fatigue life of welded specimens, expressed in the form of cycles to failure under fixed load conditions. The scope of fatigue analysis in this section included the following:

a. A post-test weld analysis of the cracks, to determine the fracture mode and crack initiation site for each specimen.
b. Identifying the distinctive characteristics of the surface appearance of a fatigue fracture in each specimen.
c. Identifying the different stages of fracture in each specimen.
d. Defining the mode of fracture for tested specimens.

4.8.1 Preparation and mounting of test specimen

The fatigue test specimen was prepared as shown in Figure 4.1. The specimen was then mounted onto the fatigue testing machine using a specially designed jig made of 30-mm thick steel plate (Figure 4.11). Twelve holes (M10) were drilled in each of the four flange corners of the specimen to hold the specimen onto the jig. The load-spreader plate was attached between the clamping bolts and the specimen flange, as shown in Figure 4.11. A load-spreader plate prevented the stresses induced on the test specimen flange from propagating to the bolt holes. Additional gussets

were welded onto the jig to provide adequate stiffness during the fatigue tests. It should be noted that the dimensions of the specimen in Figure 4.11 are the same as those in Figure 4.1 above.

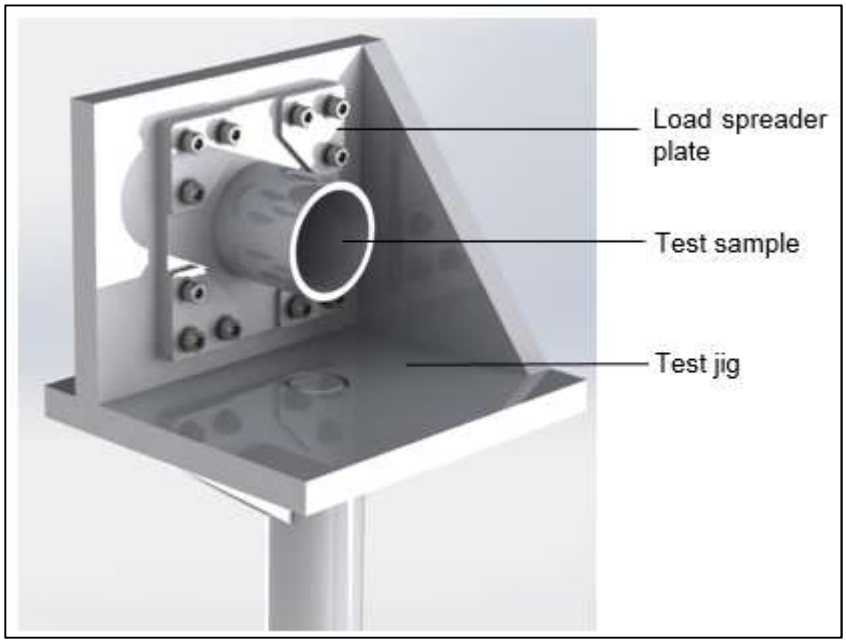

Figure 4-11: Mounting of the Fatigue Test Specimen

4.8.2 Applied bending load

The specimens were subjected to a cantilever load applied at the tip of the pipe section of the specimen. The theoretical maximum load that the specimen could withstand was first calculated using the following procedure. A dummy static load of 100 kN was applied to the portion of the sample's circumferential area, and was used to calculate the allowable stress that the pipe material could withstand (Figure 4.12). The MTU fatigue-testing machine used in this test had a maximum loading capacity of 1000 kN. The load ratio of 0.1 was applied at constant amplitude for all tests.

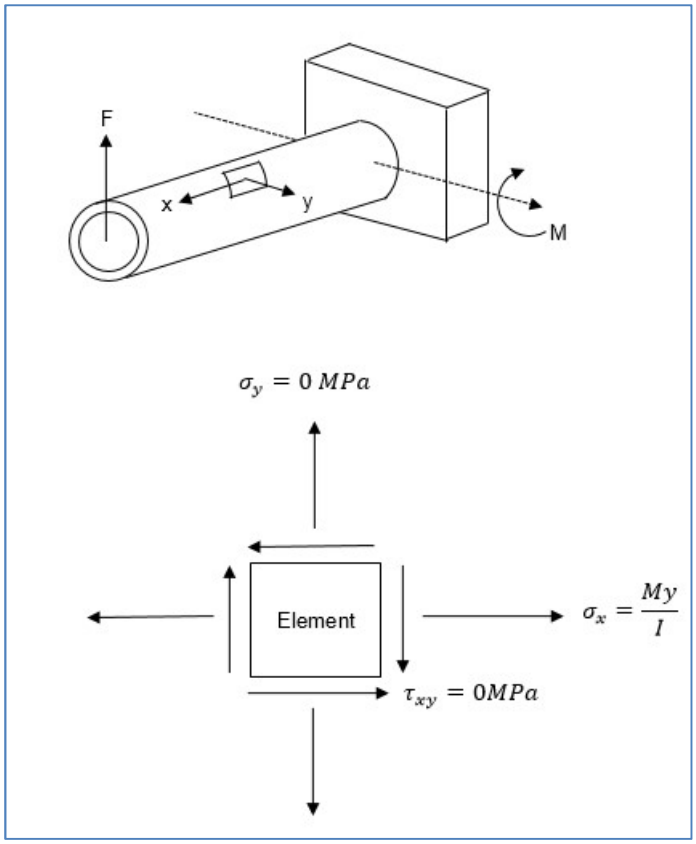

Figure 4-12: Schematic Representation of Applied Load

The stress in the x direction due the applied vertical load was calculated using Equation 4.3:

$$\sigma_x = \frac{My}{I} \quad \textbf{(4.3)}$$

The second moment of area was calculated from the following equation:

$$I = \frac{\pi(D^4 - d^4)}{64} \quad \textbf{(4.4)}$$

The cross-sectional area of the shaft was calculated from the following equation:

$$A = \frac{\pi(D^2 - d^2)}{4} \quad \textbf{(4.5)}$$

where D = 89 mm, d = 77 mm, y = 38.5 mm, F= 100 kN, l = 80 mm and M = 8 kN.m. Calculating the axial stress using Equation 4.3 resulted in $\sigma_x = 162\ MPa$.

The yield strength of the filler material at the weld was 420 MPa. The factor of safety at the welded area for an applied vertical tensile and compressive static load of 100 kN was calculated as follows:

$$\sigma_o = X_S \times \sigma_x \quad \textbf{(4.6)}$$

$$X_S = \frac{420}{162} = 2.6$$

The ultimate strength of the filler material at the weld is 520 MPa. The factor of safety at the welded area for an applied vertical tensile and compressive static load of 100 kN was calculated as follows:

$$X_S = \frac{520}{162} = 3.2$$

Thus, the weld specimen was expected to fail in bending at an applied static load calculated as follows:

$$F_S = 100 \times 2.6 = 260 \text{ kN}$$

The solid steel shaft was inserted into the pipe of the weld specimen, at the loading area, to prevent possible local deformation in the clamping contact area. The configuration is shown in Figure 4.13.

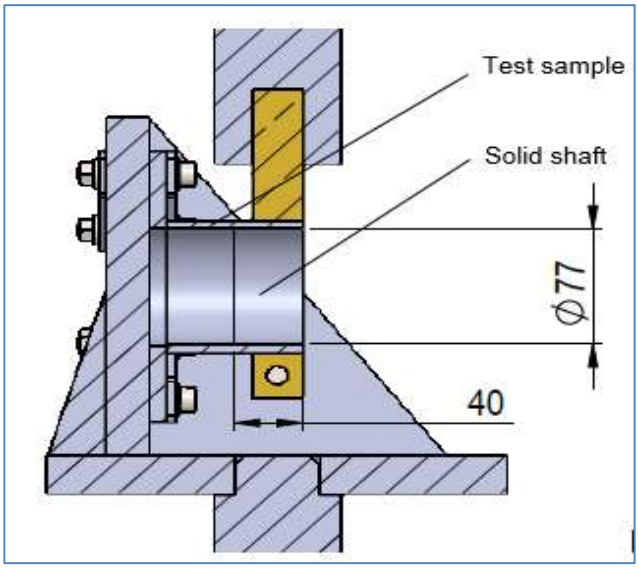

Figure 4-13: Fatigue Test Setup at Loads above 100 kN

4.8.3 Fatigue test equipment setup

Testing equipment included the MTS high-force servo-hydraulic testing machine, Vernier callipers for measurements and the wrench for tightening bolts. In fatigue testing, a specified mean load (which may be zero) and an alternating load are applied to the test specimen, and the number of cycles required until failure occurs is recorded. Table 4.6 shows the fatigue loading of the specimens. Load was applied axially by the servo-hydraulic machine (Figure 4.14).

Table 4-6: Fatigue Loading of Specimens

Unique Sample #	2x Specimen	1x Specimen
4	0.8 x max load	0.6 x max load
6	0.8 x max load	0.6 x max load
7	0.8 x max load	0.6 x max load
8	0.8 x max load	0.6 x max load
9	0.8 x max load	0.6 x max load

Three test specimens were prepared per parametric combination for the CA welding machine setup. Two specimens of each sample were tested under 80% maximum load (calculated in Section 4.7.2) and one specimen for each sample was tested under 60% maximum load.

The integrity of the weld bead was tested using non-destructive testing methods. Non-destructive testing was also used to determine crack development during fatigue testing. Two parameters were monitored during the test, namely load and displacement. The load parameter was kept constant and the displacement of the pipe was used as the failure criterion.

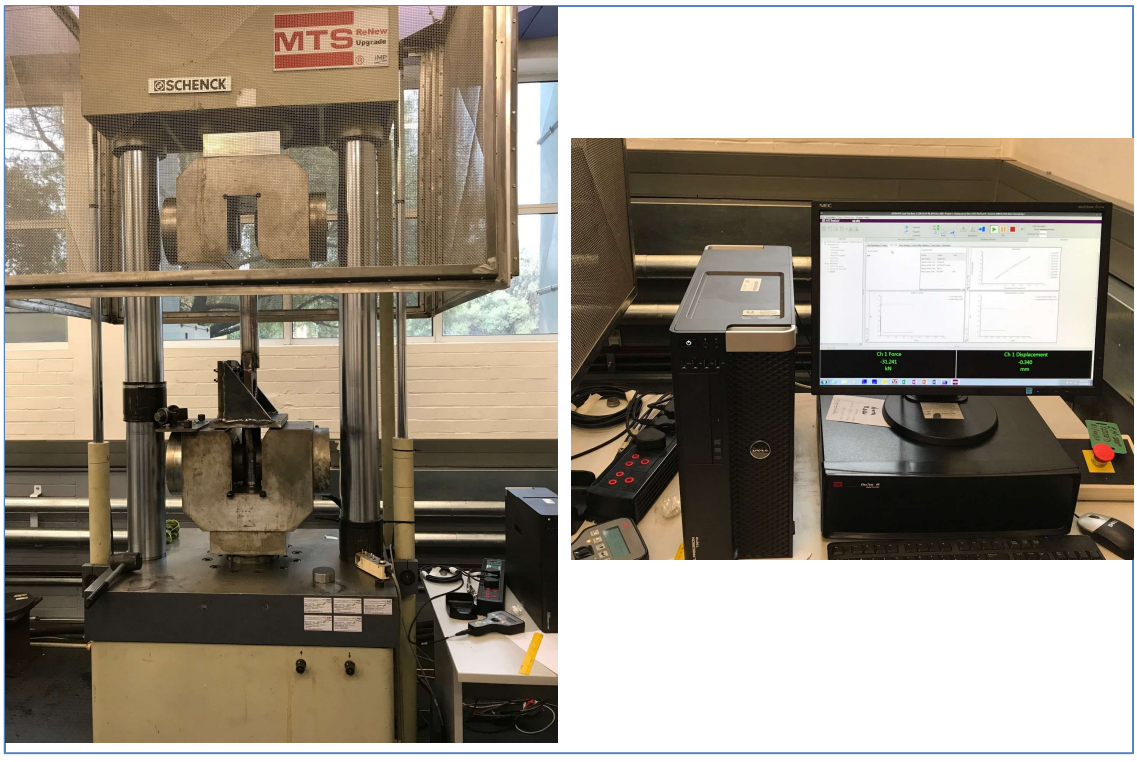

Figure 4-14: Servo-Hydraulic Machine Setup

4.9 Concluding remarks

The discussion above provided details of the experimental work performed in this study. The experiments entailed the fabrication of welding specimens in a mechanical workshop, followed by various analyses on each specimen to determine its geometry, mechanical properties, residual stress and fatigue life. The SAW process was used to manufacture the welding specimen and temperatures were recorded throughout the welding cycle, using thermal imaging. The ND technique was used to measure through-thickness residual stresses in the specimens. Microstructure characterisation and weld bead measurements were also performed through electron backscatter diffraction (ESBD) in SEM. Vickers hardness was measured through an automated indentation process, and fatigue tests were performed on a servo-hydraulic machine. The procedures followed in each experimental test are explained in detail in Appendices A to D. The results of the experimental tests are presented in Chapter 7.

CHAPTER 5: NUMERICAL ANALYSIS

5.1 Introduction

Finite element analysis (FEA) is a numerical modelling scheme for simulation of engineering structures, to virtually study the expected behaviour of the structures under specific conditions. The significance of this method is its ability to isolate essential parameters of the complex welding process and procedure, to study the effects of specific parameters on the formation of welding-induced stress and deformation. Although experimental methods are used to calibrate the simulation procedures, the latter have the advantage of being suitable for systematic investigations of parameters that might not be accommodated by experimental studies alone (Feng, 2005).

Kisioglu (2005) observed that many researchers have developed analytical and experimental methods to predict the effect of weld joints on structural behaviour. However, advances in computer-aided modelling, such as the finite element model (FEM), have even further aided the analysis of structural behaviour in welded components. The complexity of the welding simulation problem can be appreciated through considering that the enormous temperature differential in the arc area creates a non-uniform distribution of heat in the work-piece. The increasing temperature causes the following:

- a decrease in yield strength
- an increase of the coefficient of thermal expansion
- a decrease in thermal conductivity
- an increase in specific heat.

Furthermore, welding causes changes in the physical and metallurgical structures in the weld (Feng, 2005). The process of determining the welding stresses and distortions through FEA simulation is therefore an inherently difficult problem to solve.

The 3D numerical modelling is accepted as an effective method for solving complex welding problems accurately; it is regarded as more accurate than 2D modelling. Taylor et al. (2002) stipulated two alternative ways in which the welding process can be numerically simulated, namely the *thermo-fluid* approach and the *thermo-mechanical* approach (explained further in 5.2 below). In the thermo-fluid approach, the complex fluid and thermo-dynamics close to the weld pool are modelled by observing the weld pool and the HAZ. The physical characteristics of the molten weld pool and the HAZ are represented through the conservation of mass, momentum and

heat equations, together with the surface tension and latent heat boundary conditions. Alternatively, the thermo-mechanical behaviour of the weld structure can be modelled, with a focus on the heat source. Various heat source models can be used in the simulation of welding. Their accuracy depends on the empirical and theoretical parameters that describe the weld pool shape and size (Yaghi & Becker, 2004). A thermo-mechanical modelling approach incorporating a 3D model is adopted in this study.

5.2 Thermal, mechanical and metallurgical interaction

To understand the thermodynamic and physical interactions that occur during welding of steels, one must understand the individual aspects involved in this non-linear relationship. Figure 5.1 represents the schematic features of this phenomenon. During welding, the non-uniform temperature distribution experienced by the material causes thermal stress (1), and the induced phase transformation (2) affects the structural distribution in the solid–liquid transition or martensitic / pearlitic transformations in the solid phase. This process results in transformation stress (3), and interrupts the strain field in the body.

In Figure 5.1, arrows in the opposite direction indicate the following interaction. Existing stress in material performs work, some of which is converted to heat (4), thereby affecting the temperature distribution. The stress-strain aspect has the effect of accelerating phase transformation (5). In addition, latent heat is released due to phase transformation (6), which affects the temperature distribution (Feng, 2005).

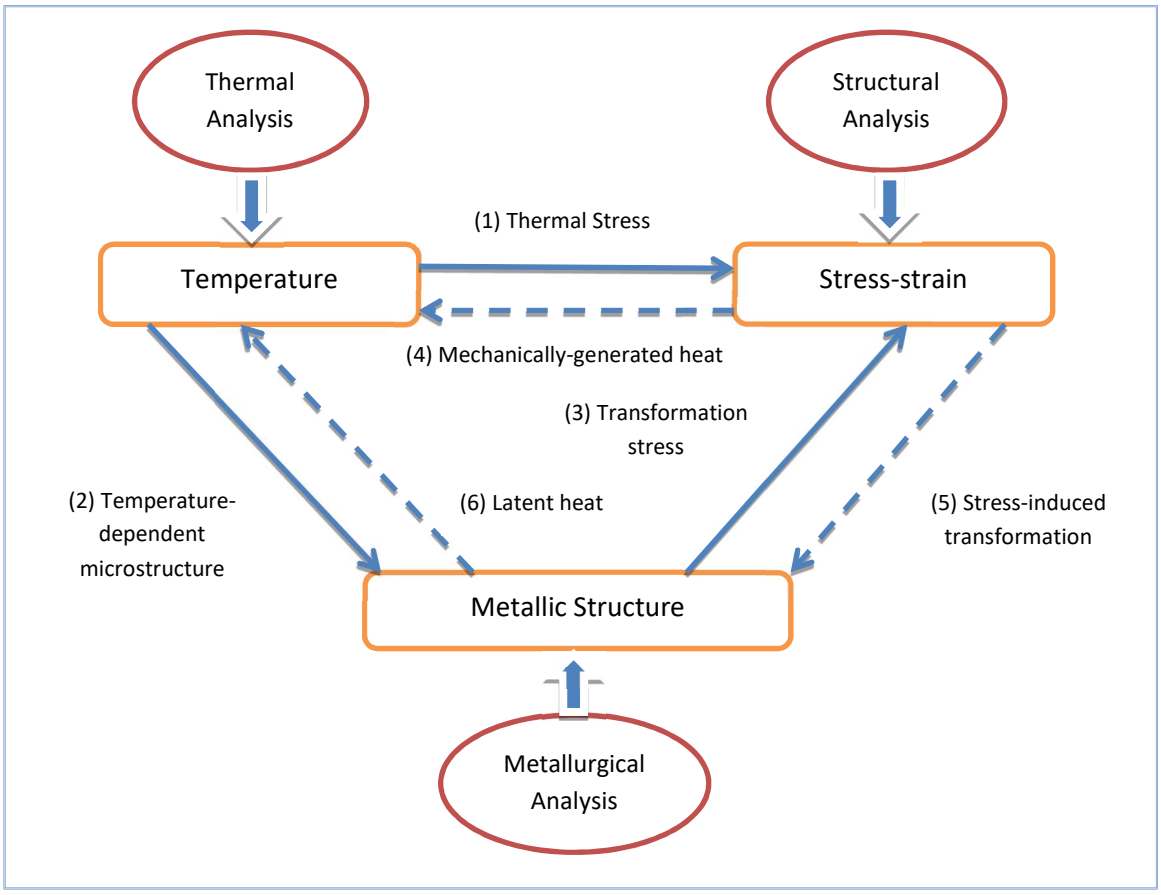

Figure 5-1: Thermo-metallo-mechanical Interaction During Welding
Source: Feng (2005)

In this study, a non-linear time-dependent thermal elastic-plastic analysis of a moving heat source was performed, to predict the thermal and mechanical behaviour of the weldment and HAZ. The solution of the non-linear transient problem was divided into two parts. Firstly, a thermal analysis (incorporating phase transformation effects) was performed to predict the temperature history of the model. Secondly, the predicted temperature fields were applied as input for the subsequent mechanical analysis.

5.3 The Finite Element Model

A 3D model was created in MSC Marc to perform a coupled thermal-mechanical analysis. The computational model, shown Figure 5.2, consisted of 28 121 eight-noded hexagonal (hex) elements, with an average mesh resolution of approximately 2 mm. The mesh was relatively more refined in the area of the weld, as shown in the figure. This is based on a concept of dynamic meshing as applied in similar studies by Nezamdost et al. (2016) and Akhlaghi (2014). The properties of the mesh are summarised in Table 5.1.

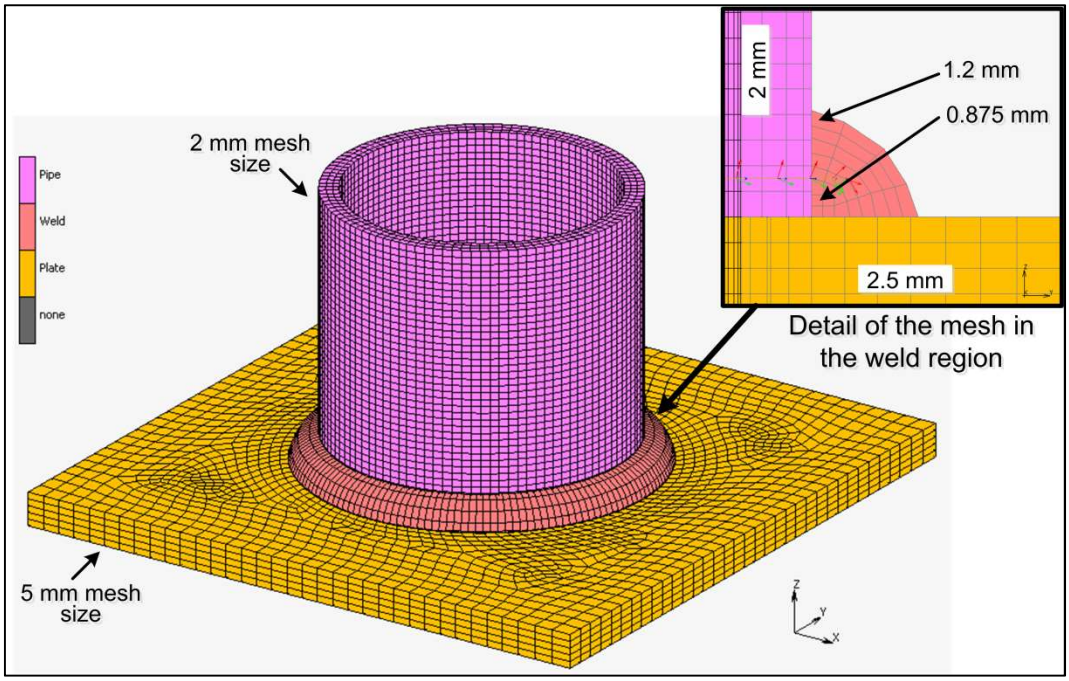

Figure 5-2: The 3D FE Model

Table 5-1: The Mesh Properties

Contact body	No. of elements	Element type	Element size (ranging from smallest to largest dimension)
Pipe	12960	Hex-8	2 mm
Weld deposit	4536	Hex-8	0.875 mm – 1.2 mm
Plate	10625	Hex-8	2 mm – 5 mm

The plate, weld deposit and pipe were modelled as three separate bodies, with contact specified between the bodies on the relevant surfaces to prevent penetration. The coupled thermal-mechanical analysis was non-linear due to the non-linearity of the material model (ie. elastic-plastic material). Beyond a certain point, known as yielding, the constitutive relation between stress and strain is non-linear. The governing equation of the thermal analysis was conservation of energy, which is used to solve for energy. The governing equations of the structural analysis were the equilibrium equations, constitutive relations and compatibility equations, to solve for the displacement, strain and stress fields. MSC Marc uses a staggered solution procedure in the coupled analysis; the heat transfer analysis is first performed, then the stress analysis. Theory and additional background information on the solver are provided by MSC Marc (2013).

The following modelling assumptions were adopted for the thermal-mechanical model:

a. The pipe, plate and weld material have the same material properties and have been modelled as an elastic-plastic isotropic material with temperature-dependent properties. Plasticity is governed by the Von Mises yielding function, associated flow rule and linear isotropic work-hardening (MSC Marc, 2013).
b. Viscous material behaviour at high temperatures is neglected.
c. Initial stresses and strains are ignored.
d. Initial temperatures are taken as 29 C.
e. Natural heat loss is due to convection and radiation only. Conduction heat loss (i.e. to the turn table) is negligible. Heat loss coefficients remain constant.
f. The welding efficiency was 85%.[10]
g. The pipe geometry is simplified (the root gap between the pipe and the plate and the chamfer on the pipe, illustrated in Figure 4.1, can be neglected).
h. The weld bead geometry is simplified.
i. The heat source model is simplified, as proposed by Goldak et al. (1984).
j. The effect of annealing is not considered.

5.4 Thermal analysis

Temperature exerts a significant influence on the microstructure, stress, strain and ultimately formation of distortions and other weld defects during the arc welding process. Hence it is essential to accurately compute the transient temperature fields. This section discusses heat source modelling, boundary conditions and metallurgical effects.

5.4.1 Heat source model

The temperature field arising from the moving heat source introduces phase transformations, thermal strains, thermal stress, distortion and residual stress. To achieve an accurate predictive model for the welding process, careful attention must be paid to modelling the transient temperature field. The physics of the weld heat source is highly complex; in the past four decades, models have been developed to simplify the physics to a level that can be implemented using available model tools. Goldak and Akhlaghi (2005) classified the evolution of welding heat source models into generations, spanning first to fifth generations. Each subsequent generation is generally an improvement on the preceding generation, with the fifth generation being the latest "state of the art" in heat source modelling. The double ellipsoid heat source configuration used

[10] The recommended SAW arc efficiency is 85% according to Kou (2003).

in the present study is the most popular heat source model for arc welding process modelling (Feng, 2005).

Consider a fixed Cartesian plane of (*x, y, z*) coordinates. A heat source located at $z = 0$ and at time $t = 0$ moves with a constant velocity v along the z-axis. Figure 5.3 graphically illustrates the moving heat source model as suggested by Goldak et al. (1984). The model follows a Gaussian distribution and has good features of density and power distribution control in the FZ and HAZ. Goldak's moving heat source model revealed that the temperature gradient in front of the heat source was lower than expected, while the trailing edge's gradient was steeper than the experimental values (Karunakaran & Subramanian, 2001). Hence, two ellipsoidal sources were combined to give the total heat flux, shown in Figure 5.3.

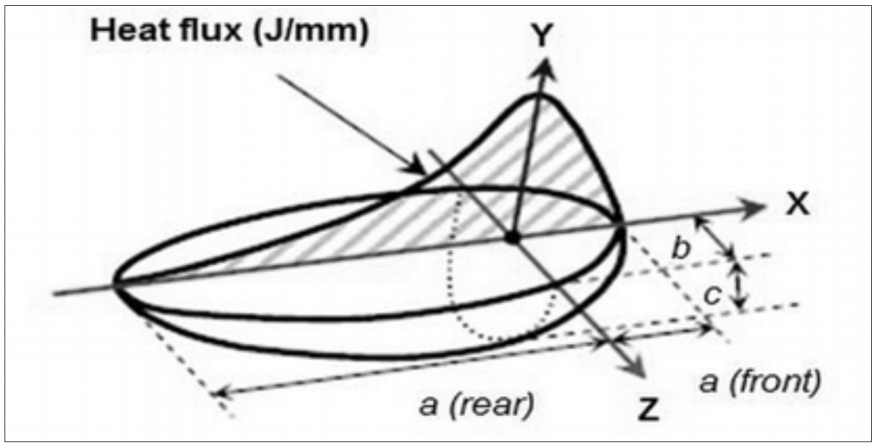

Figure 5-3: Goldak's Moving Heat Sources
Source: Goldak et al. (1984)

The corresponding heat input components for the front and rear sections are estimated through the following equations (Goldak et al., 1984):

$$q_r = \frac{6\sqrt{3}Qf_r}{\pi\sqrt{a_r}bc}\exp(-3\left(\frac{x^2}{a_r^2}+\frac{y^2}{b^2}+\frac{z^2}{c^2}\right)) \quad \textbf{(5.1)}$$

$$q_f = \frac{6\sqrt{3}Qf_f}{\pi\sqrt{a_f}bc}\exp(-3\left(\frac{x^2}{a_f^2}+\frac{y^2}{b^2}+\frac{z^2}{c^2}\right)) \quad \textbf{(5.2)}$$

where:

f_f and f_r are the front and rear fractions of the heat flux, and a_f, a_r, b and c are semi-characteristic arc dimensions in the x, z and y directions, respectively (as shown in Figure 5.3).

The z-coordinate is related to the moving coordinate as follows (Goldak et al., 1984):

$$z = v(\tau - t) \quad \textbf{(5.3)}$$

where v is the welding speed, and τ is the lag factor that defines the position of the heat source at time $t = 0$;

$$f_r = \frac{2a_r}{a_r + a_f} \; ; \; f_f = \frac{2a_f}{a_r + a_f} \; ; \; f_r + f_f = 2$$

$$Q = \eta EI \qquad \textbf{(5.4)}$$

Where Q = total heat input, η = arc efficiency, E = welding voltage and I = welding current. The parameters of the heat source model used in this study are shown in Table 5.2:

Table 5-2: Parameters of the Goldak Heat Source Model[11]

Goldak Parameter	Mm
B	5
C	3
a_f	5
a_r	12
f_f	0.6
f_r	1.4

The heat input was specified as a volumetric heat flux, which is a built-in MSC Marc welding function. The volumetric heat flux was simulated as a moving double ellipsoid heat source, as initially proposed by Goldak. The heat input was user-defined by specifying the welding parameters, such as power and efficiency, size of the heat source, the weld path, speed of the weld and the additional material elements. The weld parameters for each sample test case were described in Chapter 4. The additional material deposited per pass was defined according to Figure 5.4. Each weld deposit had approximately the same volume, and the size of the weld was measured from the weld cross-section. The "element death and birth" technique was used to model the filler material. In this technique, the weld elements are dynamically generated by the heat source when the arc reaches their position. The thermal properties are fully activated (restored to normal values) upon physical creation, and the mechanical properties are fully activated in the next increment. The weld path was defined as a curve, 3 mm radially away from the pipe and 3 mm above the plate, as shown in Figure 5.4.

[11] Values were obtained from Anca et al. (2011), and adjusted by thickness ratio between the material used in this study and that of Anca et al.

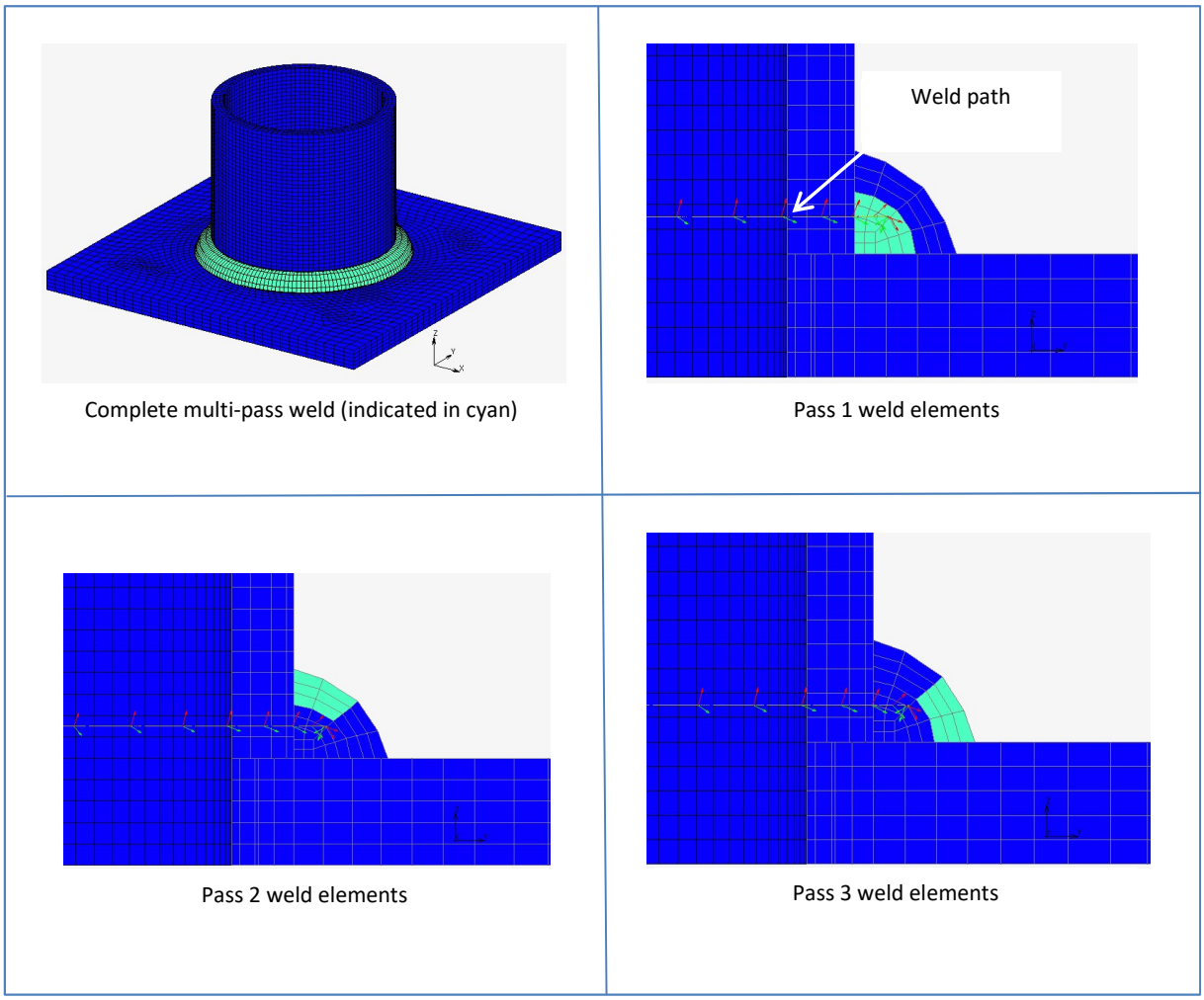

Figure 5-4: Filler Material Element Activation Technique

5.4.2 Boundary conditions

A convection and radiation heat loss boundary condition was applied to all the exposed surfaces of the sample, including the elements of the weld as soon as they were deposited. The heat loss boundary condition is shown in Figure 5.5. The heat transfer coefficient was stated as 15 W/m^{2}K, with an ambient temperature of 29°C and emissivity of 0.625 (Feng, 2005). The heat transfer coefficients for convection and radiation were used to calculate the heat flux losses on the surfaces of the weld-piece using the following equations (Feng, 2005):

$$q_c = h(T - T_0) \quad \textbf{(5.5)}$$

$$q_r = \epsilon\sigma(T^4 - T_0^4) \quad \textbf{(5.6)}$$

where T_0 is the ambient temperature; T is the surface temperature of the weld pool; ϵ is the emissivity; σ is the Stefan-Boltzmann constant and h is the convection coefficient. Losses are not applied to the weld metal surface just under the arc while the welding heat source is applied. Complete insulation is assumed in this case.

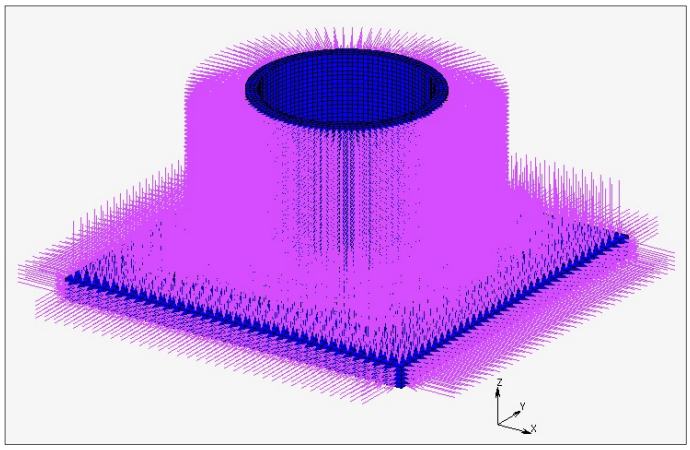

Figure 5-5: Heat Loss Boundary Condition

5.4.3 Metallurgical effects

Lindgren (2006) observed that three generic options exist for dealing with the microstructural changes in numerical analysis. They are as follows:

a. *Ignore microstructure changes*: This approach has been used for non-ferrous metals such as copper, aluminium and titanium, and in non-ferritic steels such as austenitic stainless steel. Some studies have adopted this approach for ferritic steels in which carbon levels are very low.

b. *Account for microstructure changes in a simplified manner*: This approach usually considers metallurgical effects only as far as they affect thermal dilatation and yield limit. Some researchers use the peak temperature and cooling rate from 800 C to 500°C ($\Delta t_{8/5}$) as variables to determine the phases of the material during the cooling cycle of the welding process. Understanding which phases are present in the microstructure allows for the choice of appropriate material properties to use during the cooling cycle.

c. *Thermo-mechanical-metallurgical (TMM) model*: This approach requires a model for the microstructure evolution, and another model to combine the material properties of various microstructure phases. Apart from the temperature-dependent material properties, other properties that can be considered in the TMM approach include phase-related volumetric changes, transformation plasticity and annealing. Volume changes are usually considered for the solid-state phase changes. Annealing reduces the hardening effect due to the change in dislocation structure resulting from phase change. When a phase with higher yield stress is formed during phase

transformation, the weaker phase experiences macroscopic effects of plastic yielding; this is known as transformation plasticity. It would typically occur when austenite decomposes to bainite and martensite.

Under the third option, a method that is widely used to account for solid state transformation during welding is to use isothermal temperature-time-transformation (TTT) or continuous-cooling-transformation (CCT) curves, to determine the evolution of transformation during the thermal cycle. CCT diagrams are used to predict the transformation that occurs during cooling in a thermal cycle, whereas TTT curves help to determine the rate of transformation at a constant temperature. A typical CCT diagram for low-alloy carbon steel is shown in Figure 5.6. Austenite forms during heating, once the temperature increases above $\mathbf{A_1}$ (shown in red in the figure), and it decomposes during cooling when the temperature falls below $\mathbf{A_3}$. Similarly, depending on the cooling rate ($\Delta t_{8/5}$), ferrite, pearlite, bainite or martensite will form. Martensite forms at very rapid cooling rates. In Figure 5.6, the martensite start temperature is shown in yellow and the finishing temperature (M_f) in green.

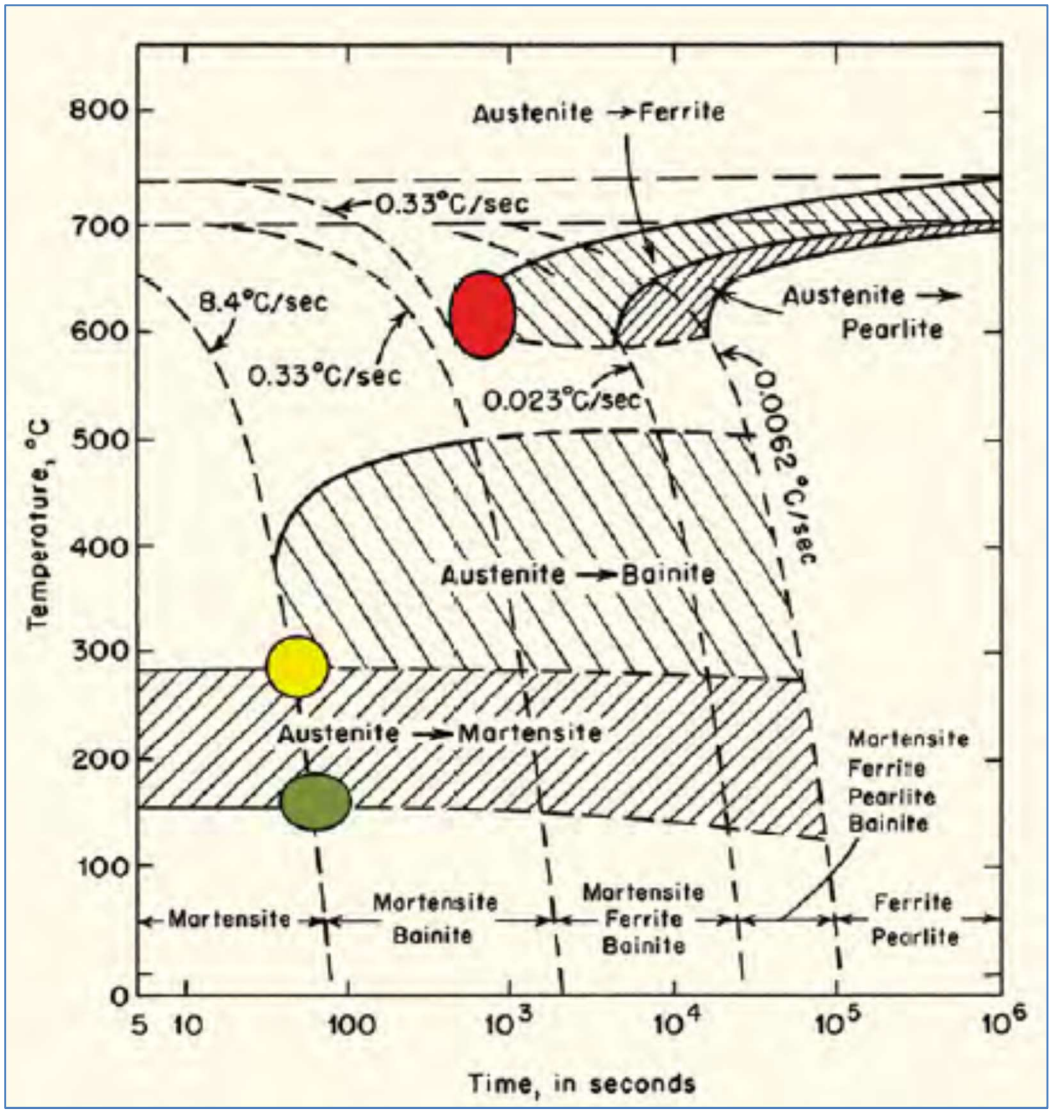

Figure 5-6: CCT Diagram for Low Carbon Low Alloy Steel
Source: Ford and Scott (2008)

The approach in this study is similar to the method used by Deng (2009). As discussed above, in the present case, the probability of martensite forming during the decomposition of austenite under conditions of rapid cooling was high. Martensitic transformation introduces volumetric dilation that increases residual stress in the welded structure. In this study, the effects of the solid-state transformation of martensite to the welding-induced residual stress by incorporating the appropriate parameters into the thermal model was considered.

Deng (2009) approached the solid-state transformation modelling problem in the following manner. Deng first calculated the volume fraction of martensite formed during the cooling cycle; then he considered the volumetric change due to phase transformation through modifying the thermal expansion coefficient over the martensitic transformation temperature range. Deng's model considers two properties to be temperature-dependent, namely *thermal conductivity* and *specific heat*. The temperatures at which austenitic transformation begins during heating (A_1) and

the temperature at which austenitic transformation is completed (A_3) have been shown to depend on the amount of alloying elements. They can be estimated using the following equations (Deng, 2009):

$$A_1 = 723 - 10.7Mn - 16.9Ni + 29Si + 16.9Cr + 290As + 6.4W \quad \textbf{(5.7)}$$

$$A_3 = 912 - 203\sqrt{C} - 30Mn - 15.2Ni + 44.7Si - 11Cr + 104V + 31.5Mo - 20Cu + 700P + 400Al + 120As + 13.1W + 400Ti \quad \textbf{(5.8)}$$

The martensite "start" temperature is determined using Equation 5.9 (Ford & Scott, 2008). The martensite "finish" temperature is given by Equation 5.10 (Piekarska et al., 2015). The relationship between M_s and M_f is described through Equation 5.11 (Back, 2017):

$$M_s = 539 - 423C - 30.4Mn - 12.1Cr - 17.7Ni - 7.5Mo \quad \textbf{(5.9)}$$

$$M_f = 381.76 - 252.44C - 111.124Mn + 54.538S_i + 114.17Cr - 23.779Ni - 57.381Mo + 215.7V + 945.4N_b + 1821.7T_i - 1746.5B \quad \textbf{(5.10)}$$

$$k = \frac{2\ln(10)}{(M_s - M_f)} \quad \textbf{(5.11)}$$

where k is the coefficient that describes martensitic development as a function of temperature. The value of k for steels as reported by Deng (2009) was 0.011. However, in this study, a value of 0.027 was calculated from Equation 5.11, which was comparable with the 0.025 obtained by Back (2017).

Solving equations 5.9 and 5.10 (using the chemical composition provided in table 4.2) yields the following temperature values:

$A_1 = 723.5°C$

$A_3 = 822°C$

$M_s = 420.2°C$

$M_f = 251.1°C$

5.4.4 Material data

In generating the temperature-dependent properties, the following logic was observed:

a. The steel at room temperature is made of a ferrite/pearlite composition.

b. Everything above austenite decomposition temperature (A_1) was considered 100% austenite phase, hence only austenite properties were used.

c. During cooling, everything between austenite decomposition temperature (A_1) and M_s was considered austenite.

d. The martensitic transformation range (M_s to M_f) involves the incremental transformation of austenite to martensite. This transformation was incorporated by calculating the fraction of martensite transformed at temperature *T* (where $M_s \geq T \geq M_f$) and using the properties of martensite for that fraction. The total value of the affected properties within the A → M transformation range therefore includes the fractional allocations of martensite (V_M) and austenite (V_A). Even distribution of martensite was assumed.

e. The affected properties that were used in the fractional apportionment were Young's modulus, specific heat, thermal expansion coefficient and thermal conductivity.

The temperature-dependent properties of low-alloy carbon steel are shown in Table 5.3.[12] For the purposes of this study, properties for parent metal and filler metal are considered the same. The properties used between 20°C and 700°C are those of ferrite/pearlite mixture, and the properties used above 700°C are those of the austenite phase.

Table 5-3: Temperature-Dependent Material Properties

Temperature (˚C)	Thermal Conductivity (J/s.m. ˚C)	Specific Heat (J/kg.˚C)	Poisson Ratio	Young Modulus (MPa)	Yield Stress (MPa)	Thermal Expansion Coefficient (10^{-6}/˚C)
20	37.7	470	0.3	210	320	15
100	39	490	0.3	204	300	15
200	40.5	525	0.3	200	275	15
250	40	545	0.3	195	262	15
300	39.5	565	0.3	190	250	15
350	38.2	590	0.3	185	241	15
400	37.7	615	0.3	180	230	15
450	36.5	648	0.3	170	216	15
500	35.3	680	0.3	159	202	15
600	33	770	0.3	135	170	15
650	31.8	815	0.3	92	138	15
700	30.2	850	0.3	80	100	23.5
750	29.3	595	0.3	66	80	23.5
800	27.1	600	0.3	50	60	23.5

[12] The properties were reported by Coret et al. (2002). The material used in that study was similar low-alloy carbon steel with comparable CE.

Temperature (˚C)	Thermal Conductivity (J/s.m. ˚C)	Specific Heat (J/kg.˚C)	Poisson Ratio	Young Modulus (MPa)	Yield Stress (MPa)	Thermal Expansion Coefficient (10^{-6}/˚C)
900	25.3	620	0.3	32	30	23.5
1000	26.9	630	0.3	30	20	23.5
1200	28.1	650	0.3	27	2	23.5

The following equation was used to calculate temperature-dependent Young's modulus E (Coret et al., 2002):

$$E\,(T) = 2.10x10^{5} - 190T + 1.19T^{2} - 2.82x10^{-3}T^{3} + 1.66x10^{-6}T^{4} \qquad \textbf{(5.12)}$$

where T is measured in ˚C and E is in MPa.

Lingamanaik and Chen (2011) established that the thermal conductivities of austenite and martensite can be determined using the equations below:

$$\lambda\,(austenite) = 0.016 + 1.3x10^{-5}\,x\,T \qquad \textbf{(5.12)}$$

$$\lambda\,(martensite) = 0.025 + 3x10^{-6}\,x\,T \qquad \textbf{(5.13)}$$

Similarly, the values of specific heat for austenite and martensite are given by the equations below:

$$C\rho\,(austenite) = 370 + 0.298\,x\,T \qquad \textbf{(5.14)}$$

$$C\rho\,(martensite) = 450 + 0.387\,x\,T \qquad \textbf{(5.15)}$$

The volume fraction of martensite was calculated using the Koistinen-Marburger (K-M) model discussed by Back (2017). Equation 5.16 was then used to calculate the fractional volume of martensite at temperature T. The fractional volume of austenite at the beginning of martensite transformation is considered to be 0.99.

$$V_M = V_A(1 - \exp[-k(M_s - T)]; \qquad M_s \geq T \qquad \textbf{(5.16)}$$

where V_M = volume fraction of martensite, V_A = austenite fraction at the beginning of the A → M transformation, T = current temperature at the chosen point, and M_s = martensitic transformation start temperature.

Equations 5.12 to 5.15 were applied to calculate values that were used to populate Table 5.4, which included proportioned values of temperature-dependent properties, according to the calculated phase fractional volume.

Table 5-4: Proportioned Temperature-dependent Properties

Temperature (˚C)	Thermal conductivity (W/mK)	Specific heat (J/kgK)	Expansion coefficient (1/˚C)	Young's modulus (GPa)	Yield stress (MPa)
20	25.1	457.7	1.50×10^{-5}	210	281
100	25.3	488.7	1.50×10^{-5}	200	275
200	25.6	527.4	1.50×10^{-5}	199.7	268
250	25.62	544.7	1.52×10^{-5}	199.3	262
300	25.61	560.87	1.54×10^{-5}	197.4	250
350	25.17	567.8	1.64×10^{-5}	193.3	240
400	23.3	537.3	2.00×10^{-5}	186.4	230
450	36.5	635	1.50×10^{-5}	176.6	215
500	35.3	680	1.50×10^{-5}	163.8	200
600	33	770	1.50×10^{-5}	130.4	170
650	31.8	815	1.50×10^{-5}	111	140
700	30.2	850	1.50×10^{-5}	91.4	100
750	25.8	593.5	2.35×10^{-5}	72.4	70
800	26.4	608.4	2.35×10^{-5}	55.7	60
900	27.7	638	2.35×10^{-5}	23.5	30
1000	29	668	2.35×10^{-5}	23.5	20
1200	31.6	727.6	2.35×10^{-5}	23.5	2
1600	63.2	727.6	2.35×10^{-5}	23.5	2

Fluid flow: Commercial FEM codes, such as MSC MARC and ANSYS, are unable to incorporate the effect of fluid flow into the thermal model of the welding process. As a result, maximum temperatures in the weld pool can be as high as 3000 C, which is not congruent with experimental evidence. Because the heat input reduction that is supposed to occur as a result of fluid flow does not in fact occur, all heat finds its way to the weld pool and increases the theoretical temperatures above the empirically observed limits. Studies show that the maximum recorded weld pool temperature for low-alloy carbon steels is approximately 1800 C (Deng, 2009). To address this shortcoming, Deng suggested that the value of *thermal conductivity* should be doubled for temperatures above the melting point. Therefore, in the present study the value of thermal conductivity above the solidus temperature (S_T) was doubled. The S_T and liquidus (L_T) temperatures are given by equations 5.17 and 5.18 (Akhlaghi, 2014):

$$T_S = 1535 - 200C - 12.3S_i - 6.8M_n - 124.5P - 189.3S - 4.3N_i - 1.4C_r - 4.1Al \quad \textbf{(5.17)}$$

$$T_L = 1537 - 88C - 8S_i - 5M_n - 30P - 25S - 4N_i - 1.5C_r - 5C_u - 2M_o - 2V - 18Ti \quad \textbf{(5.18)}$$

The resultant values of T_S and T_L, after inserting the chemical composition values given in Chapter 4, were 1481°C and 1510°C respectively. The thermal conductivity values above 1500 C

were therefore doubled, in line with Deng's recommendations. Solid-liquid transformation was accounted for by specifying a latent heat of fusion of 270 kJ/kg with a solidus temperature of 1481 C and liquidus temperature of 1510°C.

5.5 Mechanical analysis

Temperature histories from thermal analyses were used as inputs for the mechanical problem. The filler metal passes were tied to adjacent passes and the parent metal through contact surfaces. Thermo-mechanical analysis can be performed through one of the three constitutive models, namely elasto-plastic, elasto-viscoplastic and unified plasticity. Rate-independent elasto-plastic models are the most frequently used for simulating thermal processes that involve high heating or cooling rates (Simsir & Gur, 2008). Therefore, during mechanical analysis, either the common rate-independent plasticity model – based on von Mises yield criterion – could be used, or the rate-dependent plasticity model could be used. In this study, the accumulated rate-dependent plasticity was neglected given the high temperature gradients experienced by the material during a relatively short thermal cycle. The pressure loading was omitted and only the thermal loading from the temperature histories was used. The thermo-elastic-plastic constitutive model was developed to describe the deformation behaviour.

The following principles were adopted when generating the constitutive models (Goldak & Akhlaghi, 2005):

a. The load in the weldment arises as the result of thermal strains; if there are no constraints, this is the only source of loading.
b. The mechanical properties are both temperature-dependent and history-dependent. History dependency includes both microstructure and plasticity.
c. A localised heat source results in a localised load.
d. Resultant thermal stresses are high enough to cause plastic deformation.
e. Phase transformation affects the resultant stresses, either by increasing them or by partially releasing them.

Given the above principles, the total stress experienced by the material is an algebraic sum of elastic, plastic, thermal and phase transformation strains. Applying the effective stress function discussed by Goldak and Akhlaghi (2005), the stress-strain constitutive equations can be written as follows:

$$T = \frac{E}{1+\nu}(e - \varepsilon^{p} - \varepsilon^{c} - \varepsilon^{Trp}) \qquad \textbf{(5.19)}$$

$$\sigma_m = \frac{E}{1-2\upsilon}(\varepsilon_m - \varepsilon^{th} - \varepsilon^{Trv}) \quad \textbf{(5.20)}$$

where:

T	=	deviatronic stress tensor ($\sigma - \sigma_m$)
e	=	deviatronic strain tensor ($\varepsilon - \varepsilon_m$)
ε_p	=	plastic strain tensor
ε_c	=	creep strain tensor
ε^{Trp}	=	transformation plastic strain tensor
σ_m	=	strain tensor
ε_m	=	strain tensor
ε^{th}	=	thermal strain tensor
ε^{Trv}	=	strain due to volumetric change during phase transformation
E	=	Young's modulus
υ	=	Poisson's ratio

The displacement boundary condition is governed by the manner in which the specimen is clamped according to the experimental setup. It is assumed that light clamping of a sample does not significantly affect the residual stress. The model was fixed in all translational degrees of freedom at the edges of all four corners of the plate, and at the top surface of the pipe, as shown in Figure 5.7. The fixed boundary condition was applied far from the area of interest so as not to affect the results in the area of interest.

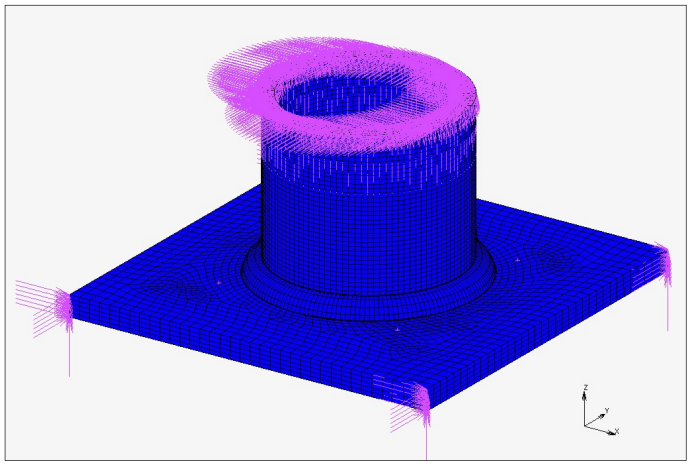

Figure 5-7: Fixed Displacement Boundary Condition

5.6 Concluding remarks

The 3D FEM was successfully developed to simulate the SAW process. The thermal-mechanical model was sequentially coupled, starting with the thermal modelling process before progressing to mechanical analysis. The temperature history of the welding cycle was used as loading in the subsequent mechanical model for stress analysis. The model includes metallurgical effects caused by solid-phase transformation during the cooling cycle of the welding process. The results of numerical analysis are presented and discussed in detail in Chapter 7.

CHAPTER 6: PARAMETRIC OPTIMISATION OF THE SAW PROCESS

6.1 Introduction

During the SAW process, the direct involvement of the human operator is limited. That is, he or she does not have sight of the weld pool, which is submerged, and he or she cannot interact directly with the welding process. As the SAW process ascends the automation curve, therefore, the fine-tuning of welding parameters becomes more important than operator skill. The process through which welding process parameters are fine-tuned to produce desired optimal output characteristics is called *parametric optimisation*. To effectively perform a parametric optimisation exercise, four main steps must be followed: design of experiments (DoE), process characterisation, optimisation and verification (Anawa, 2008).

The DoE step includes the planning and execution of experiments. Firstly, the required resources must be identified (e.g. equipment, appropriate facility, welding procedure, consumables, auxiliary equipment, human resources and funding). Secondly, the scoping of envisaged activities, experimental objectives and expected outputs must be clearly articulated and documented. All the above must be contained in the experimental execution plan that will direct the experiment. The third step is to choose the appropriate experimental design methods – that is, either fractional factorial, full factorial, CCD or Taguchi designs. The experiments are then performed according to the developed design matrix and the experimental execution plan. The responses per experimental run are then measured and the results recorded. An input/response matrix, containing input parameters at various levels and the corresponding response values, is developed for further analysis.

Process characterisation is the process whereby the developed model is reduced to focus only on significantly influential factors. Statistical analysis is applied to determine the relationship between input parameters and response variables, and to test the significance of model terms and reduce the model to include only the critical parameters. Optimisation of variables that were identified and quantified should then occur, to determine the optimal values of explanatory variables that will produce the best quality of desired results. This step is achieved by solving the minimisation, maximisation or target-value-centric function of the objective function through appropriate optimisation methods. The final step includes verifying the predicted results using physical experiments and/or simulation. This includes performing experiments using the optimal

input parameters (determined in the third stage discussed above) and comparing the responses with the predicted values. In this study, these steps were followed and the fractional factorial method was used as the experimental design; the multiple objective genetic algorithm (MOGA) was used for optimisation.

In this chapter, the identification of influential welding parameters and the responses required for the SAW process (see Chapters 2 and 3) is discussed. The chapter presents several topics, namely the analysis of the nature of relationships between input parameters and responses, the relevance of explanatory variables to responses, and singular and interactive parametric effects.

6.2 Fractional factorial design

Fractional factorial design is used in situations where it is impractical or too costly to perform *full factorial* research (i.e. full population of experiments). The idea of the fractional factorial design is to run only a subset of experiments but still to obtain representative results. There are k number of factors and L number of levels in a factorial design matrix (i.e. L^{k-1} designation). The results obtained and conclusions drawn from a reduced experimental study are valid for the whole experimental region covered by the control factors.

Model significance is tested using ANOVA. In the ANOVA table, F-values compare the model variance (i.e. term mean square) with residual (error) variance (i.e. residual mean square). Values close to unity indicate that a parameter has an insignificant effect on the response. Probability values lower than 0.05 signify that the model is adequate within the selected confidence interval. Precision adequacy, which is a ratio of the range of predicted values at points of the design to the average predicted error, indicates the model's ability to discriminate. A precision adequacy value of 4 or higher indicates adequate discrimination. The elimination of insignificant model terms is called *model reduction* and is achieved through regression analysis. The achievement of the highest possible performance (which is the desired outcome of the objective function) occurs when the optimum design factors have been determined. Objective function may minimise, maximise or target the assigned nominal value. The steps involved in the DoE method used in this study are shown in Figure 6.1.

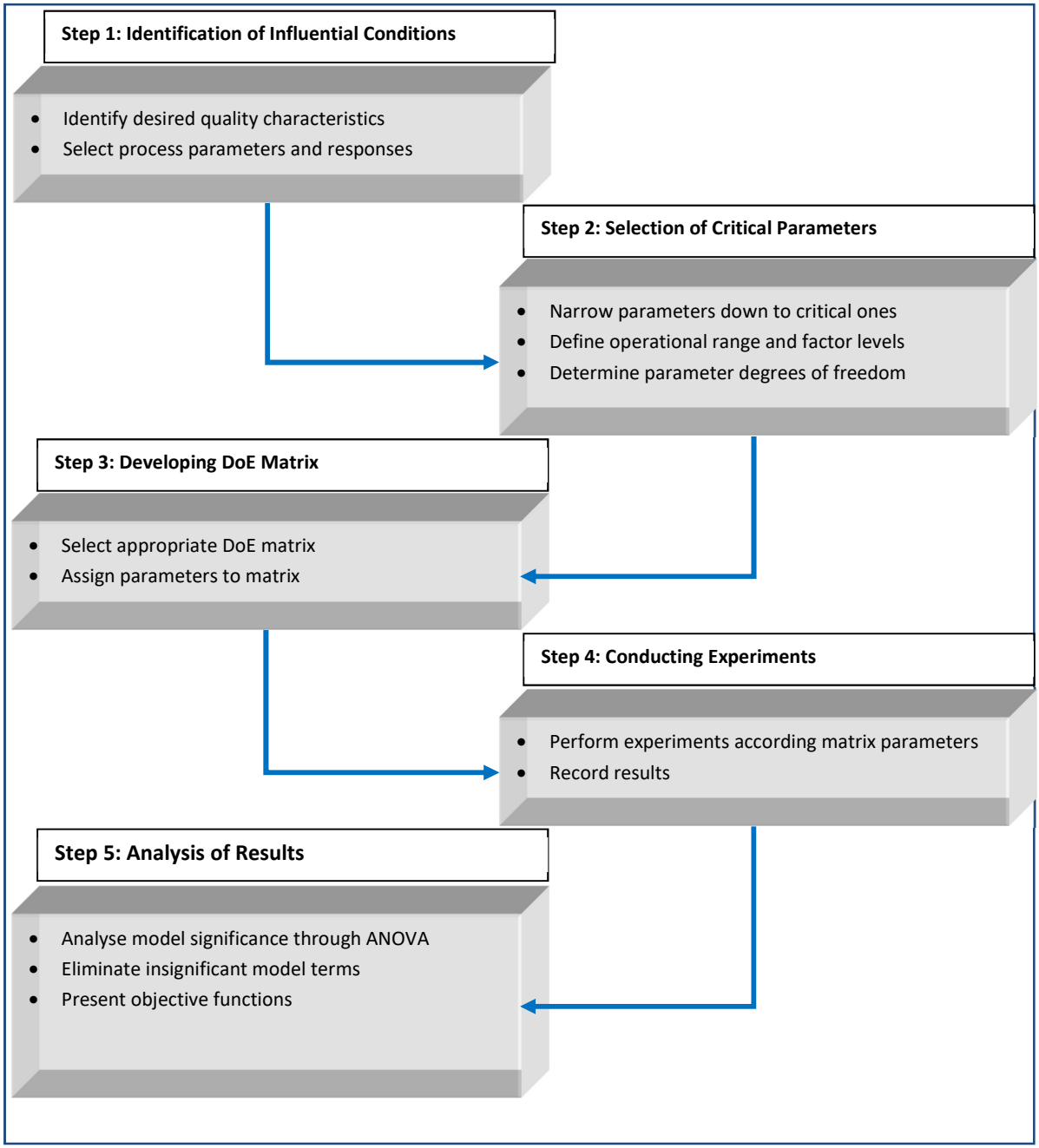

Figure 6-1: The DoE Process

6.2.1 SAW process parameters

The main parameters of the SAW process include welding current, arc voltage, travel speed, electrode stick-out, wire-feed rate, type of flux, depth of flux and polarity. It is clear from the summary of previous studies on parametric optimisation (Chapter 2) that four SAW parameters have consistentl displayed significant effects on the outputs – the outputs being weld geometry,

HAZ size, mechanical properties and residual stress. These four variables are welding current (I), arc voltage (V), travel speed (S) and wire-feed rate (FR). These parameters are therefore considered in this study.

An additional parameter was used in the experiments for this research, namely *welding mode*. The welding mode of the SAW machine used can be set either to CA (constant amperage) or to CW (constant wire). Each of the four parameters, but not welding mode, has upper (+) and lower (-) limits that were chosen according to safe operational ranges. The output variables included bead width (BW), bead height (BH), bead penetration (BP), HAZ size (HAZ), hardness (VHN) and residual stress (RS). Figure 6.2 illustrates the bead geometry of the envisaged multi-pass full penetration weld.

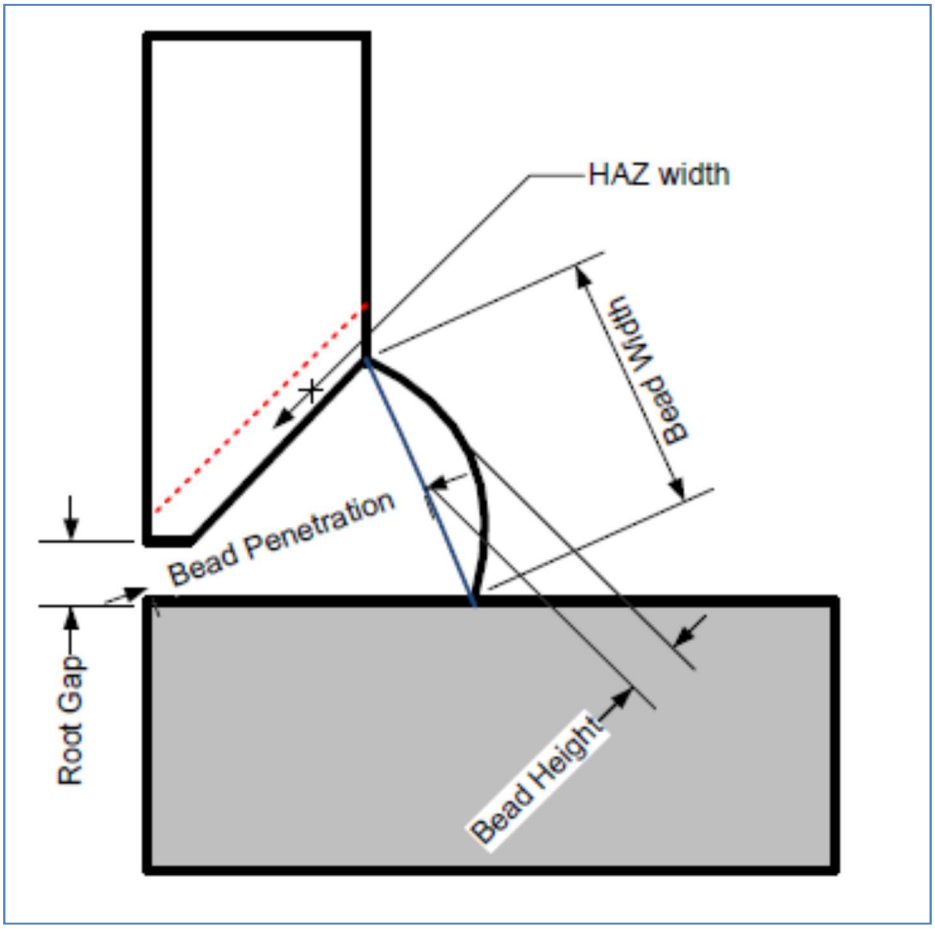

Figure 6-2: Weld Bead Geometry

Table 6.1 shows the two levels of parameters applied in the welding experiments. The range of values was chosen according to guidelines from the SAW machine operating manual and the researcher's experience from similar studies. When choosing the operational range for SAW parameters, care should be taken to include only parametric combinations that will not result in burn-through (i.e. too much heat) or lack of penetration (i.e. too little heat).

Table 6-1: Welding Parameters

Parameter	Units	Lower L (-)	Upper L (+)
Current (I)	Amps	360	380
Voltage (V)	Volts	25	30
Speed (S)	mm/s	8	10
Wire-feed Rate (FR)	mm/s	16.7	18.3

The response variables were chosen according to their effect on the resultant residual stress fields, and hence fatigue life, of a welded pressure vessel structure. The integrity of weld bead geometry indicates the quality of the weld, and it influences weld strength and life expectancy of the structure. The residual stress affects the fatigue life of a welded structure either by assisting crack initiation and growth (tensile) or by retarding crack growth and increasing the toughness (compressive). Hardness influences hydrogen-induced cracking, which shortens the fatigue life of the welded structure. The DoE matrix chosen in this study had five factors, four of which had two levels, namely an L^{5-1} design.

Table 6.2 shows the resultant matrix with five columns and two levels. Experiments were conducted in a random order to lessen noise sources. Response variables were captured for each specimen after the third pass. (The procedure for conducting the experiments was discussed in Chapter 4.)

Table 6-2: DoE Matrix for this study

S.No.	Input Parameters				
	I	V	S	FR	Mode
1	+	+	+	+	CA
2	+	-	-	+	CA
3	-	-	-	+	CA
4	-	-	+	+	CA
5	+	-	+	+	CA
6	-	+	-	-	CW
7	-	+	-	+	CW
8	-	-	-	+	CW
9	-	-	-	-	CW

6.2.2 Conducting the experiments

Experiments were conducted according to the DoE matrix in Table 6.2. Nine experimental iterations, comprising three runs each, were performed using the mechanised SAW machine with

settings as shown in Table 6.1. The experimental responses were determined as described in Chapter 4, and the experimental results were recorded according to the matrix discussed in Chapter 7. The objective of this study was to minimise RS, BW, BH, VHN and HAZ, and to maximise BP. As mentioned earlier, the specimen numbers do not necessarily follow a sequence because some of them were spoiled during the experiment [e.g. through burn-through or lack of penetration (LOP)] and were not used further.

6.2.3 Statistical analysis and optimisation

ANOVA was used to analyse the statistical differences between the mathematical means of multiple samples, through subdividing the total sum of squares (R^2). ANOVA calculates the level of significance associated with the effect of a specific process parameter on the response variables. It is also used to test the adequacy of a developed model. The mathematical model was designed through DesignExpert® Ver.10 program, using data from experiments. The software automatically assigns letters to the columns containing factor effects (i.e. factor-effect columns are labelled A, B, C, D and E). To understand which letter was assigned to which factor effect, the following notational replacements were made:

$$\text{I} \rightarrow \text{A, V} \rightarrow \text{B, S} \rightarrow \text{C, FR} \rightarrow \text{D, MODE} \rightarrow \text{E,}$$

The objective function that represents each of the response variables can be expressed according to the following general function:

$$y = f(I, V, S, FR) \quad \textbf{(6.1)}$$

Multiple regression analysis (MRA) was performed to determine the coefficients of each parameter. MRA is a statistical multivariate data analysis tool that maps relationships between input process parameters and responses. The resultant polynomial equation for each response variable becomes:

$$f(x) = \beta_0 + \beta_1 I + \beta_2 V + \beta_3 S + \beta_4 FR \quad \textbf{(6.2)}$$

where $f(x)$ is the response variable, β is the coefficient and β_0 is the model constant.

In DesignExpert, the factor "MODE" was entered as a categorical rather than a numeric value. This meant that coded factors of MODE could have coefficients, but the actual factors could not. Each objective function therefore ended with two equations, one in each mode. The equation in terms of coded factors can be used to make predictions about the response for given levels of each factor. By default, the higher level of each factor was coded as +1, whereas the lower level

factors were coded as -1. The coded equation is useful for identifying the relative impact of the factors by comparing the factor coefficients.

It was mentioned earlier that an effective strategy for solving a multi-objective problem is through a multi-objective genetic algorithm (MOGA). Like most engineering problems, the welding process parametric optimisation problem (WPPOP) is a complex problem with multiple objectives that are usually in conflict. The MOGA used to solve the WPPOP in this study followed the generalisation outlined in Figure 2.7 in Chapter 2. The algorithm followed a Pareto strategy, in which all objectives were assigned the same level of priority (Fonceca, 1995). The optimisation was performed using the "multi-objective optimisation" toolbox in MATLAB® software. The 14 objective functions, which were aligned to the response variables, were all loaded and optimised at the same time to determine the Pareto set of non-dominated solutions.

6.3 Concluding remarks

This chapter discussed the methodological approach to experiments, using an appropriate fractional factorial design. An L_9 matrix was generated and experiments were performed on a randomised basis, while the response variables were recorded for each parametric setting. ANOVA was applied to determine the model's adequacy and MRA was used to produce objective functions of all the response variables. The MOGA was used to solve the multi-objective problem and to generate a Pareto set of optimal solutions.

CHAPTER 7: RESULTS AND DISCUSSION

In the preceding chapters, a presentation of methods and techniques, as well the details of conducted experiments, were given. The results for the said experimental and analytical work are tabled and discussed in this chapter. The results obtained using various analytical and experimental methods are compared to each other and related to similar research work within the confines of the scope and objectives of this thesis. The sections covered in this chapter include results from temperature measurements, residual stress measurements, bead geometry measurements, microstructure analysis, hardness testing, fatigue testing, numerical analysis and parametric optimisation.

7.1 Experimental Temperature Histories

The temperature versus time relationship was monitored during the welding experiments, and the results presented in this section focus on these two parameters. The expected time to complete a half perimeter revolution from P1 to P3 (as illustrated in Figure 4.5) is 45 π/S seconds as shown in Equation 7.1, using the measured welding specimen diameter of 90mm. The time for Specimen 4 to do a half revolution from P1 to P3 is shown in Equation 7.1, where 'S' is the speed indicated in Table 4.4 above.

Weld piece diameter $d = 90$ *mm*

$$t = d\pi/2.S = 45\pi/S \text{ seconds} \quad \textbf{(7.1)}$$

The measuring error is approximated by comparing the calculated time using Equation 7.1 with the time measured from the IR thermal camera. Equation 7.2 is then used to calculate the error, and the results are tabulated in Table 7.1. Note that inter-pass temperature refers to the time between weld passes. The IR camera records continuously and hence inter-pass time between first and second passes can be determined by obtaining the difference between the time at which the first weld pass ends and the time at which the second weld pass begins.

$$error = (Expected - Measured)/Expected \quad \textbf{(7.2)}$$

It is observed from Table 7.1 that the measuring error is relatively large in the beginning of the measurements as the thermal footprint of the specimen is much lower in the beginning of the welding process. The result of the low initial thermal footprint is that the marker cannot be viewed clearly at the beginning of the welding cycle. As the weld specimen temperature increases, the

error decreases thereby increasing the accuracy of agreement between the calculated and the measured temperature values. The IR camera was calibrated to measure temperature from 200°C up to 1700°C and all values below 200°C are therefore reflected as zero.

Table 7-1: Temperature History for Sample 4 at P1 and P3

State	Time(s)	$P1\ ^{\circ}C$	$P3\ ^{\circ}C$	Error
1	19.030	422.9	251.9	N/A
2	35.030	381.8	470.3	0.132
3	47.470	413.7	551.9	0.12
4	63.310	437.7	285.8	0.12
5	78.150	219.8	320.6	0.05
6	91.150	277.6	0	0.08
7	106.23	0	209.5	0.07
8	119.59	316	0	0.05
9	133.31	472	613.5	0.03
10	147.83	525.9	659	0.03
11	159.47	556	439.4	0.18
12	176.23	381.7	450.8	0.19
13	191.07	400	337.9	0.05
14	204.31	318	355.7	0.06
15	219.16	323.4	291.1	0.05
16	232.7	273	302.5	0.04
17	247.54	293.7	253.4	0.05
18	260.82	280.7	557.3	0.06
19	275.1	551.9	530.3	0.01
20	289.18	520	474.8	0.004

Figures 7.1 to 7.4 show experimental results for measuring temperatures for a three-pass weld performed in Sample 4. As mentioned above, when starting, the welding process (Figure 7.1), marker is not clearly visible and the marker position can be approximated by adding theoretical 45 π/S seconds from the previously known marker time. Further to the times recorded by the IR camera and those calculated using Equation 7.1, the stop watch was also used to manually record times from the beginning of each weld pass until the end.

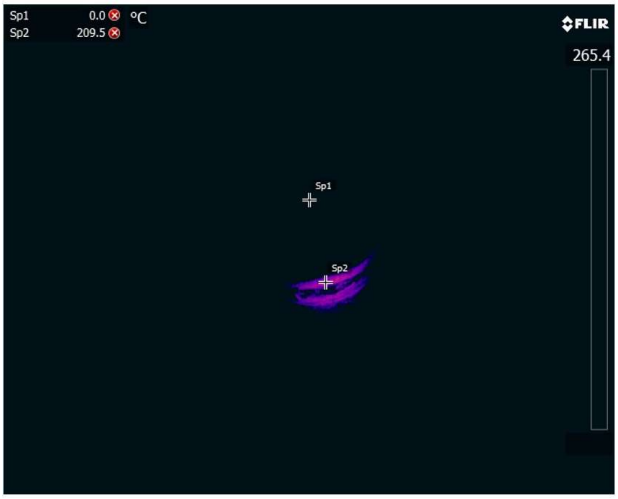

Figure 7-1: Sample 4 Frame at Weld Start

The frames from the IR camera clearly show the temperature recording points on the weld specimen, namely Sp1 (P1) and Sp2 (P3). The temperatures can be read directly from the frames on the top left corner. Figure 7.1 shows the time immediately after the start of the welding process for the first pass. The specimen is still cold and hence the relatively small thermal footprint. Progress in the welding process can be seen in Figure 7.2, which shows the temperatures for states 1 and 2 in Table 7.1. State 1 represents approximately half of the first revolution of the first weld pass, whereas state 2 represents the end of the full revolution for the first weld pass. The incremental growth of the thermal footprint from Figure 7.2(a) to Figure 7.2(b) is clearly visible in the presented frames.

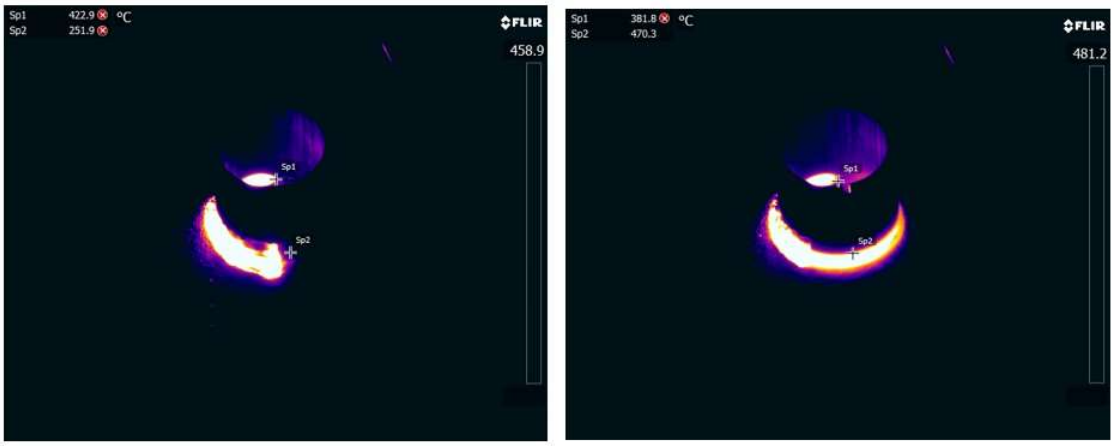

Figure 7-2: IR Camera Frames at 19.03 seconds – State 1 (a) and 35.03 seconds – State 2 (b)

Since the experiment comprises a three-pass weld, two inter-pass temperatures are measured on two states. The first inter-pass time occurs from state 3 to state 8. In other words, the temperature in state 8 is the last recorded temperature before commencement of the second pass. Figure 7.3

illustrates the temperature footprint of states 9 and 10. The improvement in the overall visibility of the thermal image is indicative of the increased overall temperature of the specimen during the execution of the second weld pass.

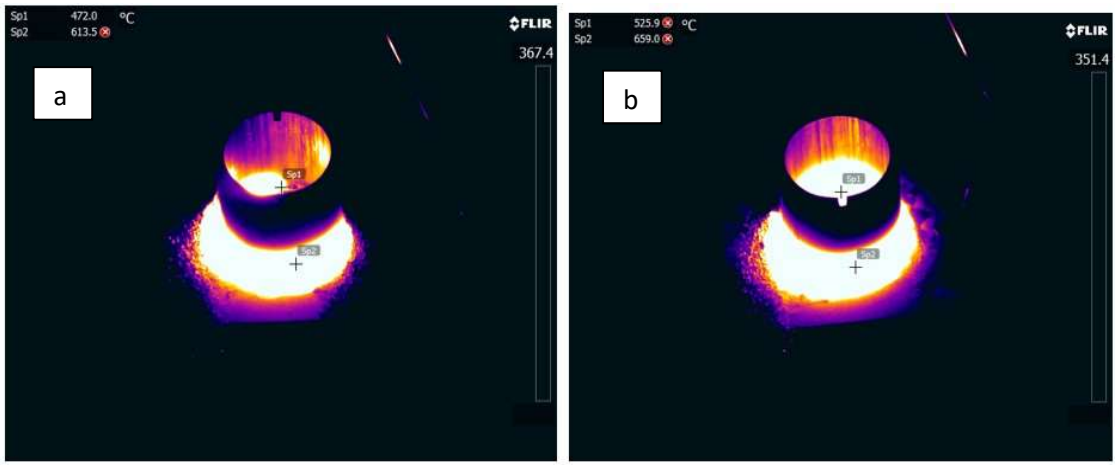

Figure 7-3: IR Camera Frames at 133.31 seconds – State 9 (a) and 147.83 seconds – State 10 (b)

The third and final weld pass is represented in the frame in Figure 7.4. The thermal image presented in this figure is the most clear of all the images, and the accuracy is the highest given the low error against the temperature values of states 19 and 20 in Table 7.1. The marker is clearly visible in Figure 7.4, and a circle is drawn around it to indicate its location. The reference marker is used to locate the specimen as it rotates relative to the position of Sp1 and Sp2.

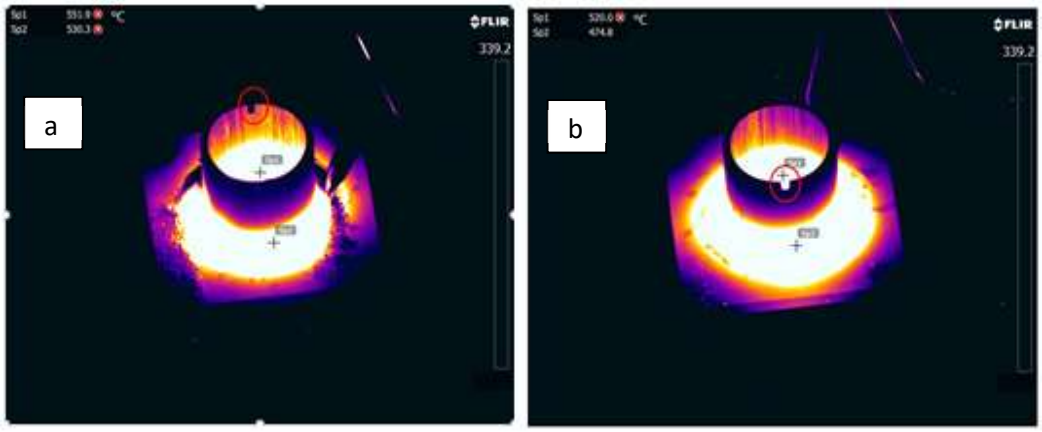

Figure 7-4: IR Camera Frames at 133.31 seconds – State 19 (a) and 147.83 seconds – State 20 (b)

Note that only six states from Table 7.1 were chosen to demonstrate the illustration of the frames, and hence not all frames were presented in this write-up. The chosen states in Table 7.1 have been highlighted for ease of reference. Table 7.2 presents results for P2 and P4 of specimen 4. The temperature recorded over time is similar to that shown in Table 7.1.

Table 7-2: Temperature History of Sample 4 at P2 and P4

State	Time(s)	*P2 ◦C*	*P4 ◦C*	Error
1	19.030	321.3	0	**N/A**
2	35.030	365.4	281.4	**0.132**
3	47.470	0	419.9	**0.12**
4	63.310	199.4	193.5	**0.12**
5	78.150	0	257.9	**0.05**
6	91.150	0	0	**0.08**
7	106.23	0	0	**0.07**
8	119.59	334.8	0	**0.05**
9	133.31	428.3	101.3	**0.03**
10	147.83	372.9	464.6	**0.03**
11	159.47	309	580.9	**0.18**
12	176.23	337.5	341.3	**0.19**
13	191.07	266.3	294.8	**0.05**
14	204.31	302	383	**0.06**
15	219.16	237.8	323	**0.05**
16	232.7	251.9	243.5	**0.04**
17	247.54	245.3	242.3	**0.05**
18	260.82	330.6	188.4	**0.06**
19	275.1	395.4	423.3	**0.01**
20	**289.18**	**350.6**	**560.9**	**0.004**

Figure 7.5 shows the temperature history plots of P1 and P3 in Sample 4. The values used in generating the Temperature vs. Time graphs were taken from Table 7.1. A close look at P1 graph shows that at 19 seconds (which is approximately half a revolution), the temperature is already above 400°C, which is evidence of the fact that the welding torch has already passed through the measuring point. This is in line with the IR image frames presented in Figure 7.2.

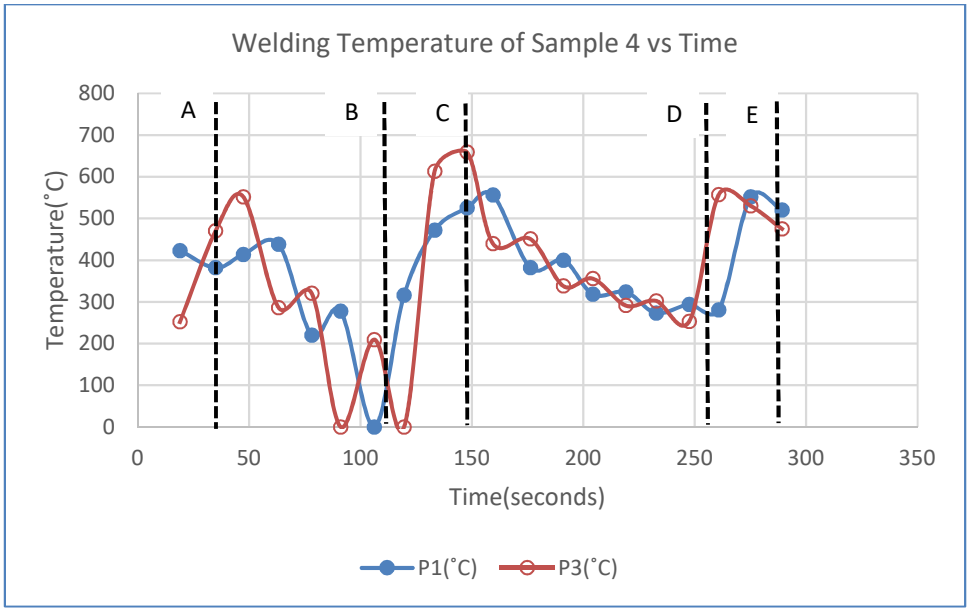

Figure 7-5: Sample 4 Temperature History at P1 and P3

Point A represents the completion of the first weld pass, i.e. one revolution. Point B represents the commencement of the second weld pass. The segment AB therefore is the inter-pass time between the two passes. Given that there is no welding during the inter-pass time, it is expected that the weld would cool slowly under room temperature to lower temperatures. The profile of Figure 7.5 however shows that the temperature at P1 increases slightly before falling every time. This can be accredited to the error between the calculated value (i.e. when the marker is not clearly visible), and the measured value (which is recorded by the camera). As explained above, the camera is calibrated between 200°C and 1700°C, and hence values outside this range are not detectable. The segment BC represents the duration for the second weld pass. It can be seen that higher peak temperatures are achieved during the second pass, and this is due to the temperature differences at inter-pass temperature (i.e. when the second pass begins) compared to room temperature (i.e. when the first pass begins). Similarly, the slope of the BC segment is less than that of the AB segment, signifying the lower cooling rate due to smaller temperature gradients of the latter.

The general profile of the graphs in Figure 7.5 is indicative of the temperature distribution in a welding process observed in similar studies (Zondi, 2014). It can be seen that the peak temperatures recorded in the P3 curve are higher than those observed in the P1 curve. This could be due to the positioning of the respective measurement points. P3 is located at the weld-toe on the plate side, while P1 is located at the root at point (0,0). The thermal footprints produced by the thermal camera images (Figures 7.1 to 7.4) show that the overall temperature of the specimen increases as more weld passes are added. This is because the accumulated heat input increases with the increase in weld passes. It can also be observed that the peak temperatures are relatively

low as a result of flux insulation of the weld pool. This is an important point to note when validating the numerical model. It was mentioned in Chapter 4 above that MIG process was used for the test run. The highest temperature recorded for P1 during the MIG process was 1280^0C.

7.2 Thermal Analysis Results

The numerical model was validated using temperature measurements obtained as illustrated in Figure 7.6. The region of interest is a 5 x 5 pixel grid. The measurement region is located on the outside of the pipe, 6 mm above the weld and 180˚ from the arc. The average temperature of the region is plotted. The standard deviation was also monitored and was observed to be relatively insignificant. Seven samples were analysed in the numerical model, namely 4, 6, 7, 8, 9, 15 and 16.

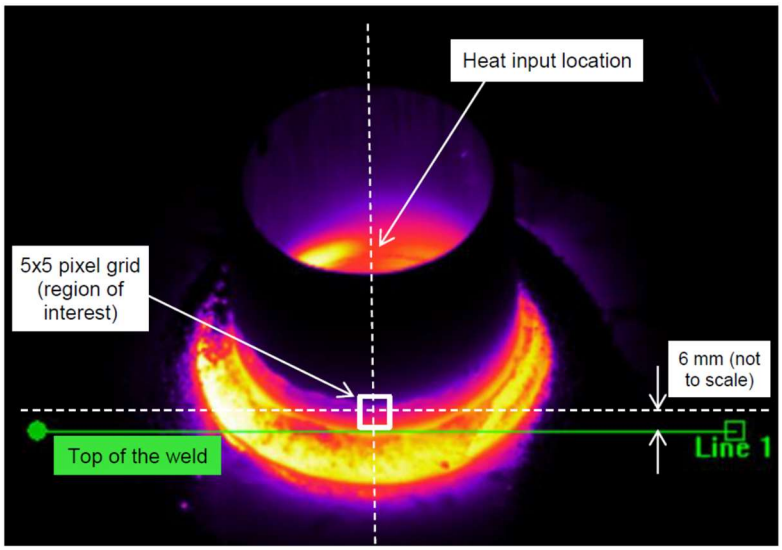

Figure 7-6: Temperature Measurement Location for Numerical Model Validation

The location identified in Figure 7.6 was carefully chosen to be away from weld start/stop interruptions, and also outside the flux protection pool so that the temperature readings obtained experimentally would be as comparable with the numerical model as possible. Figure 7.7 presents the temperature history plot of a fixed region on the pipe for a chosen number of samples, namely 4, 6, 7 and 9. Temperatures are taken from the SWIR Camera system in the location presented in Figure 7.6 for each specimen. Note that only four samples were chosen in order to illustrate the procedure followed in the model validation, but the rest of the samples have similar temperature history curves.

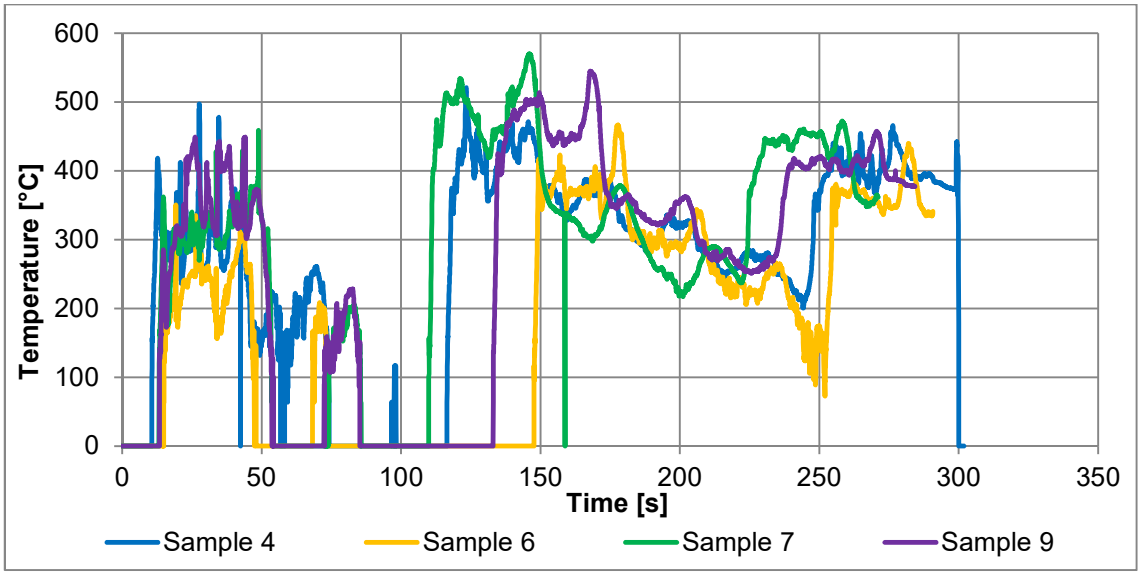

Figure 7-7: Temperature History Plots (Samples 4, 6, 7 & 9)

The profiles of the plots presented in Figure 7.7 are similar to that of the curves presented in Figure 7.5, even though the measuring points are different. Figures 7.8 to 7.14 show the comparison between the measured temperatures and those from the numerical model.

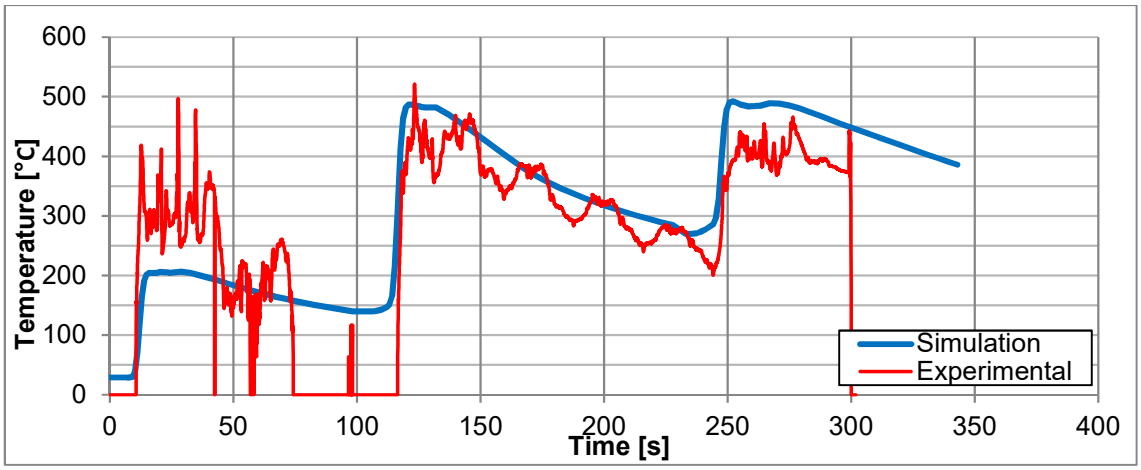

Figure 7-8: Simulation vs. Experimental Temperature History Plots (Sample 4)

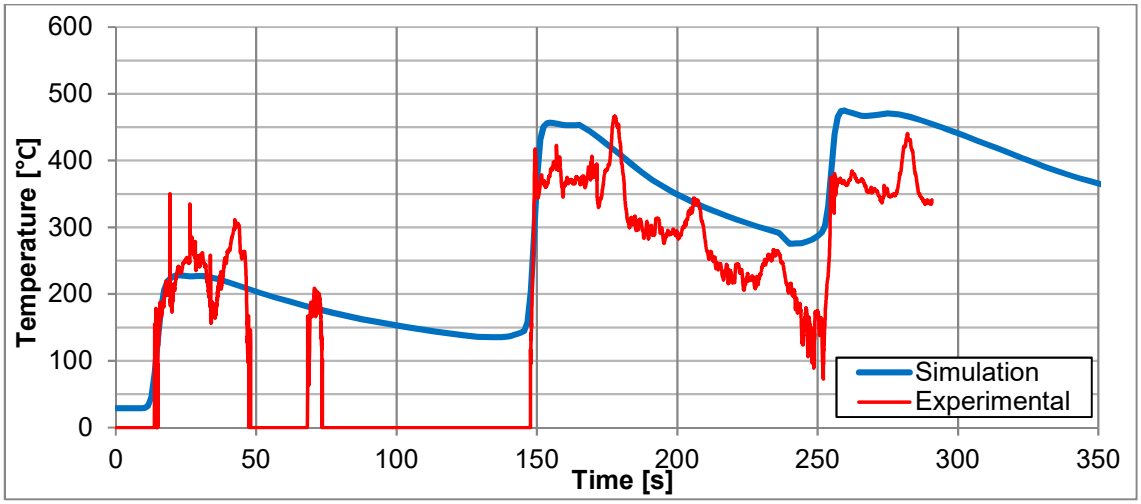

Figure 7-9: Simulation vs. Experimental Temperature History Plots (Sample 6)

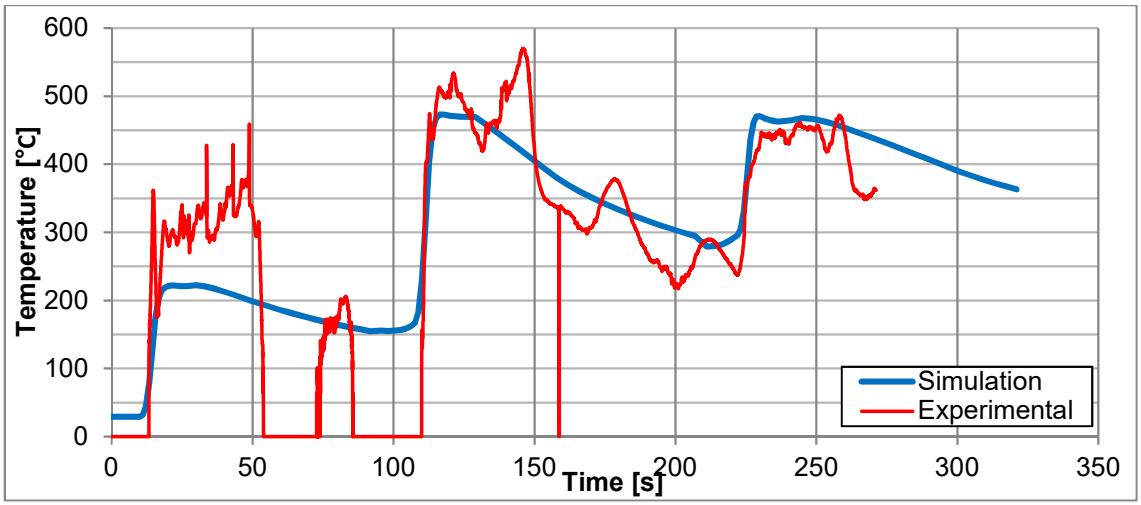

Figure 7-10: Simulation vs. Experimental Temperature History Plots (Sample 7)

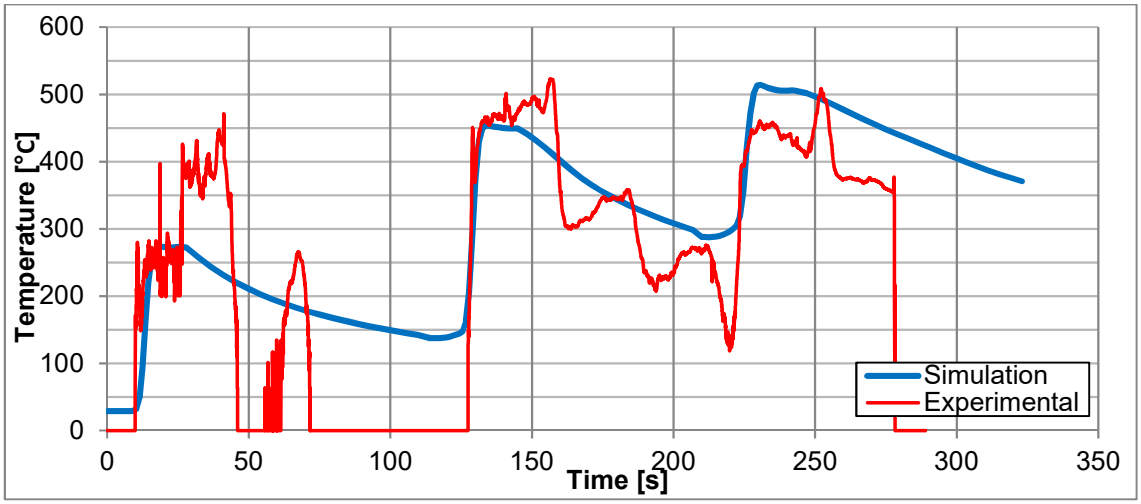

Figure 7-11: Simulation vs. Experimental Temperature History Plots (Sample 8)

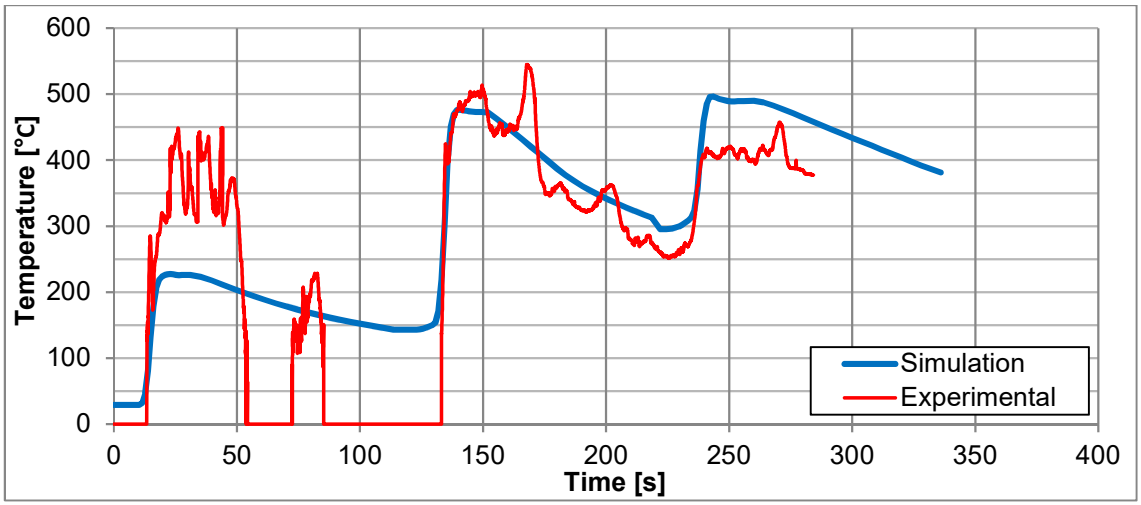

Figure 7-12: Simulation vs. Experimental Temperature History Plots (Sample 9)

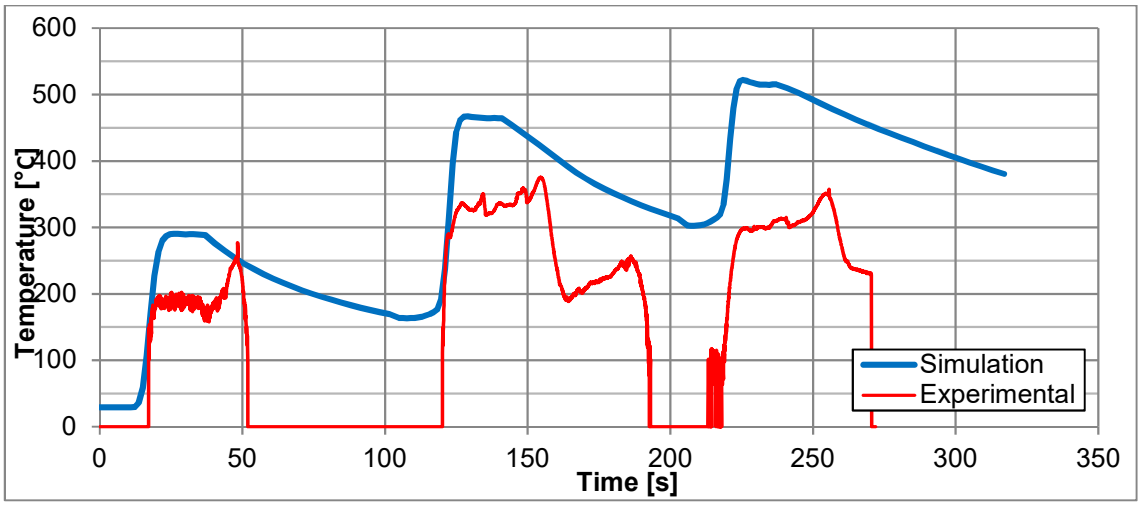

Figure 7-13: Simulation vs. Experimental Temperature History Plots (Sample 15)

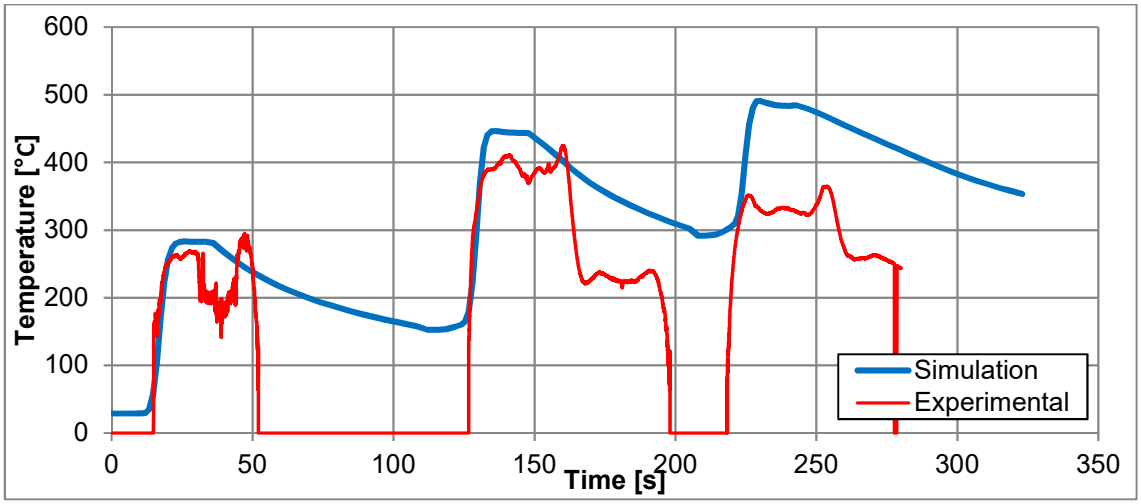

Figure 7-14: Simulation vs. Experimental Temperature History Plots (Sample 16)

The welding process is not perfectly smooth; therefore, the temperature measurements also do not produce a smooth curve, as shown in Figure 7.7. Chipping of the welding slag during the experiment also caused sharp peaks in the temperature readings (evident in Figure 7.7). The comparison of simulation and experimental resultant temperature histories is shown in Figures 7.8 to 7.14. The simulation results produce a smoother curve than the IR thermal camera; however, the profile of the two curves is comparatively similar. The correlation between the two sets of results is therefore considered to be fair. The trends and the rate of cooling (gradient of the slope) correspond. The minor differences in the results can be accredited to the following reasons:

a. The simulated welding process is an idealised process, and external, uncontrollable factors are not taken into account. This refers to reflections from surrounding surfaces, the presence of other heat sources, oversaturation of the detector, uncertainties in the measurements and errors in camera calibration.

b. Other differences between reality and the simulated environment, such as the actual welding efficiency, convection heat loss coefficient, ambient temperature and the exact volume of the weld.

c. Errors/limitations in the detector.

d. Temperature-dependent material properties used were taken from literature.

7.3 Residual Stress Measurement Results

The stress results for each sample are given in Figure 7.15. The stress distribution illustration shows that in all the specimens the hoop stress is highly tensile close to the weld centre-line (WCL) and decreases as the distance from the WCL increases. The flange-side values show that hoop stress becomes compressive at 15 mm – 20 mm. The change in direction of hoop stress takes place at a distance of 25 mm – 30 mm on the pipe side. Axial and radial stresses are much lower (i.e. less than half of hoop) than hoop stresses in both flange and pipe sides. The dotted lines show the approximate position of the WCL. The weld toe is located at approximately twice the distance from point (0,0,0) to WCL.

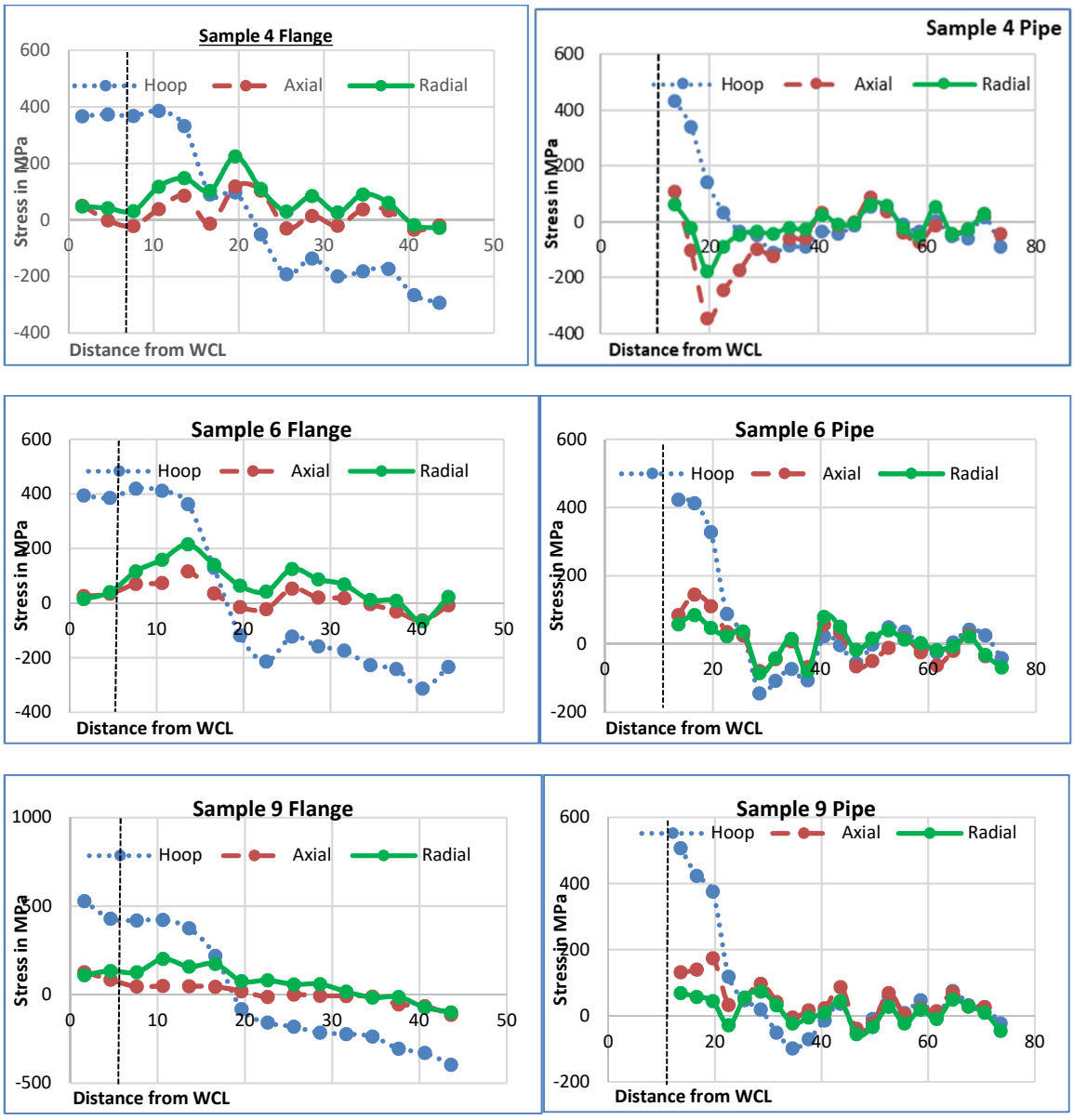

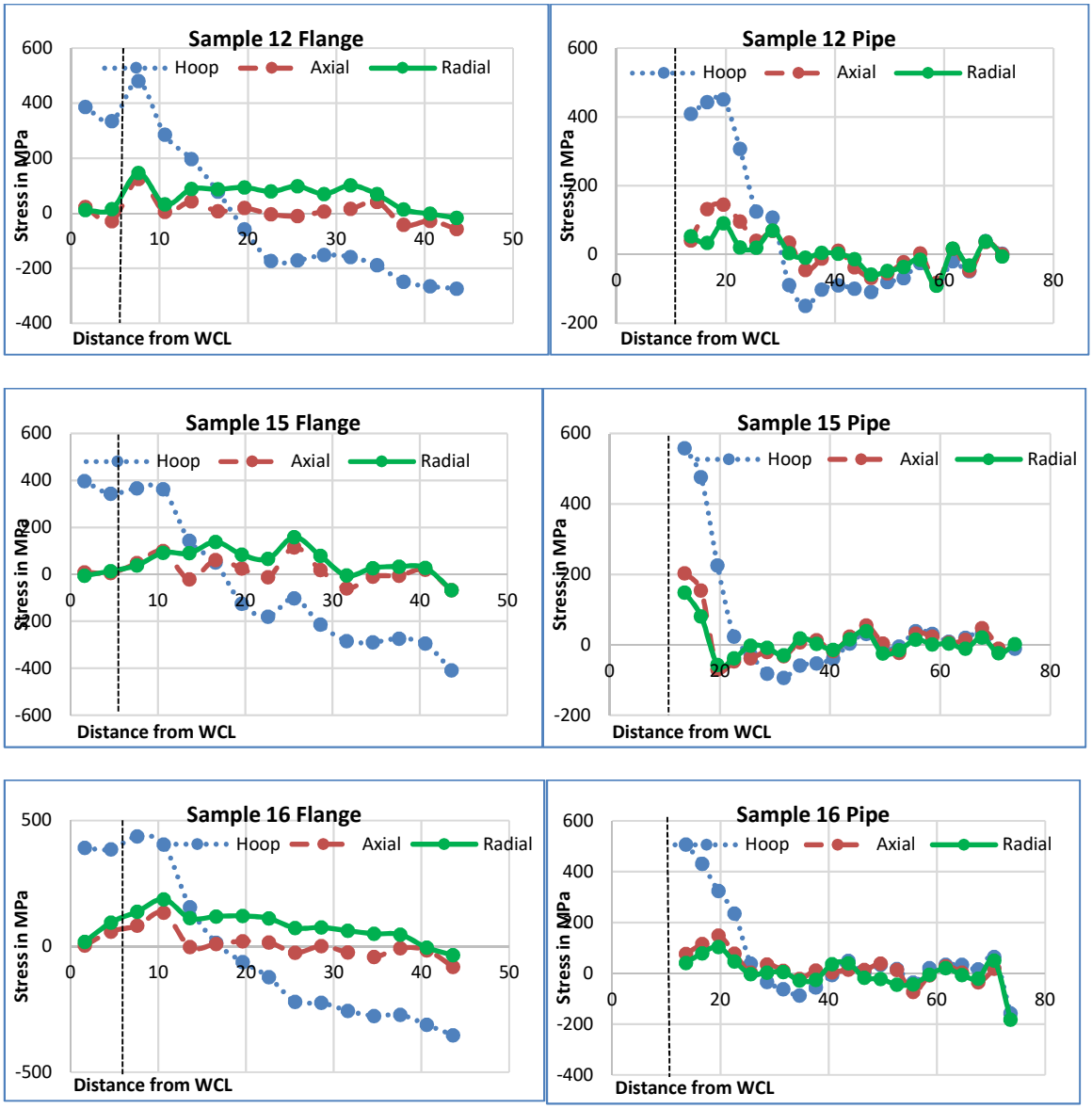

Figure 7-15: Stress Profiles for Weld Specimens

The three components of stress (i.e. hoop, axial and radial) that were measured in each welded sample are listed in Table 7.3. The stress values given were recorded at the point closest to the weld centreline (i.e. 6 mm away from point 0,0,0 on the flange side, and 13.6 mm away from point 0,0,0 on the pipe side, as indicated in Figure 4.5 above). It can be observed from the table that hoop stress is the highest of all the three dimensions of stress. The highest observed hoop stress on the flange side is 425 MPa in Sample 9, whereas the lowest hoop stress is observed in Sample 8 at 292 MPa. On the pipe side the highest hoop stress is 558 MPa in Sample 15, and the lowest is 295 MPa in Sample 7. The yield stress of the filler metal is approximately 440 MPa; the recorded tensile hoop stresses are therefore very close to or above the yield strength.

Table 7-3: Residual Stress Results at WCL

Sample	I (Amp)	V (Volts	S (mm/s)	FR (mm/s)	Mode	Flange (MPa)			Pipe (MPa)		
						Hoop	Axial	Radial	Hoop	Axial	Radial
4	380	30	10	18.3	CA	371	-11	37	431	106	61
6	380	25	8	18.3	CA	402	52	78	423	85	58
7	360	25	8	18.3	CA	359	12	36	295	-74	-16
8	360	25	10	18.3	CA	292	64	82	357	150	1
9	380	25	10	18.3	CA	425	66	130	507	132	69
12	360	30	8	16.7	CW	407	51	80	409	41	53
13	360	30	8	18.3	CW	375	49	42	381	-11	-26
15	360	25	8	18.3	CW	355	27	65	558	203	148
16	360	25	8	16.7	CW	412	70	117	507	76	41

Hoop stress is also the most dangerous as it is in tensile form and it contributes to stress-induced cracking and hence reduction of fatigue life of the welded structure. Hemmesi et al. (2014) showed that the behaviour of residual stresses that are exposed to multiaxial loading is completely different from those exposed to uniaxial loading. Farajian et al. (2014) also noted that residual stresses are multiaxial in nature. Hence, the superpositioning of WRS and load stress in one direction is inadequate to properly account for stresses experienced by the welded structure under fatigue loading. The authors showed that in circumferential welds, the principal residual stresses in the WCL and weld toe are parallel and normal to the weld bead, respectively. It is for these reasons that in the present study the effect of each of the three components of stress is not considered to be linear. The study by Lu (2002) also showed that the dominant components of residual stress in a circumferential weld are hoop and axial stresses. It was therefore decided to rank the two components of residual stress as follows:

Radial component has a factor of 1.0

Axial component has a factor of 1.1

Hoop component has a factor of 1.25

Table 7.3 was then updated with the ranking shown above, and the resultant stresses are shown in Table 7.4.

Table 7-4: Ranked Residual Stress Results at WCL

Sample	Mode	Flange (MPa)				Pipe (MPa)			
		Hoop	Axial	Radial	Net WRS	Hoop	Axial	Radial	Net WRS
4	CA	464	-12	37	489	539	117	61	717
6	CA	502	57	78	637	529	94	58	681
7	CA	449	13	36	498	368	-81	-16	271
8	CA	365	70	82	517	446	165	1	612
9	CA	531	73	130	734	634	145	69	848
12	CW	509	56	80	645	511	45	53	609
13	CW	469	54	42	565	476	-12	-26	438
15	CW	444	30	65	539	698	223	148	1069
16	CW	515	77	117	709	634	84	41	759

The lowest net stresses are highlighted in Table 7.4. Samples 4, 7 and 8 (in that order) have the lowest net stresses from the plate side. Samples 7, 12 and 13 have the lowest net stresses from the pipe side.

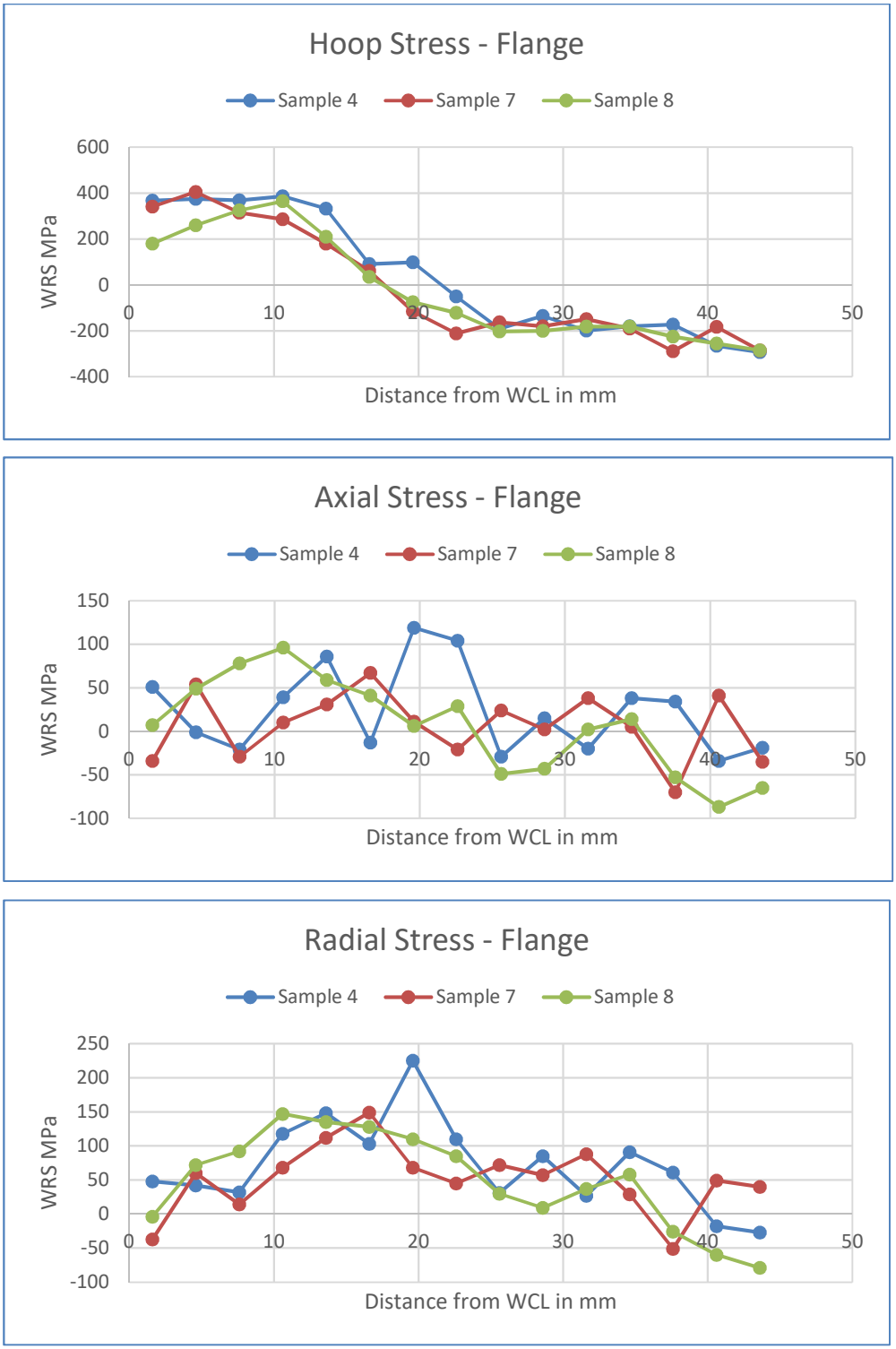

Figure 7-16: Flange Side Residual Stress Distribution for Samples 4, 7 and 8

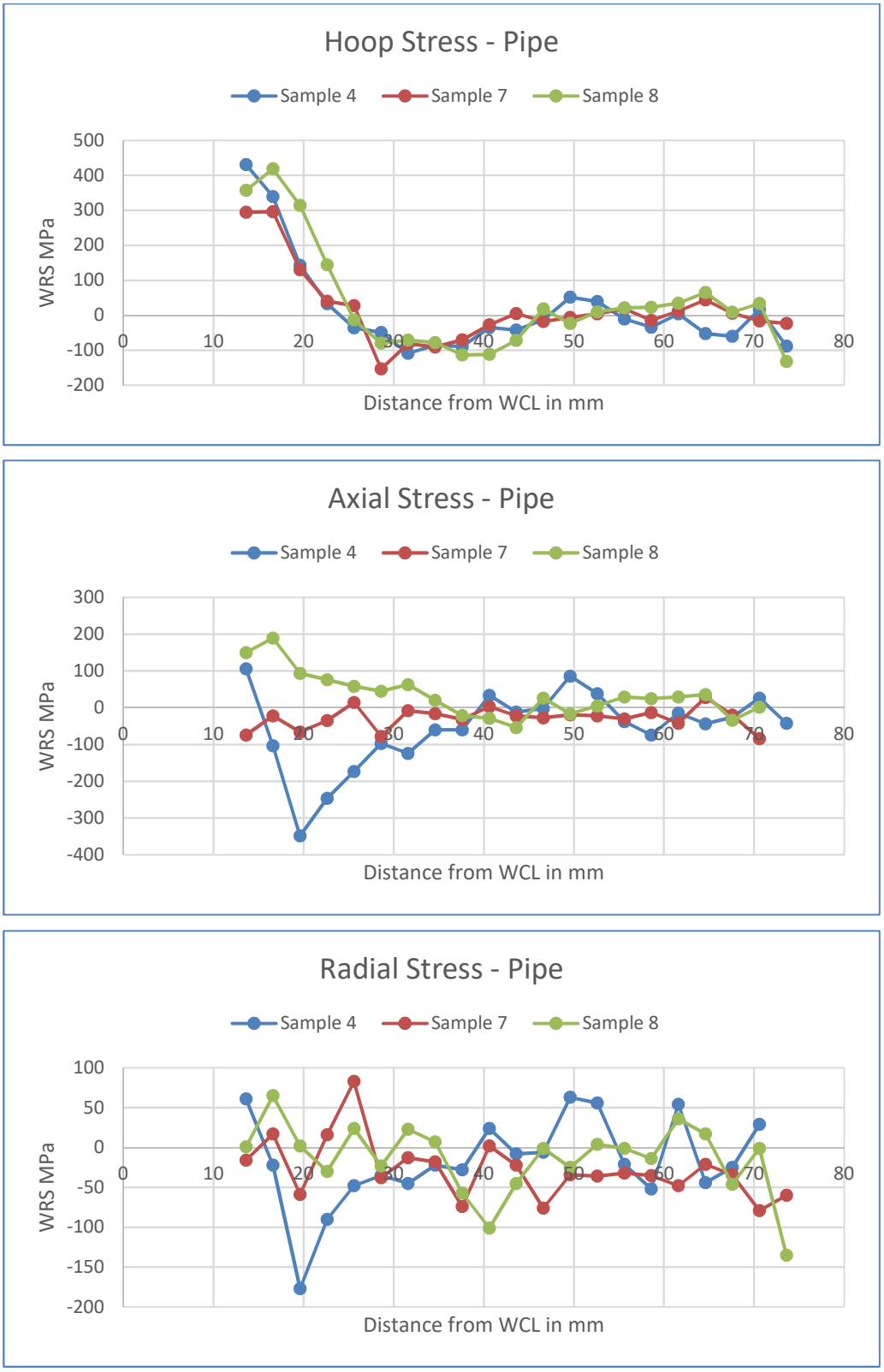

Figure 7-17: Pipe Side Residual Stress Distribution for Samples 4, 7 and 8

The stress distribution of the "lowest three" specimens is shown in Figure 7.16 and Figure 7.17. The stress profiles for hoop stress in both the flange and pipe sides are very similar for all three specimens. Axial stresses for the flange side show very different readings closer to the weld region, and they seem to become more steady as the distance away from WCL increases. Axial and radial stresses for Sample 4 are highly compressive on the pipe side at distance of about 20 mm from the starting point. This distance coincides with the location of the weld toe region. A number of studies discussed in this thesis, as shown in Chapter 2, involved fatigue failures that originated from the weld toe, wherein the weld toe experienced tensile mean stresses as a result of WRS (Rading, 1993; Lu, 2002; Rosenfeld & Kiefner, 2006). However, some researchers have shown that weld toes of circumferential welds can be under compressive stress (Pasta & Reynolds 2007). Although the multiaxiality of residual stress is such that one component of stress doesn't unilaterally determine the position of the maximum principal stress in a welded structure, such significant compressive stresses as observed in this case would make it unlikely for failure to occur at the weld toe. Apart from Sample 4 early readings, the rest of the samples seem to have similar distributions of radial residual stresses across the measured distance.

Table 7-5: Parametric Combination for Samples 4, 7, 8, 12 and 13

Sample	I (Amp)	V (Volts	S (mm/s)	FR (mm/s)	Mode	Heat Input (kJ/mm)
4	380	30	10	18.3	CA	969
7	360	25	8	18.3	CA	956
8	360	25	10	18.3	CA	765
12	360	30	8	16.7	CW	1148
13	360	30	8	18.3	CW	1148

The identified samples are chosen as the best using the applied criteria of lowest net WRS; however, it may still happen that fatigue properties of the said samples are not necessary in agreement with this finding given other factors that influence the latter. Furthermore, since the parametric combination of the identified three samples is known, this could still be used further to identify welding parameters that produce the most optimal welds in terms of WRS distribution. Table 7.4 presents the welding combination for the three "best performing" samples in terms of residual stress distribution from the flange (or plate) side, and the three from the pipe side. It can be seen that the three best samples on the flange side all have the same wire feed rate (FR) of 18.3 mm/s, and they all have the same mode setting of constant amperage (CA). Sample 7 appears both on the flange and pipe sides. The rest of the samples from the pipe side have the same mode setting of constant wire (CW) and have the same power input. The settings of current, voltage and speed is also the same on the pipe side samples. This effectively means that both mode

settings can produce optimal parametric combinations depending upon which residual stress distribution is used as criteria between the flange side and the pipe side. The choice of residual stress distribution will be influenced by the point and direction of loading of the welded structure. For example, a case where the cantilever load is applied at the tip of the free side of the pipe, with the flange fixed, would require the flange side stresses to be considered since the forces will be acting in that direction.

The parametric combination of the five samples that are highlighted in Table 7.4 is given in Table 7.5 together with the heat input of each iteration. The heat input of Sample 4 and Sample 7 are very similar in magnitude. Both these samples were generated using the CA mode setting of the welding machine. The heat input of Sample 12 and Sample 13 are exactly the same in magnitude, even though the wire feed rate of the two is different. The two samples were generated using a CW mode setting of the welding machine. It should be noted that the heat input of the two CA mode samples differ significantly from that of the two CW mode settings. It is clear, therefore, that if the four samples with different heat inputs can all have favourable residual stress properties compared to the rest of the samples, then the mode setting clearly plays a role in determining the resultant conditions of the residual stress fields in the welds.

7.4 Mechanical Analysis Results

Typical stress results are given in Figure 7.18 and Figure 7.19. The final deformation of the sample is shown in Figure 7.20 (deformation is exaggerated by a factor of 5). The measurements are taken after 4 hours of simulation time, at which point the sample has cooled to 29°C. High stresses can be seen in the weld area and the heat affected zone as would be expected. It can also be observed from the figures that stresses are higher in the areas where the weld specimen was constrained during welding, as shown in Figure 5.7 above. Such high stresses at the points of constraints are however far from the area of interest and hence can be ignored for the purposes of analysing results. The stress magnitude reflecting on the von Mises mapping can be read from the left of the schematic and these are discussed further below. The presented stress results are linked to the temperature histories presented in section 7.2

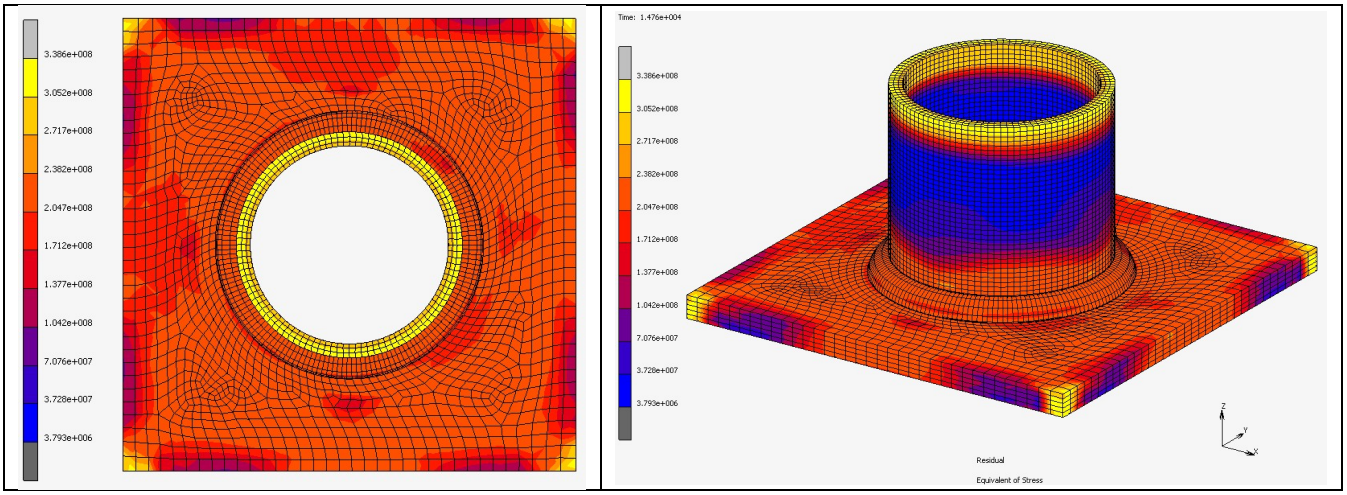

Figure 7-18: Equivalent stress results

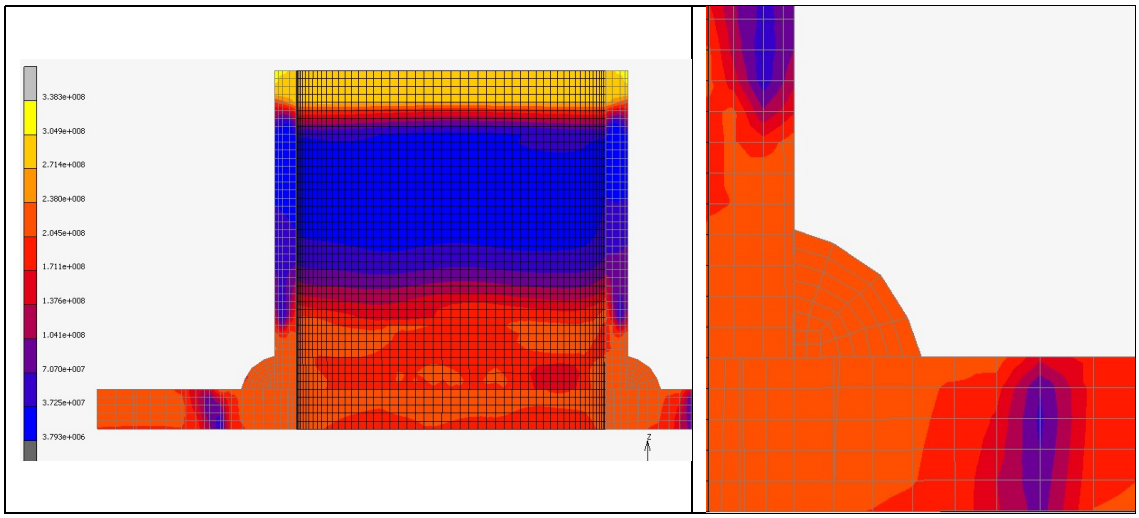

Figure 7-19: Equivalent stress results (section view)

Closer examination of Figure 7.20 shows that the regions of significant distortion are in the middle of the plate. This is due to buckling of the section of the plate that was not fixed as shown in Figure 5.7 above. The maximum observed distortion of approximately 0.22 mm (i.e. 1.12/5) is considered reasonable in a plate of 10 mm thickness after a three-pass weld bead. The results shown in the stress contours are in line with results observed from similar studies discussed in section 2.2 above.

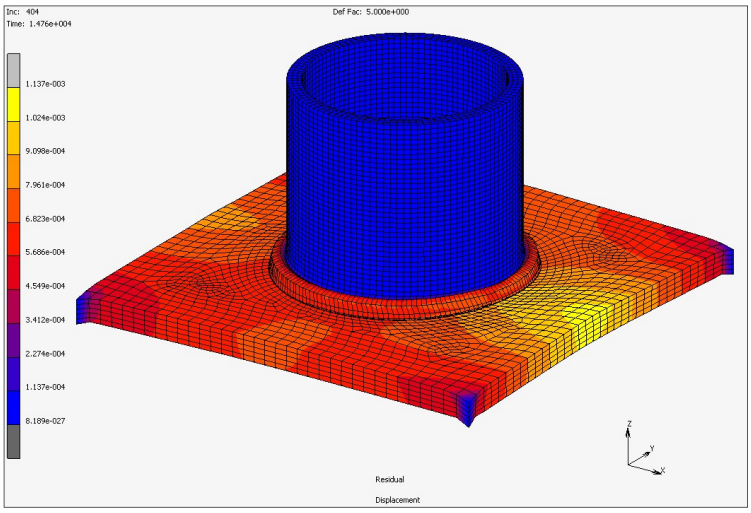

Figure 7-20: Final deformation

7.5 Comparison of experimental and simulation results

Figure 7.21 shows the comparison between the physical weld obtained through experimentation and the simulated version. It can be seen through the shape of the multi-pass weld bead that the penetration between the two compares well.

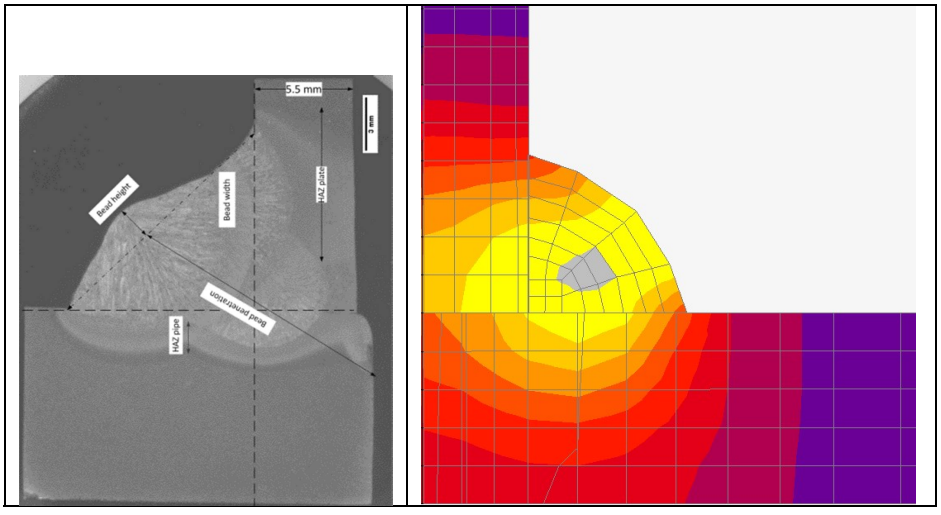

Figure 7-21: Weld Penetration for Sample 4

The simulated results are compared to the experimental results in Figure 7.22 to Figure 2.29.

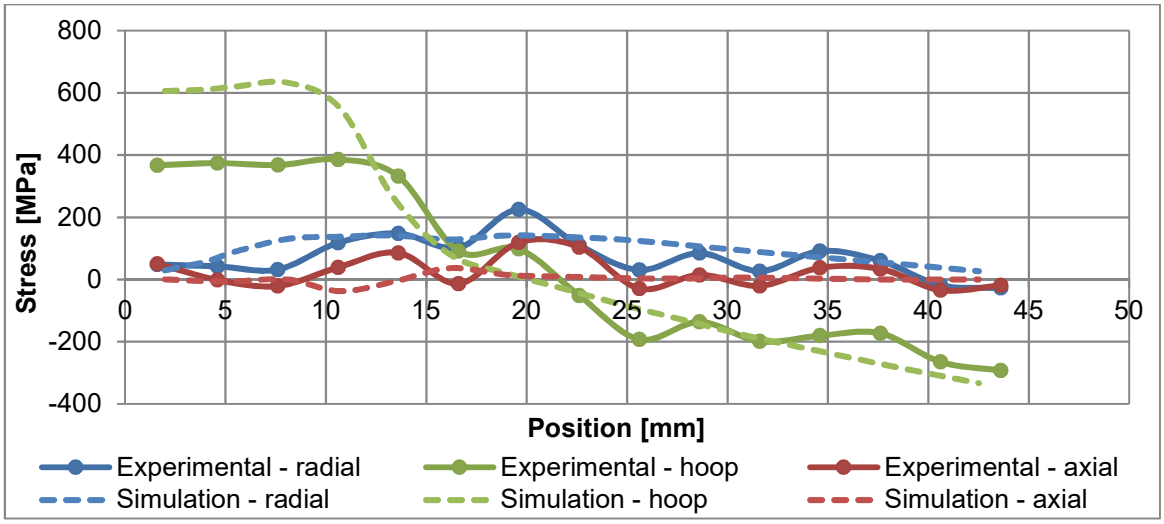

Figure 7-22: Comparison between the mechanical experimental and simulation results (Sample 4; flange)

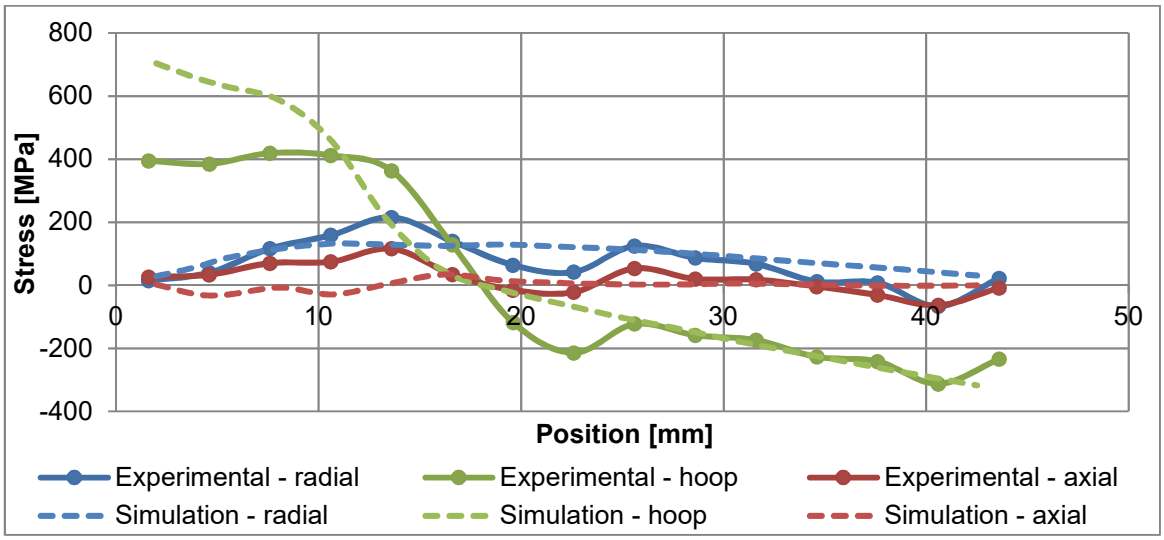

Figure 7-23: Comparison between the mechanical experimental and simulation results (Sample 6; flange)

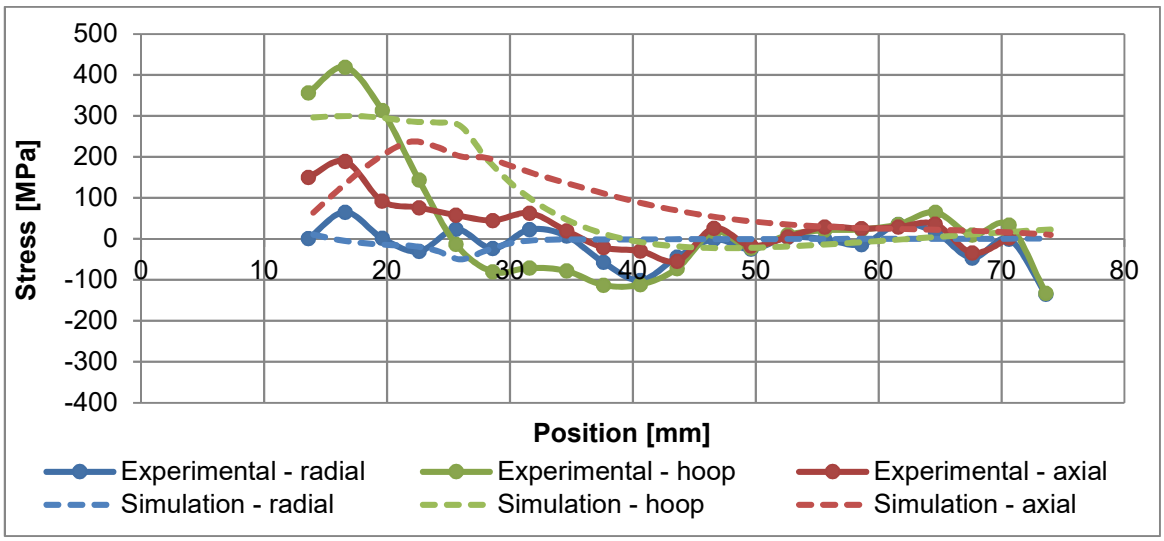

Figure 7-24: Comparison between the mechanical experimental and simulation results (Sample 8; pipe)

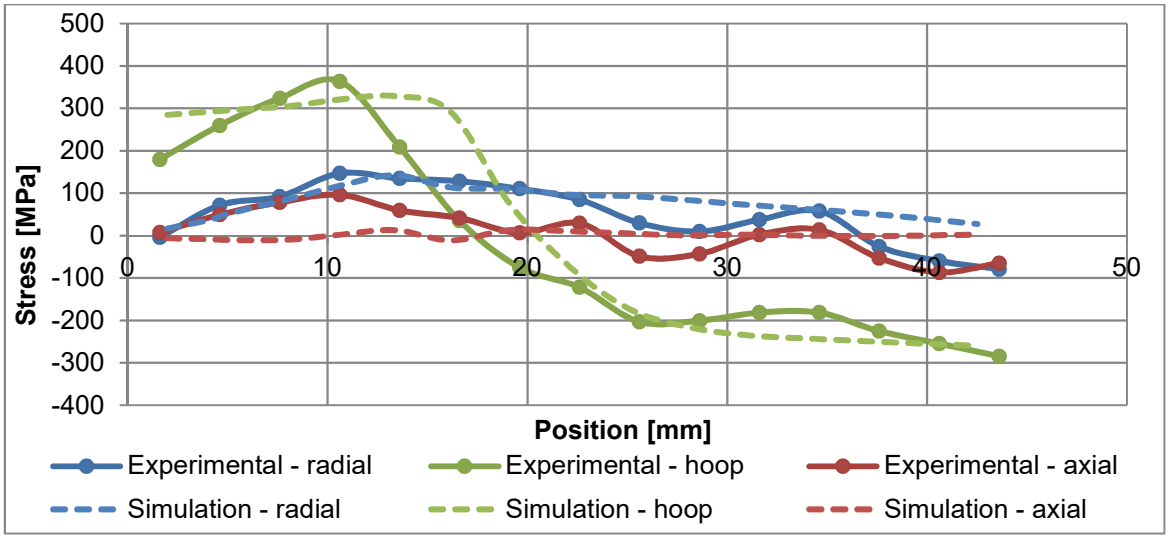

Figure 7-25: Comparison between the mechanical experimental and simulation results (Sample 8; flange)

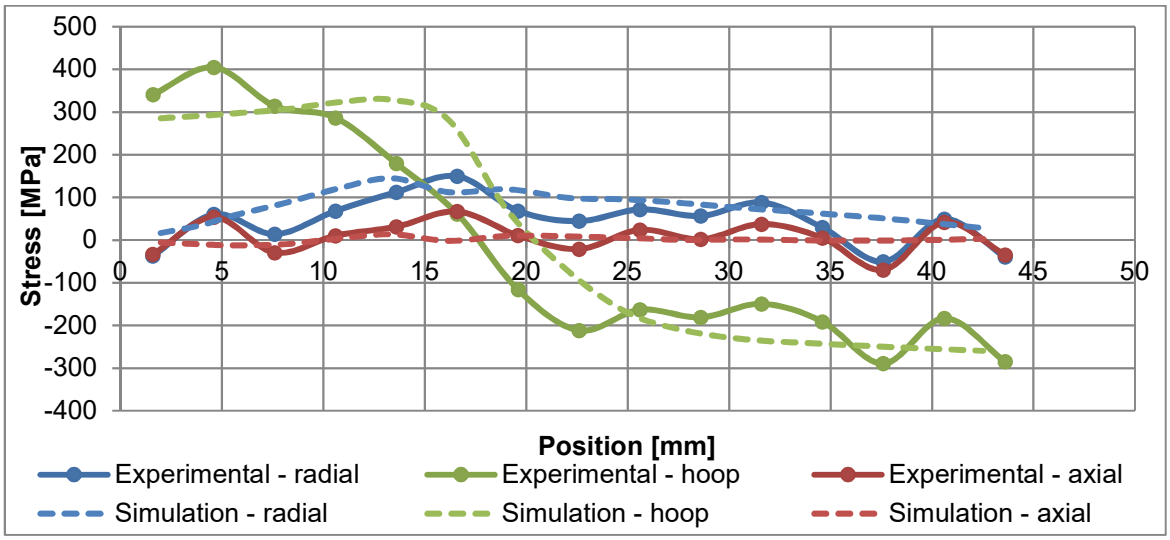

Figure 7-26: Comparison between the mechanical experimental and simulation results (Sample 7; flange)

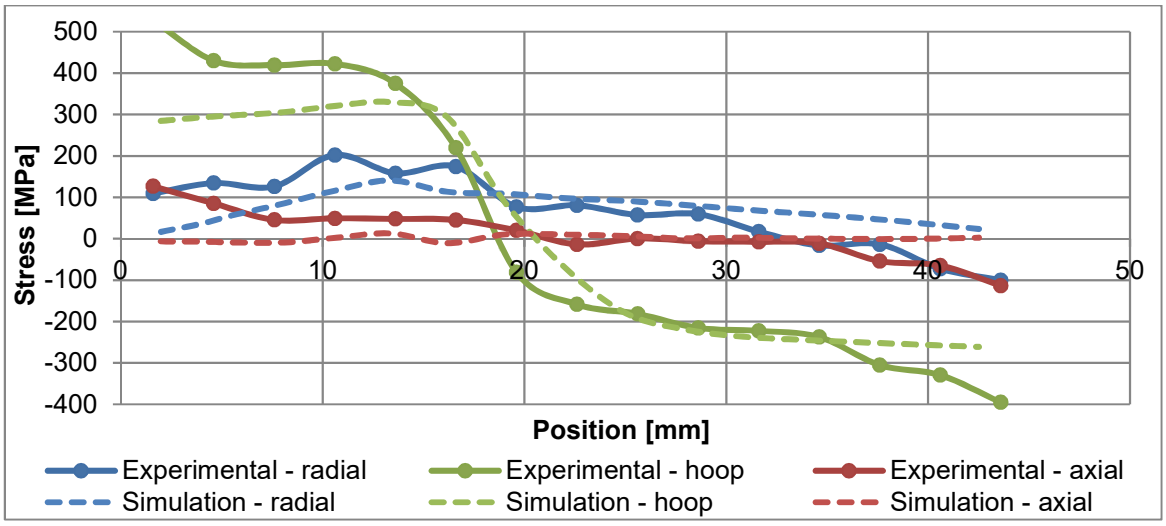

Figure 7-27: Comparison between the structural experimental and simulation results (Sample 9; flange)

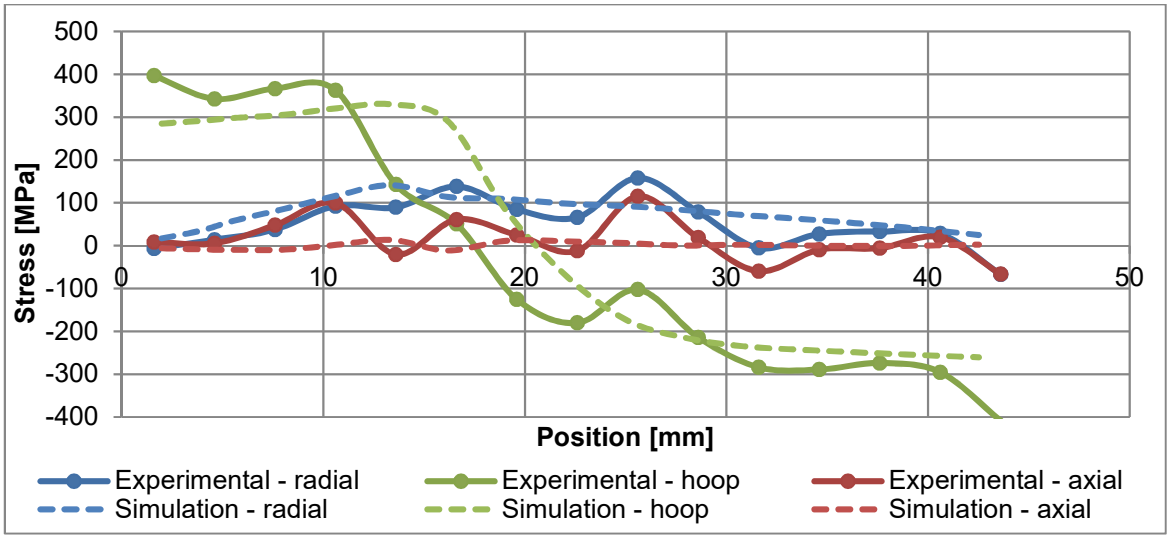

Figure 7-28: Comparison between the structural experimental and simulation results (Sample 15; flange)

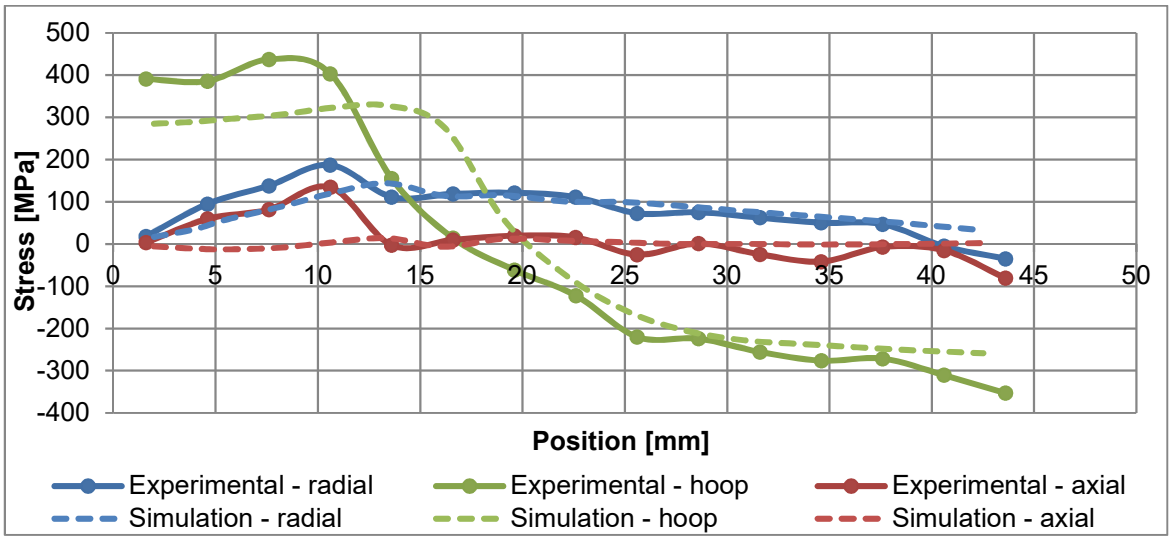

Figure 7-29: Comparison between the structural experimental and simulation results (Sample 16; flange)

In general, there is a clear correlation between the simulated and experimental results for all three components of residual stress, especially when one observes the general profiles of the curves. The pronounced differences in some curves can be observed closer to the weld centre line or the starting point of measurement. Hoop stresses for simulation and experiments for example at the starting point seem to differ significantly in some curves.

The differences in results can be explained as follows:

a. The parent materials of the plate and pipe, as well as filler material, were all assumed to have the same material properties. In reality these differ, and significant changes can be observed in the weld metal whose properties are different to parent metal.

b. The residual stress state of the material before welding has not been considered. To determine stress, the complete history of the loading of the material must be considered.

c. Welding defects from the physical welding process that have not been accounted for in the simulation.

d. Annealing has not been included in the model.

e. It is likely that the position of the simulation's stress measurement points differ slightly from the actual measuring points. The geometry of the welded specimen makes it difficult to ascertain the exact point of measurement consistently in all cases.

f. Uncertainties/errors in the neutron diffraction stress measurements, the measurement process is not perfect.

7.6 Bead Geometry Results

Bead geometry was measured as stipulated in Figure 4.5 above. The results are tabulated in Table 7.6.

Table 7-6: Bead Geometry Results

Bead Geometry					
	BW (mm)	**BP (mm)**	**BH (mm)**	**HAZ Plate (mm)**	**HAZ Pipe (mm)**
Sample 4	12.89	8.96	1.39	1.28	4.43
Sample 6	12.4	8.3	1.7	1.6	3.3
Sample 7	12.7	9.9	1.8	0.9	3.8
Sample 8	12.3	8.61	1.2	1.4	3.3
Sample 9	13.3	8.6	2.1	0.9	3.8
Sample 12	10.8	7.4	0.7	2.1	5.8
Sample 13	9.8	6.3	0.8	1.3	6.2
Sample 15	9.8	6.6	1.0	1.4	2.8
Sample 16	9.4	6.6	1.1	2.8	1.7

It must be noted that all measurements were done only after the third pass, such that the dimensions given in Table 7.6 are those of a multi-pass weld. The objective as discussed in Chapter 6 was to minimise all response variables except for BP, which should be maximized. If one applies the bead geometry as criterion to determine which samples have the best dimensions according to the optimization objectives, the results shown in Table 7.7 are obtained. It can be seen that Samples 7 and 16 are at the top, followed by Samples 12, 13, and 15. Sample 4 is in third place. Four samples that were found to be the best according to the residual stress criteria also appear is the list of Table 7.7, namely Samples 4, 7, 12 and 13. This is indicative of the consistency in the experimental results.

Table 7-7: Ranking of Samples Using Bead Geometry as Criterion

#	BW	BP	BH	HAZ PT	HAZ PP
1	16	7	12	7, 9	16
2	13, 15	4	13	4	15
3	12	8	15	13	6, 8

7.7 Microstructural Analysis

The parent material of the pipe is the same for all samples, so is the one for the plate, since all specimens were cut from the same material. Waterjet cutting was used to section the pipe into 100 mm lengths and the plate into 178 x 178 mm squares. Figure 7.30(a) is a low magnification image of the test specimen, to indicate the position of the unaffected plate material. Figure 7.30(b) and (c) are micrographs, revealing a typical pearlite and ferrite grain structure typical in steels with a grain size average of ±0.11 µm. An indication of the chemical composition was obtained through Energy-Dispersive Spectroscopy (EDS) analysis from SEM. Although the carbon content is included and measured, it is well understood that carbon cannot be accurately quantified using this method. All the macrographs and micrographs shown below were taken using Sample 4, 6, 7 and 8 for illustration purposes. Appendix E gives the macrographs for each sample for reference purposes.

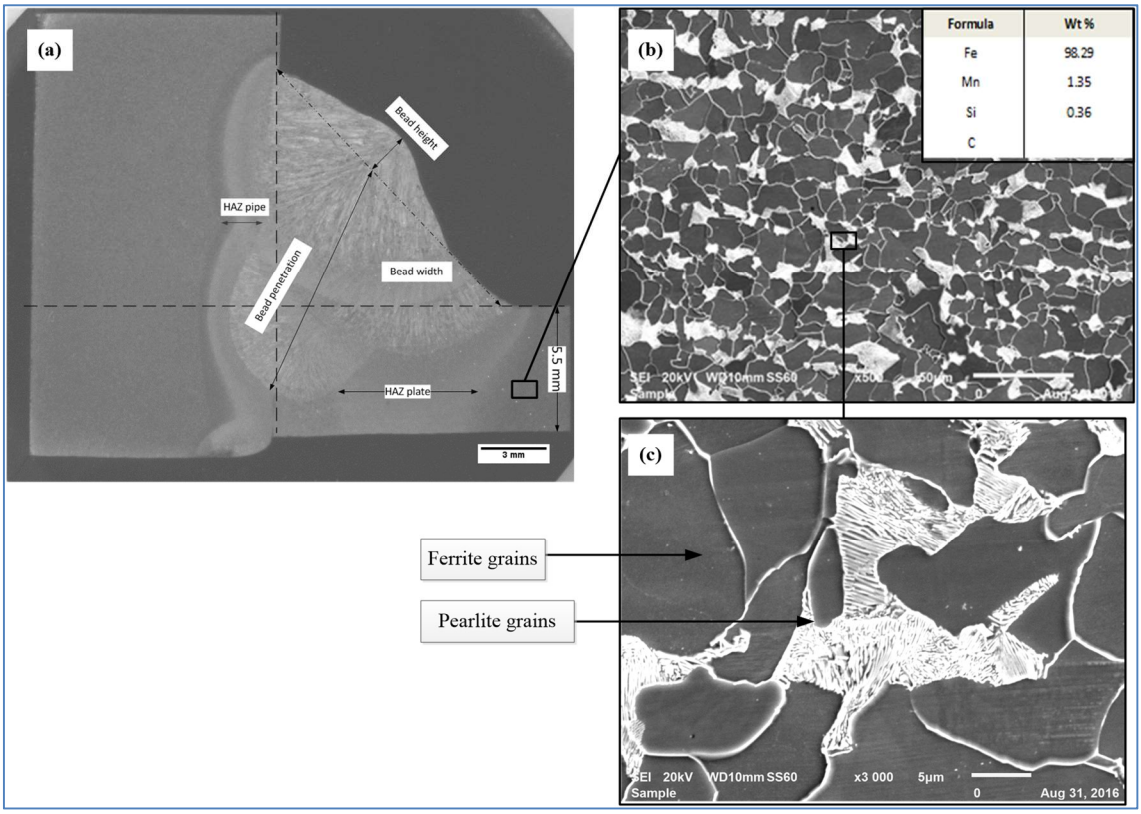

Figure 7-30: (a) A macrograph of the overall test specimen showing the position of the unaffected plate material. (b) A micrograph obtained at a magnification of 500x of the as-received plate material. (c) A micrograph obtained at 3000x magnification to show the lamellae cementite (Fe3C) grains within the pearlite grains

Figure 7.31 shows the microstructure of the plate parent material. The PM is composed of the ferrite-pearlite structure which is common in steels. The average grain size of the plate PM is ±0.14 µm. The average grain size is obtained by using the line intercept method on scaled images.

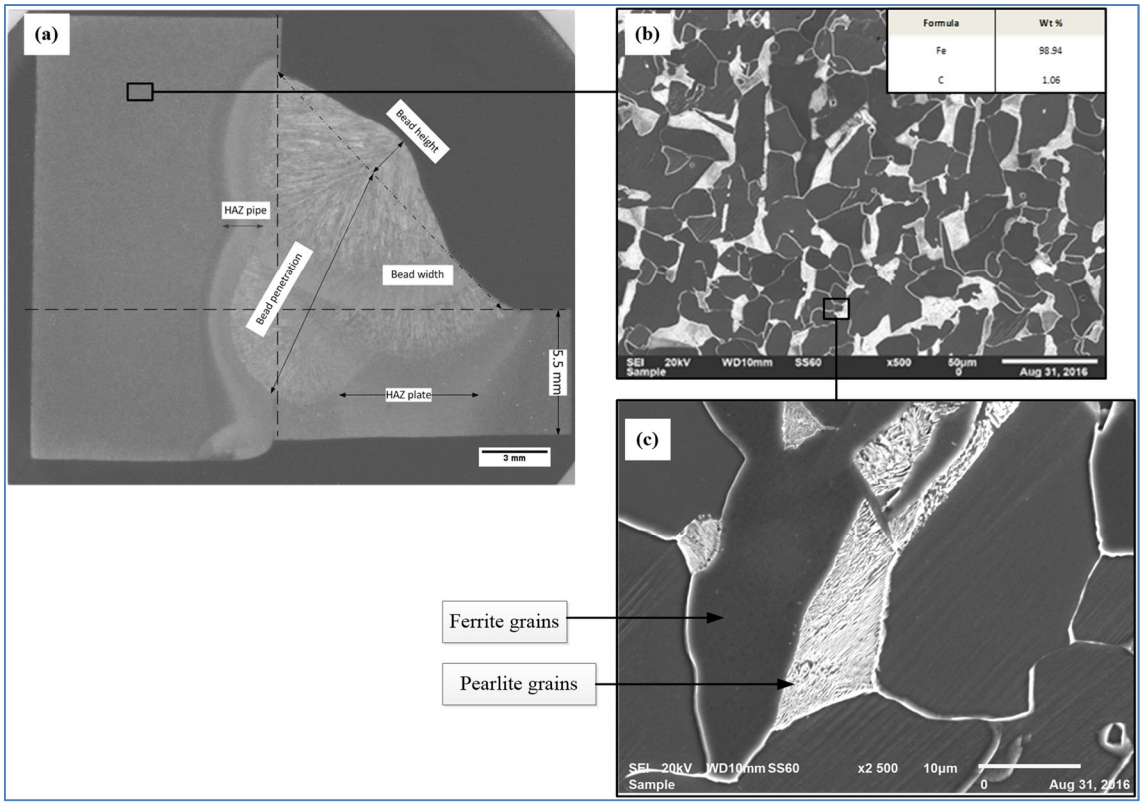

Figure 7-31: Plate PM Micrograph (All Samples)

Figure 7.32 shows: (a) Macrograph of the coarse grain region within the HAZ of the pipe side in Sample 6, obtained at a magnification of 500x. (b) High resolution micrograph of the HAZ of the pipe side in Sample 6 at a magnification of 2000x. (c) Chemical analysis obtained through EDS. The grains in this region are relatively large.

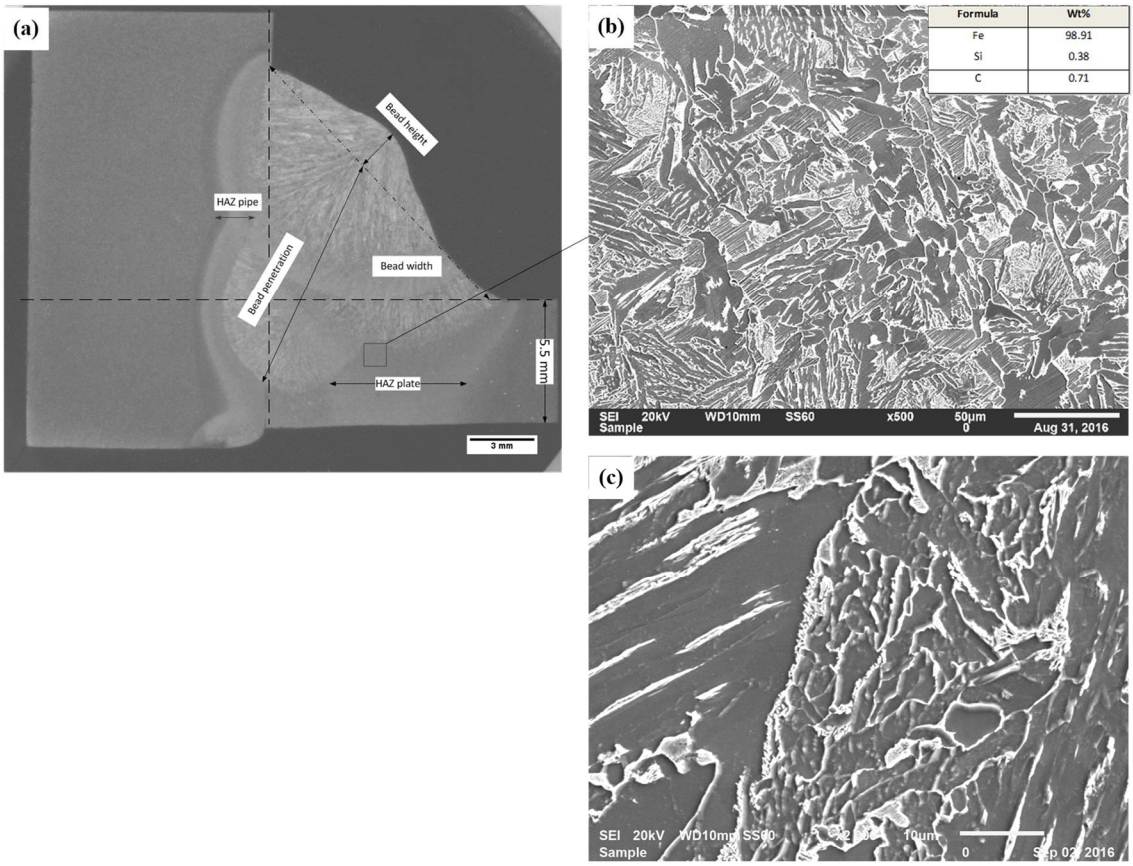

Figure 7-32: Sample 6 Coarse Grain Region within the HAZ Micrograph

Figure 7.33 shows a micrograph of the fine grain region within HAZ of the pipe side where the Fe3C lamellae structures have dissolved into smaller spheroids. This microstructure is composed of a mixture of ferrite grains, martensite, and retained pearlite grains.

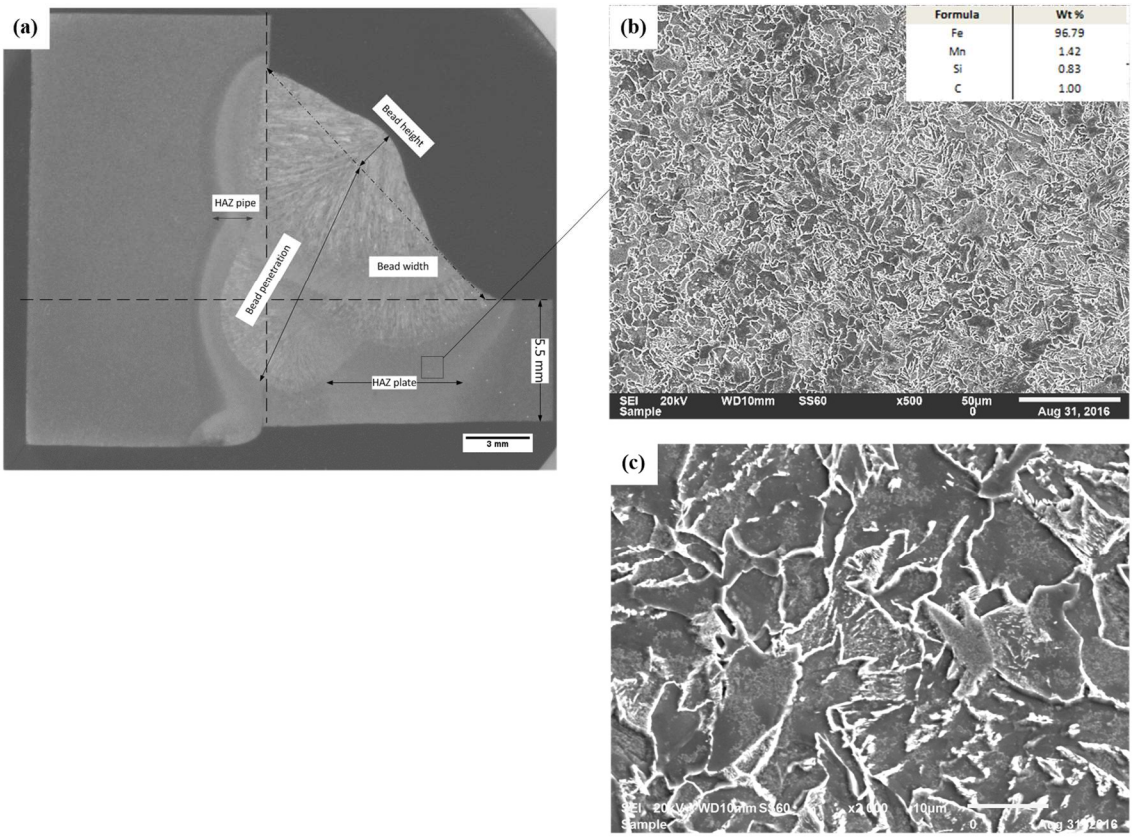

Figure 7-33: Sample 6 Fine Grained Region within the HAZ Micrograph

Figure 7.34 is a micrograph of the sub-critical region within the HAZ of the plate metal. In this micrograph pearlite and ferrite grains are observed. The pearlite grains have formed smaller colonies and the ferrite grains appear to have enlarged as a result of parent metal grain merging with HAZ grains to form new grains.

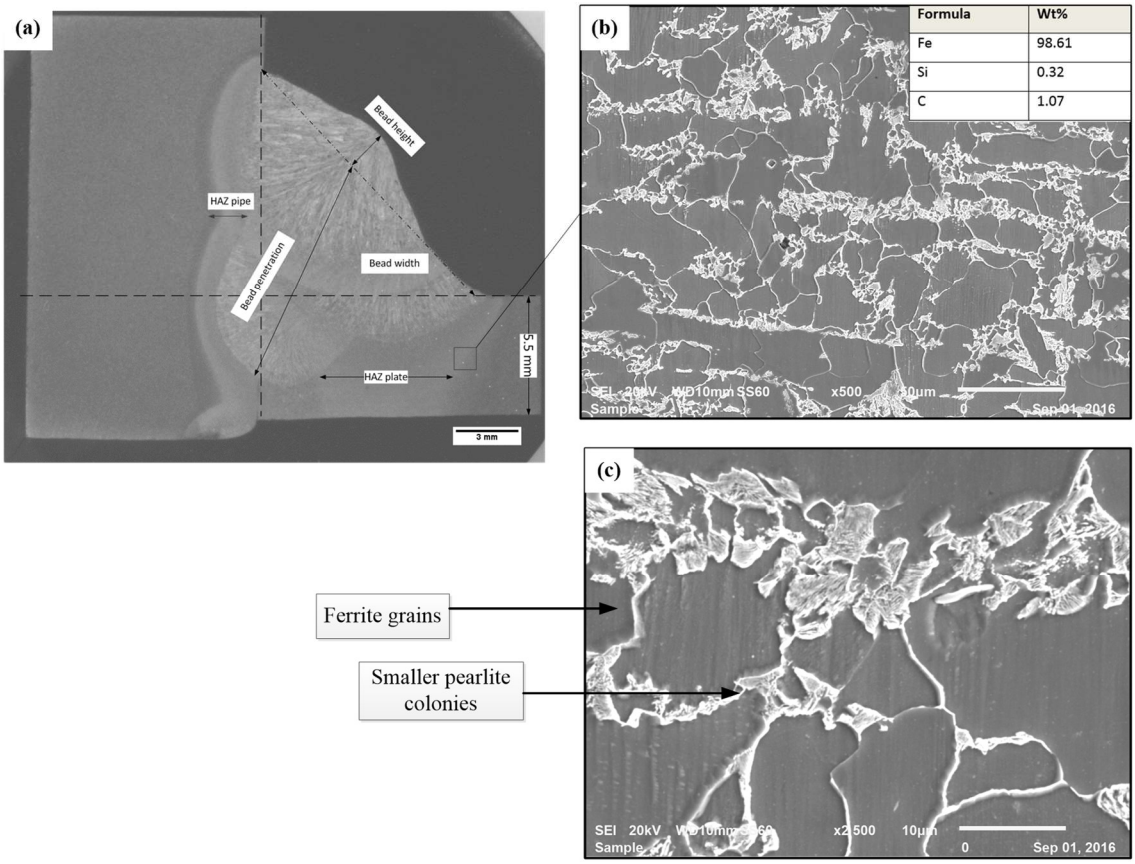

Figure 7-34: Sample 7 Sub-Critical Region within the HAZ

Figure 7.35 is a micrograph of the primary weld. The microstructure observed in this figure appears to be a tempered martensite microstructure. It can be seen that the WM shows a micrograph with a featherlike structure. The featherlike or branch like structure occurs as a result of the formation of dendrites, which occur when molten metal is cooled rapidly. The weld is composed of pro-eutectoid ferrite with the Widmaenstaetten morphology often seen as a result of rapid phase transformation that occurs due to rapid cooling.

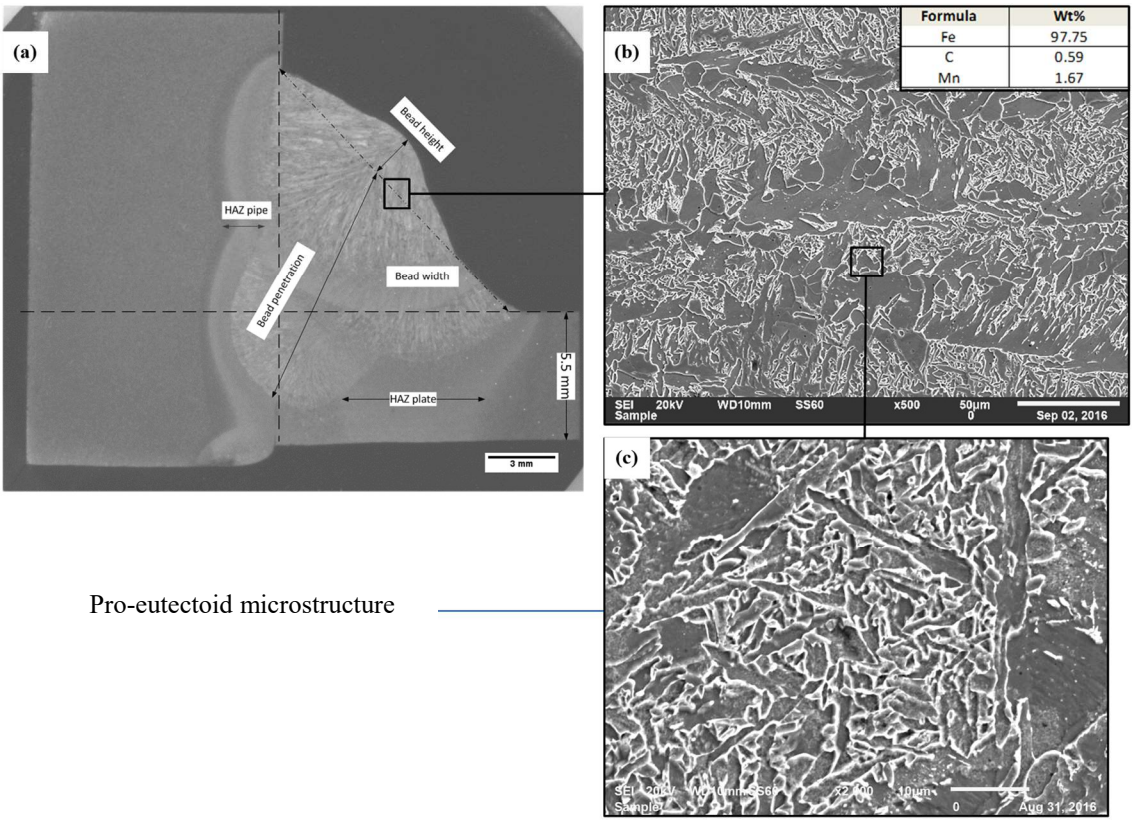

Figure 7-35: Sample 6 WM Micrograph

Figure 7.36 shows a micrograph of the plate as-received. A micrograph with a typical grain structure of carbon steel is observed, with pearlite and ferrite grains and an average grain size of 0.14 μm.

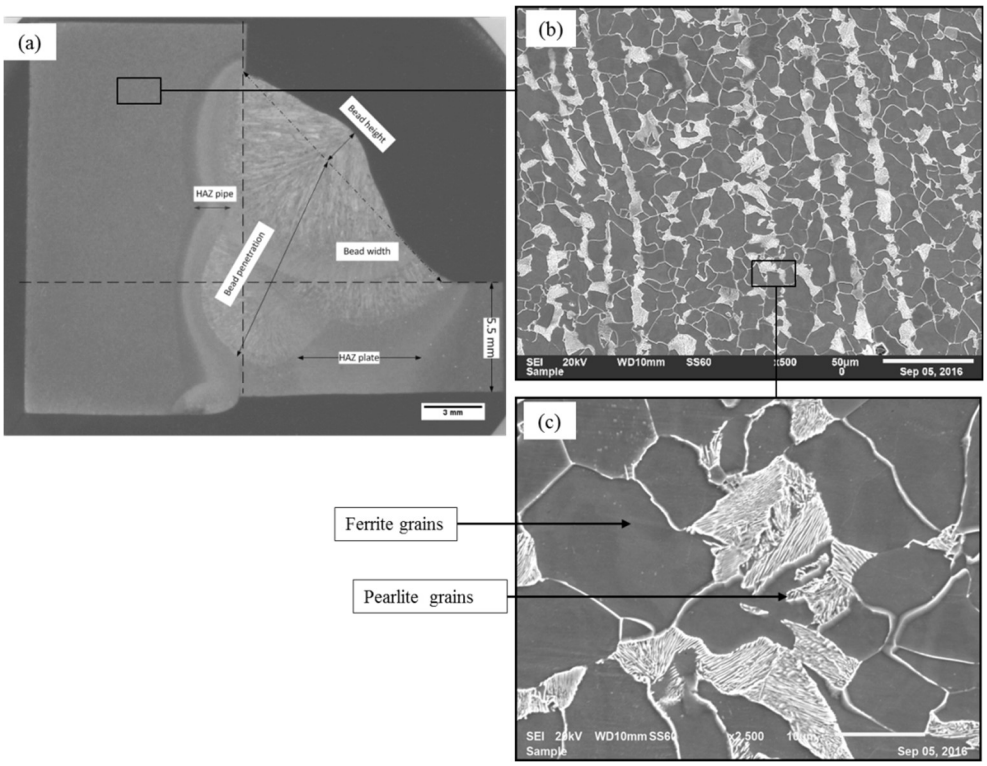

Figure 7-36: Micrograph of the parent material of the plate (All Samples)

Figure 7.37 shows the coarse-grained region of the plate material, where the large grains have formed sub-grain pearlite lathes within the initial grain structure.

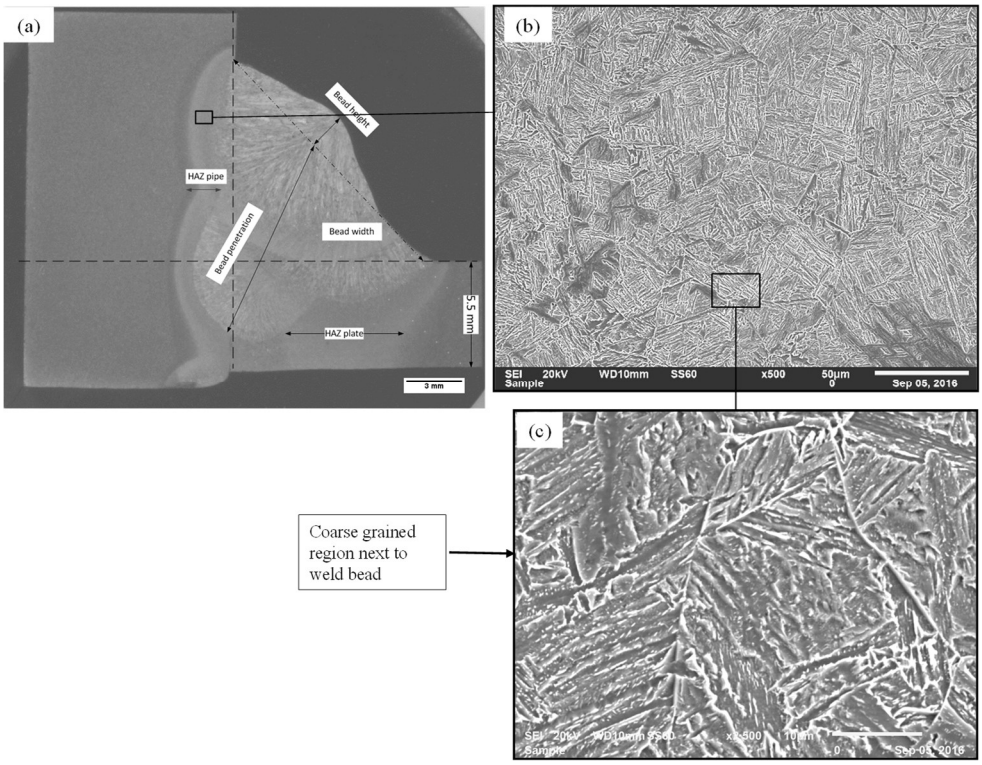

Figure 7-37: Micrograph of the coarse-grained region next to the weld bead (Sample 7)

Figure 7.38 and Figure 7.39 show micrographs of the region within the HAZ that comprises both the coarse grains and smaller pearlite grains. The average grain size was calculated to be ±0.37 µm. Smaller grains and the lamellar structure has begun to form spheroids as a result of the heat input from welding.

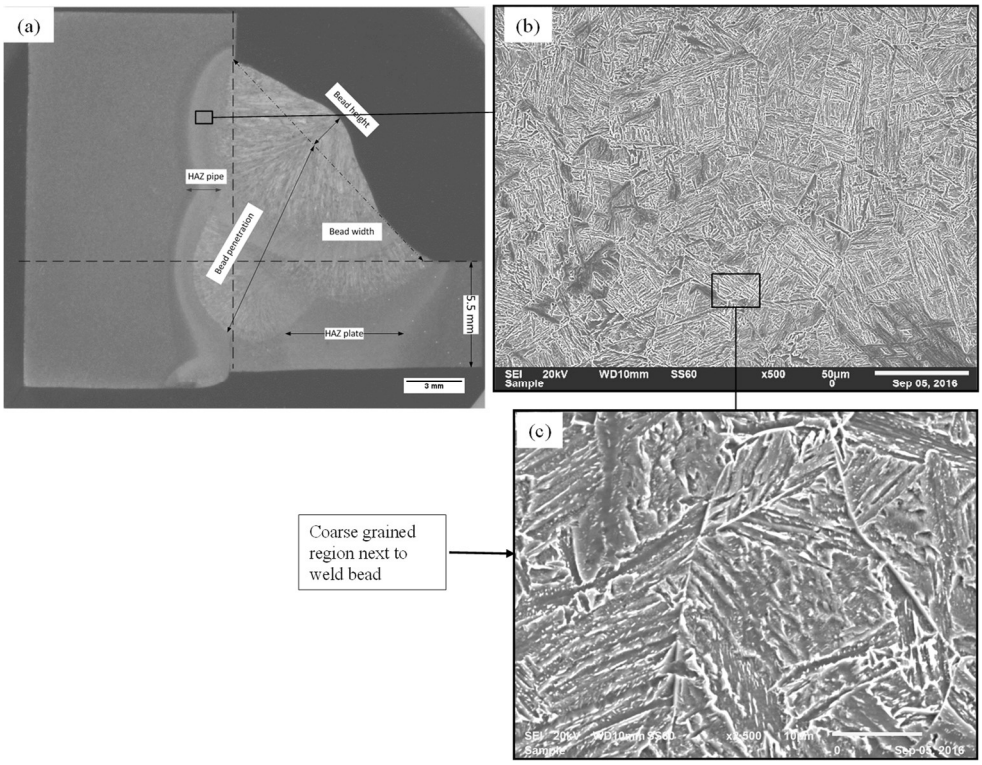

Figure 7-38: The coarse grain region on the plate side (Sample 7)

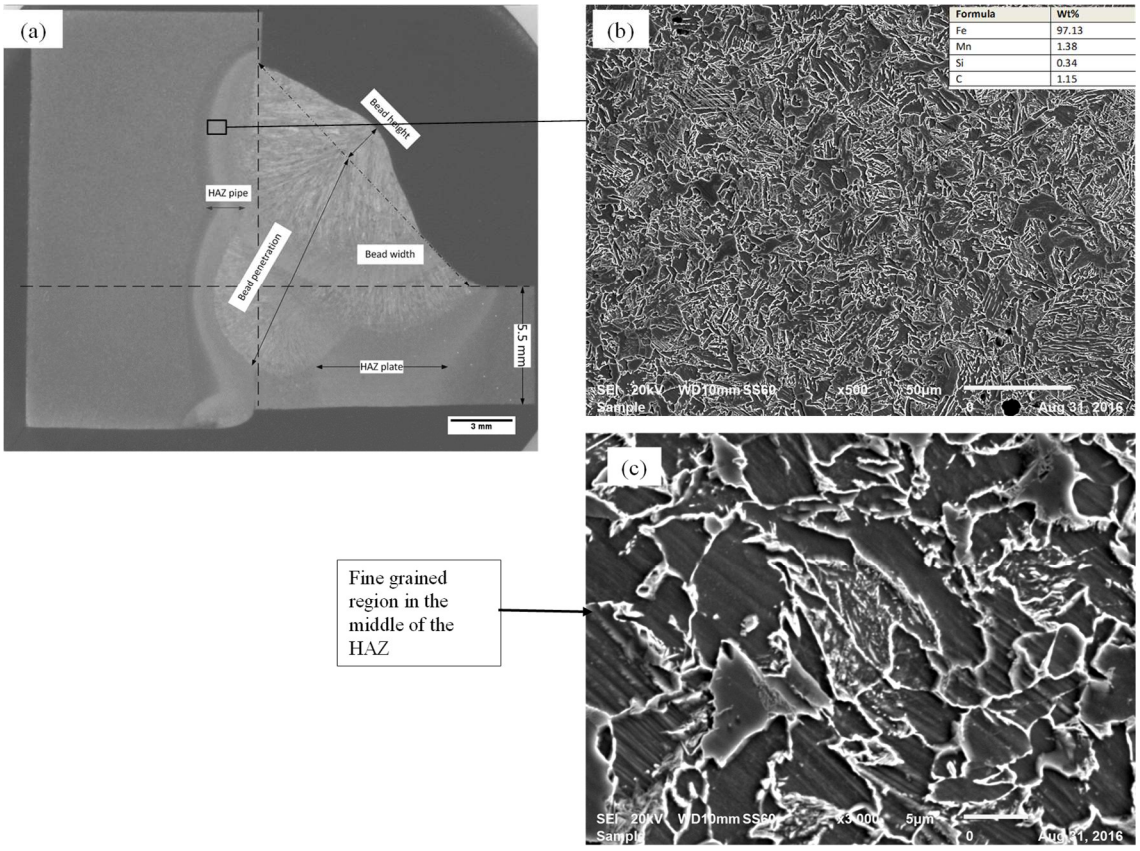

Figure 7-39: Fine grained region with the HAZ of the plate (Sample 7)

A summary of the microstructure of all specimens is given in Table 7.8. It is clear from the table that the HAZ area has significant portions of martensitic phase, which contributes to residual stress magnification as a result of phase-related volumetric changes. The weld metal is mainly made of proeutectoid ferrite. The formation of both phases is influenced by the cooling rate during the weld thermal cycle. The cooling rate therefore affects phase transformation, which in turn can have an effect on the formation of welding-induced residual stresses.

Table 7-8: Summary of Specimen Microstructures

Sample	PTHAZ	WM	PPHAZ
4	Tempered martensite	Proeutectoid ferrite	Tempered martensite
6	Tempered martensite	Featherlike dendrites	martensite
7	Lamellar pearlite	Proeutectoid ferrite	Pearlite-ferrite
8	Lamellar pearlite	Proeutectoid ferrite	Ferrite-martensite
9	Lamellar pearlite	Proeutectoid ferrite	Ferrite-pearlite
12	Tempered martensite	Proeutectoid ferrite	Ferrite, pearlite, bainite, martensite
13	Tempered martensite	Proeutectoid ferrite	Ferrite, pearlite, martensite
15	Tempered martensite	Proeutectoid ferrite	Ferrite, martensite
16	Tempered martensite	Proeutectoid ferrite	Ferrite, martensite, pearlite

7.8 Hardness Results

7.8.1 Hardness Experimental Results

Hardness measurements were performed as explained in Chapter 4. The obtained hardness results are tabulated in Table 7.9.

Table 7-9: Hardness Results for All Specimens (Load of 100gf)

Sample		Pipe PM	Pipe HAZ	Weld Metal	Plate HAZ	Plate PM
4	VHN	185.4± 5.4	193.6 ± 4.6	211.8 ± 7.4	216.6 ± 8.8	180.4 ± 6.2
	Accuracy	3.0	2.5	3.7	5.6	4.4
	Equivalent UTS(MPa)	591.7	622.3	690.2	708.1	573.1
6	VHN	191.8 ± 4.4	198 ± 8.1	210.2 ± 18.9	234.8 ± 9.6	187 ± 25.1
	Accuracy	2.6	4.5	10.4	4.8	19.6
	Equivalent UTS(MPa)	615.6	638.7	684.2	776.0	597.7
7	VHN	171.4 ± 2.8	186.8 ± 1.6	213.8 ± 9.3	208.6 ± 10.7	178.8 ±11.9
	Accuracy	1.9	0.8	5.6	5.6	11.2
	Equivalent UTS(MPa)	539.5	596.9	697.7	678.3	567.1
8	VHN	180.2 ± 6.7	185.8 ± 10.6	209 ±23.4	226.3 ± 3.9	169 ±9.0
	Accuracy	3.8	12.7	13	5.1	3.2
	Equivalent UTS(MPa)	572.3	593.2	679.8	744.1	530.6
9	VHN	205.4 ± 26.3	183.6 ± 3.3	201.8± 17.3	202.8 ±8.7	166.2±7.4
	Accuracy	14.4	3.8	12.4	3.7	7.4
	Equivalent UTS(MPa)	666.3	585.0	652.9	656.5	520.1
12	VHN	176.6 ± 7.7	207.2 ± 12.1	247.8 ± 16.8	275.8 ± 7.0	178.8 ± 6.2
	Accuracy	4.8	6.1	7.5	3	3.4
	Equivalent UTS(MPa)	559	673.1	824.5	928.9	567.1
13	VHN	169.4 ±10.2	200.4 ±10.8	243.6± 19.8	233.6 ± 16.9	172.4± 5.3
	Accuracy	5.5	9.9	13	8.3	3.4
	Equivalent UTS(MPa)	532.0	647.7	808.8	543.3	542
15	VHN	180.6 ± 8.2	214 ± 8.9	225 ± 17.0	280 ± 28.1	168.8 ±10.0
	Accuracy	4.8	4.2	12.1	13.2	8
	Equivalent UTS(MPa)	573.8	698.4	739.5	944.6	529.8
16	VHN	174.8±4.4	186.9± 8.1	210.4± 18.9	219.8 ± 9.6	184.3± 25.1
	Accuracy	2.6	4.5	10.4	4.8	19.6
	Equivalent UTS(MPa)	552.0	597.2	684.9	719.9	587.7

It can be observed from Table 7.9 that the parent metal has the lowest hardness on both plate side and pipe side compared to the HAZ and the weld metal. For all but two specimens, hardness increases in the manner of PPHAZ→WM→PTHAZ (PPHAZ = pipe side HAZ, PTHAZ = plate side HAZ), wherein the plate-side HAZ is the highest. The highest observed value of hardness is 280, which is PTHAZ of Sample 15. The lowest hardness value observed (excluding PM) is 183.6 in the plate side HAZ of Sample 9. Given that the objective is to minimise hardness, the top three samples in terms of results tabulated in Table 7.9 are 9, 8 and 7, in that order. The said samples are highlighted in Table 7.9. It should be noted that "accuracy" values are calculated as half the difference between upper and lower hardness value in each case

7.8.2 Maximum Hardness Calculations

Cold cracking or hydrogen-induced-cracking [HIC] is one of the most significant factors that reduces life expectancy of a welded structure. The main factors that contribute to HIC include microstructure of high hardness, hydrogen content and tensile restraint stresses. The maximum HAZ hardness (often limited to 350 HV for HSLA steels) is generally regarded as an approximate index for susceptibility to cold cracking (Bang et al., 2002).

Kasuya et al. (1995) suggested a formula to work out maximum hardness as follows:

$$HV = \frac{H_M + H_B}{2} - (H_M - H_B).\frac{\arctan(X)}{2.2} \quad \textbf{(7.3)}$$

Where;

H_M is the hardness value where martensite volume fraction reaches 100% in CG HAZ

H_B is the hardness value where martensite volume fraction becomes almost zero percent in CG HAZ.

X is defined by: $X = \frac{4.\log(\frac{\tau}{\tau_M})}{\log(\frac{\tau_B}{\tau_M})} - 2$ **(7.4)**

Where;

τ is the cooling time between 800°C and 500°C [$t_{8/5}$]

τ_M is the cooling time corresponding to H_M

τ_B is the cooling time corresponding to H_B

The four constants [H_M, τ_M, H_B and τ_B] depend on the chemical composition of steel [i.e. weight - %] and are defined as follows:

$$H_M = 884C(1 - 0.3C^2) + 297 \quad \textbf{(7.5)}$$

$$\tau_M = \exp(10.6CE1 - 4.8) \quad \textbf{(7.6)}$$

$$CE1 = C_p + \frac{S_i}{24} + \frac{M_n}{6} + \frac{C_u}{16} + \frac{N_i}{12} + \frac{C_r(1-0.16.\sqrt{C_r})}{8} + \frac{M_o}{4} + \Delta H \quad \textbf{(7.7)}$$

$C_p = C$ for $C \leq 0.3$ and $\frac{C}{6} + 0.25$ for $C > 0.3$

$\Delta H = 0$ for $B \leq 1ppm$; $0.03f_N$ for $B = 2ppm$; $0.06f_N$ for $B = 3ppm$; $0.09f_N$ for $B \geq 4$; where 'B' is the boron content for S $\leq$ 0.016 wt.%

$$f_N = \frac{(0.02-N)}{0.02} \quad \textbf{(7.8)}$$

$$H_B = 145 + 130\tanh(2.65CE2 - 0.69) \quad \textbf{(7.9)}$$

$$CE2 = C + \frac{S_i}{24} + \frac{M_n}{5} + \frac{C_u}{10} + \frac{N_i}{18} + \frac{C_r}{5} + \frac{M_o}{2.5} + \frac{V}{5} + \frac{N_b}{3} \quad \textbf{(7.10)}$$

$$\tau_B = \exp(6.2CE3 + 0.74) \quad \textbf{(7.11)}$$

$$CE3 = C_p + \frac{M_n}{3.6} + \frac{C_u}{20} + \frac{N_i}{9} + \frac{C_r}{5} + \frac{M_o}{4} \quad \textbf{(7.12)}$$

The above equations are used to calculate maximum HAZ hardness from the chemical composition, and calculate cooling time from the thermal analysis. Cold cracking is determined through comparing the calculated maximum HAZ hardness with limiting hardness of 350 HV. The geometry of FZ and HAZ is predicted from the peak temperature distribution. Average peak temperatures of 1316°C and 954°C represent CG HAZ and FG HAZ respectively (Bang et al., 2002).

The chemical composition of filler metal, plate material and pipe material as given in Chapter 4 was used to calculate the maximum hardness of the FZ, the HAZ on the plate side and the HAZ on the pipe side respectively. Energy input per unit length was calculated using equation 5.1 to 5.4 in Chapter 5. The same was then used to calculate the cooling rate t_{8-5}. Appendix F provides a graph from where the value of the cooling rate can be read using the heat input value. The average heat input value for the experiments conducted in this study is 0.7 MJ/m, which results to t_{8-5} of 3.2 seconds. The Boron content is assumed to be 2, thereby giving a value of ΔH of 0.03. The resultant maximum hardness values are given in Table 7.10 for all targeted parts of the weld-piece.

Table 7-10: Calculated Hardness Values

Hardness	Fusion Zone	Pipe-side HAZ	Plate-side HAZ
H_M	376	472	472
H_B	195	211	192
HV_{max}	209	243	213

As can be seen from Table 7.10, all maximum hardness values are well below the 350 limit, which means that the structure is less susceptible to HIC.

7.9 Fatigue Test Results

The fatigue tests were conducted on several specimens prepared according to the CA mode settings of the parametric combination discussed in Chapter 4. This is to say that all specimen were prepared according to welding parameters used for Samples 4, 6, 7, 8 and 9. Two tests were conducted for each sample under same load conditions and the algebraic average of cycles to failure was taken as indication of fatigue life of the sample.

7.9.1 Static and Fatigue Trial Tests

Static tests were first conducted to establish the maximum load on a trial test specimen as indicated in Chapter 4. The first test was conducted at a crosshead speed of 2 mm/min. The maximum load measured was 260 kN. The specimen did not fracture and the pipe was deformed. The load displacement graph was analysed and the yield strength determined as 140 kN. Figure 7.40 shows the position of the yield point on the Load-Displacement curve.

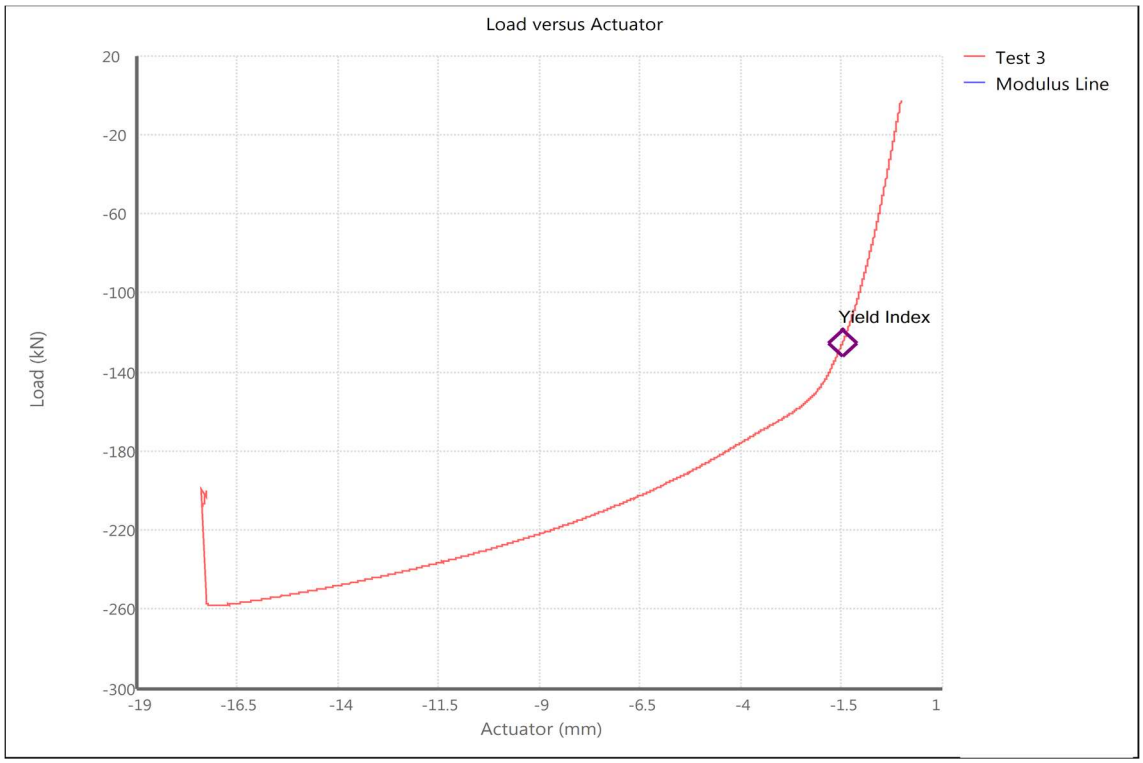

Figure 7-40: Trial Fatigue Test to Determine Yield Point

Figure 7.41 shows images of the static test specimen. (a) As can be observed, there was deformation or buckling of the pipe. This problem was resolved by manufacturing a steel plug to

insert at the tip of the pipe for support; this was used in all the tests. (b) This is the side view of the statically loaded specimen. (c) The top view of the static test specimen where the buckling of the plate is observed.

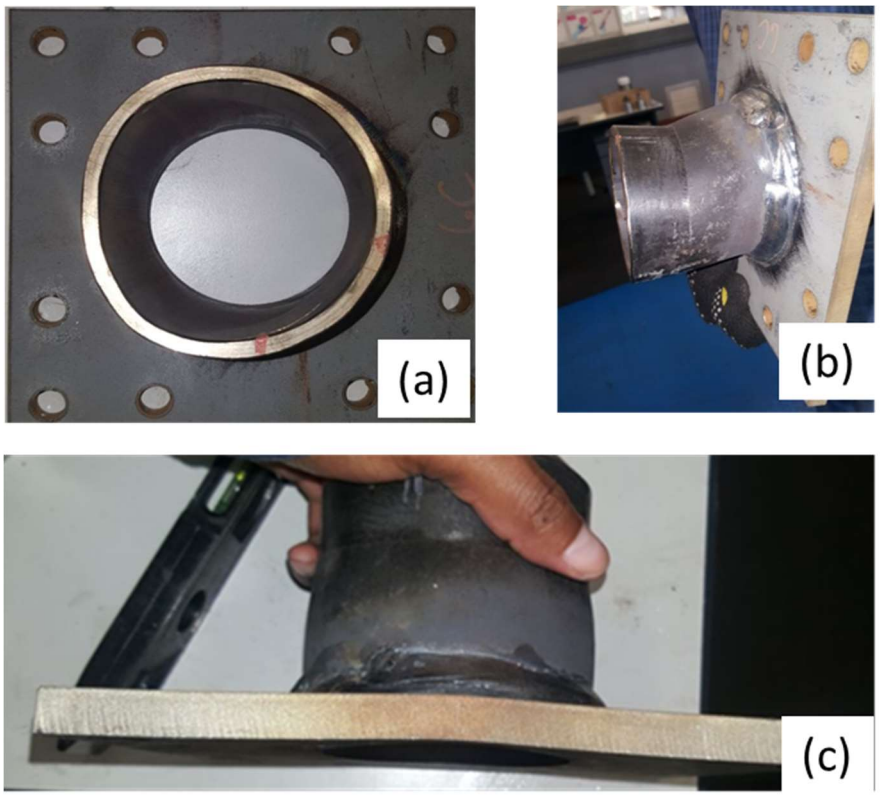

Figure 7-41: The Static Test Specimen after the Test

Following the static tests, fatigue tests were conducted on two trial specimens applying a maximum load of 90% of yield strength, i.e. 126 kN. The first trial specimen based on Sample 4 characteristics failed at approximately 73,494.7 cycles as shown in Figure 7.42.

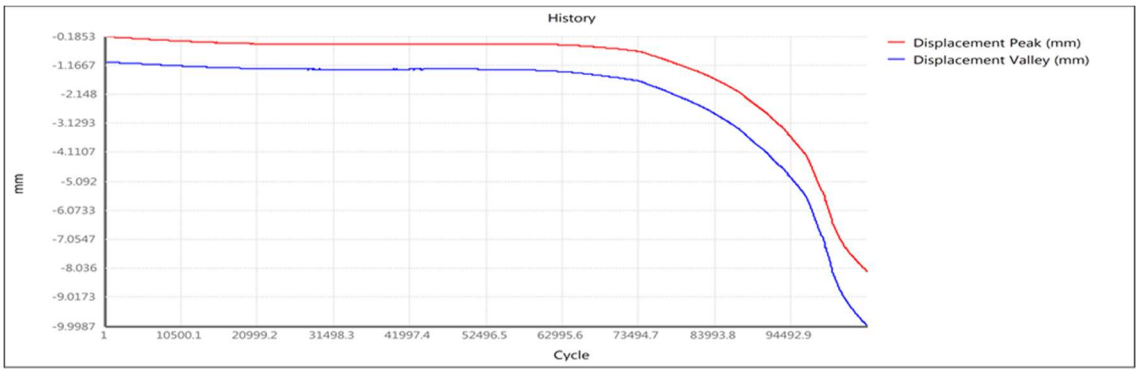

Figure 7-42: Number of cycles vs. Fatigue load for 1st Trial Specimen (4A) at 126 kN

Figure 7.43 (a) shows the front of the specimen loaded at 126 kN, at a frequency of 5 Hz. (b) shows the damage observed on the specimen on face where the compressive load was applied directly. Two primary cracks are observed. The first crack is an open crack and can be clearly noticed in the weld. This crack propagates along the length of the third weld pass, through the first weld pass and into the parent material. The second crack can be seen originating from the third weld pass, through the heat affected zone of the pipe as shown in Figures 7.43 (c) and (d). It is not easy to identify the origin of the crack in this case.

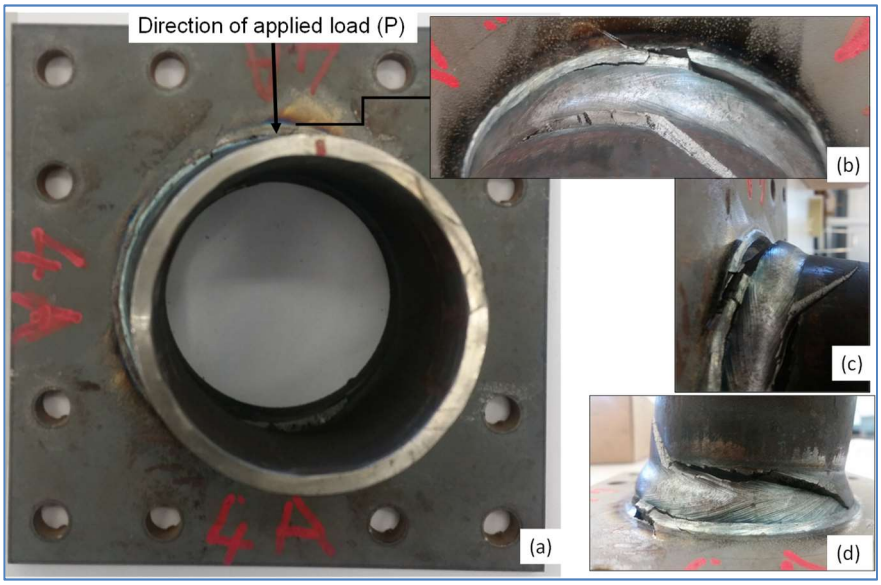

Figure 7-43: Failed Specimen of 1st Trial Test at 126 kN

The second trial test (Sample 4C) was tested under a maximum load of 112 kN, i.e. 80% of the yield load, at a frequency of 8 Hz. The displacement failure criteria was reduced from 5 mm to 2 mm displacement of the actuator. The graph shown in Figure 7.44 illustrates a plot of the test data as received from the laboratory report. The vertical axis is a record of the displacement measured by the machine actuator, the horizontal axis represents the number of cycles to failure. At the specified load the specimen started to fail at approximately 140 000 cycles. The data set shown in Figure 7.43 however is representative of the 2 mm failure criterion; and hence a new test had to be redone at 5 mm criterion after this trial test.

Figure 7-44: Displacement vs. Number of Cycles for 2nd Trial Test at 112kN

Figure 7.45 (a) shows the front of Sample 4C. (b) shows a featherline crack that originates from the weld toe on the flange side and propagates into the weld metal.

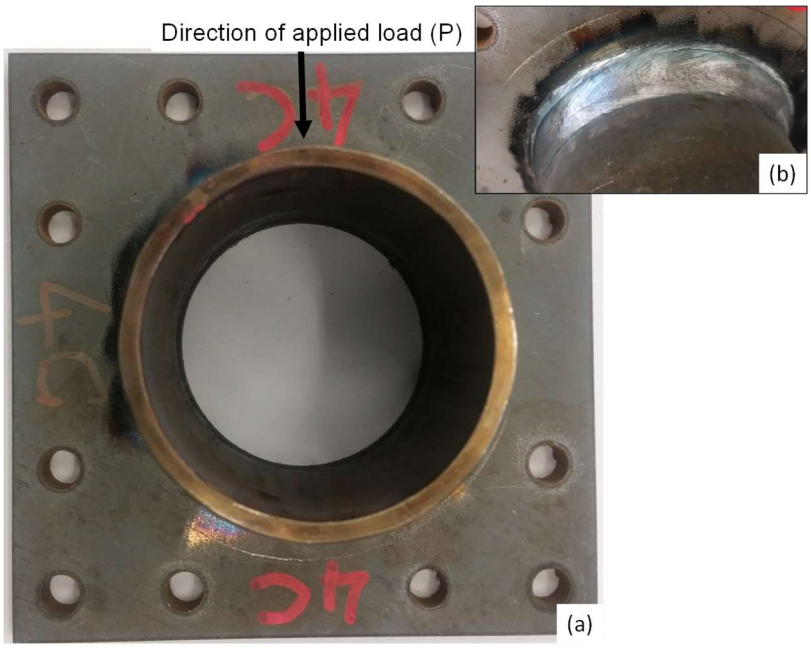

Figure 7-45: (a) Sample 4C front face. (b) top view of damage observed on the welded specimen

7.9.2 Specimen Fatigue Tests

On completion of the trial tests it became clear that the load 112 kN, at frequency of 8 Hz and 5 mm failure criterion was ideal for the envisaged fatigue tests. The first specimen to be tested under these conditions was Sample 4D. At this load 116,000 cycles were recorded before failure at the displacement limit of 5 mm. Figure 7.46 shows a plot of the test data as received from the laboratory report. The vertical axis is a record of the displacement measured by the machine actuator, the vertical axis represents the number of cycles recorded to failure. It can be observed that at displacement of approximately 2 mm the slope of the graph changes, which means that there was yielding experienced by the specimen. However, the test carried on until the set displacement limit of 5 mm was reached.

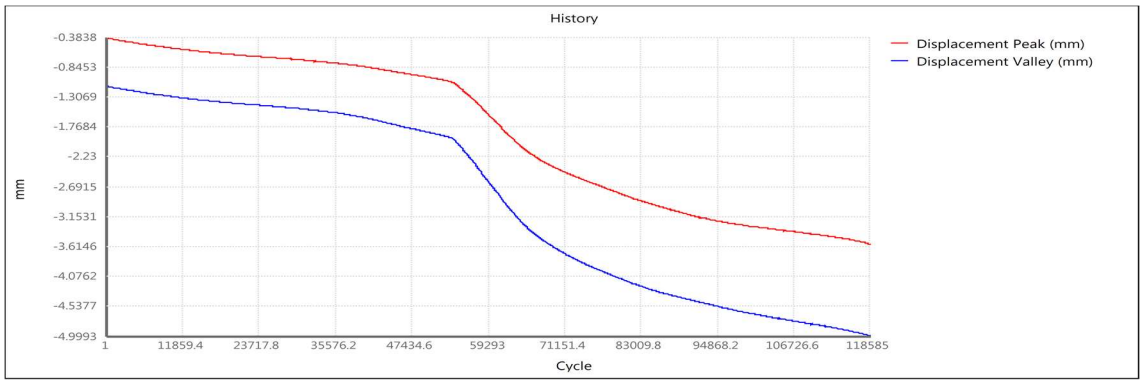

Figure 7-46: Displacement vs Cycles to failure for Sample 4C

Sample 4E was tested at a load of 112 kN at a frequency of 8 Hz and a displacement limit of 5 mm. At this load 164,400 cycles were recorded before failure. Figure 7.47 shows a plot of the test data as received from the laboratory report.

Figure 7-47: Displacement vs Cycles to Failure for Sample 4E

Sample 6C was tested at a load of 112 kN, at a frequency of 8 Hz and a displacement limit of 5 mm. At this load 86,500 cycles were recorded before failure. Figure 7.48 shows a plot of the test data as received from the laboratory report.

Figure 7-48: Displacement vs Cycles to Failure for Sample 6C

Figure 7.49 (a) shows the front face of Sample 6C. (b) shows a top view of the crack through the weld and the plate. (c) shows the propagation of the crack from the weld through the thickness of the plate. It can be seen that the weld failed at the weld toe on the plate side.

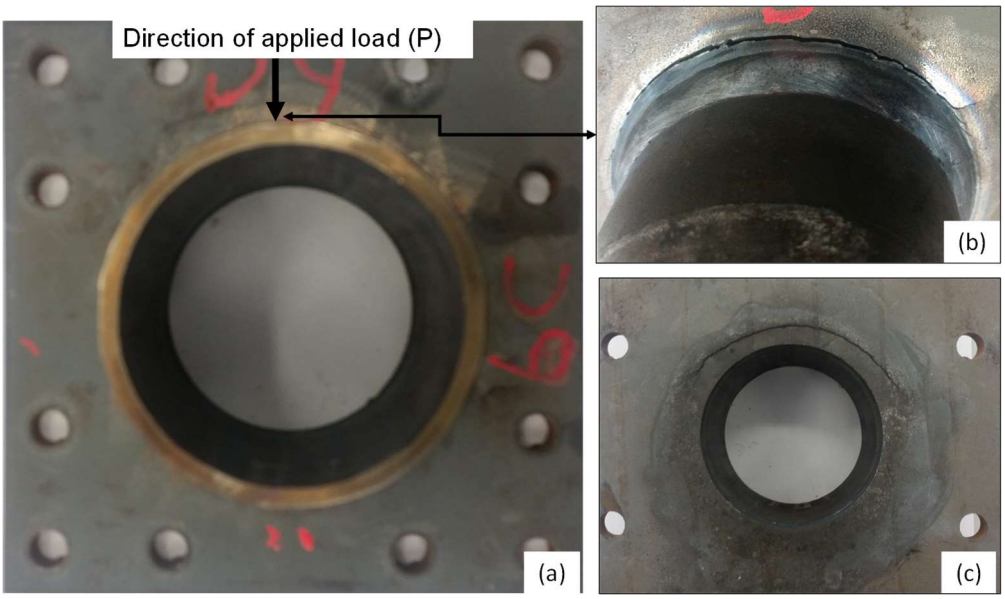

Figure 7-49: The Damaged Specimen of Sample 6C

Sample 7A was tested at a load of 112 kN, at a frequency of 8 Hz and a displacement limit of 5 mm. At this load 104,600 cycles were recorded before failure. Figure 7.50 shows a plot of the test data as received from the laboratory report.

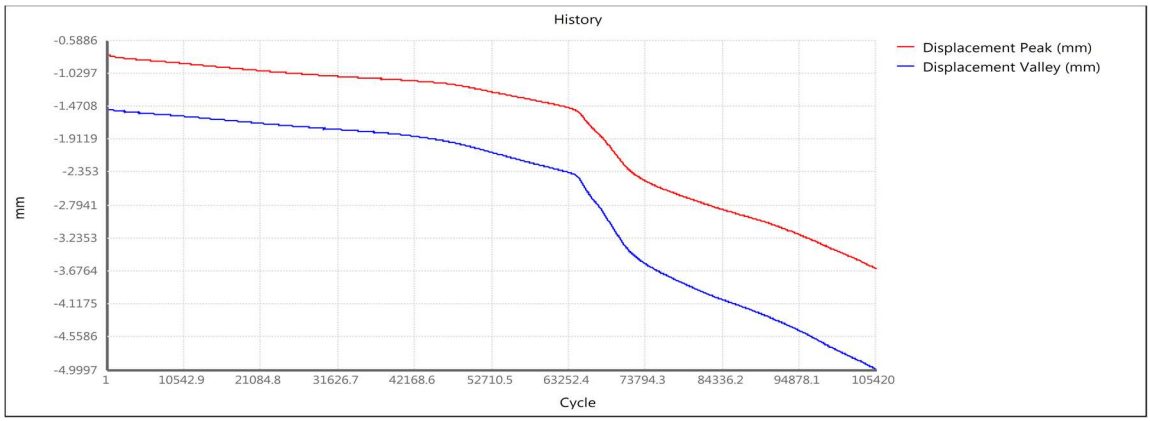

Figure 7-50: Displacement vs Cycles to Failure for Sample 7A

Figure 7.51 shows the front view of Sample 7A. (b) Shows the crack through the weld metal and the plate. (c) shows the back view of the crack, that has penetrated through the weld and the plate. The weld failed at the weld toe region

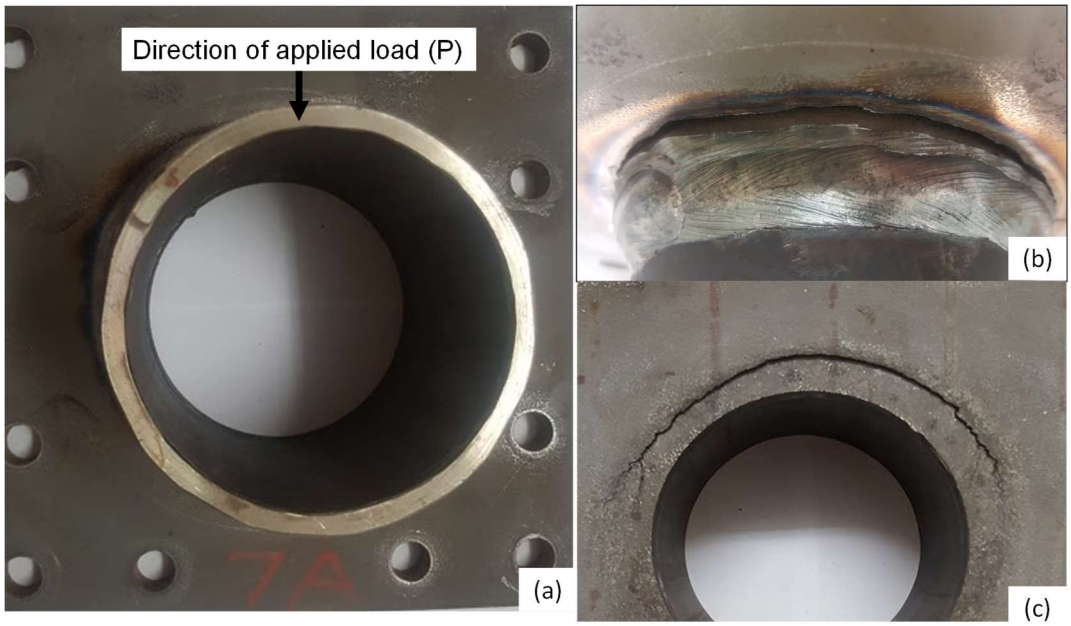

Figure 7-51: The Damaged specimen of Sample 7A

Sample 8C was tested at a load of 112 kN at a frequency of 8 Hz and a displacement limit of 5 mm. At this load 70,545 cycles were recorded before failure. Figure 7.52 shows a plot of the test data as received from the laboratory report.

Figure 7-52: Displacement vs Cycles to Failure for Sample 8C

Sample 9C was tested at a load of 112 kN at a frequency of 8 Hz and a displacement limit of 5 mm. At this load 77,200 cycles were recorded before failure. Figure 7.53 shows a plot of the test data as received from the laboratory report

Figure 7-53: Displacement vs Cycles to Failure for Sample 9C

Table 7.11 gives a summary of all the test results for each specimen. Two specimens were tested for each sample, and then an average of the two tests was taken. It is clear that Sample 4 has the highest number of cycles, followed by Sample 7, and then Sample 6.

Table 7-11: Summary of Number of Cycles to Failure for Each Specimen

Sample no	Number of cycles		Average cycles
	1st Specimen	2nd Specimen	
4	116,000	164,400	140,200
6	86,500	86,300	86,400
7	104,600	164,600	134,600
8	75,400	70,545	72,972.5
9	76,900	77,200	77,050

Figure 7.54 illustrates the relationship between the net residual stresses that were tabulated in Table 7.4 and the cycles to failure for each sample. It should be noted that fatigue tests were performed on five specimens that were generated using the constant amperage mode of the welding machine. The CW mode was therefore not considered for the fatigue tests. It is clear from figure 7.54 that Sample 4, which has the highest number of cycles, also has the lowest residual stress. Sample 6 has a larger amount of residual stress compared to Sample 4, and also a corresponding lower number of cycles. Sample 7 has the second highest number of cycles and also second lowest residual stress. Sample 9 has the highest residual stress the second lowest number of cycles. Sample 8 is an outlier in the data set. It has lowest stress levels and lower number of cycles. This could be caused by the fact that the specimen's actual stress condition was different from the predicted one. Four out of five specimens however behaved as expected during the fatigue tests. This proves therefore that residual stresses affect fatigue life of the welded pressure vessel. The tensile hoop stresses in the circumferential nozzle-shell joint shorten fatigue life of the welded structure.

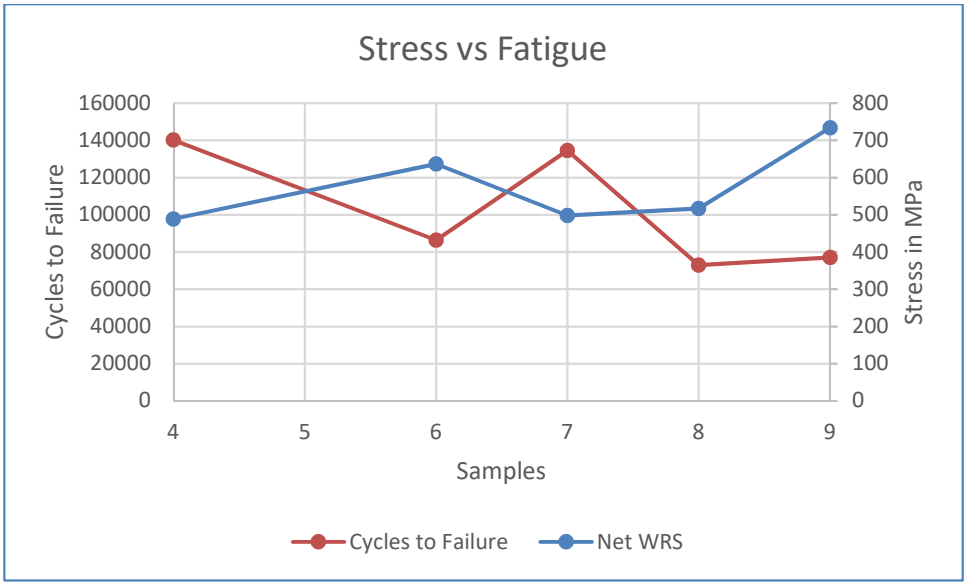

Figure 7-54: Cycles to Failure vs Net Residual Stress

7.10 Parametric Optimisation Results

Table 7.12 is the input/output parameter matrix for all input parameters and response variables studied in the present research. There are five input parameters and ten response variables. The table was populated using the results from experiments conducted as explained in Chapter 4.

Table 7-12: Input/Output Parameter Matrix

Exp. No.	Input Parameters					Response Variables								
	I	V	S	FR	MODE	BW	BH	BP	PPHAZ	PTHAZ	VHN (PPHAZ)	VHN (WM)	VHN (PTHAZ)	PTRS
4	380	30	10	18.3	CA	12.89	1.39	8.96	4.43	1.28	193.6	211.8	216.6	371
6	380	25	8	18.3	CA	12.44	1.7	8.3	3.27	1.59	198	210.2	234.8	402
7	360	25	8	18.3	CA	12.7	1.8	9.94	3.76	0.97	186.8	213.8	208.6	359
8	360	25	10	18.3	CA	12.32	1.19	8.61	3.28	1.35	185.8	209	226.3	292
9	380	25	10	18.3	CA	13.29	2.1	8.61	3.76	0.97	183.6	201.8	202.8	425
12	360	30	8	16.7	CW	10.76	0.7	7.37	5.84	2.13	207.2	247.8	275.8	407
13	360	30	8	18.3	CW	9.81	0.82	6.29	6.15	1.31	200.4	243.6	172.4	375
15	360	25	8	18.3	CW	9.79	1.05	6.61	2.77	1.36	214	225	280	355
16	360	25	8	16.7	CW	9.41	1.05	6.61	1.67	2.83	186.86	210.39	219.75	412

The response variables recorded above are the following:

BW = Bead width in mm

BH = Bead height in mm

BP = Bead penetration in mm

PTHAZ = HAZ with on plate side in mm

PPHAZ = HAZ width on pipe side in mm

VHN (PTHAZ) = Vickers hardness on HAZ of plate side in HV

VHN (WM) = weld metal hardness in HV

VHN (PPHAZ) = Vickers hardness on HAZ of pipe side in HV

7.10.1 Statistical Analysis Results

The data in Table 7.12 is used to develop mathematical models using regression analysis. Table 7.13 presents the ANOVA table for BW. This ANOVA table is presented for purposes of explaining the statistical analysis, and the rest of the ANOVA tables are given in Appendix F.

Table 7-13: ANOVA For Bead Width (BW)

Source	Sum of Squares	DoF	Mean Square	F-Value	p-value Prob > F	Remarks		
Model	17.78693	5	3.557386	10.25902	0.041927	significant	Std. Dev	0.588861
A-I	0.050205	1	0.050205	0.144783	0.728915		Mean	11.49
B-V	0.254294	1	0.254294	0.733349	0.454753		C.V. %	5.124984
C-S	0.009645	1	0.009645	0.027814	0.878155		PRESS	8.665858
D-FR	0.081225	1	0.081225	0.234242	0.661528		R-Sqd	0.944746
E-MODE	5.553693	1	5.553693	16.0161	0.027972		Adj. R-Sqd	0.852657
Residual	1.04027	3	0.346757				Pred. R-Sqd	0.539716
Cor Total	18.8272	8					Adeq. Precsn	7.433119

The Model F-value of 10.26 implies the model is significant. There is only a 4.19% chance that an F-value this large could occur due to noise. In this case factor ‘E’ is significant. Note that the factors on the first column of Table 7.13 are linked back to Table 7.12. The difference between ‘Adjusted R-Squared’ and ‘Predicted R-Squared’ values is not too big, but could have been closer. "Adeq Precision" measures the signal to noise ratio. A ratio greater than 4 is desirable. The ratio of 7.433 indicates an adequate signal. This model can be used to navigate the design space.

Sum of squares due to error (SSE) is also referred to as summed square of residuals and it measures the total deviation of the response values from the fit. A good result is a value closer to zero. *R-Squared* is a ratio of the regression sum of squares to the total sum of squares. A good result is A value closer to one. *Adjusted R-Squared* is the R-Square value adjusted based on residual degrees of freedom. A value closer to unity indicates good result.

The Model for BH has a F-value of 3.38, which implies the model is not significant relative to the noise. There is a 17.23 % chance that an F-value this large could occur due to noise. In this case there are no significant model terms. The "Adeq Precision" ratio of 5.064 is greater than 4 and indicates an adequate signal. The model can be used to navigate the design space. The BP model is also insignificant. Only factor 'E' is significant. The model has adequate signal though. PPHAZ model is also not significant; with an adequacy ratio of only 3.9, this model does not have an adequate signal to be used to navigate the design space. The PTHAZ model is not significant and none of the model terms are significant. The model is however adequate to be used for navigating design space. The VHN (PPHAZ) model is insignificant and inadequate, whereas the VHN (WM) is insignificant and adequate, and the VHN (PTHAZ) is not significant and not adequate. The residual stress model is not significant on the plate side (PTRS), but the model is adequate. The PPRS model is adequate and significant.

Table 7-14: Summary of Significant Model Terms

Response	Model & p-value	Active Effect & p-value	Adequacy
BW	0.0419	E (p = 0.0280)	Adequate
BH	0.1723		Adequate
BP	0.0773	E (p = 0.0210)	Adequate
PPHAZ	0.2648	B (p = 0.0481)	Inadequate
PTHAZ	0.1694	D (p = 0.0557)	Adequate
VHN(PPHAZ)	0.5353		Inadequate
VHN(WM)	0.1058	B (p = 0.0541)	Adequate
VHN(PTHAZ)	0.9717		Inadequate
PTRS	0.2647	A (p = 0.0672)	Adequate
PPRS	0.0479	A (p = 0.0175)	Adequate
		B (p = 0.0236)	
		C (p = 0.0745)	
		E (p = 0.0092)	

Table 7.14 gives a summary of significant model terms, and those with p-values closest to 0.05. Out of ten response models, two have significant model p-values, four have significant active effects, and seven are adequate. The most active factors seem to be 'MODE' and 'Voltage', given their frequency of appearance in Table 7.14.

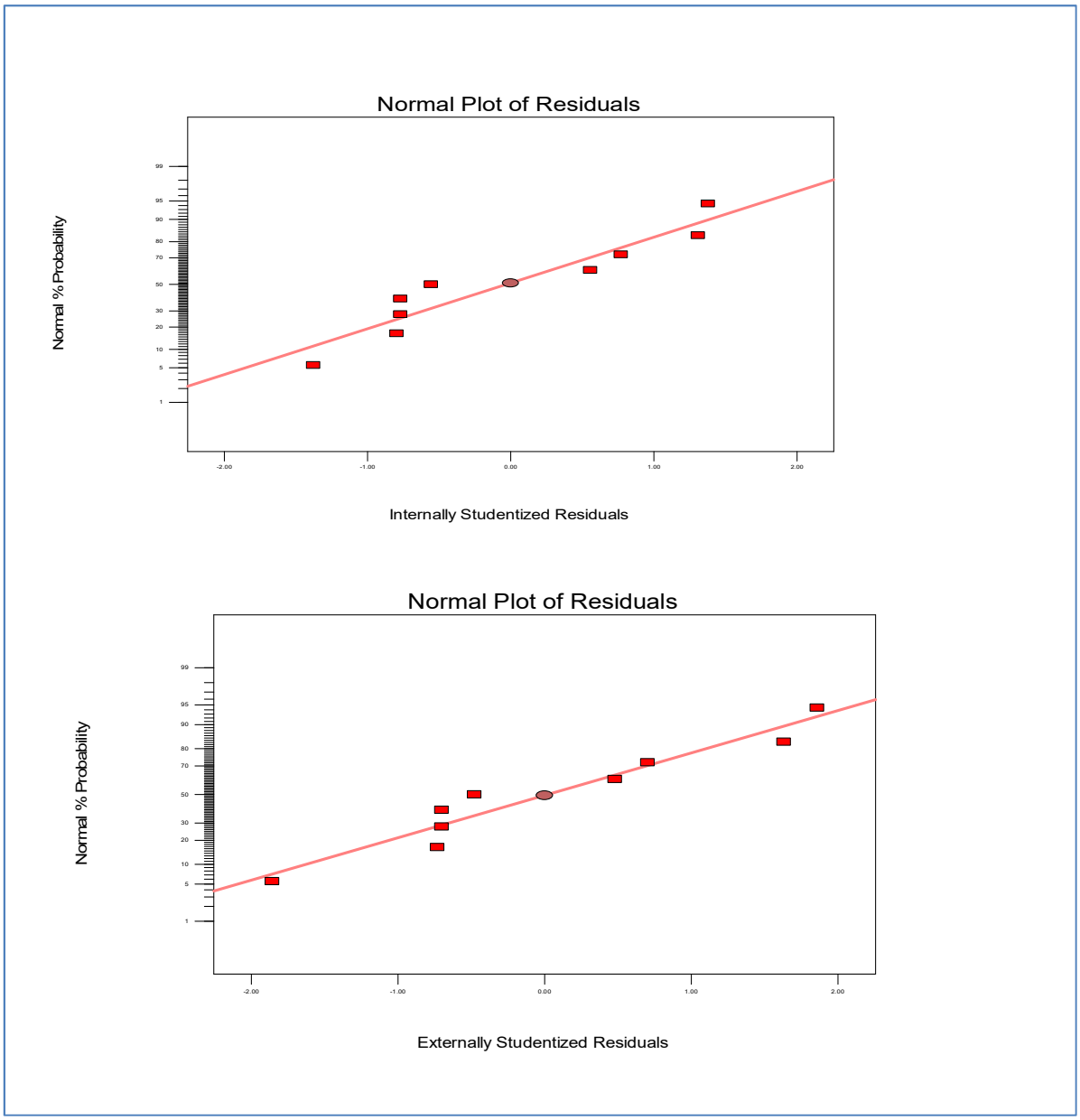

Figure 7-55: Normal Plot of Residuals for BW

The BW normality plot shown in Figure 7.55 shows that the residuals are relatively normal. The 'externally studentised residuals' show that there are no significant outliers. Only the two significant models' plots were considered here.

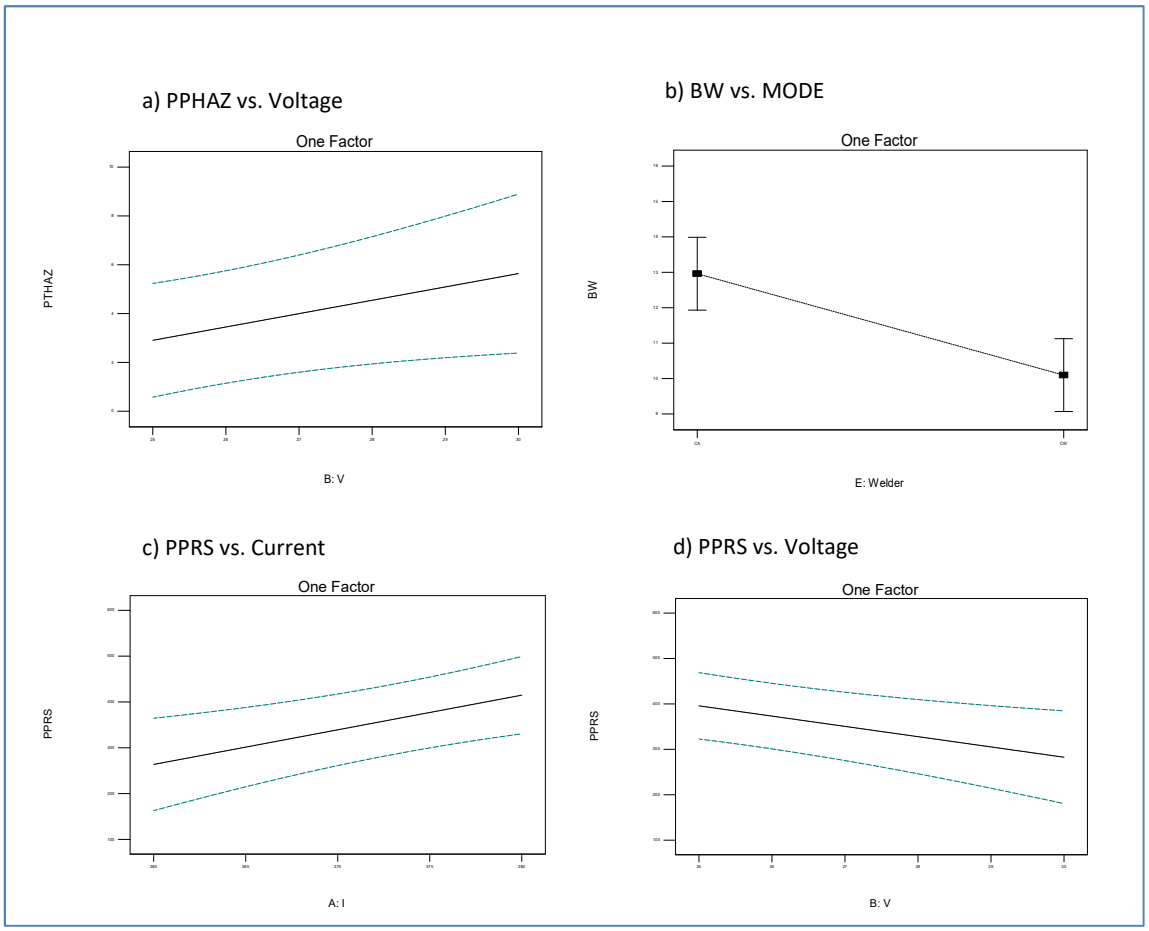

Figure 7-56: One Factor Plots for Active Effects

Figure 7.56 shows the one factor correlation curves for the active effects of the significant models. The proportional relationship between PPHAZ and voltage is clear; and since voltage directly affects heat input, it can be deduced that PPHAZ is directly affected by heat input. Bead width is affected by the categorical factor "MODE". The residual stress on the pipe side varies proportionally with current and inversely with voltage.

The following equations are presented for optimisation:

The following objective equations were developed:

$$BW(CA) = 9.491 + 0.0107I + 0.805V + 0.0468S - 0.178FR \quad \textbf{(7.13)}$$

$$BW(CW) = 6.627 + 0.0107I + 0.805V + 0.0468S - 0.178FR \quad \textbf{(7.14)}$$

$$BH(CA) = -3.569 + 0.0187I - 0.0702V - 0.0677S + 0.0375FR \quad \textbf{(7.15)}$$

$$BH(CW) = -4.021 + 0.0187I - 0.0702V - 0.0677S + 0.0375FR \quad \textbf{(7.16)}$$

$$BP(CA) = 28.215 - 0.0361I + 0.0833V - 0.206S - 0.3375FR \quad \textbf{(7.17)}$$

$$BP(CW) = 24.976 - 0.0361I + 0.0833V - 0.206S - 0.3375FR \quad \textbf{(7.18)}$$

$$PTHAZ(CA) = 11.94 + 0.00996I - 0.0434V - 0.0205S - 0.7156FR \quad \textbf{(7.19)}$$

$$PTHAZ(CW) = 12.20 + 0.00996I - 0.0434V - 0.0205S - 0.7156FR \quad \textbf{(7.20)}$$

$$VHN(WM)CA = 250.4 - 0.44I + 4.23V - 5.02S + 3.253FR \quad \textbf{(7.21)}$$

$$VHN(WM)CW = 257.8 - 0.44I + 4.23V - 5.02S + 3.253FR \quad \textbf{(7.22)}$$

$$PTRS(CA) = -457.58 + 4.05I - 1.34V - 14.55S - 27.8FR \quad \textbf{(7.23)}$$

$$PTRS(CW) = -429.28 + 4.05I - 1.34V - 14.55S - 27.8FR \quad \textbf{(7.24)}$$

$$PPRS(CA) = -2344.4 + 7.56I - 22.63V + 42.59S + 7.19FR \quad \textbf{(7.25)}$$

$$PPRS(CW) = -2101.78 + 7.56I - 22.63V + 42.59S + 7.19FR \quad \textbf{(7.26)}$$

7.10.2 Multi-Objective Optimisation Results

Simultaneous optimisation of all the objective functions produced a set of 43 non-dominated solutions ranked at unity in Figure 7.57. The other five solutions ranked second on the histogram are dominated, and hence do not form part of the Pareto front. MATLAB plots two functions at a time within the Pareto front. Some of the Pareto curves are shown in Figure 7.58.

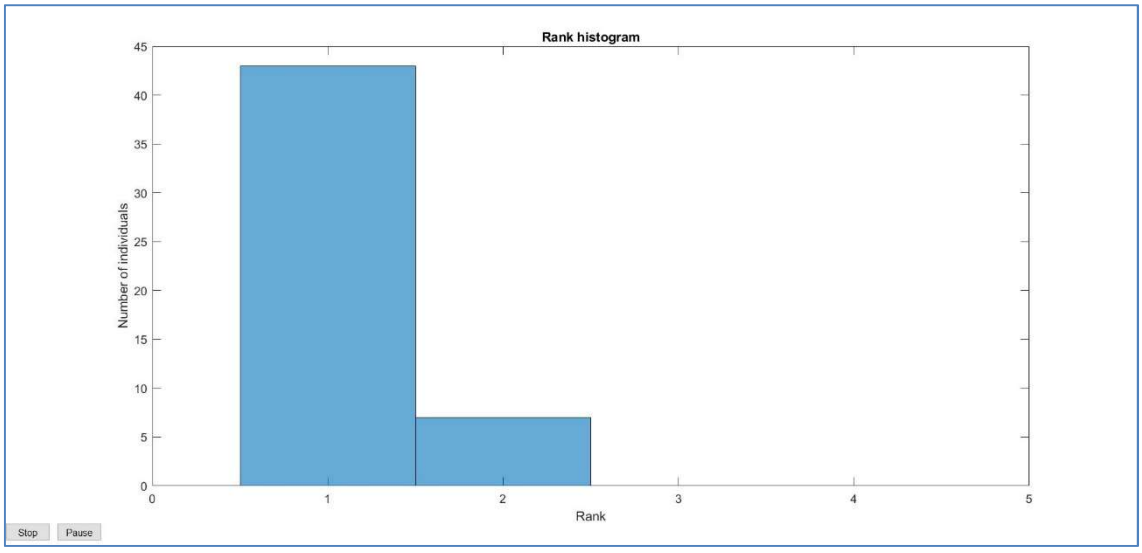

Figure 7-57: The Rank Histogram for Optimal Solutions

a) BH vs. BW

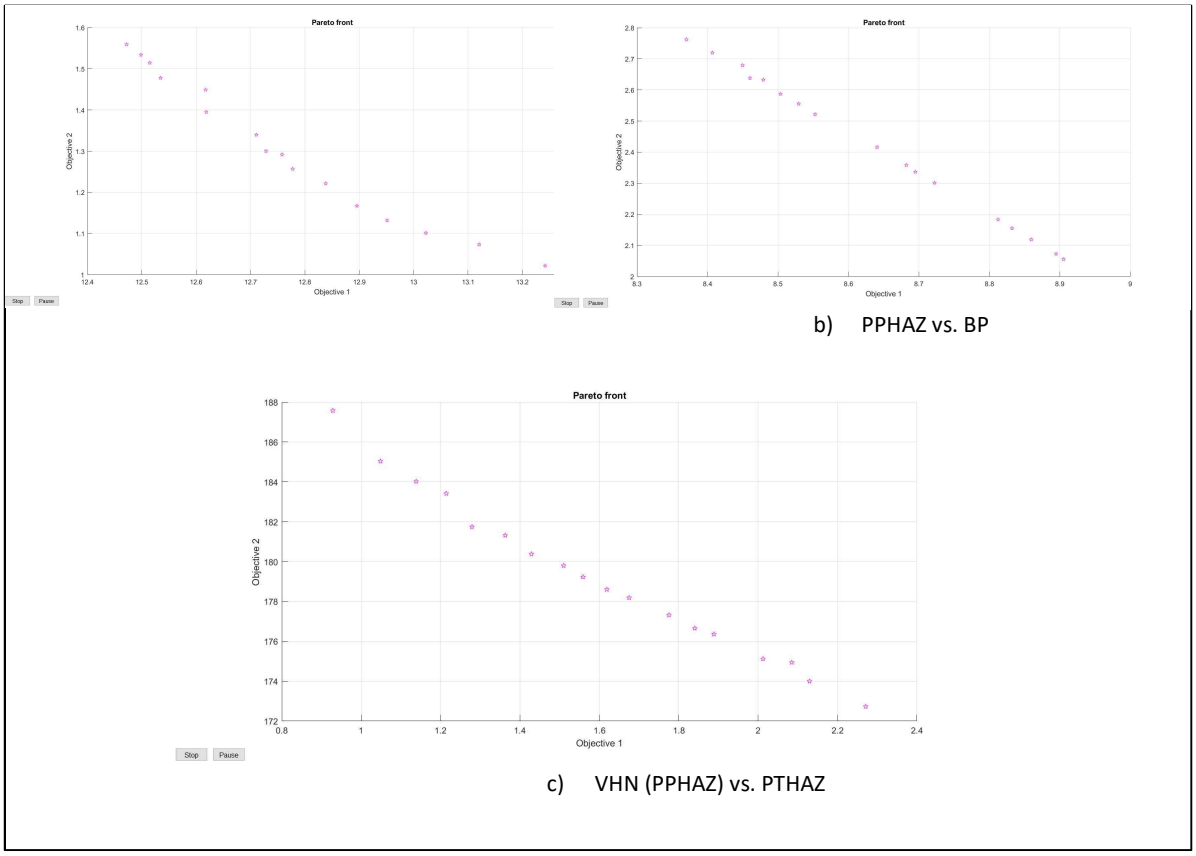

b) PPHAZ vs. BP

c) VHN (PPHAZ) vs. PTHAZ

Figure 7-58: Pareto Front for a) BH vs. BW, b) PPHAZ vs. BP, c) VHN PPHAZ vs PTHAZ

Observing the curves in Figure 7.58 and Figure 7.59, one can see that members of the Pareto set lie within the Pareto front curve and that there are no significant outliers. This demonstrates that the Pareto set comprises non-dominated solutions whose optimality has been verified by the multiobjective optimisation algorithm.

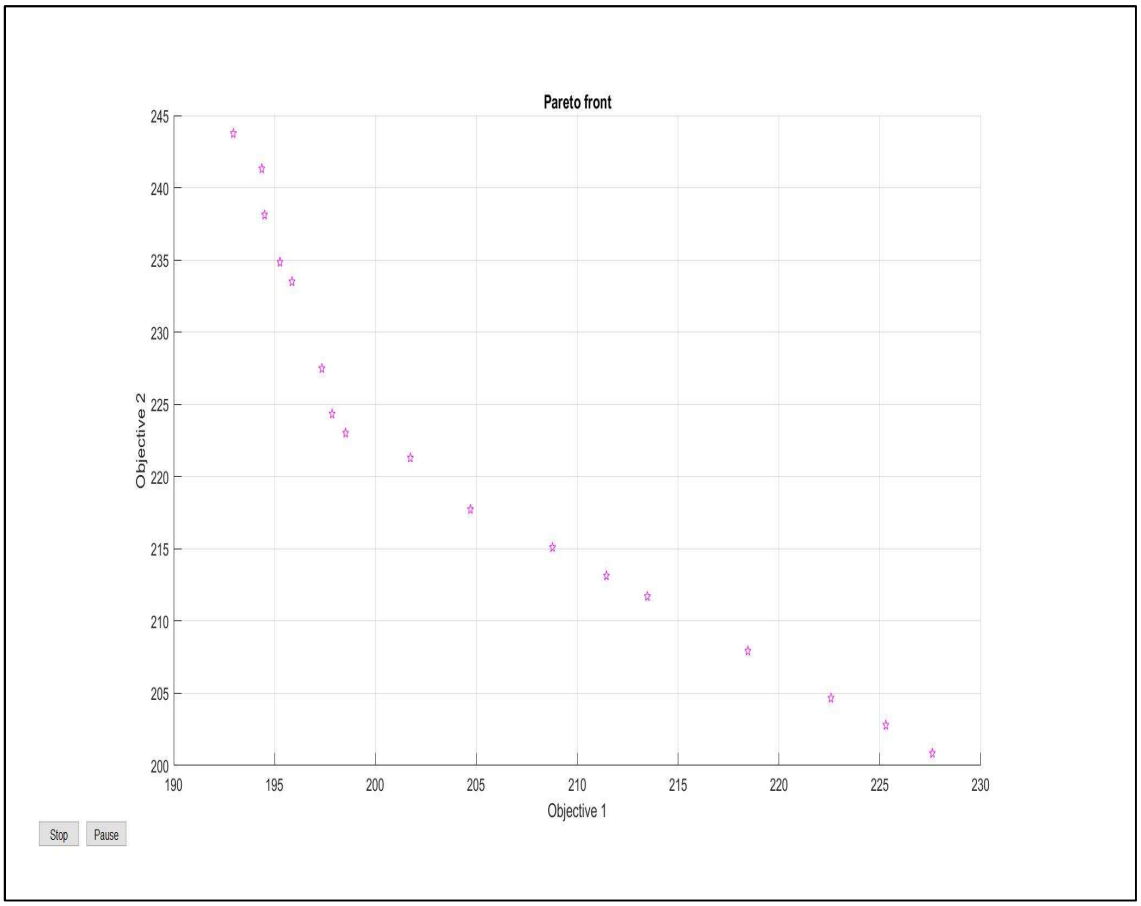

Figure 7-59: Pareto Front for VHN (PTHAZ) vs. VHN (WM)

As mentioned above, the Pareto front is a curve of non-dominated solutions. The MOGA searches the solution space and brings forth a set of optimal solutions. Optimization Settings for CA with a combination of Multi Objective Equations VHN(PTHAZ), VHN(WM), VHN(PPHAZ), PTRS and PPRS are presented in Table 7.15. Note that the full set of optimal solutions is given in Appendix H below; the list of 10 solutions given in Table 7.15 is in no particular order since all the solutions are equally optimal. The sample of solutions presented in Table 7.15 are all from the CA mode setting, whereas the full pareto set have both CW and CA solutions.

Table 7-15: Members of the Pareto Set

Solutions	Current (I)	Voltage (V)	Speed (S)	Feed Rate (FR)
1	362.9764	29.7644	8.3396	16.7304
2	363.1314	29.9996	8.8308	18.2983
3	362.7722	25.0994	8.2192	18.2292
4	362.9360	29.9881	8.2209	18.2987
5	364.7993	28.8771	8.4667	16.7333
6	365.6500	27.5152	8.8202	18.2931
7	374.1201	25.0571	9.7722	18.0495
8	377.9203	25.0333	9.7808	16.8932
9	379.1523	25.0527	9.8088	18.2519
10	379.1073	25.0628	8.4838	18.2810

A closer look at some parametric combinations given in Table 7.15 reveals that some samples that have presented better results in the analysis above have similar parametric combinations. These include Samples 6, 7 and 9 who's welding parametric combination matches closely those that are highlighted in Table 7.15. The optimal solutions therefore presented by the parametric optimisation process of the MOGA is in agreement with those that were obtained through experiments.

7.11 Concluding Remarks

The results for temperature recording, residual stress measurements, bead geometry measurements, microstructure measurements, hardness tests and fatigue tests have been tabled. Furthermore, numerical analysis results as well as parametric optimisation have been presented in this chapter. The thermal imaging technique successfully provides continuous temperature measurement that is able to characterise the thermal cycle of the arc welding process. Neutron diffraction provides through-thickness stress measurements that are in line with similar studies in the literature. Tension hoop stresses are shown to be equal or greater than the material yield strength. The magnitude of stresses can be correlated to the parametric combination used to fabricate each specimen. Bead geometry measurement results are used to determine the parametric combination that produced the most optimal bead geometric parameters. The microstructure of the HAZ is shown to be martensitic, where the weld metal is mainly composed of proeutectoid ferrite. Hardness values of the PTHAZ are shown to be the highest; however both measured and calculated VH values are smaller than the cut-off point of 350 for hydrogen-induced cracking.

Further analysis of the results from experiments reveals that there is a cause and effect relationship between welding induced residual stress and fatigue properties of the welded

structure. Tensile hoop stress has an adverse effect on fatigue life of the welded structure. Consistency between results from the residual stress measurements, bead geometry measurements and fatigue tests in terms of samples that perform comparatively better than others have been demonstrated in the above analysis. The results from the numerical model have been shown to be in reasonable agreement with experimental results. Optimisation using MOGA produced results that are in line with experiments and simulations.

CHAPTER 8: CONCLUSIONS AND RECOMMENDATIONS

The subject of the present study is the fatigue behaviour of the nozzle-shell joint of carbon steel pressure vessel under welding induced residual stress resulting from parametric combination of the SAW process. The importance of this kind of study was discussed in Chapter 3 in detail; and subsequent chapters sought to demonstrate such importance. The study successfully employs the hybrid methodology comprising experimental work, numerical methods and mathematical programming to determine the effect of residual stress on fatigue life of welded structures with specific emphasis on the welding parameters that are responsible for generation of the residual stress fields in the multi-pass circumferential nozzle-shell weld joint. This final chapter sums up how the objectives of the study have been fulfilled through answering the research questions. The chapter also addresses the contribution of the present study to the body of knowledge of the research field of interest, including the contribution of published research work. Furthermore, the chapter recommends further work in the field of interest in order to enhance the body of knowledge.

8.1 Factors that Affect WRS

The literature review presented in Chapter 2 discussed various factors that affect welding-induced residual stress conditions of the nozzle-shell joint that is fabricated using the SAW process. The lessons learned from reviewing the current state of the art within the field of interest can be represented through a proposed classification framework illustrated in Figure 8.1. The diagram describes sequential components of three interacting processes, namely: welding process flow, welding influential factors and mitigation techniques. The welding process commences when welding preparatory work occurs, and terminates when welding is finished and the completed weld-piece is presented. The influential factors corresponding to each step of the welding process are enlisted below the respective process steps. The one-directional arrow between the two blocks indicates that each process step affects factors directly below it. In a similar manner, mitigation techniques below each process step will affect the influential factors directly above them. The ‘outcomes’ column at the end demonstrates that the condition of the weld-piece is a function of the completed welding process and the quality and integrity of the weld. In the case of the present study, quality is measured by the favourable magnitude and distribution of residual stresses, while integrity is evaluated through the favourable weld fatigue properties. The utility of the proposed

framework is that, given a particular stage in the welding process, one would know which influential factors are applicable, and which corresponding mitigation techniques to use. The proposed classification framework can therefore be used to determine applicable influential factors and corresponding mitigation techniques for WRS throughout the SAW welding process.

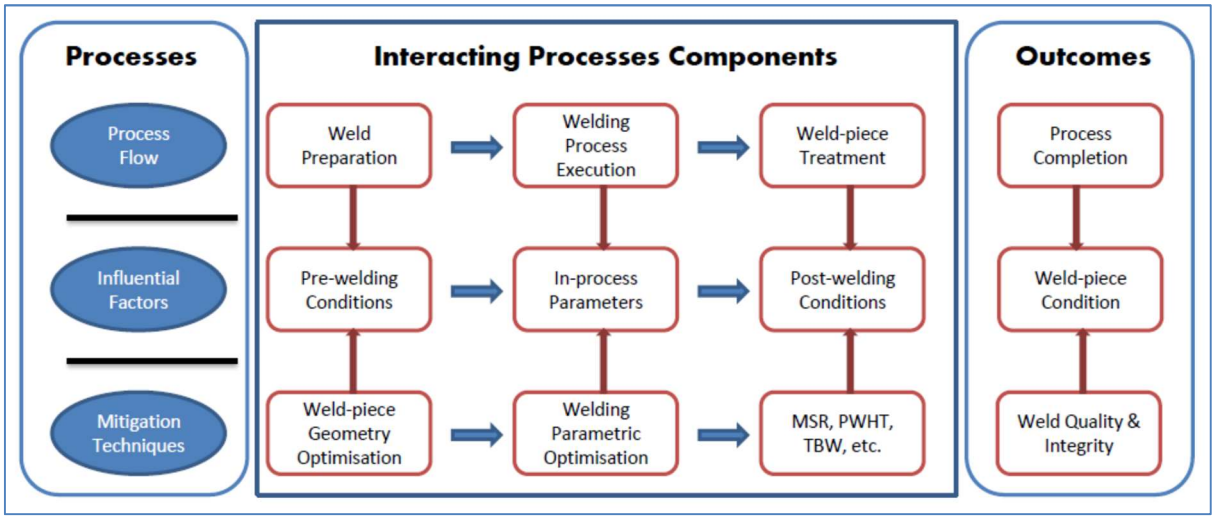

NB: MSR = Mechanical stress relief; PWHT = post weld heat treatment; TBW = temper bead welding

Figure 8-1: Proposed Classification Framework

8.2 Temperature Characterisation Through IR Imaging

Thermal imagery characteristics of the SAW process, including temperature histories, inter-pass time, and cooling period have been clearly demonstrated in the present study. The readings taken at specific fixed locations within the rotating weld specimens and plotted accordingly, are easily verified against the thermal images produced by the camera. Thermal imaging provides continuous measurement of temperatures, thereby allowing Temperature-Time graphs to be plotted incorporating the cooling periods during welding cycles. This allows for better understanding of thermal behaviour of the weld pool during welding cycles. Furthermore, continuous temperature measurements, as well as the ability of the IR Imaging technique to measure a wider area of interest, also provide more accurate means to calibrate simulation models using recorded experimental temperatures. This becomes quite useful in a process like SAW, where the weld pool is insulated by the flux and hence direct temperature measurements are difficult. Any point in the weld specimen can be identified and used to calibrate the model as long as the temperature of the same point is used in both the physical weld specimen and the numerical model. The correlation between recorded temperatures and the FEA model bears evidence to the reliability of thermal imaging as a temperature recording technique. The study has successfully shown that thermal imaging is a reliable technique to characterise temperature distribution during

arc welding thermal cycles. The temperature history curves presented are consistent with similar studies in literature.

8.3 Distribution of WRS Fields

The stress distribution of nozzle-shell welded joints for pressure vessel applications was studied. A number of experiments were conducted under various welding parametric combinations, thereby producing specimens with different characteristics. ND stress measurements showed that the hoop stresses are highly tensile and their magnitude is close to or more than that of the yield strength of the filler material in the WCL. The magnitude of stresses decreases as the distance away from WCL increases; and eventually they change direction to compressive. The highest observed hoop stress in the experiments was 558 MPa on the pipe side of Sample 15, which is higher than the yield strength of the filler metal. The axial and radial stresses are much smaller compared to hoop stresses. Considering the net effect of the various components the triaxial stresses indicate that the samples with the lowest net WRS are 4, 7 and 8 (in that order) based on the stress distribution found at the plate side of the weld specimens. It is interesting to note that all the said specimens were generated using the CA mode of parametric settings of the welding machine. Axial and radial stresses of Sample 4 are highly compressive closer to the weld toe of the plate side, which is what brings the net value of the total triaxial stress of the sample down. The direction of loading is an important aspect to consider when one evaluates the probable effect of residual stress fields on service life of the welded structure. Some of the mentioned samples also showed favourable results when their weld geometry was used as a criterion to evaluate their weld quality. The measured stresses are also successfully used to calibrate finite element models for further analysis of thermo-mechanical behaviour in the selected types of weld joints. Neutron diffraction is an effective method to measure through-thickness residual stress, which other methods such as hole-drilling are unable to do.

8.4 Numerical Analysis

In the present study, a non-linear time-dependant thermal elastic-plastic analysis of a moving heat source was performed to predict the thermal and mechanical behaviour of the weldment and HAZ. The solution of non-linear transient problem is divided into two parts. Firstly, a thermal analysis (incorporating phase transformation effects) was performed to predict the temperature history of the model. Secondly, the predicted temperature fields were applied as input for the subsequent mechanical analysis. The generated 3D model generated using MSC Marc software adopted a Gaussian double ellipsoid heat source to model thermal strains arising from the weld thermal cycle. The presented temperature history plots for different samples were compared with results

from experiment and showed good agreement. The minor differences between simulation and experimental results were considered fair for the subject under investigation.

The mechanical analysis produced residual stress distribution curves whose profile is comparable with that of experimental results. The pronounced differences in some areas between simulation and experimental results could be accredited to pertinent differences in the characteristics of an idealised simulation environment and the realistic experimentation process. The highest magnitude of distortion is visible around the centre of the plate where the constraint is decreased, given the manner in which the specimen was mounted on the turntable. The value of 0.22 mm is considered fair given the size and the material of the weld specimen. The developed numerical model adequately represents the welding process for the conditions under investigation in the present study, and can be used to study the various process parameters of the process.

8.5 Microstructural Characteristics

A number of studies have shown that phase transformation (especial at rapid cooling rates) results in volumetric changes that affect the generation and magnitude of residual stresses in welded structures. The present study provides an extensive analysis of the microstructure for the PTHAZ, WM, PPHAZ and PM regions of each weld specimen. It is shown that the HAZ regions have generally martensitic microstructures whereas the weld regions' microstructure mainly comprise proeutectoid ferrite. This situation is expected since the HAZ regions are subjected to higher cooling rates than the weld metal given the former's proximity to cooler parent metal. This finding augments the modelling decision of including the metallurgical effects into the FEA model. Phase transformation is therefore an important factor whose effect on residual stress generation should be considered under conditions such as the ones applicable in the present study.

8.6 Weld Properties

Hardness is an important characteristic that influences the welded structure's susceptibility to hydrogen-induced cracking (HIC). The present study performed various hardness tests on a number of samples and presented the results for further analysis. The results show that for most specimens PTHAZ has the highest hardness values, followed by WM and then PPHAZ. The results of hardness are in line with the microstructure analysis which showed that the HAZ region contains martensite, which is harder than other phases contained in the weld. The highest observed hardness value is 280 VH, and the maximum calculated hardness value is 243 VH. Both values are significantly lower than the cut-off HIC value of 350 HV. Samples 9, 8 and 7 are shown to have the lowest hardness values in the HAZ and WM regions. This supports the analysis done using weld bead geometry and residual stress fields. Weld properties are shown to be good

indicators of weld bead quality, and hence these results can be used to assess the welding parameters that will produce beads with favourable weld properties.

8.7 Fatigue Properties

Fatigue tests were performed on each of the five samples produced using the CA mode settings. Two specimens were tested for each sample, and then an average of the two tests was taken. It is shown through the tabulated results that Sample 4 has the highest number of cycles to failure and also the lowest residual stress. Sample 6 has a larger amount of residual stress compared to Sample 4, and also a corresponding lower number of cycles. Sample 7 has the second highest number of cycles and also second lowest residual stress. Sample 9 has the highest residual stress the second lowest number of cycles. This proves therefore that residual stresses affect fatigue life of a welded pressure vessel. The tensile hoop stresses in the circumferential nozzle-shell joint shorten fatigue life of the welded structure. Understanding the generation, profile and magnitude of residual stress fields during the SAW process is therefore the first step towards enhancement of fatigue life of welded joints. The second step is to understand how to contain, reduce or mitigate the effect of WRS in order to enhance fatigue life; this includes choosing an optimal parametric combination that will ensure minimal tensile residual stresses in the weld. These results are in line with numerous examples in the literature discussed above, which asserts that welding induced residual stress creates mean stress effects that affect fatigue properties of welded structures.

8.8 Optimal Parameters

The optimisation of input welding parameters is performed using a combination of DoE techniques and evolutionary algorithms. Statistical analysis reveals the significance of various response models, and regression is used to generate objective functions for adequate response variables. The objective functions for all but PPHAZ, VHN (PPHAZ) and VHN (PTHAZ) are successfully generated. The one-factor plots reveal that the welding mode is the most significant factor that affects the response variables. Residual stress (PPRS), bead width (BW), and bead penetration (BP) are all affected by the welding ‘MODE’. The multiobjective genetic algorithm is used to simultaneously optimise the objective functions in order to determine the Pareto front. The Pareto set has a number of members that are all optimal solutions. Comparison between the members of the Pareto set and the parametric combinations of the DoE matrix reveals that some of the best weld beads were produced using welding parameters aligned to the Pareto optimal solutions. The produced objective functions as well as the optimal parametric combinations can therefore be used in similar welding applications to produced welds of acceptable weld bead geometry, good weld properties and low residual stresses.

8.9 Response to the Research Questions

The above conclusions provide a summary of the responses to the research questions that are presented in Chapter 3 above. The research questions relate to the residual stress fields distribution, the welding distortions, the factors that influence WRS, weld mechanical properties, weld bead geometry and fatigue properties. The above discussion has successfully addressed all the said research questions.

8.10 Recommendations for Future Work

The present study has successfully addressed some of the important questions within the subject of the relationship between SAW parameters, welding-induced residual stress, and fatigue properties of nozzle-shell weld joints in pressure vessels. It is therefore recommended that the information tabled in the present study be used in industrial applications in order to improve fatigue performance of nozzle-shell joints in pressure vessels. It is recommended that the provided information is included into the standard operating procedures for pressure vessel fabrication, repairs and preventive maintenance. It is also recommended that the techniques discussed in this study are employed to predict the fatigue life of the pressure vessel structures under specific operating conditions.

Some of the challenges experienced during experimentation included the proper calibration of the thermal camera within the required temperature thresholds, the positioning of the camera vis-a-vis the rotating weld-piece for optimal temperature recordings, and the insulating effect of the flux in SAW in the process. It is recommended that future studies look into improving such aspects.

The FEA code used in this study is MSC Marc software. MSC Marc is generic simulation code that does not have some of the advanced welding simulation capabilities found in other codes such as ABAQUS and ANSYS. User subroutines for the input heat flux model and the phase transformation model would improve the accuracy of the entire simulation model. However, such capabilities do not exist in MSC Marc. It is recommended that future studies consider this limitation and rectify it accordingly.

Further to the above, it is recommended that future studies are conducted within the following subjects of interest in order to enhance the work done in this study:

a. The link between welding residual stress and fatigue life and the link between residual stress and welding parameters have been shown in the above work. It would be useful if the link between fatigue life of a welded structure and each of the welding input

parameters could also be mapped out through further studies. This would ensure that researchers and practitioners are able to predict the outcome of the fatigue properties based on the level of variance of specific welding parameters.

b. The above study did not look at the effect of internal pressure. In real life pressure vessels operate under positive or negative pressures and hence considering the impact of such pressure on the stress state of the welded structure could provide further knowledge that can be used for pressure vessel welding applications. This study could be done for several pressure ranges that are usually found in industrial applications.
c. Pressure vessel design codes provide guidelines on how residual stresses should be incorporated when predicting fatigue lives of pressure vessels. It would be useful to conduct a study that compares what the codes provide and what experiments and analysis reveal in the field. This would show whether the provisions of the codes are still relevant or not.

8.11 Contribution of Published Work

Five academic articles were generated as a result of work done in this thesis. Below is a brief overview of the subject matter of each academic publication as well as their contribution to the research body of knowledge.

PAPER 1

Title: *Factors That Affect Welding-Induced Residual Stress and Distortions in Pressure Vessel Steels and Their Mitigation Techniques: A Review*

This paper comprises a review of current literature with regards to the factors that have an impact on the generation of residual stress, and how such impact can be mitigated. The objective of this review is to organise such literature according to the specific areas of analysis in order to enhance access thereto and elucidate relevance thereof for purposes of reference work and further studies. The paper specifies three categories of influential factors, namely, pre-welding conditions, in-process parameters and post-welding conditions. It is shown that pre-welding conditions, such as the choice of welding process, must in line with the nature of materials to be welded, operational application of the structure, and trade-offs between service life and production costs. Heat input (which is the function of arc voltage, welding current and travel speed) is the most influential machine-related in-process parameter in residual stress generation during welding. It is also observed that when applying mitigating factors, care should be taken not to exacerbate the residual stress situation through sub-optimal parametric set-up.

The contribution of this paper to the body of knowledge is twofold. Firstly, it provides a reference guide for applicable literature, which provides researchers with a repository of references. Secondly it provides a classification framework, which is a valuable tool in assisting researchers to easily match the category of influential factors to applicable mitigation techniques. This classification framework had not been done before.

PAPER 2

Title: *Characterisation of Submerged Arc Welding Using Infrared Imaging Technique*

In this paper, IR thermography is used to record the temperature distribution during a submerged arc welding (SAW) process experiment; and to validate the numerical model developed to simulate the said SAW process of a multi-pass circumferential weld on pressure vessel steel. The Flir Short Wave Infrared Radiometer (FSIR) is used during SAW experiments using a welding unit from ESAB. The weld pool and the surrounding area are continuously monitored and their temperature recorded through the use of a thermal camera. The recorded temperatures are plotted against time on Temperature-Time curves to reveal the temperature profiles of each welding cycle. Comparison of the resultant temperature profiles with those of the numerical model show good agreement. It is therefore concluded that temperature measurement through thermal imaging is a suitable method to characterise the temperature distribution of the SAW multi-pass circumferential weld as well as to effectively validate the numerical model developed to simulate the said welding process.

The contribution of this paper is that it provides an alternative temperature measurement method, which is IR thermal imaging. Although this method had been used before to measure temperature during welding, to the author's knowledge it had not been used for the kind of joint and welding process discussed in the paper. The validation of the simulation model using experiments adds value to the study performed in this paper.

PAPER 3

Title: *Characterization of Welding-Induced Residual Stress Using Neutron Diffraction Technique*

The present paper applies the Neutron Diffraction technique to formulate the stress field distribution of a nozzle-to-shell weld joint of a pressure vessel. A number of experiments are conducted using the Submerged Arc Welding (SAW) process at various parametric combinations to develop a number of specimens with different stress profiles. It is shown that the hoop stresses close to the weld centre line (WCL) are highly tensile and have values close to the yield strength

of the material. The ideal parametric combination is also determined based on the results with lowest stresses. The results obtained in this study are congruent with the results of similar studies in literature.

The contribution of the paper to the body of knowledge is in the application of ND technique to measure the nozzle-shell full penetration multipass weld bead. This type of joint is difficult to measure using the ND technique given its awkward geometry. The application of experimental results to obtain optimal welding parameters is also a novelty of the present paper. The obtained results can be used in similar applications in the future, or as the basis for additional work.

PAPER 4

Title: *A 3D Submerged Arc Welding Numerical Model to Estimate Welding-Induced Residual Stress in a Nozzle-Shell Circumferential Weld Joint of High Strength Carbon Steel*

The present paper proposes a 3D finite element sequentially-coupled thermo-mechanical model for prediction of residual stress in a nozzle-to-shell multi-pass weld bead. The developed model is successfully validated using experimental work. IR imaging is used for temperature characterisation and Neutron Diffraction is used for residual stress measurement. The comparison between measured and predicted values show reasonably good agreement, thereby proving the numerical model to be suitable for predicting residual stress under the stated conditions. The magnitude of the hoop residual stress reaches values that are equal to or larger than the yield strength of the material. This is in line with similar studies reported in the literature. The magnitude of hoop stress reaches its peak closer to the weld centre-line (WCL) and decreases as the distance from the WCL increases.

The contribution of the paper is to provide an FE model for the specific conditions that were studied in this particular case. Although numerical modelling is used extensively in welding applications, most weld joints in the literature are either bead-on-plate or bead-on-joint; the nozzle-shell joint has not been studied much in the past. The work presented in this paper can therefore be used as a basis for further research.

PAPER 5

Title: *The Effect of Welding-Induced Residual Stress on Fatigue Strength of Nozzle-Shell Weld Joint of High Strength Carbon Steel*

This paper considers the effect that welding induced residual stress has on fatigue properties of a multipass nozzle-shell weld. A number of welding specimens are prepared using the submerged arc welding process. Neutron diffraction is used to measure the multiaxial residual stress field of each specimen, and stress distribution curves are formulated using the results. The specimens are then subjected to fatigue testing using a servo-hydraulic fatigue testing machine. The cycles to failure are plotted against applied load for each specimen. All specimens failed at the weld toe, where stresses were found to be highly tensile. Specimens with higher tensile residual stresses failed at fewer cycles compared to those with lower stresses. The study demonstrates that tensile residual stress detrimentally affects fatigue life of a welded structure.

The contribution of the paper is in the linking of residual stress and fatigue life in a cause-and-effect relationship. While some engineering standards have suggested empirical formulae to incorporate the effect of residual stress on fatigue life, there are still few published studies experiments performed to generate empirical evidence of the cause-and-effect relationship between the two parameters.

8.12 Originality of the Present Work

The work presented and discussed in this thesis is the author's original work. The experiments performed in various laboratories over a number of years have resulted in the data collected, analysed and presented herein. No component of this work has been used for other purposes other than towards the completion of this thesis report. No part of this work was taken from any existing source other than those that have been duly referenced herein.

REFERENCES

ADEYEYE, A.D.; OYAWALE, F.A. (2010). Multi-Objective Methods for Welding Flux Performance Optimisation. RMZ – Materials and Geo-environment, vol. 57(2), pp. 251-270.

AKHLAGHI, F.Z. (2014). Welding Simulation and Fatigue Assessment of Tubular K-Joints in High Strength Steel. PhD Thesis. Ecole Polytechnique Federale De Lausanne, Switzerland.

AL-MUKHTAR, A.M. (2010). The Safety Analysis Concept of Welded Components Under Cyclic Loads Using Fracture Mechanics Method. PhD Thesis. Technische Univesitat Bergakademie Freiberg.

ANCA, A.; CARDONA, A.; RISSO, J.; FACHINOTTI, V.D. (2010). Finite Elements Modelling of Welding Process. Applied Mathematical Modelling – Article in Press. Available: www.elsevier.com/locate/apm (Accessed 18 November 2010.

ANDERSSON, B.A.B. (1978). Thermal Stresses in a Submerged Arc Welded Joint Considering Phase Transformations. Journal of Engineering and Technology, ASME, vol. 100, pp. 356-362.

ANDERSSON, J. (n.d.). A Survey of Multi-Objective Optimisation in Engineering Design. Available from EMOO Repository: http://delta.cs.cinvestav.mx/~ccoello/emoo (Accessed 10 January 2013).

ANL (2016). Thermal-Mechanical Stress Analysis of Pressurised Water Reactor Pressure Vessel and Nozzles Under Grid Load-Following Mode. Argonne National Laboratory (ANL) for the US Dept of Energy.

ASTM E647-15$^{\varepsilon 1}$. (2016). Standard Test Method for Measurement of Fatigue Crack Growth Rates. American Society for Testing and Materials.

BACK, J.G. (2017). Modelling and Characterisation of the Martensite Formation in Low Alloyed Carbon Steels. PhD Thesis. Lulea University of Technology, Sweden.

BAI, X.; ZHANG, H.; WANG, G. (2013). Improving Prediction Accuracy of Thermal Analysis for Weld-Based Additive Manufacturing by Calibrating Input Parameters Using IR Imaging. International Journal of Advanced Manufacturing Technology, vol. 69, pp. 1087-1095.

BALASUBRAMANIAN, V.; GUHA, B. (1998). Influence of Flux-Cored Arc Welded Cruciform Joint Dimensions on Fatigue Life of ASTM 517 F Grade Steels. International Journal of Pressure Vessels and Piping. Vol. 75, pp. 765-772.

BALASUBRAMANIAN, V.; GUHA, B. (2004). Fatigue Life Prediction of Load-Carrying Cruciform Joints of Pressure Vessel by Statistical Tools. Journal of Material Design, vol. 25, pp. 615-623.

BALOC, M.; GRBOVIC, A.; PETROVIC, A. (2015). Numerical Predictions of Crack Growth in a Pressure Vessel with Welded Nozzles. Structural Integrity and Life, Vol. 15(1), pp. 55-61

BANG, I.-W.; SON, Y.-P.; OH, K.H.; KIM, Y.-P.; KIM, W.-S. (2002). Numerical Simulation of Sleeve Repair Welding of In-service Gas Pipelines. Welding Journal, Dec. 2002, pp. 273-282.

BENYOUNIS, K.Y.; BETTAMER, A.H.; OLABI, A.G.; HASHMI, M.S.J. (2004). Predicting the Impact Strength of Spiral Welded Pipe Joints in Submerged Arc Welding of Low Carbon Steel. Proceedings of IMC21, September 2004, Limerick, pp. 200-210

BENYOUNIS, K.Y.; OLABI, A.G.; HASHMI, M.S.J. (2005). Effect of Laser Welding Parameters on the Heat Input and Weld Bead Profile. Journal of Materials Processing Technology. Vol. 164, pp. 978-985

BOZIC, Z. (2016). The Effect of Residual Stresses on Fatigue Crack Growth in Welded Stiffened Panels. 16th International Conference on New Trends in Fatigue and Fracture, May 24-27, Dubrovnik, Croatia.

BUCHELY, M.F.; GUTIERREZ, J.C.; LEON, L.M.; TORO, A. (2005). The Effect of Microstructure on Abrasive Wear of Hardfacing Alloys. Wear, vol.259, pp.52-61

BZYMEK, A.; CZUPRY, A.; FIDALI, M.; JAMROZIK, W.; TIMOFIEJCZUK, A. (2008) Analysis of images recorded during welding processes. Available: http://www.thermo.p.lodz.pl/qirt/abstracts/QIRT%202008-002.pdf (Accessed 17 September 2016).

CAINE, L.; FRAIN, E. (2016). Investigation of the ElectroPuls E3000 Testing Machine for Fatigue Testing of Structural Materials. DST-GROUP – TR – 3319. Department of Defence, Australia.

CANYURT, O.E. (2005). Estimation of Welded Joint Strength Using Genetic Algorithm Approach. International Journal of Mechanical Sciences. Vol. 47, pp. 1249-1261.

CHAN, B.; PACEY, J.; BIBBY, M. (1999). Modelling Gas Metal Arc Weld Geometry Using Artificial Neural Network Technology. Journal of Canadian Metallurgical Quarterly, vol. 38(1), pp.43-51.

CHAND, R.R.; KIM, I.S.; LEE, J.P.; KIM, Y.S.; KIM, D.G. (2013). Numerical and Experimental Study of Residual Stress and Strain in Multi-pass GMA Welding. Journal of Achievements in Materials and Manufacturing Engineering, vol. 57(1), pp. 31-37.

CHANDRASEKHAR, N.; VASUDEVAN, M.; BHADURI, A.K.; JAYAKUMAR, T. (2015). Intelligent Modelling for Estimating Weld Bead Width and Depth of Penetration from Infrared Thermal Images of the Weld Pool. Journal of Intelligent Manufacturing, vol. 26, pp. 59-71.

CHAUDHARI, S.B.; BELKAR, S.B. (2014). Experimental and Analytical Investigation in Circumferential Joint. International Journal of Mechanical Engineering and Information Technology, vol. 2(6), pp. 453-465.

CHEN, Z.; GAO, X. (2014). Detection of Weld Pool Width Using Infrared Imaging During High-Power Fibre Laser Welding of Type 304 Austenite Stainless Steel. International Journal of Advanced Manufacturing Technology, vol. 74, pp. 1247-1254.

CHOKKALINGHAM, S.; VASUDEVAN, M.; SUDARSAN, S.; CHANDRASEKHAR, N. (2012). Predicting Weld Bead Width and Depth of Penetration from Infrared Thermal Image of Weld Pool Using Artificial Neural Networks. Insight, vol. 54(5), pp. 272-277.

COELLO COELLO, C.A. (2009). A Tutorial on Multi-Objective Optimisation Using Metaheuristics. Available from EMOO Repository: http://delta.cs.cinvestav.mx/~ccoello/emoo (Accessed 10 January 2013).

COELLO COELLO, C.A.; LAMONT, G.B.; VAN VELDHUIZEN, D.A. (2007), Evolutionary Algorithm for Solving Multi-Objective Problems. 2nd Ed. Springer Science + Business Media, New York, USA. p. 800.

CORET, M.; CALLOCH, S.; COMBESCURE, A. (2002). Experimental Study of the Phase Transformation Plasticity of 16MND5 Low Carbon Steel Under Multiaxial Loading. International Journal of Plasticity, vol. 18, pp. 1707-1727.

CORREIA, D.S.; GONCALVES, C.V.; DA CUNHA JNR, S.S.; FERRARESI, V.A. (2003a). GMAW Welding Optimisation Using Genetic Algorithms. Presented at COBEF 2003 – II Brazillian Manufacturing Congress, 18 – 21 May 2003, Uberlandia, Brazil.

CORREIA, D.S.; GONCALVES, C.V.; DA CUNHA JNR, S.S.; FERRARESI, V.A. (2003b). Comparison Between Genetic Algorithms and Response Surface Methodology in GMAW Welding Optimisation. Journal of Material Processing Technology, vol. 160, pp. 70-76.

COSTA, L.; OLIVIERA, P. (n.d.). An Evolution Strategy for Multi-Objective Optimisation. Available from EMOO Repository: http://delta.cs.cinvestav.mx/~ccoello/emoo (Accessed 10 January 2013).

COULES, H.E.; COZZOLINO, L.D.; COLEGROVE, P.; GANGULY, S.; WEN, S.W.; PIRLING, T. (2013). Neutron Diffraction Analysis of Complete Residual Stress Tensors in Conventional and Rolled Gas Metal Arc Welds. Experimental Mechanics, vol. 53, pp. 195-204.

CULHA, O. (2014). Finite Element Modelling of Submerged Arc Welding Process for a Symmetric T-Beam. Materials and Technology, vol. 48(2), pp. 243-248.

DATTA, S.; MAHAPATRA, S.S. (2010a). Multi-objective Optimisation of Submerged Arc Welding Process. Journal of Engineering Research. Vol. 7(1), pp. 42-52

DATTA, S.; MAHAPATRA, S.S. (2010b). Simultaneous Optimisation of Correlated Multiple Surface Quality Characteristics of Mild Steel Turned Products. Intelligent Information Management, Vol. 2, pp. 26-39.

DATTA, S.; NANDI, G.; BANDYOPADHYAYA, A. (2009). Application of Entropy Measurement Technique in Grey Based Taguchi Method for Solution of Correlated Multiple Response Optimisation Problems: A Case Study in Welding. Journal of Manufacturing Systems. Vol. 28, pp. 55-63.

DENG, D. (2009). FEM Prediction of Welding Residual Stress and Distortion in Carbon Steel Considering Phase Transformation Effects. Materials and Design. Vol. 30, pp. 359-366.

DENG, D.; MURAKAWA, H. (2006). Prediction of Welding Residual Stress in Multi-Pass Butt-welded Modified 9 Cr-1Mo Steel Pipe Considering Phase Transformation Effects. Computational Material Science, Vol. 37, pp. 209-219.

DENG, D.; MURAKAWA, H. (2008). Finite Analysis of Temperature field, Microstructure and Residual Stress in Multi-Pass Butt-welded 2.25 Cr-1Mo Steel Pipes. Computational Materials Science, Vol. 43, pp. 681-695.

DERRINGER, G.; SUICH, R. (1980). Simultaneous Optimisation of Several Response Variables. Journal of Quality Technology, vol. 12 (4), pp. 214-219.

DEY, V.; PRATIHAR, D.K.; DATTA, G.L.; JHA, M.N.; SAHA, T.K.; BAPAT, A.V. (2008). Optimisation of Bead Geometry in Electron Beam Welding Using a Genetic Algorithm. Journal of Materials Processing Technology, vol. 209, pp. 1151-1157.

DHAS, E.R.; DHAS, J.H. (2012). A Review on Optimisation of Welding Process. Procedia Engineering. Vol. 38, pp. 544-554.

DHAS, J.E.R.; KUMANAN, S. (2011). Optimisation of Parameters of Submerged Arc Welding Using Non-Conventional Techniques. Applied Soft Computing, vol. 11, pp. 5198-5204.

DONG, P.; HONG, J.K.; BOUCHARD, P.J. (2005). Analysis of Residual Stresses at Weld Repairs. International Journal of Pressure Vessels and Piping, Vol. 82, pp. 258-269.

DUTTA, P.; PRATHAR, D.K. (2007). Modelling of TIG Welding Process Using Conventional Regression Analysis and Neural Network-based Approaches. Journal of Materials Processing Technology. Vol. 184, pp. 56-68.

EL-MIHOUB, T.A.; HOPGOOD, A.A.; NOLLE, L.; BATTERSBY, A. (2006). Hybrid Genetic Algorithms: A Review. Engineering Letters, 13:12.

ERICKSON, J. (2009). Algorithms: Lecture 21, NP-Hard Problems. Available: http://www.cs.uluc.edu/-jeffe/teaching/algorithms. (Accessed 21 May 2013)

FARAJIAN, M.; NITSCHKE-PAGEL, T.; SIEGELE, D. (2014). Welding Residual Stress Behaviour in Tubular Steel Joints Under Multiaxial Loading. Journal of Heat Treatment and Materials. Vol. 69(1), pp. 6-13.

FENG, Z. (2005). Processes and Mechanisms of Welding Residual Stress and Distortion. Woodhead Publishing in Materials, Cambridge England.

FONSECA, C.M.; FLEMING, P.J. (1993). Genetic Algorithms for Multi-Objective Optimisation: Formulation, Discussion and Generalisation. In Forrest (1993), pp. 416-423.

FRICKE, W. (2010). IIW Recommendations for the Fatigue Assessment by Notch Stress Analysis for Welded Structures. International Institute of Welding. IIW-Doc.XIII-2240r2-08/XV-1289r2-08.

FRICKE, W. (2012). IIW Guideline for the Assessment of Weld Root Fatigue. International Institute of Welding. IIW-Doc.XIII-2380r3-11/XV-1383r3-11.

FRIEDMAN, E. (1978). Analysis of Weld Puddle Distortion. Welding Journal Research Supplement, pp. 161-166.

GARCIA, C.; LOTZ, T.; MARTINEZ, M.; ARTEMEV, A.; ALDERLIESTEN, R.; BENEDICTUS, R. (2016). Fatigue Crack Growth in Residual Stress Fields. International Journal of Fatigue. DOI: 10.1016/j.ijfatigue.2016.02.020.

GHOSH, A.; CHATTOPADHYAYA, S.; SARKAR, P.K. (2011). Critical Analysis of Confounded Parameters of SAW Process. Procedia Engineering. Vol. 10, pp. 2786-2790.

GOLDAK, J.; CHAKRAVARTI, A.; BIBBY, M. (1984). A New Finite Element Model for Welding Heat Sources. Metallurgical Transactions B, Vol. 15(b), pp. 299-305.

GOLDAK, J.A.; AKHLAGHI, M. (2005). Computational Welding Mechanics. Springer, New York, USA, p. 325.

GOLDBERG, D.E. (1989). Genetic Algorithms in Search, Optimisation and Machine Learning, Addison-Wesley, p. 435.

GUNURAJ, V.; MURUGAN, N. (1999). Prediction and Comparison of the Area of the Heat-Affected Zone for the Bead-on-Plates and Bead-on-Joints in Submerged Welding of Pipes. Journal of Material Processing Technology, vol. 95, pp. 246-261.

GUNURAJ, V.; MURUGAN, N. (2002). Prediction of Heat-Affected Zone in Submerged Arc Welding of Structural Steel Pipes. Welding Journal, AWS, pp. 94-98.

GUPTA, V.K.; PARMAR, R.S. (1989). Fractional Factorial Technique to Predict Dimensions of the Weld Bead in Automatic Submerged Arc Welding. IE(I) J-MC, 70, pp. 67-75.

HAIGH, R.D.; HUTCHINGS, M.T.; JAMES, J.A.; GANGULY, S.; MIZUNO, R.; OGAWA, K.; OKIDO, S.; PARADOWSKA, A.M.; FITZPATRICK, M.E. (2013). Neutron Diffraction Residual Stress Measurements on Girth-Welded 304 Stainless Steel Pipes with Weld Metal Deposited up to Half and Full Pipe Wall Thickness. International Journal of Pressure Vessels and Piping, vol. 101, pp 1-11.

HAJELA, P.; LIN, C-Y. (1992). Genetic Search Strategies in Multi-Criterion Optimal Design. Structural Optimisation, vol. 4(2), pp. 99-107.

HE, Z.; ZHU, P-F.; PARK, S-H. (2012). A Robust Desirability Function Method for Multi-Response Surface Optimisation Considering Model Uncertainty. European Journal of Operational Research, vol. 221, pp. 241-247.

HEINZE, C.; SCHWENK, C.; RETHMEIER, M. (2012). Numerical Calculation of Residual Stress Development of Multi-pass Gas Metal Arc Welding. Journal of Constructional Steel Research. Vol. 72, pp. 12-19.

HEMMESI, K.; FARAJIAN, M.; SIEGELE, D. (2014). Numerical Investigation of Residual Stress Field and Its Behaviour Under Multiaxial Loading in Tubular Joints. Advanced Materials Research, vol. 996, pp. 788-793.

HIBBITT, H.D.; MARCAL, P.V. (1973). A Numerical Thermo-Mechanical Model for the Welding and Subsequent Loading of a Fabricated Structure. Composite Structures, vol. 3, pp. 1145- 1174.

ILO, S.; JUST Ch.; XHIKU, F. (2012). Optimisation of Multiple Quality Characteristics of Hard-facing Using Grey-Based Taguchi Method. Materials and Design. Vol. 33, pp. 459-468.

ISLAM, M.; BUIJK, A.; RAIS-ROHANI, M.; MOTOYAMA, K. (2014). Simulation-Based Numerical Optimisation of Arc Welding Process for Reduced Distortion in Welded Structures. Finite Elements in Analysis and Design, vol. 84, pp. 54-64.

JUANG, S.C.; TARNG, Y.S. (2002). Process Parameters Selections for Optimising Weld Pool Geometry in the Tungsten Inert Gas Welding of Stainless Steel. Journal of Material and Process Technology, vol. 122, pp. 33-37.

JUANG, S.C.; TARNG, Y.S.; LII, H.R. (1998). A Comparison Between the Back-Propagation and Counter-Propagation Networks in the Modelling of TIG Welding Process. Journal of Material Processing Technology, vol. 75, pp. 54-62.

KARAOGLU, S.; SECGIN, A. (2008). Sensitivity Analysis of Submerged Arc Welding Process Parameters. Journal of Materials Processing Technology, Vol. 202, pp. 500-507.

KARUNAKARAN, N.; BALASUBRAMANIAN, V. (2011). Multipurpose Three-Dimensional Finite Element Procedure for Thermal Analysis in Pulsed Current Gas Tungsten Arc Welding of AZ 31B Magnesium Alloy Sheets. International Journal of Aerospace and Mechanical Engineering, vol. 5(4), pp. 267-274.

KASUYA, T.; YURIOKA, N.; OKUMURA, M. (1995). Methods for Predicting Maximum Hardness of HAZ and Selecting Necessary Preheat Temperature for Steel Welding. Nippon Steel Technical Report, vol. 65(4), pp. 7-14.

KHAN, N.M.A.; ROMOLI, L.; FIASCHI, M.; DINI, G.; SARRI, F. (2011). Experimental Design Approach to the Process Parameter Optimisation of Laser Welding of Martensitic Stainless Steels in a Constant Overlap Configuration. Optics and Laser Technology. Vol. 43, pp. 158-172.

KHURSHID, M. (2017). Static and Fatigue Analyses of Welded Steel Structures – Some Aspects Towards Lightweight Design. PhD Thesis. KTH Royal Institute of Technology, Sweden.

KHURSHID, M.; BARSOUM, Z.; DAUWEL, T.; BARSOUM, I. (2017). Root Fatigue Strength Assessment of Fillet Welded Tube-to-Plate Joints Subjected to Multiaxial Stress State Using Stress Based Local Methods. International Journal of Fatigue, vol. 101, pp. 209-223.

KHURSHID, M; MUMTAZ, N. (2011). Static and Fatigue Design of Load Carrying Welded Joints in High Strength Steels. Masters Thesis. Royal Institute of Technology, Sweden

KIM, D.; KANG, M.; RHEE, S. (2005). Determination of Optimal Welding Conditions with a Controlled Random Search Procedure. Welding Journal, August 2005, pp. 125-130.

KIRAN, D.V.; BASU, B.; DE, A. (2012). Influence of Process Variables on Weld Bead Quality in Two Wire Tandem Submerged Arc Welding of HSLA Steel. Journal of Materials Processing Technology, vol. 212, pp. 2041-2050.

KISIOGLU Y. (2005). Effects of Weld Zone Properties on Burst Pressures and Failure Locations. Turkish Journal of Engineering and Environmental Science, vol. 29, pp. 21-28.

KONAK, A.; COIT, D.W.; SMITH, A.E. (2006). Multi-Objective Optimisation Using Genetic Algorithms: A Tutorial. Reliability Engineering and System Safety, vol. 91, pp. 992 – 1007

KOU, S. (2003). Welding Metallurgy, 2nd Edition. John Wiley and Sons, USA.

KUMANAN, S.; DHAS, J.E.R.; GOWTHAMAN, K. (2007). Determination of Submerged Arc Welding Process Parameters Using Taguchi Method and Regression Analysis. Indian Journal of Engineering and Materials Sciences, vol. 14, pp. 177-183.

LAKSHMINARAYANAN, A.K.; BALASUBRAMANIAN, V. (2008). Process Parameter Optimisation for Friction Stir Welding of RDE-40 Aluminium Alloy Using Taguchi Technique. Transactions of Non-ferrous Metals Society of China, vol. 18, pp. 548-554.

LAZZARIN, P.; SONSINO, C.M.; ZAMBARDI, R. (2004). A Notch Stress Intensity Approach to Assess the Multiaxial Fatigue Strength of Welded Tube-to-Flange Joints Subjected to Combined Loadings. Fatigue and Fracture of Engineering materials and Structures, vol. 27, pp. 127-140.

LEE, C-H.; CHANG, K-H. (2009). Finite Element Simulation of the Residual Stresses in High Strength Carbon Steel Butt Weld, Incorporating Solid-State Phase Transformation. Computational Material Science, vol. 46, pp. 1014-1022.

LEGGATT, R.H. (2008). Residual Stress in Welded Structures. International Journal of Pressure Vessels and Piping, vol. 85, pp. 144-151.

LEWINSKI, J. (2015). The Effect of Manhole Shape and Wall Thickness on Stress State in a Cylindrical Pressure Vessel. Journal of Theoretical and Applied Mechanics, vol. 53(1), pp.5 9-68.

LILJEDAHL, C.D.M.; BROUARD, J.; ZANELLATO, O.; LIN, J.; TAN, J.F.; GANGULY, S.; IRVING, P.E.; FITZPATRIC, M.E.; ZHANG, X.; EDWARDS, L. (2007). Weld Residual Stress Effects on Fatigue Crack Growth Behaviour of Aluminium Alloy 2024-T3. First International Conference on Damage Tolerance of Aircraft Structures, Delft, Netherlands

LIM, D.H.; BAE, I.H.; NA, M.G.; KIM, J.W. (2010). Prediction of Residual Stress in the Welding Zone of Dissimilar Metals Using Data-based Models of Uncertainty Analysis. Nuclear Engineering and Design, vol. 240, pp. 2555-2564.

LINDGREN, L.-E. (2006). Numerical Modelling of Welding. Computer Methods in Applied Mechanics and Engineering, vol. 195, pp. 6710-6736.

LINGAMANAIK, S.N.; CHEN, B.K. (2011). Thermo-mechanical Modelling of Residual Stresses Induced by Martensitic Phase Transformation and Cooling During Quenching of Railway Wheels. Journal of Materials Processing Technology, vol. 211, pp. 1547-1552.

LORZA, R.L.; BOBADILLA, M.C.; CALVO, M.A.M.; ROLDAN, P.M.V. (2017). Residual Stresses with Time-Independent Cyclic Plasticity in Finite Element Analysis of Welded Joints. Metals, 2017,7,136. DOI: 10.3390/met7040136

LU, X. (2002). Influence of Residual Stress on Fatigue Failure of Welded Joints. PhD Thesis. Graduate Faculty, North Carolina State University, USA.

LU, X. (2002). Influence of Residual Stress on Fatigue Failure of Welded Joints. PhD Thesis. North Carolina State University, USA.

MACHIN, G.; SIMPSON, R.; BROUSSELY, M. (2008). Calibration and Validation of Thermal Imagers. [Online] Available: http://citeseerx.ist.psu.edu/viewdoc/download?doi=10.1.1.451.7737&rep=rep1&type=pdf (Accessed 18 September 2016).

MENAKA, M.; VASUDEVAN, M.; VENKATRAMAN, B.; RAJ, B. (2005). Estimating Bead Width and Depth of Penetration During Welding by Infrared Thermal Imaging. Insight, vol. 47(9), pp. 564-568.

MENEGHETTI, G. (2012). The Use of Peak Stresses for Fatigue Strength Assessments of Welded Lap Joints and Cover Plates With Toe and Root Failures. Engineering Fracture Mechanics, Vol. 89, pp .40-51.

MENEGHETTI, G. (2013). The Peak Stress Method for Fatigue Strength Assessment of Tube-to-Flange Welded Joints Under Torsion Loading. Welding in the World, vol. 57, pp. 265-275.

MORADPOUR, M.A.; HASHEMI, S.H.; KHALILI, K. (2015). Multi-objective Optimisation of Parameters in Submerged Arc Welding API X65 Steel Plates. Journal of Iron and Steel Research, International, vol.22(9), pp.870-878

MSC Software Corporation (2013). MSC Marc Volume A: Theory and user information, pp. 272-278.

MURANSKY, O.; SMITH, M.C.; BENDEICH, P.J.; HOLDEN, T.M.; LUZIN, V.; MARTINS, R.V.; EDWARDS, L. (2012). Comprehensive Numerical Analysis of a Three-pass Bead-in-slot Weld and its Critical Validation Using Neutron and Synchrotron Diffraction Residual Stress Measurements. International Journal of Solids and Structure. Vol. 49, pp. 1045-1062.

MURUGAN N.; GUNURAJ, B. (2005). Prediction and Control of Weld Bead Geometry and Shape Relationships in Submerged Arc Welding of Pipes. Journal of Material Processing Technology, vol. 168, pp. 478-487.

MURUGAN, N.; PARMAR, R.S. (1994). Effects of MIG Process Parameters on the Geometry of the Bead in the Automatic Surfacing of Stainless Steel. Journal of Material Processing Technology, vol. 41, pp. 381-398.

MURUGAN, N.; PARMAR, R.S. (1997). Effect of Welding Conditions on Microstructure and Properties of Tube 316L Stainless Steel SAW Cladding. Welding Journal, AWS, vol. 76(5), 210-220.

MUSLIH, M.R. SUMIRAT, I.; SAIRUN; PURWANTA (2008). Internal Stress Distribution Measurement of TIG Welded SUS304 Samples Using Neutron Diffraction Technique. International Conference on Neutron and X-Ray Scattering, pp. 92-95.

NABHANI, F.; LADOKUN, T.; ASKARI, V. (2012). Reduction of Stresses in Cylindrical Pressure Vessels Using Finite Element Analysis: From Biomedical Applications to Industrial Developments; Dr. D. Moratal (Ed.), InTech. Available: http://www.intechopen.com

NAGESH, D.S.; DATTA, G.L. (2010). Genetic Algorithm for Optimisation of Welding Variables for Height-to-Width Ratio and Application of ANN for Prediction of Bead Geometry for TIG Welding Process. Applied Soft Computing, vol. 10, pp. 897-907.

NEERAJ, T.; GNAUPEL-HEROLD, T.; PRASK, H.J. and AYER, R. (2011). Residual Stresses in Girth Welds of Carbon Steel Pipes: Neutron Diffraction Analysis. Science and Technology of Welding and Joining, vol. 16(3), pp. 249-253.

NEGI, V.; CHATTOPADHYAYA, S. (2013). Critical Assessment of Temperature Distribution in Submerged Arc Welding Process. Advances in Material Science and Engineering, (2013), p. 9.

NEZAMDOST, M.R.; ESFAHANI, M.R.N.; HASHEMI, S.H.; MIRBOZORGI, S.A. (2016). Investigation of Temperature and Residual Stress Fields of Submerged Arc Welding by Finite Element Method and Experiments. International Journal of Advanced Manufacturing Technology, DOI: 10.1007/s00170-016-8509-4

NGIAM, S.S. (2007). The Influence of Surface Residual Stress on Fatigue Crack Growth. PhD Thesis. Department of Mechanical Engineering, University College London, UK.

NI, X.; ZHOU, Z.; WEN, X.; LI, L. (2011). The Use of Taguchi Method to Optimise the Laser Welding of Sealing Neoro-Stimulator. Optics and Lasers in Engineering. Vol.49, pp. 297 – 304.

OHMS, C.; WIMPORY, R.C.; KATSAREAS, D.E.; YOUTSOS, A.G. (2009). NET TG1: Residual Stress Assessment by Neutron Diffraction and Finite Element Modelling on a Single Bead Weld on a Steel Plate. International Journal of Pressure Vessels and Piping, vol. 86(1), pp. 63-72.

OLABI, A.G.; CASALINO, G.; BENYOUNIS, K.Y.; HASHMI, M.S.J. (2006). An ANN and Taguchi Algorithms Integrated Approach to the Optimisation of CO_2 Laser Welding. Advances in Engineering Software. Vol. 37, pp. 643-648.

OLSON, M.D.; HILL, M.R.; CLAUSEN, B.; STEINZIG, M.; HOLDEN, T.M. (2015). Residual Stress Measurements in Dissimilar Weld Metal. Experimental Mechanics, vol. 55, pp. 1093-1103.

PARADOWSKA, A.; PRICE, J.W.H.; IBRAHIM, R.; FINLAYSON, T.R.; BLEVINS, R.; RIPLEY, M. (2006). Residual Stress Measurements by Neutron Diffraction in Multi-Bead Welding. Physicia B, vol. 385-386, pp. 890-893.

PARASCHIVA, B.; MARIANA-FLORENTINA, S.; ADRIAN, G. (2016). Study of Stress and Stress Concentrations in Pressure Vessels. Journal of Business Economics and Information Technology, vol. 3(1), p. 25.

PASHA, R.A.; CHOUDARY, N.A.; NASIR, M.A. (2008). Fatigue Design and Validation of ASME-Coded Pressure Vessel. Technical Journal, University of Engineering and Technology Taxila, vol. 13, pp. 28-30.

PASTA, S.; REYNOLDS, A.P. (2007). Evaluation of Residual Stresses During Fatigue Test in a Friction Stir Welding Joint. Published in "Experimental Analysis of Nano and Engineering Materials" – Proceedings of the 13th International Conference in Experimental Mechanics, Alexandropoulos, Greece

PATNAIK, A.; BISWAS, S.; MAHAPATRA, S.S. (2007). An Evolutionary Approach to Parameter Optimisation of Submerged Arc Welding in the Hard-facing Process. International Journal of Manufacturing Research, Vol. 2(4), pp. 462-483.

PAVLINA, E.J.; VAN TYNE, C.J. (2008). Correlation of Yield Strength and Tensile Strength with Hardness for Steels. Journal of Material Engineering and Performance, vol.17, pp.888-893

PENG, J. (2011). Study on Distortion Control in Nozzle Welding of Stainless Steel Pressure Vessels. Master Thesis. University of Waterloo, Canada

PETROVIC, A.L.; BALAC, M.M.; JOVOVIC, A.; DEDIC, A. (2011). Oblique Nozzle Loaded by the Torque Moment-Stress State in the Cylindrical Shells on the Pressure Vessel. Journal of Mechanical Engineering Science. DOI: 10.1177/0954406211415907

PIEKARSKA, W.; GOSZCZYNSKA, D.; SATERNUS, Z. (2015). Application of Analytical Methods for Predicting the Structures of Steel Phase Transformations in Welded Joints. Journal of Applied Mathematics and Computational Mechanics, vol. 14(2), pp. 61-72.

PIERRET, S.; EVANS, A.; PARADOWSKA, A.M.; KAESTNER, A.; JAMES, J.; ETTER, T. and VAN SWYGENHOVEN, H. (2012). Combining Neutron Diffraction and Imaging for Residual Strain Measurements in a Single Crystal Turbine Blade. NDT&E International, vol. 45, pp. 39-45.

PILIPENKO, A. (2001). Computer Simulation of Residual Stress and Distortion of Thick Plates in Multi-Electrode Submerged Arc Welding. Their Mitigation Techniques. A PhD Dissertation, Department of Machine Design and Materials Technology, Norwegian University of Science and Technology, Trondheim, Norway.

PRATIHAR, S.; STELMUKH, V.; HUTCHINGS, M.T.; FITZPATRICK, M.E.; STUHR, U.; EDWARDS, L. (2006). Measurement of the Residual Stress Field in MIG-Welded Al-2024 and Al-7150 Aluminium Alloy Compact Tension Specimens. Material Science and Engineering, vol. 437(A), pp. 46-53.

PRATT, P.; FELICELLI, S.D.; WANG, L.; HUBBARD, C.R. (2008). Residual Stress Measurement of Laser-Engineered Net Shaping AISI410 Thin Plates Using Neutron Diffraction. Metallurgical and Materials Transactions, vol. 39A, pp. 3155-3163.

PUROHIT, G.K.; DIGAMBER (2012). Optimisation of Bead Geometry Parameters of Bead-on-Plate Weldments Prepared by Submerged Arc Welding Using Taguchi Technique. International Journal of Engineering Research and Development, vol. 1 (10), pp. 9-5.

RADAJ, D.; SONSINO, C.M.; FRICKE, W. (2009). Recent Developments in Local Concepts of Fatigue Assessment of Welded Joints. International Journal of Fatigue, vol. 31, pp. 2-11.

RADING, G.O. (1993). The Effect of Welding on the Fatigue Crack Growth Rate in a Structural Steel. Welding Research Supplement, July 1993, pp. 307-312.

RAMESH, B.T.; BANAGAR, A.R.; SWAMY, R.P. (2015). Modelling, Stress and Welding Strength of Pressure Vessel. International Journal of Analytical, Experimental and Finite Element Analysis, vol. 2(1), pp. 17-23.

RAO, R.V.; PAWAR, P.J. (2010). Parameter Optimisation of a Multi-Pass Milling Process Using Non-Traditional Optimisation Algorithms. Applied Soft Computing, vol.10, pp. 445-456.

REDDY, K.S. (2013). Optimisation and Prediction of Welding Parameters and Bead Geometry in Submerged Arc Welding. International Journal of Applied Engineering, vol. 3(3), pp. 1-6.

ROSENBERG, R.S. (1967). Simulation of Genetic Populations with Biochemical Properties. PhD Thesis, University of Michigan, Ann Arbor, Michigan.

ROSENFELD, M.J.; KIEFNER, J.F. (2006). Basics of Metal Fatigue in Natural Gas Pipeline Systems – A Primer for Gas Pipeline Operations. Pipeline Research Council International

ROSSINI, N.S.; DASSISTI, M.; BENYOUNIS, K.Y.; OLABI, A.G. (2012). Methods of Measuring Residual Stresses in Components. Materials and Design, vol. 35, pp. 572-588.

RUSU, C.C.; SCUTELNICU, E.; MISTODI, L.R.; TEODOR, V. (2013). Numerical Models for Simulation of Submerged Double Arc Welding Process. Recent Advances in Industrial and Manufacturing Technologies, 2013, pp. 233-238.

RYBICKI, E.F., SCHMUESER, D.W., STONESIFER, R.W., GROOM, JJ,, AND MISHLER, H.W. (1978). A Finite Element Model for Residual Stresses and Deflections in Girth Butt Welded Pipes, Journal of Pressure Vessel Technology, vol. 100, pp. 256-262.

RYBICKI, E.F; SCHUESER, D.W.; STONESIFER, R.B.; GROOM, J.J.; MISHLER, H.W. (1977). A Finite Element Model for Residual Stress. ASME Winter Annual Meeting, Nov 1977, Atlanta, GA.

SALUJA, R.; MOEED, K.M. (2012). Modelling and Parametric Optimisation Using Factorial Design Approach of Submerged Arc Bead Geometry Butt Joint. International Journal of Engineering Research and Applications, vol. 2(3), pp. 505-508.

SAPAKAL, S.V.; TELSANG, M.T. (2012). Parametric Optimisation of MIG Welding Using Taguchi Design Method. International Journal of Advanced Engineering Research and Studies, vol.I(IV), pp. 28-30

SATHIYA, P.; PANNEERSELVAM, K.; JALEEL, M.Y.A. (2012). Optimisation of Laser Welding Process Parameters for Super Austenitic Stainless Steels Using Artificial Neural Networks and Genetic Algorithm. Materials and Design, vol. 36, pp. 490-498.

SCHAFFER, J.D. (1985). Multiple-Objective Optimisation with Vector Evaluated Genetic Algorithm. In Genetic Algorithms and their Applications: Proceedings of the First International Conference on Genetic Algorithms, Lawrence Erlbaum, pp.93-100.

SCHARENBERG, R. (2008). DLR in Space, Aeronautical, Transport and Energy. International Conference in Bio-, Nano- and Space Technologies, EU and Science Centres Collaboration, Ljubljana, Slovenia, March 2008.

SCHIJVE, J. (2009). Fatigue of Structures and Materials, 2nd Ed. Springer, Netherlands, p. 627.

SERASLI, K.; CAVE, D.; KINGSTON, E. (2016). Residual Stress Measurements Using Contour, Deep-Hole Drilling and Neutron Diffraction Methods in T-Section Specimens. Proceedings of the ASME 2016 Pressure Vessels and Piping Conference, July 17 – 21, Vancouver, Canada.

SHEN, S.; OGUOCHA, I.N.A.; YANNACOPOULOS, S. (2012). Effect of Heat Input on Weld Bead Geometry of Submerged Arc Welded ASTM A709 Grade 50 Steel Joints. Journal of Materials Processing Technology, vol. 212, pp. 286-294.

SIDDIQUE, M. (2005). Experimental and Finite Element Investigation of Residual Stresses and Distortions in Welded Pipe-flange Joints. PhD thesis, Ghulam Ishaq Khan Institute of Engineering Sciences and Technology, Pakistan.

SKOURAS, A.; PARADOWSKA, A.; PEEL, M.J.; FLEWITT, P.E.J.; PAVIER, M.J. (2013). Residual Stress Measurements in Ferrite Steel/ln625 Superalloy Dissimilar Metal Weldment Using Neutron Diffraction and Deep-Hole Drilling. International Journal of Pressure Vessels and Piping, vol. 101, pp. 143-153.

SLOMA, J.; SZCZYGIEL, I.; SACHAJDAK, A. (2014). Verification of Heat Phenomena During Surfacing Using a Thermal Imaging Camera. Welding International, vol. 28(8), pp. 610-616.

SMITH, M.C.; SMITH, A.C. (2009a). NeT Bead-on-plate Round Robin: Comparison of Transient Thermal Predictions and Measurements. International Journal of Pressure Vessels and Piping, vol. 86, pp. 96-109.

SMITH, M.C.; SMITH, A.C. (2009b). NeT Bead-on-Plate Round Robin: Comparison of Residual Stress Predictions and Measurements. International Journal of Pressure Vessels and Piping, vol. 86, pp. 79-95.

SMITH, M.C.; SMITH, A.C.; WIMPORY, R. and OHMS, C. (2014). A Review of the NeT Task Group1 Resdual Stress Measurement and Analysis Round Robin on a Single Weld Bead-on-Plate Specimen. International Journal of Pressure Vessel and Piping, vol. 120-121, pp. 93-140.

SONG, Y-A.; PARK, S.; CHAE, S-W. (2005). 3D Welding and Milling: Part II – Optimisation of the 3D Welding Process Using an Experimental Design Approach. International Journal of Machine Tools & Manufacture, vol. 45, pp. 1063-1069.

SREEDHAR, U.; KRISHNAMURTHY, C.V.; BALASUBRAMANIAM, K.; RAGHUPATHY, V.D.; RAVISANKAR, S. (2012). Automatic Defect Identification Using Thermal Image Analysis for Online Weld Quality Monitoring. Journal of Materials Processing Technology, vol. 212, pp. 1557-1566.

STERJOVSKI, Z. (2003). Investigation of Post Weld Heat Treatment of Quenched and Tempered Pressure Vessel Steel. PhD Thesis, University of Wollongong, Australia.

STERJOVSKI, Z.; DUNNE, D.P.; AMBROSE, S. (2004). Evaluation of Cross-weld Properties of Quenched and Tempered Pressure Vessel Steel Before and After PWHT. International Journal of Pressure Vessels and Piping, vol. 81, pp. 465-470.

SUDAKARAN, R.; VEL, M.V.; SIVA S.P.S. (2010). Optimisation of Process Parameters to Minimise Angular Distortion in Gas Tungsten Arc Welded Stainless Steel 202 Grade Plates Using Genetic Algorithms. International Journal of Engineering Science and Technology, vol. 2(5), pp. 731-748.

SUDHAKARAN, R.; MURUGAN, V.V.; KUMAR, K.M.S.; JAYARAM, R.; PUSHPARAJ, A.; PRAVEEN, C.; PRABHU, N.V. (2011). Effect of Welding Process Parameters on Weld Bead Geometry and Optimisation of Process Parameters to Maximise Depth-to-Width Ratio for Stainless Steel Gas Tungsten Arc Welded Plates Using Genetic Algorithm. European Journal of Scientific Research, vol. 62(1), pp. 76-94.

SUMIN, V.V.; SHEVEREV, S.G.; SCHNEIDER, R.; WIMPORY, R. and BALAGUROV, A.M. (2010). Results of Measuring the Residual Strains in the WWER-1000 Reactor Vessel. Physics of the Solid State, vol. 52(5), pp. 930-933.

SUZUKI, T.; OIKAWA, H.; IMAFUKU, M.; SUZUKI, H.; SUGIYAMA, M.; NOSE, T.; TOMOTA, Y.; MORIAI, A. (2011). Residual Stress Measurement of Welding Area by Neutron Diffraction Method. Nippon Steel Technical Report, No. 100, pp. 47-50.

TARNG, Y.S.; JUANG, S.C.; CHANG, C.H. (2002). The Use of Grey-Based Taguchi Methods to Determine Submerged Arc Welding Process Parameters in Hardfacing. Journal of Materials Processing Technology, Vol. 128, pp. 1-6.

TJELTA, F. (2012). A Comparison Study of Pressure Vessel Design Using Different Standards. Master's Thesis. University of Stavanger.

UEDA, Y., YAMAKAWA, T. (1971). Analysis of Thermal-Elastic Stress and Strain During Welding by Finite Element Method, JWRI, vol. 2(2).

USAMENTIAGA, R.; VENEGAS, P.; GUEREDIAGA, J.; VEGA, L.; MOLLEDA, J.; BULNES, F.G. (2014). Infrared Thermography for Temperature Measurement and Non-Destructive Testing. Sensors 2014, vol. 14, pp. 12305-12348.

VASUDEVAN, M.; CHANDRASEKHAR, N.; MADURAIMUTHU, V.; BHADURI, A.K.; RAJ, B. (2011). Real-time Monitoring of Weld Pool During GTAW Using Infrared Thermography and Analysis of Infrared Thermal Images. Welding in the World, vol. 55, pp. 83-89.

VENKATRAMAN, B.; MENAKA, M.; VASUDEVAN, M.; AND RAJ, B. (2006). Thermography for Online Detection of Incomplete Penetration and Penetration Depth Estimation. 12th A-PCNDT 2006 – Asia Pacific Conference on NDT5 – 6 November 2006, Aukland New Zealand.

WIKLE III, H.C.; KOTTILINGAM, S.; ZEE, R.H.; CHIN, B.A. (2001). Infrared sensing techniques for penetration depth control of the submerged arc welding process. vol. 113: pp. 228-233.

WOHLFAHRT, H. (2007). Reports on Experimental Round Robin Tests on Residual Stresses, IIW Doc. XIII-2144-06 / XV-1227-06.

WOHLFAHRT, H. and DILGER, K. (2008). New Results on the IIW Round Robin Residual Stress Measurements, Doc. XIII-2241 / XV-1283-08.

WOHLFAHRT, H.; NITSCHKE-PAGEL, T.H.; DILGER, K.; SIEGELE, D.; BRAND, M.; SAKKIETTIBUTRA, J. and LOOSE, T. (2012). Residual Stress Measurements – Review and Assessment of the IIW Round Robin Results. Welding in the World, vol. 56, pp. 120-140.

WOO, W.; AN, G.B.; EM, V.T. and DE WALD, A.T. (2015). Through-Thickness Distributions of Residual Stresses in an 80mm Thick Weld Using Neutron Diffraction and Contour Method. Journal Material Science, vol.5 0, pp. 784-793.

XUEDONG, C.; TIECHENG, Y.; CHUANQING, C. (2002). Experimental Research on Fracture and Fatigue of SCT Specimen Simulating High-Strain Region of Pressure Vessel Nozzles. ICF100237.

YAGHI, A.; BECKER, A. (2004). State of the Art Review: Weld Simulation Using Finite Element Methods. Publication of the University of Nottingham, UK.

YANG, D.; LI, X.; HE, D.; NIE, Z; HUANG, H. (2012). Optimisation of Weld Bead Geometry in Laser Welding with Filler Wire Process Using Taguchi's Approach. Optics and Laser Technology, vol. 44, pp. 2020-2025.

YANG, Y. (2008). The Effect of Submerged Arc Welding Parameters on the Properties of Pressure Vessel and Wind Turbine Steels. Master's Thesis. Department of Mechanical Engineering, University of Saskatchewan, Canada.

YOUSEFIEH, M.; SHAMANIAN, M.; SAATCHI, A. (2011). Optimisation of the Pulsed Current Gas Tungsten Arc Welding (PCGTAW) Parameters for Corrosion Resistance of Super Duplex Stainless Steel (UNS S32760) Welds Using the Taguchi Method. Journal of Alloys and Compounds, vol. 511, pp. 782-788.

YUEN, B.K.C.; TAHERI, F. and GHARGHOURI, M. (2008). Experimental Investigation into the Fatigue of Welded Stiffened 350WT Steel Plates Using Neutron Diffraction Method. Strain, vol. 46, pp. 526-537.

ZABEEN, S. (2012). Fatigue Crack Growth in Complex Residual Stress Fields Due to Surface Treatment and Foreign Object Damage Under Simulated Flight Cycles. PhD Thesis. School of Materials, University of Manchester, UK.

ZONDI, M.C. (2014). Factors that affect welding-induced residual stress and distortions in pressure vessel steels and their mitigation techniques: a review. Journal of Pressure Vessel Technology, vol. 136 (4), 9 p

APPENDICES

APPENDIX A: Protocol for Weld Specimen Preparation and Temperature Recordings

Protocol for Weld Specimen Preparation and Temperature Recordings

1. Introduction

This is a test procedure for preparation of weld specimens for a research welding experiment that includes temperature recordings using infrared imaging. The experiments are for research work commissioned for purposes of post-grad engineering studies at the University of KZN. The intention is to weld up a number of specimens of the as prescribed below and prepare them for further testing.

2. Purpose

The aim of this protocol is to provide a detailed guideline for the preparation of weld specimens and recording of temperatures in the investigation of submerged arc welding process.

3. Weld-piece Preparation

The weld-piece is prepared as given in figure 1. A steel pipe of 80mm bore (i.e. 3 inches) is welded onto a 10mm steel plate through a full penetration multi-pass weld joint. The plate represents the cylindrical shell part of the pressure vessel shell, and the pipe is a nozzle, such that the welded specimen is a nozzle-shell weld joint.

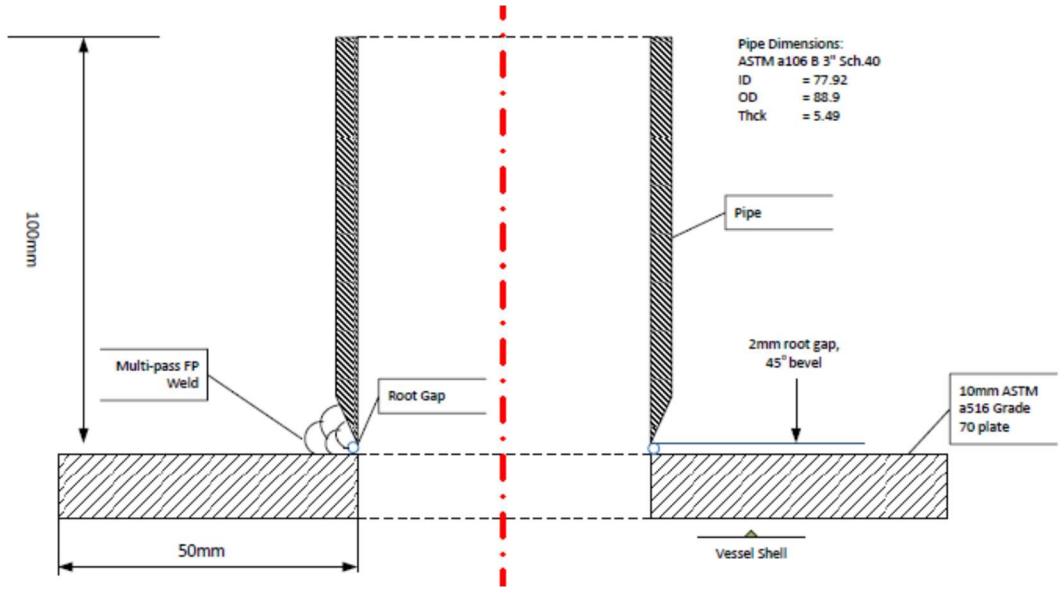

Figure 1: Weld-Piece Preparation

Table 1 gives the welding conditions that exist during the preparation of the weld-piece specimens.

Table 1: Welding Conditions

Welding Conditions
Room temperature: (to be recorded)
No preheat
Cooling at room temperature
Welding procedure: Semi-automatic SAW @ 85% efficiency
High strength pressure vessel plate 178 x 178 x 10mm
80mm (3 inch) seamless carbon steel pipe bevelled @ 45°
Root gap of 2mm
OK Autrod 12.22 (EM12K) low hydrogen electrode – 2.5mm
OK Flux 10.72

3.1. Welding Procedure

The high strength carbon steel pipe is welded onto the pressure vessel plate of similar strength using low hydrogen high strength EM12K electrodes. Materials ASTM A106 and ASTM A516, for the pipe and plate respectively, are chosen for practical purposes since these materials are typically used for pressurised system application. A hole of the same size as the internal diameter

of the pipe is drilled through the plate in order to position the pipe in the same way that the nozzle would be positioned on the pressure vessel. The root gap of 2mm is attained through mounting the pipe on the plate by inserting a 2mm steel rod in between the pipe and the plate, and placing four equi-spaced tag welds around the weld groove. A three pass full penetration weld is then performed using the SAW process. Assume a welding efficiency of 85% in order for heat input to be in line with the finite element model.

3.2. SAW Process Parameters

The SAW parameters of interest in this study are welding current (I), arc voltage (V), travel speed (S) and wire-feed rate (FR). The applicable welding parameters are given in table 2, and the welding machine should be adjusted accordingly.

Table 2: Welding Parameters

Parameter	Units	Lower L (-)	Upper L (+)
Current (I)	Amps	360	380
Voltage (V)	Volts	25	30
Speed (S)	mm/s	8	10
Wire-feed Rate (FR)	mm/s	16.7	18.3

Table 2 shows the two levels of parameters applied in the welding experiments. The range of values is chosen using guidelines from SAW machine operator's manual and experience from similar studies. When choosing the operational range for SAW parameters, care should be taken to only include parametric combinations that will not result in burn-through (i.e. too much heat) or lack of penetration (i.e. too little heat). The orthogonal array chosen in this study is L_9 with eight degrees of freedom. The input parameters include the four welding parameters mentioned above and the machine setting of either Constant Current (CA) or Constant Wire (CW). The resultant matrix is shown in table 3.

Table 3: Orthogonal Array Matrix (L9)

Exp.No.	*Input Parameters*				
	I	**V**	**S**	**FR**	**Mode**
1	+	+	+	+	CA
2	+	-	-	+	CA
3	-	-	-	+	CA
4	-	-	+	+	CA
5	+	-	+	+	CA
6	-	+	-	-	CW
7	-	+	-	+	CW
8	-	-	-	+	CW
9	-	-	-	-	CW

3.3. Specimen Material

The target materiel for steel plate is that of high-strength carbon steel used in pressure vessel applications, with specification of ASTM 516 Gr. 70. The pipe material specification is ASTM A106 Gr B, seamless schedule 40. Only the cylindrical part of the pressure vessel is considered in this study, the hemispherical end is not considered.

3.4. Welding Machine Set-up

The experimental setup shall consist of the Esab SAW machine and the Short Wave Infrared (SWIR) camera as shown in Figure 2. The SAW machine has two major components, viz. the wire feeder and the turn table. The turn-table is set up to perform circumferential weld. The linear speed of the machine should first be aligned with rotational speed of the turntable through a calibration process described in the manual of the machine. The wire feeder is used to supply the welding electrode or wire to the weld piece during welding process. The wire feed rate (FR) is controlled by the Esab controller as can be seen in Figure 2.

The controller of the Esab machine operates in one of two modes; the user can either select a constant current (amperage) mode (CA) or a constant wire feed rate mode (CW). In constant current mode, the current is set on the controller and the FR automatically sets itself during welding. In constant wire feed rate mode, the FR is set on the controller and the current settings are automatically set by the machine during welding. The turn table speed is set using an analogue dial from one to nine on the turn table controller as calibrated against the linear speed.

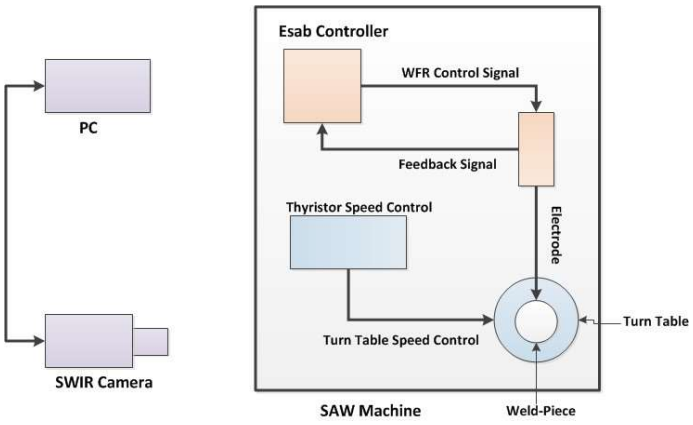

Figure 2: SAW Machine and SWIR Camera Set-up

During measurement, the FSIR radiometer is placed at a focus range of 3m as shown in Figure 2. Power to the FSIR is supplied via the standard 220V, 50Hz, single phase municipal supply and the FSIR is connected to the controller (PC) using the original equipment manufacturer (OEM) supplied camera link cable. The FSIR is left for 5 minutes to acclimatise to ambient temperature before operation. The Flir RnD version 3.3 software is accessed on the controller and the configuration setup which matches the temperature of the scene is selected. This includes the sensitivity parameters i.e. integration time and the neutral density filter. The radiometer lens is adjusted to focus on the scene. Before measurement could begin, a non-uniformity correction is performed to compensate for the variations in camera operating conditions and to improve image quality. Note all this information is available in the FSIR manual

4. Temperature Measurements

Temperatures are continuously recorded using the thermal camera from four measurement locations (i.e. P1, P2, P3 and P4). Figure 3 shows the location of measurement points. P1 and P2 are located on the inner edge of the pipe at coordinate (0,0,0). P3 and P4 are located at (6,0,0), in terms of (x, y, z).

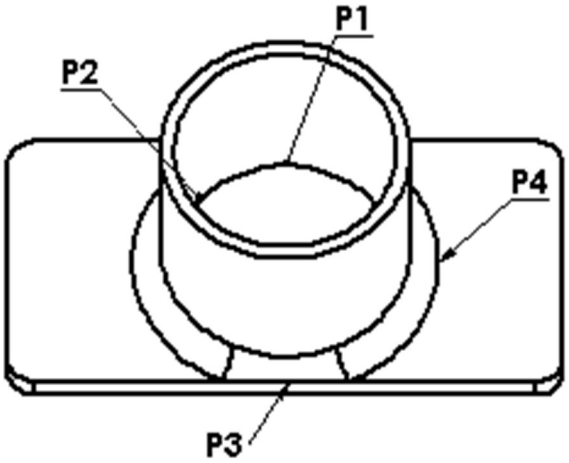

Figure 3: Temperature Measurement Points

The exact location of the measurement points around the circumferential weld is given in table 4. The recorded temperatures should be plotted against time in order to obtain the temperature distributions.

Table 4: Location of Temperature of Interest

Temperature	Location
$P1$	0 deg. on pipe side
$P2$	60 deg. on pipe side
$P3$	180 deg. on plate side
$P4$	240 deg. on plate side

5. Conclusion

The procedure given above is meant to guide the process of experimental set-up, preparation and execution. It is submitted that the protocol is not exhaustive of all details of the required scope; it is not meant to be. It is merely a guide that purports to show direction towards what should happen.

APPENDIX B: Protocol for Stress Measurements

Protocol for Stress Measurements

1. Introduction

This is a procedure for residual stress measurements on the welded specimens using neutron diffraction. The weld specimens were prepared using the submerged arc welding and consist of a three-pass full penetration weld bead. Through-thickness residual stress measurements are to be taken at specified points for each weld specimen.

2. Residual Stress Measurements

The residual stresses in each weld sample will be analysed using the neutron diffraction (ND) method. The ND technique requires that a stress-free reference point be determined prior to taking readings from the component under stress. A section is therefore cut out of each weld-piece using a waterjet cutter as shown in figure 1. The point on the inside of the weld-piece, which is indicated as the 'heel' of the cut-out reference piece, is designated as point (0,0,0) in terms of (x,y,z,) coordinates. The spacing between measurement points is chosen as 3 mm. The flange is measured from 1.6 mm to 43.6 mm (15 points) and the pipe was measured from 10.6 mm to 73.6 mm (22 points). At each measurement point, strain must be measured in three orthogonal directions, i.e. hoop, or ε_h (y-axis), axial or ε_a (z-axis) and radial or ε_r (x-axis). This is achieved by mounting the weld-piece in three different orientations. The flange line of measurement is illustrated using the yellow colour in figure 1, whereas the pipe-side measurements are indicated through a green line. For the purposes of measurement, the weld centreline (WCL) is considered to be in the proximity of the coordinates (6,0,11). Measurement time is varied due to path length changes with the aim of providing strain errors of not more than 50με.

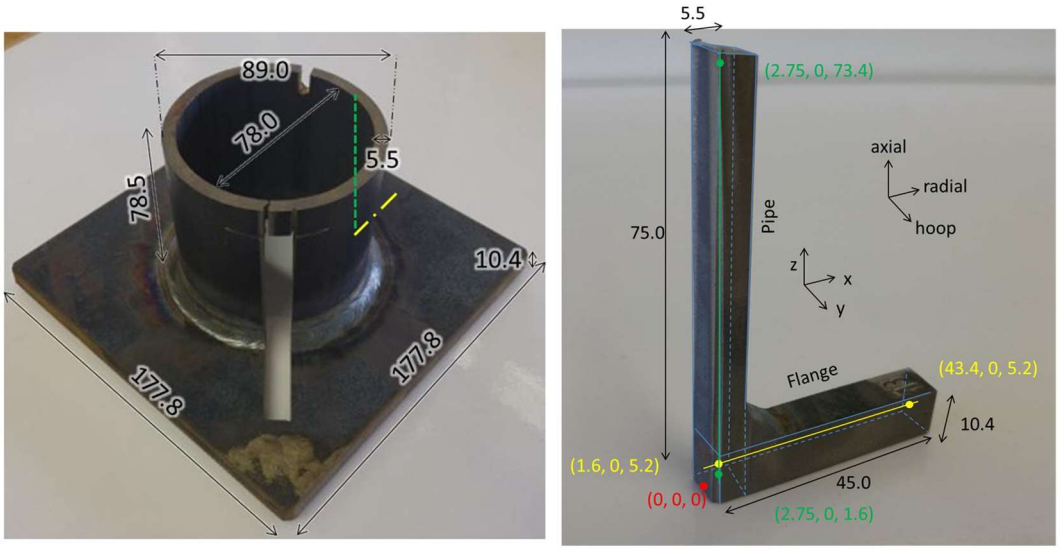

Figure 1: Stress Measurement Points

The Materials Probe for Internal Strain Investigations (MPISI) to be set up using a 2 mm radial collimator on the detector side and the primary slit adjusted to have a 2 mm x 2 mm window. A nominal gauge volume of 8 mm^3 is therefore defined. Pre-calibrated theodolites to be used and aligned at the instrument centre of rotation. Positioning using the theodolites can be assumed to be accurate within 0.1 mm which is less than the 10% margin normally applied for the setup accuracy. The measurement positions are chosen to be as far away from the reference cut-out and start/stop position of the weld as possible, preferably 180 degrees from weld start/stop position. To reduce sample setup complexity, the measurement positions are chosen to be tangential to a flat edge of the flange. In order to ensure that the gauge volume is always fully submerged in the sample material, the centre of the gauge volume was always at least 1.6 mm away from the sample surface. All measurements are taken along the mid thicknesses of the sections. The three components of stress are measured, namely hoop, axial and radial. The mounting setup for each measurement is shown in Figure 2.

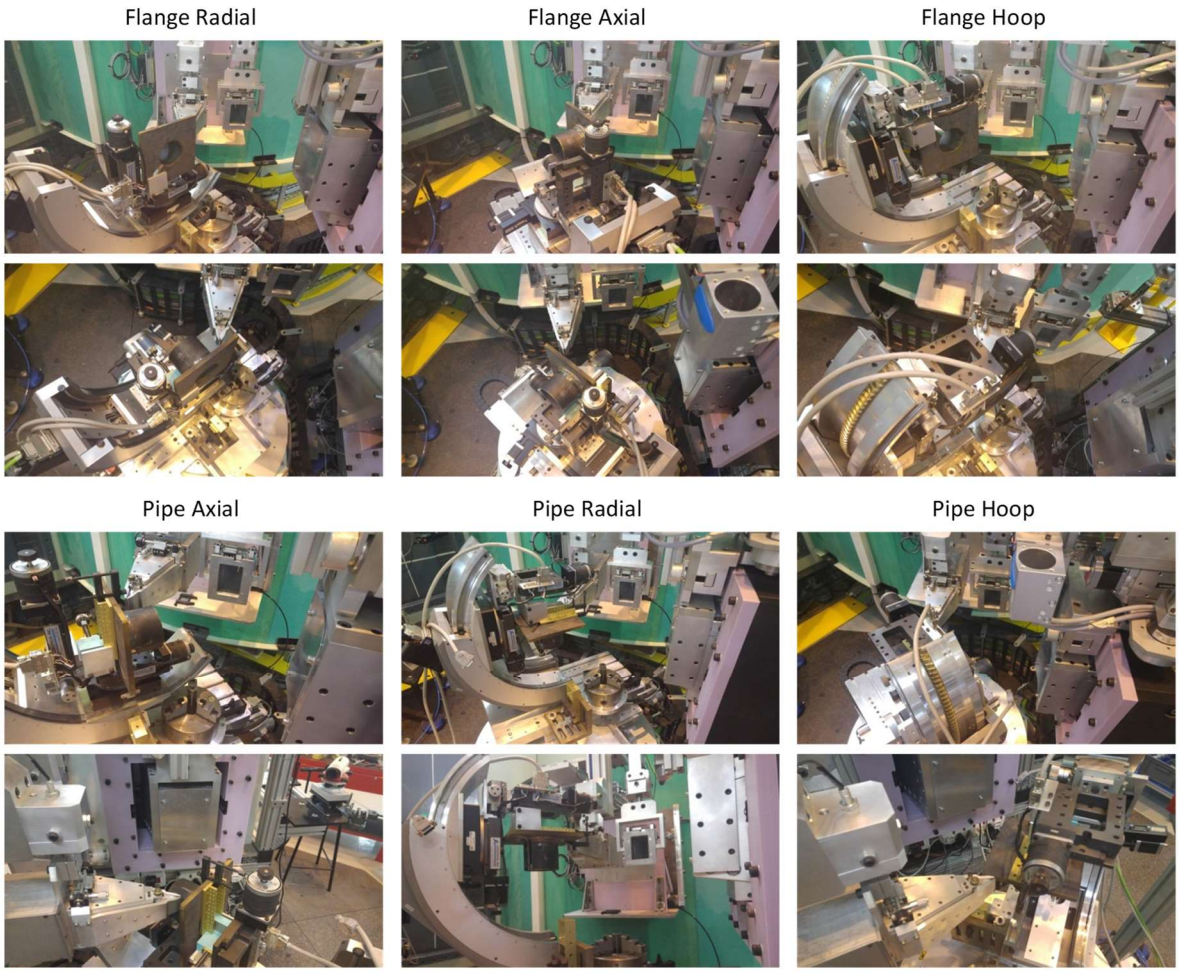

Figure 2: Welding Specimen Mounting for 3D Stress Measurements

3. Conclusion

The recorded residual stress data should be used to generate stress field distribution plots that will be used for further analysis. The stress test report should note and record any information that is considered relevant to give context when interpreting the stress results.

APPENDIX C: Protocol for Microstructural Analysis and Hardness Testing

Protocol for Microstructural Analysis and Hardness Testing

1. Introduction

This is a procedure for bead geometry measurements, microstructural analysis and Vickers Hardness testing. A smaller specimen should be cut out of each of the main samples such that it includes parent metal (of both plate and pipe), weld metal and HAZ (of both plate and pipe). This specimen can be used for all the tests mentioned below.

2. Microstructural Analysis and Weld Bead Measurements

In order to avoid undesired heat effects, samples have to be cut by using abrasive water-jet cutting process. Samples must also be cut well away from start/end and tack weld locations. For fusion zone and HAZ macrograph measurement, the following steps must take place:

a. Sample preparation by water-jet cutting
b. The sample must be mounted on cast
c. Sequential grinding by using silicone carbine abrasive paper with varying grit sizes [300, 500, 800, 1000]
d. Diamond paste polishing with particle sizes of 9 µm, 6 µm, 3 µm, and 1 µm.
e. Etching the sample with 2% nital solution or equivalent for 30 seconds and rinse
f. Study the sample to reveal HAZ and FZ dimensions

Bead geometry should be measured for every three-pass weld of each specimen. All bead dimensions are to be recorded in a spreadsheet or table and be submitted for further analysis. The dimensions to be measured for the weld bead include bead width (BW), bead height (BH), bead penetration (BP) and width of the Heat Affected Zone (HAZ width). Figure 1 shows the exact location of each dimension in the weld specimen. Bead geometry is measured using stereo microscopy to enlarge the weld bead, and the mapping out of the dimensions is performed using appropriate software embedded in the microscope. All dimensions should only be recorded after the third weld pass.

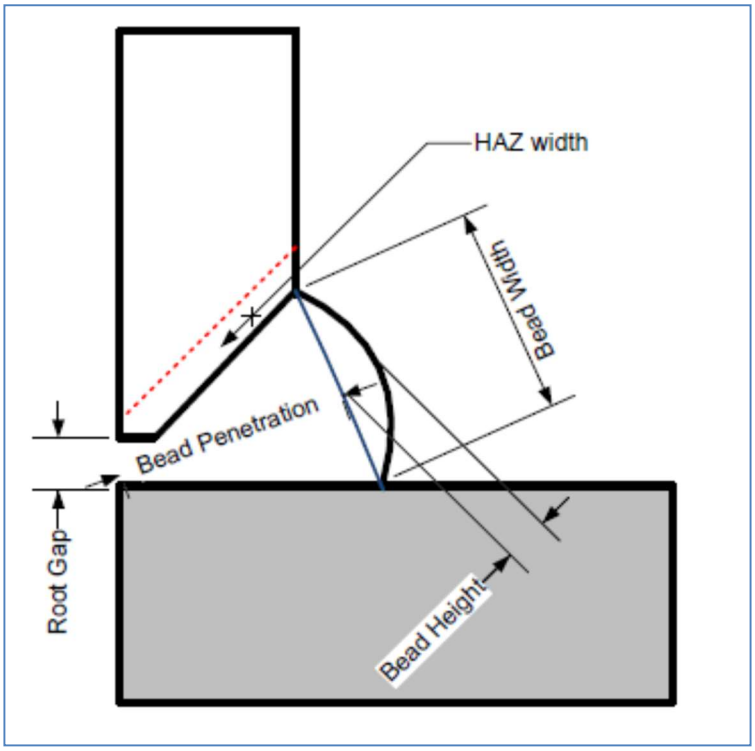

Figure 1: Weld Bead Geometry

The microstructural characterisation of the parent material (as-received), the weld metal and the HAZ are performed using the instrumentation scan electron microscopy. Received samples are subjected to grinding as detailed above. The test specimens are etched in 2% Nital to reveal the size of the heat affected zone before sectioning the L-shaped test specimen to fit into the mounting machine. The sample is then hot mounted into a conductive resin, and subjected to further grinding, polishing and etching in 2% Nital for 5 seconds. After polishing the sample is then placed under the microscope and analysed accordingly. Results are recorded using the appropriate embedded software.

3. Hardness Testing

Mechanical properties of the weld specimen are tested through the Rockwell B hardness test. Hardness is known as a measure of the material's resistance to plastic deformation. The Electronic Rockwell Hardness Tester is used for hardness measurement. The specimen is prepared such that the surface is smooth, and a number of points are marked in a straight line spanning through the weld metal, HAZ and parent metal from both the plate and the pipe sides. The results are recorded as given in table 1. The ultimate tensile strength values, that are equivalent to the determined hardness, are determined using appropriate formulae and also included in the table.

Table 1: Measured Hardness Values

Specimen	Plate		Plate HAZ		Weld metal		Pipe HAZ		Pipe	
	HRB	**HV**	**HRB**	**HV**	**HRB**	**HV**	**HRB**	**HV**	**HRB**	**HV**
Specimen 1										
Specimen 2										
Average										
UTS MPa										

APPENDIX D: Protocol for Fatigue Analysis

Protocol for Fatigue Analysis

1. Introduction

Fatigue testing involves the determination of fatigue life of welded specimens expressed in the form of cycles to failure under fixed load conditions. The scope of fatigue analysis under this section includes the following:

a. A post-test weld analysis of the cracks to determine the fracture mode and crack initiation site for each specimen.
b. Identifying the distinctive characteristics of the surface appearance of a fatigue fracture in each specimen.
c. Identifying the different stages of fracture in each specimen.
d. Defining the mode of fracture for tested specimens.

2. Preparation and Mounting of Test Specimen

The fatigue test specimen is prepared as shown in Appendix A. The specimen is then mounted onto the fatigue testing machine using a specially designed jig made of 30mm thick steel plate as shown in Figure 1. Three holes (M10) are drilled in each of the four flange corners of the specimen in order to hold the specimen down onto the jig. The load spreader plate is attached between the clamping bolts and the specimen flange as shown in Figure 1. The reason for the load spreader plate is to prevent the stresses induced on the test specimen flange from propagating to the bolt holes. Additional gussets are welded onto the jig to provide adequate stiffness during the fatigue tests.

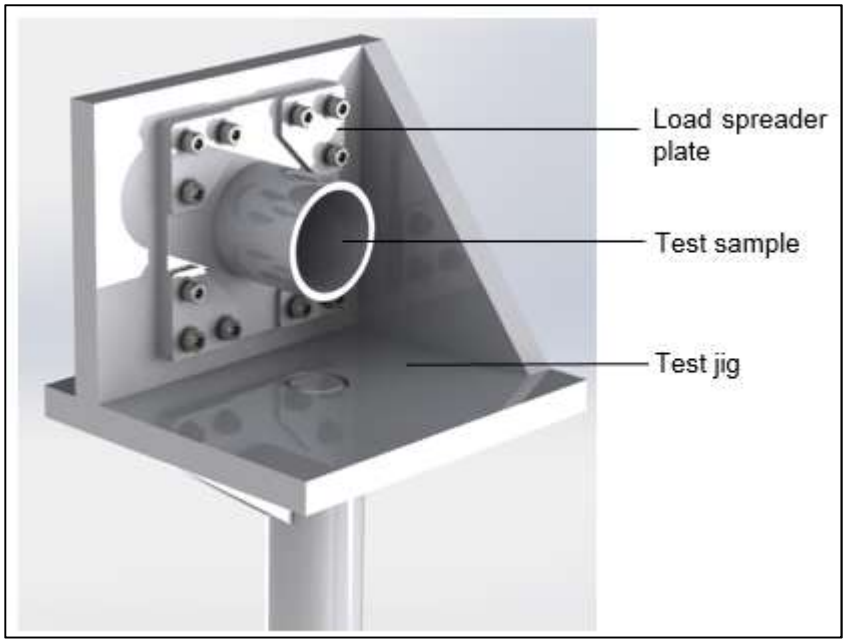

Figure 1: Mounting of the Fatigue Test Specimen

3. The Applied Bending Load

The specimens are subjected to the cantilever load applied at the tip of the pipe section of the specimen. Firstly, the theoretical maximum load that the specimen could withstand is calculated using the following procedure:

A theoretical static load of 100 kN is applied onto the portion of sample's circumferential area and used to calculate the allowable stress that the pipe material could withstand as shown on the schematic diagram in Figure 2. The MTS fatigue testing machine used in this particular test has a maximum loading capacity of 1000 kN.

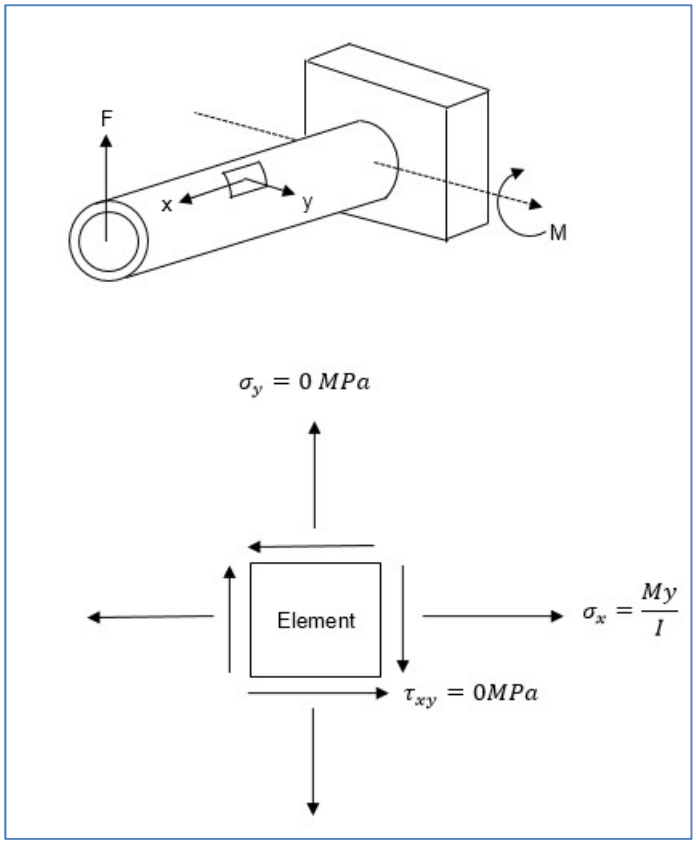

Figure 2: Schematic Representation of Applied Load

The stress in the x direction due the applied vertical load is calculated using the equation 1:

$$\sigma_x = \frac{My}{I} \quad \textbf{(1)}$$

The second moment of area is calculated from the following equation:

$$I = \frac{\pi(D^4 - d^4)}{64} \quad \textbf{(2)}$$

The cross sectional area of the shaft is calculated from the following equation:

$$A = \frac{\pi(D^2 - d^2)}{4} \quad \textbf{(3)}$$

Where D = 89 mm; d = 77 mm; y = 38.5 mm; F= 100 kN; l = 80 mm; M = 8 kN.m;

Calculating the axial stress using equation 1 results in $\sigma_x = 162MPa$

The yield strength of the filler material at the weld is 420 MPa. The factor of safety at the welded area for an applied vertical tensile and compressive static load of 100 kN is calculated as follows:

$$\sigma_o = X_S \times \sigma_x \quad \textbf{(4)}$$

$$X_S = \frac{420}{162} = 2.6$$

The ultimate strength of the filler material at the weld is 520 MPa. The factor of safety at the welded area for an applied vertical tensile and compressive static load of 100 kN is calculated as follows:

$$X_S = \frac{520}{162} = 3.2$$

Thus, the weld specimen is expected to fail in bending at an applied static load of:

$$F_S = 100 \times 2.6 = 260 \text{ kN}$$

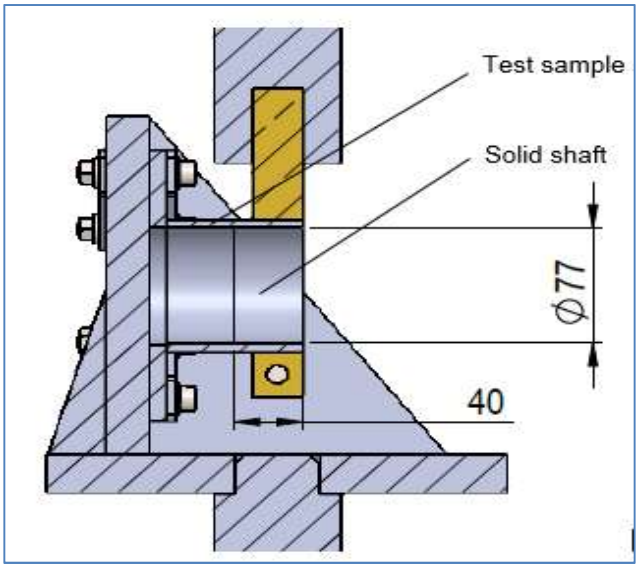

Figure 3: Fatigue Test Setup at Loads Above 100kN

The solid steel shaft is inserted into the pipe of the weld specimen, at the loading area, to prevent possible local deformations on the clamping contact area as shown in Figure 3. A point load of 260 kN is applied to the specimen, and a curve of Load vs. Displacement is generated in order to identify the yield point before failure. One the yielding load is identified, then a load of 80% of the yield strength is then applied in a few trial tests at a frequency of 8Hz using different displacement limits to see how the specimens perform.

4. Fatigue Test Equipment Setup

Testing equipment includes the MTS High-force servo-hydraulic testing machine, Vernier callipers for measurements and the wrench for tightening the bolts. In fatigue testing a specified mean load (which may be zero) and an alternating load are applied to the test specimen and the number of cycles required to failure is recorded. Load was applied axially by the servo hydraulic machine.

Table 1: Fatigue Loading of Specimens

Unique Sample #	2x Specimens
4	0.8 x Max Load
6	0.8 x Max Load
7	0.8 x Max Load
8	0.8 x Max Load
9	0.8 x Max Load

Two test specimens are prepared per parametric combination for the CA welding machine setup. The two specimens of each sample are tested under 80% maximum load as calculated above; and cycles to failure as well as the displacement of the specimen is monitored throughout each test. The integrity of the weld bead is tested using non-destructive testing (NDT) methods. NDT is also used to determine crack development during fatigue testing. The load parameter is kept constant and the displacement of the pipe is used as the failure criterion. The displacement of 5mm is used as a failure criterion for each specimen. In other words, once the actuator has been displaced for 5mm the specimen is considered to have experienced adequate crack growth to regard it as having failed.

APPENDIX E: Cooling Time vs. Arc Energy

Cooling Time vs. Arc Energy for Air and Water-Cooled SMAW Welds for ASTM A517 grade 70 Steel

Source: Johnson (1997)

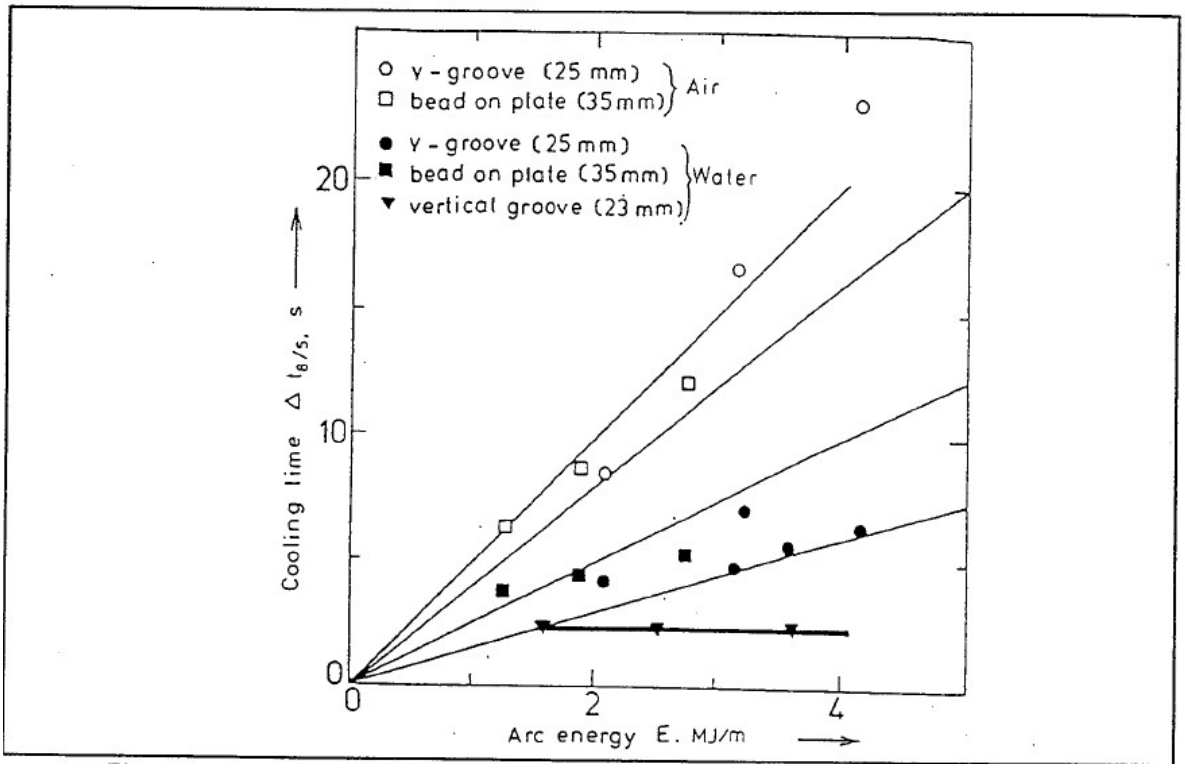

APPENDIX F: Bead Geometry Measurements

BEAD GEOMETRY MEASUREMENTS

Sample 2

The mounted sample was then analysed using a stereo microscope to get the overall size of the weld

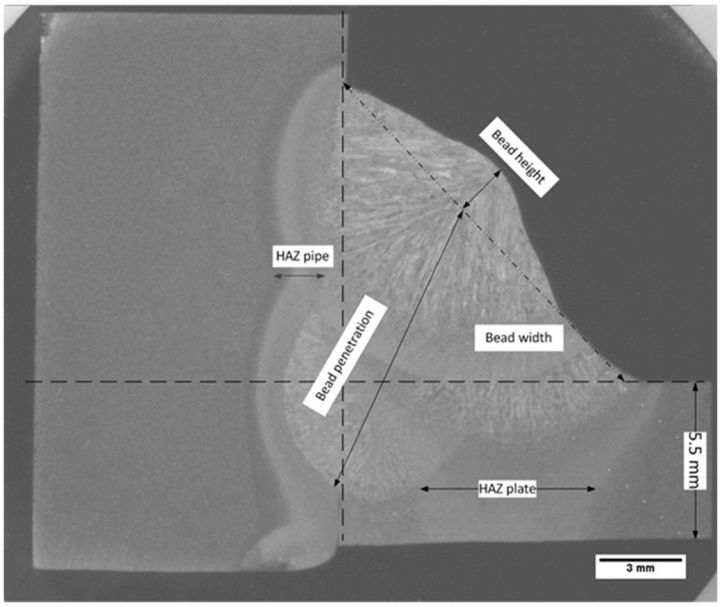

Figure: Image of Sample 2 at a magnification of 0.8x

Sample 3

A macrograph of Sample 3 shows the bead geometry of the welded sample 3. The bead geometry of specimen was measured using a scaled image and Image J software.

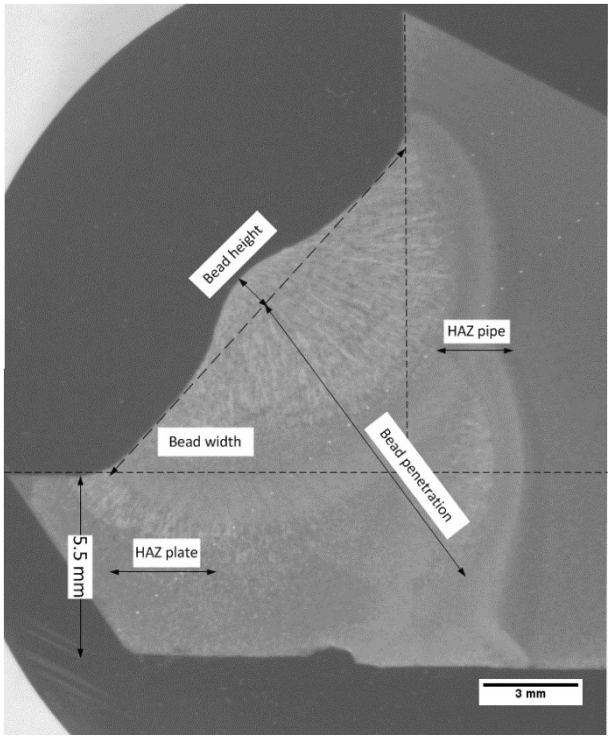

Figure 7 Image of the Bead geometry of Sample 3 at a magnification 0.8x

Sample 4

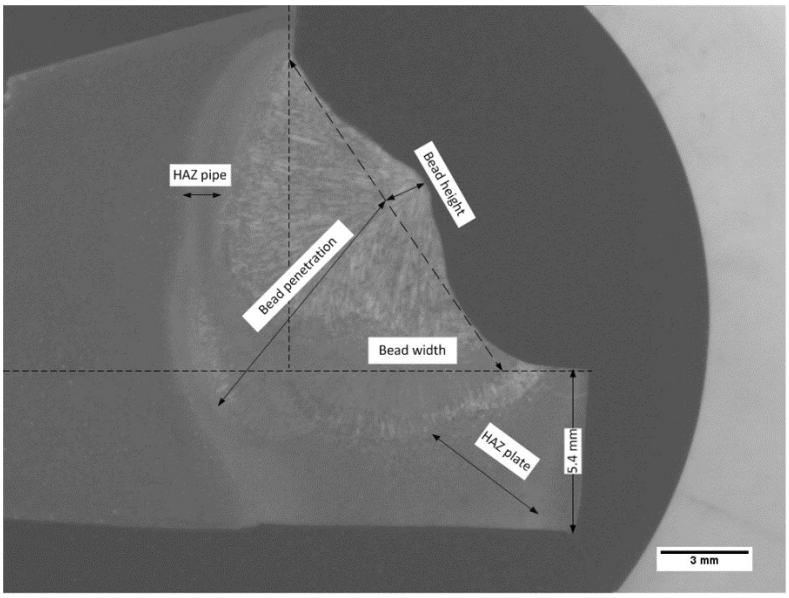

Figure 15: Image of bead geometry of sample 4

Sample 6

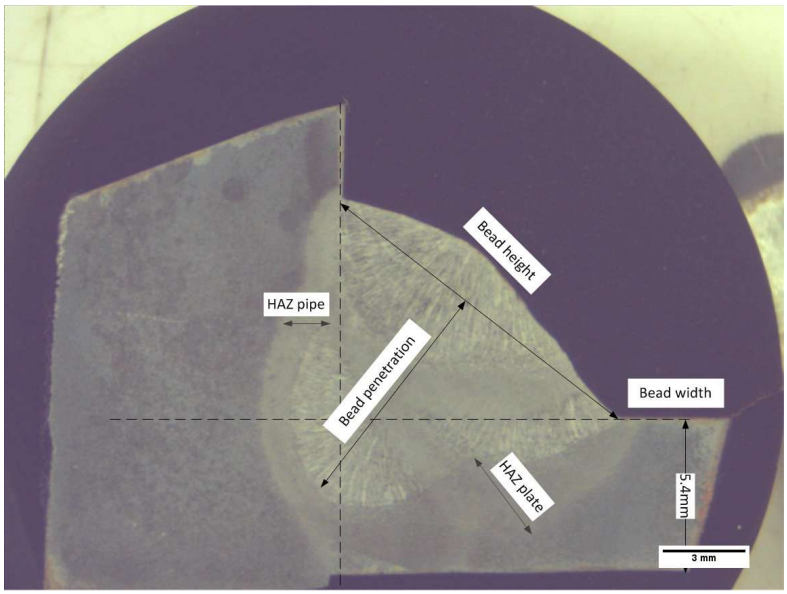

Figure 15: Image of the Bead geometry of Sample 3 at a magnification 0.8x

Sample 7

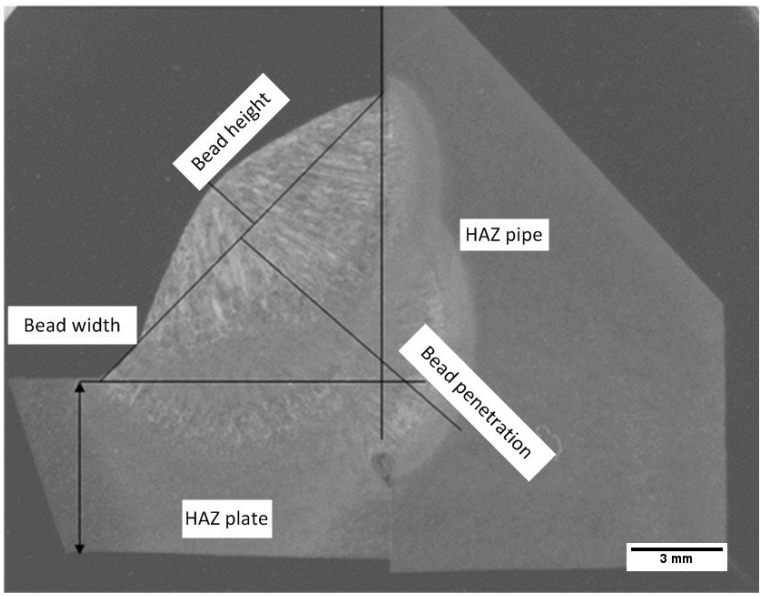

Figure 19. Micrograph obtained using a stereo microscope obtained at a magnification of 0.8x

Sample 8

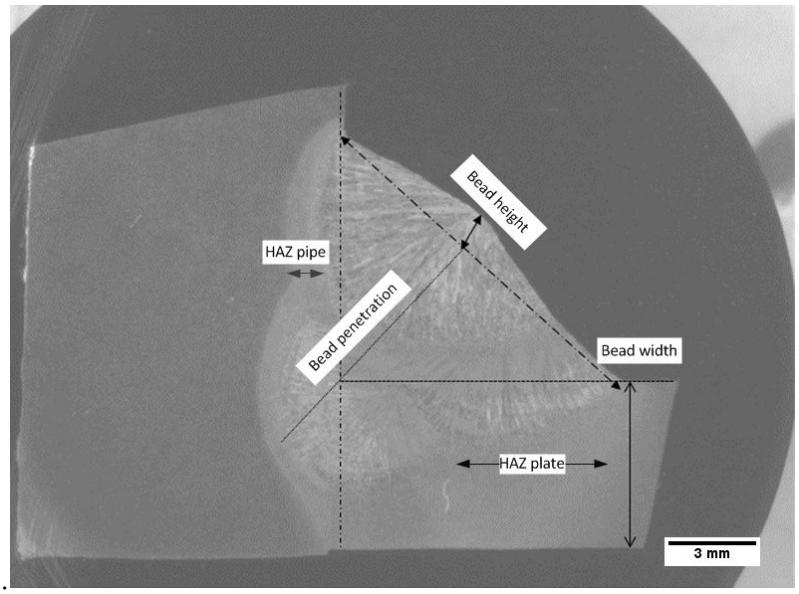

Figure 23. Micrograph obtained using a stereo microscope obtained at a magnification of 0.8x

Sample 9

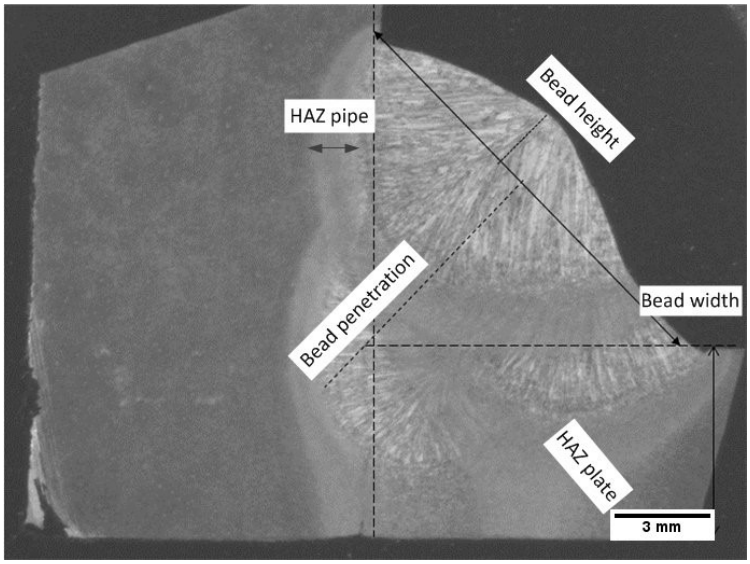

Figure 27. Micrograph obtained using a stereo microscope obtained at a magnification of 0.8x

Sample 10

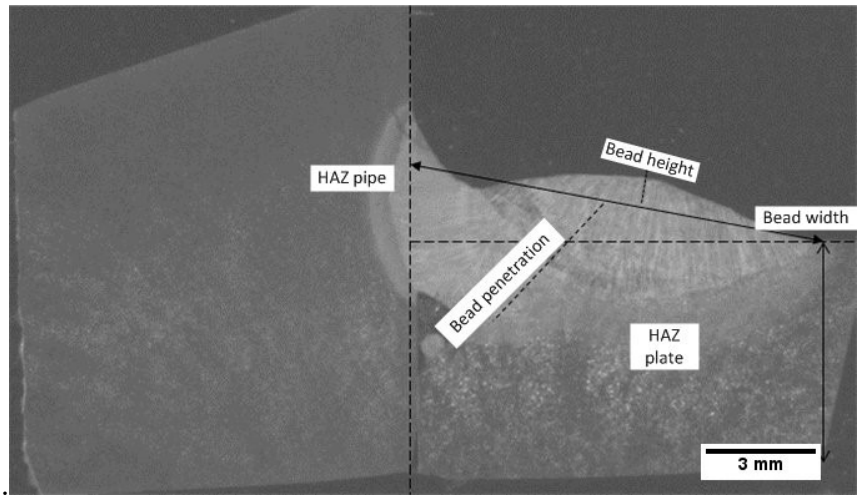

Figure31. Micrograph obtained using a stereo microscope obtained at a magnification of 0.8x

Sample 12

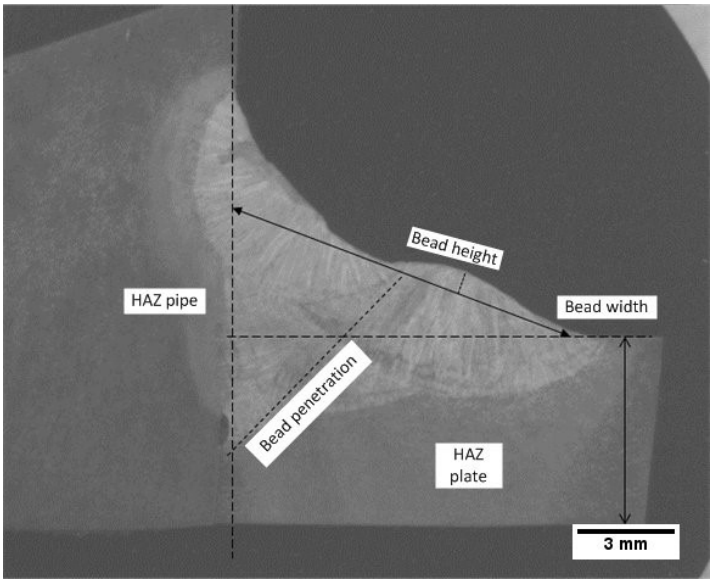

Figure 35. Micrograph obtained using a stereo microscope obtained at a magnification of 0.8x

Sample 13

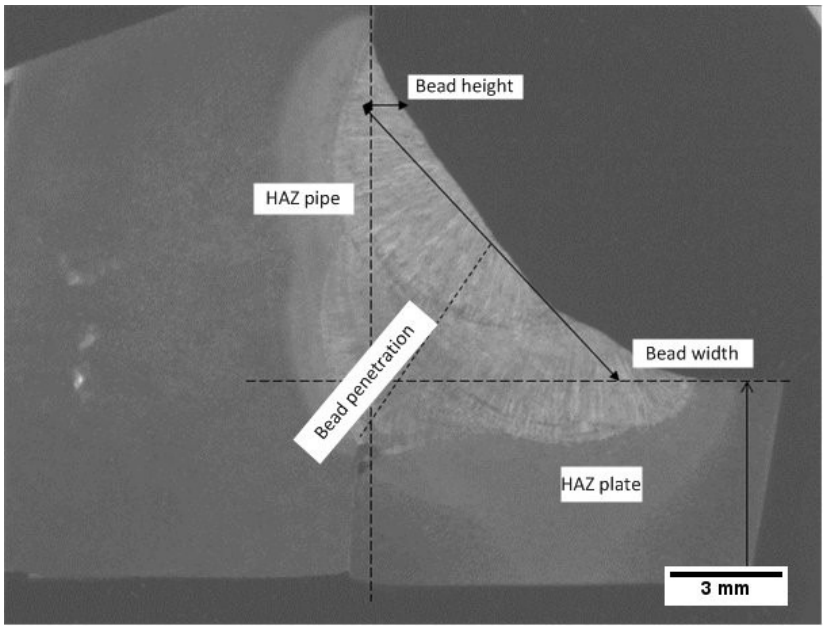

Figure 39:a stereo micrograph of the overall weld and the bead geometry

Sample 15

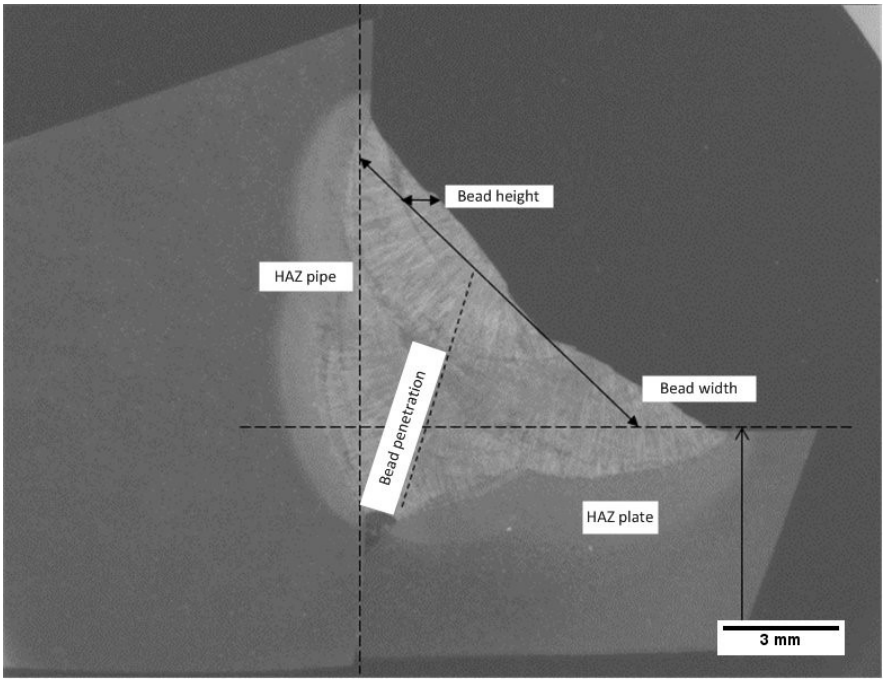

Figure 43: A stereo micrograph of the overall weld and the bead geometry at a magnification of 0.8x

Sample 16

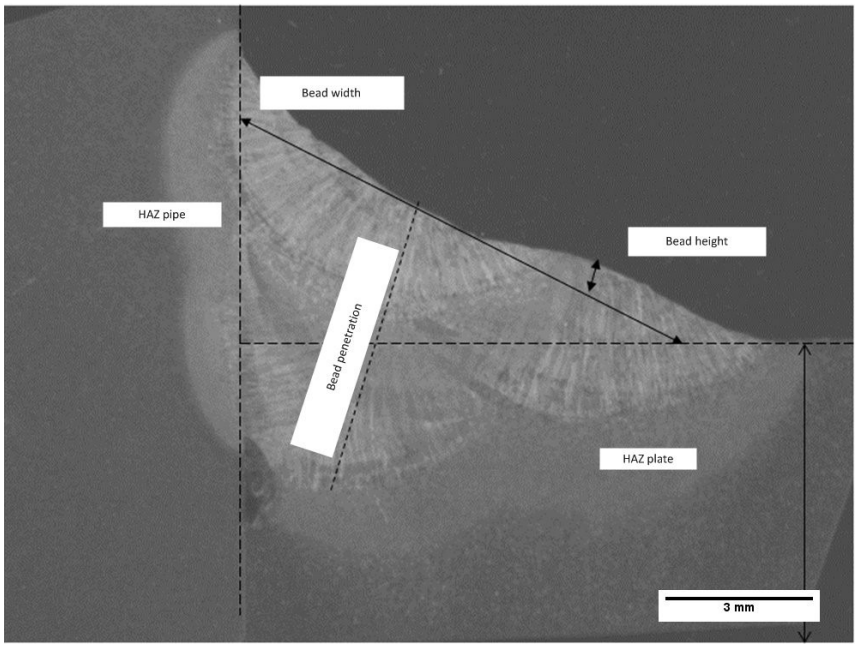

***Figure** 47: A stereo micrograph of the overall weld and the bead geometry at a magnification of 0.8x*

APPENDIX G: Anova Tables

ANOVA TABLES

ANOVA For Bead Width (BW)

Source	Sum of Squares	DoF	Mean Square	F-Value	p-value Prob > F	Remarks		
Model	17.78693	5	3.557386	10.25902	0.041927	significant	Std. Dev	0.588861
A-I	0.050205	1	0.050205	0.144783	0.728915		Mean	11.49
B-V	0.254294	1	0.254294	0.733349	0.454753		C.V. %	5.124984
C-S	0.009645	1	0.009645	0.027814	0.878155		PRESS	8.665858
D-FR	0.081225	1	0.081225	0.234242	0.661528		R-Sqd	0.944746
E-MODE	5.553693	1	5.553693	16.0161	0.027972		Adj. R-Sqd	0.852657
Residual	1.04027	3	0.346757				Pred. R-Sqd	0.539716
Cor Total	18.8272	8					Adeq. Precsn	7.433119

ANOVA For Bead Height (BH)

Source	Sum of Squares	DoF	Mean Square	F-Value	p-value Prob > F	Remarks		
Model	1.515662	5	0.303132	3.38283	0.172349	not significant	Std. Dev	0.299348
A-I	0.154313	1	0.154313	1.722066	0.280801		Mean	1.311111
B-V	0.193501	1	0.193501	2.159394	0.238037		C.V. %	22.83161
C-S	0.020183	1	0.020183	0.225231	0.66749		PRESS	2.79199
D-FR	0.0036	1	0.0036	0.040174	0.853958		R-Sqd	0.849353
E-MODE	0.138465	1	0.138465	1.545212	0.302142		Adj. R-Sqd	0.598276
Residual	0.268827	3	0.089609				Pred. R-Sqd	-0.56459
Cor Total	1.784489	8					Adeq. Precsn	5.06401

ANOVA For Bead Penetration (BP)

Source	Sum of Squares	DoF	Mean Square	F-Value	p-value Prob > F	Remarks		
Model	11.58012	5	2.316024	6.493304	0.077266	not significant	Std. Dev	0.597226
A-I	0.573124	1	0.573124	1.606834	0.294386		Mean	7.922222
B-V	0.272421	1	0.272421	0.763771	0.446475		C.V. %	7.538616
C-S	0.186554	1	0.186554	0.52303	0.521839		PRESS	11.96735
D-FR	0.2916	1	0.2916	0.817542	0.432549		R-Sqd	0.915413
E-MODE	7.102081	1	7.102081	19.9117	0.020959		Adj. R-Sqd	0.774435
Residual	1.070036	3	0.356679				Pred. R-Sqd	0.053976
Cor Total	12.65016	8					Adeq. Precsn	6.642478

ANOVA For Plate-side HAZ (PTHAZ)

Source	Sum of Squares	DoF	Mean Square	F-Value	p-value Prob > F	Remarks		
Model	12.80324	5	2.560647	2.278932	0.264769	not significant	Std. Dev	1.060008
A-I	0.303713	1	0.303713	0.270299	0.639058		Mean	3.881111
B-V	11.74683	1	11.74683	10.45447	0.048094		C.V. %	27.31198
C-S	0.292263	1	0.292263	0.260109	0.645198		PRESS	23.93894
D-FR	0.497025	1	0.497025	0.442344	0.553555		R-Sqd	0.791589
E-MODE	0.317418	1	0.317418	0.282497	0.631908		Adj. R-Sqd	0.444238
Residual	3.370852	3	1.123617				Pred. R-Sqd	-0.48008
Cor Total	16.17409	8					Adeq. Precsn	3.973563

ANOVA For Pipe-side HAZ (PPHAZ)

Source	Sum of Squares	DoF	Mean Square	F-Value	p-value Prob > F	Remarks		
Model	2.428521	5	0.485704	3.433072	0.169449	not significant	Std. Dev	0.376136
A-I	0.043601	1	0.043601	0.308181	0.617507		Mean	1.532222
B-V	0.073873	1	0.073873	0.522152	0.522162		C.V. %	24.54837
C-S	0.001841	1	0.001841	0.013012	0.916388		PRESS	3.757495
D-FR	1.311025	1	1.311025	9.266633	0.055686		R-Sqd	0.85123
E-MODE	0.046806	1	0.046806	0.330835	0.605473		Adj. R-Sqd	0.60328
Residual	0.424434	3	0.141478				Pred. R-Sqd	-0.31705
Cor Total	2.852956	8					Adeq. Precsn	4.775404

ANOVA For Plate-side HAZ Hardness (VHN PTHAZ)

Source	Sum of Squares	DoF	Mean Square	F-Value	p-value Prob > F	Remarks		
Model	561.1002	5	112.22	0.999635	0.535277	not significant	Std. Dev	10.59533
A-I	28.57021	1	28.57021	0.254498	0.648647		Mean	195.14
B-V	32.71475	1	32.71475	0.291417	0.62681		C.V. %	5.429604
C-S	55.50781	1	55.50781	0.494453	0.532605		PRESS	2963.761
D-FR	103.4289	1	103.4289	0.921325	0.407937		R-Sqd	0.624914
E-MODE	153.6676	1	153.6676	1.368842	0.326503		Adj. R-Sqd	-0.00023
Residual	336.783	3	112.261				Pred. R-Sqd	-2.30083
Cor Total	897.8832	8					Adeq. Precsn	3.090166

ANOVA For Weld Metal Hardness (VHN WM)

Source	Sum of Squares	DoF	Mean Square	F-Value	p-value Prob > F	Remarks		
Model	1874.6	5	374.92	5.07432	0.105847	not significant	Std. Dev	8.595683
A-I	85.90713	1	85.90713	1.162702	0.359881		Mean	219.2656
B-V	701.6367	1	701.6367	9.496237	0.054068		C.V. %	3.920216
C-S	110.8215	1	110.8215	1.499904	0.308081		PRESS	1889.379
D-FR	27.09203	1	27.09203	0.366674	0.587563		R-Sqd	0.89426
E-MODE	36.23288	1	36.23288	0.490391	0.534176		Adj. R-Sqd	0.718028
Residual	221.6573	3	73.88577				Pred. R-Sqd	0.098689
Cor Total	2096.257	8					Adeq. Precsn	6.742491

ANOVA For Pipe-side HAZ Hardness (VHN PPHAZ)

Source	Sum of Squares	DoF	Mean Square	F-Value	p-value Prob > F	Remarks		
Model	1733.021	5	346.6042	0.137162	0.971678	not significant	Std. Dev	50.26894
A-I	43.4702	1	43.4702	0.017203	0.903951		Mean	226.3389
B-V	397.3864	1	397.3864	0.157258	0.718218		C.V. %	22.20959
C-S	5.390205	1	5.390205	0.002133	0.966065		PRESS	65087.12
D-FR	465.4806	1	465.4806	0.184205	0.69674		R-Sqd	0.186068
E-MODE	164.616	1	164.616	0.065144	0.815041		Adj. R-Sqd	-1.17049
Residual	7580.898	3	2526.966				Pred. R-Sqd	-5.98816
Cor Total	9313.919	8					Adeq. Precsn	1.193801

ANOVA For Plate-side Residual Stress (PTRS)

Source	Sum of Squares	DoF	Mean Square	F-Value	p-value Prob > F	Remarks		
Model	10389.88	5	2077.976	2.279865	0.264659	not significant	Std. Dev	30.19018
A-I	7200.909	1	7200.909	7.900524	0.067249		Mean	377.5556
B-V	70.15909	1	70.15909	0.076976	0.799459		C.V. %	7.996222
C-S	930.9091	1	930.9091	1.021353	0.386634		PRESS	24401.16
D-FR	1980.25	1	1980.25	2.172644	0.236921		R-Sqd	0.791657
E-MODE	541.9668	1	541.9668	0.594622	0.496804		Adj. R-Sqd	0.444418
Residual	2734.341	3	911.447				Pred. R-Sqd	-0.85925
Cor Total	13124.22	8					Adeq. Precsn	4.462442

ANOVA For Pipe-side Residual Stress (PPRS)

Source	Sum of Squares	DoF	Mean Square	F-Value	p-value Prob > F	Remarks		
Model	51373.94	5	10274.79	9.302341	0.047909	significant	Std. Dev	33.23459
A-I	25141.54	1	25141.54	22.76204	0.017495		Mean	429.7778
B-V	20114.03	1	20114.03	18.21036	0.023614		C.V. %	7.73297
C-S	7981.536	1	7981.536	7.226132	0.074531		PRESS	29229.93
D-FR	132.25	1	132.25	0.119733	0.752169		R-Sqd	0.939408
E-MODE	39859.56	1	39859.56	36.08709	0.009241		Adj. R-Sqd	0.838422
Residual	3313.614	3	1104.538				Pred. R-Sqd	0.46551
Cor Total	54687.56	8					Adeq. Precsn	8.942355

APPENDIX H: Pareto Optimal Set

PARETO OPTIMAL SET

Optimization Settings for CA with combination of Multi Objective Equations BW, BH, BP, PTHAZ and PPHAZ

The settings are in the following order I(Amps), V(Volts), S(mm/s) and FR(mm/s)

361.4735 25.0004 8.0040 18.2946

377.2664 29.9673 9.9888 16.7529

361.8191 29.9869 8.0617 18.2980

379.8291 25.0781 8.1206 18.1953

360.6255 29.9986 9.8966 16.7516

378.2137 25.0762 9.9660 16.7078

378.7066 25.0771 8.4523 18.0045

379.3570 25.0175 9.9810 18.2900

378.2137 25.0762 9.9660 16.7078

369.9529 25.5221 8.6398 18.2726

361.2804 29.9826 9.1355 16.8823

376.1446 27.8768 9.8706 17.9500

360.7878 29.1275 8.7109 16.7846

368.4015 26.8535 9.9290 18.0238

361.2325 29.1064 8.4735 18.2647

362.3814 26.0426 9.7152 18.2805

378.7011 25.4507 9.8446 16.7100

374.3785 29.9847 9.9729 16.7525

361.0944 29.9328 9.9884 18.2999

360.6255 29.9986 9.8966 16.8766

Optimization Settings for CW with combination of Multi Objective Equations BW, BH, BP, PTHAZ and PPHAZ

The settings are in the following order I(Amps), V(Volts), S(mm/s) and FR(mm/s)

377.3188 25.1371 9.2808 16.7156

377.5324 25.1115 9.9968 16.7087

360.4651 29.9870 9.7726 18.2820

360.1216 29.3639 9.8994 18.2731

368.5625 25.0922 9.9915 16.7177

360.3681 29.9490 8.0379 18.2892

360.3134 29.9842 8.2098 17.0626

378.5741 25.1812 9.9973 17.8701

362.9675 25.8217 8.4040 16.8547

366.1595 29.9733 8.1718 18.0369

372.6023 25.4133 9.6333 17.9072

360.2109 29.8925 8.6725 18.2770

363.6004 29.9264 9.3745 17.5821

363.1565 25.8316 9.4344 18.0208

370.7539 28.8981 9.4438 18.1513

360.8681 29.9490 8.0379 18.2892

360.6181 29.9490 8.5379 18.2892

362.4840 29.9867 9.9442 18.2829

Optimization Settings for CA with combination of Multi Objective Equations VHN(PTHAZ), VHN(WM), VHN(PPHAZ), PTRS and PPRS

The settings are in the following order I(Amps), V(Volts), S(mm/s) and FR(mm/s)

362.9764	29.7644	8.3396	16.7304
363.1314	29.9996	8.8308	18.2983
362.7722	25.0994	8.2192	18.2292
362.9360	29.9881	8.2209	18.2987
364.7993	28.8771	8.4667	16.7333
365.6500	27.5152	8.8202	18.2931
374.1210	25.0571	9.7722	18.0495
377.9203	25.0333	9.7808	16.8932
379.1523	25.0527	9.8088	18.2519
367.3939	26.4335	8.8208	17.7096
363.0623	29.9987	9.6786	16.8526
379.1073	25.0628	8.4838	18.2810
369.5476	25.0580	9.0927	18.2403
363.1611	25.8826	8.4274	16.9934
371.5626	29.8680	9.6586	16.7230
373.8232	27.0183	8.4694	17.9095
376.9506	25.0368	9.6872	17.0493
367.1698	27.7540	9.0964	17.3690
363.2077	28.8975	8.7139	18.2176
370.1373	28.8540	8.8939	17.5275
363.0773	29.0017	8.2921	18.2300
377.1927	25.4850	8.7615	18.2723
370.2249	25.8494	8.8466	17.3368
369.9622	29.9636	8.6977	18.1499

375.4018 25.1306 9.3637 16.9128

Optimization Settings for CW with combination of Multi Objective Equations VHN(PTHAZ), VHN(WM), VHN(PPHAZ), PTRS and PPRS

The settings are in the following order I(Amps), V(Volts), S(mm/s) and FR(mm/s)

360.0173 29.9868 9.9547 18.2987

378.4695 25.1175 9.9917 16.7441

360.1174 29.9926 8.1559 16.7040

377.5512 26.6916 9.0386 17.0898

363.3897 25.0312 9.9370 16.7050

379.3680 25.1331 9.9917 18.2754

370.9343 26.4684 9.7217 16.9207

373.0903 25.5628 8.7403 16.9931

369.0966 29.1968 9.2984 16.8410

376.3169 25.5214 9.6008 18.1057

360.1030 29.9921 8.0018 18.2788

363.8591 27.0263 9.6894 16.7220

363.2636 26.8283 9.1702 17.8931

360.2909 29.8977 8.1804 17.3563

360.5933 29.5041 8.6331 18.1324

378.4160 25.1594 9.7831 16.7433

378.0328 25.7888 9.8332 16.9803

365.1754 29.0837 9.6083 17.9871

378.6268 25.1177 9.9917 17.7230

363.6126 27.9062 9.1215 16.9088

360.1019 29.9892 8.4630 18.2714

374.7043 27.0756 9.4391 17.5410